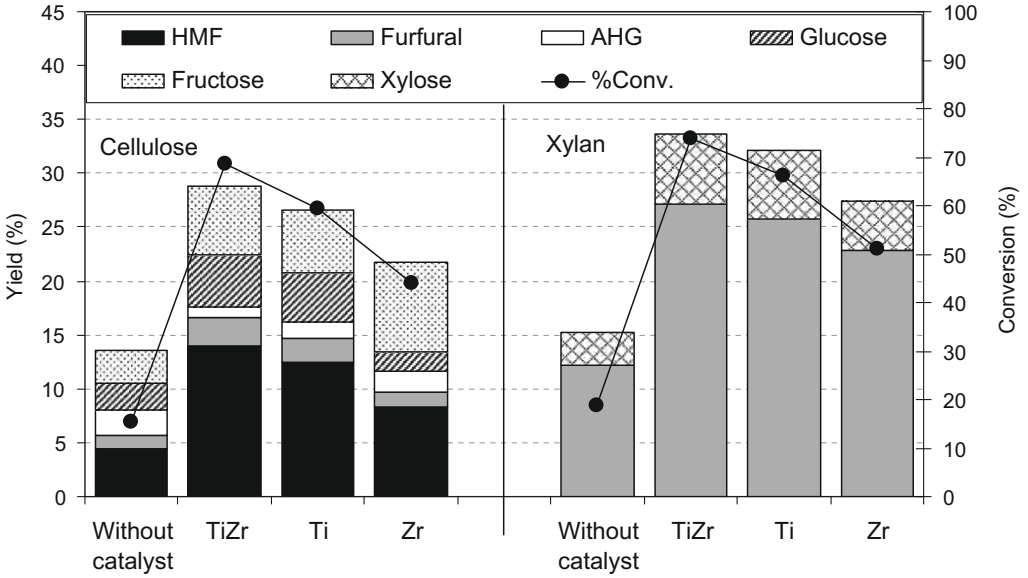

Fig. 5. Conversions and yield of liquid products from the reactions of cellulose and xylan at 523 K and 5 min with and without the presence of catalysts.

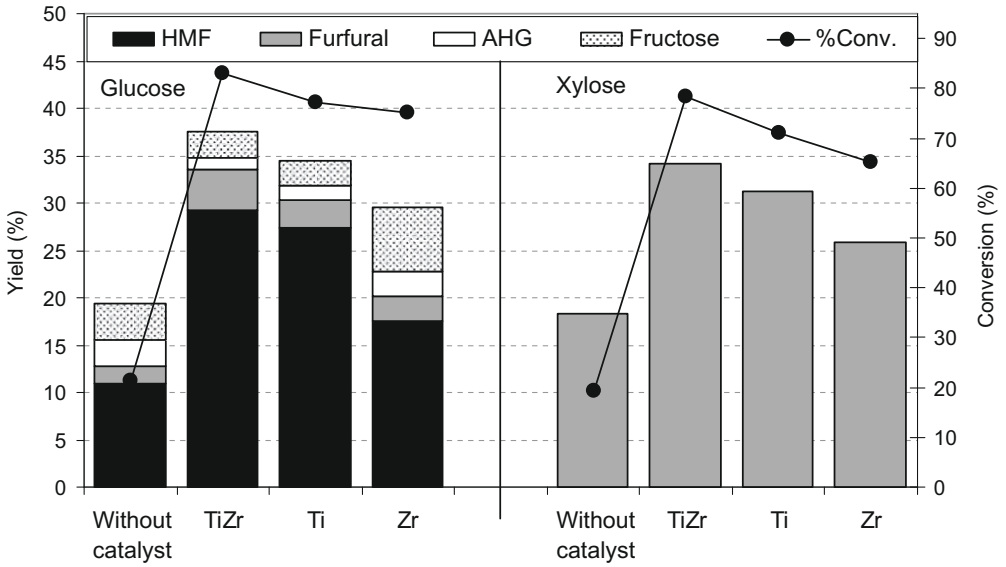

Fig. 6. Conversions and yield of liquid products from the reactions of glucose and xylose at 523 K and 5 min with and without the presence of catalysts.

profiles, are listed in Table 2. Along with these values, the distribution of acid and base site on the catalyst surface (namely the density of acid and base site; μmol m^{-2}) and the strength of acid and base sites (the top peak of TPD spectra) are also given in the table since these parameters are important indicators to determine the catalytic reactivity of acid and base reactions (Maniriquez et al., 2004; Tomishige et al., 2000). Among all catalysts, TiO_2–ZrO_2 with Ti/Zr molar ratio of 1/1 shows the greatest amounts and densities for both acid and base sites; in addition, the highest peaks of NH_3- and CO_2-TPD spectra for this catalyst was relatively lower than other two catalysts indicated that the strengths of acid and base sites for TiO_2–ZrO_2 were weak. It should be noted that the calcinations temperature and preparation procedure also affect the acidity–basicity properties of catalysts; the amount of acid sites decreased with increasing the calcinations temperature whereas the base sites increased for all catalysts. As for the preparation procedure, the catalysts prepared by co-precipitation method gained the greatest acidity–basicity properties, whereas those from physical mixing were the lowest.

According to the catalyst reactivity and all characterization results, it can be concluded that the catalyst reactivity, phase formation and acidity–basicity properties are closely related. The catalyst with high acid site density and weak acid site can enhance the great reactivity toward hydrolysis and dehydration reactions, while the catalyst with high base site density and weak base site provides high reactivity toward isomerization reaction. Hence, high HMF and furfural productions can be achieved from TiO_2–ZrO_2 (prepared by co-precipitation method with Ti/Zr molar ratio of 1/1) since this catalyst shows the bifunctionality for both acidity and basicity properties, according to the TPD experiments. It is noted that the acidity of TiO_2 and ZrO_2 decreased with increasing temperature, thus the reactivities of catalysts that calcined at low temperature (773 K) is greater than those calcined at higher temperatures. Nevertheless, for TiO_2–ZrO_2 the best reactivity was

Table 1
N_2 physisorption (BET) results of TiO_2, ZrO_2 and TiO_2–ZrO_2 (prepared by various methods and treated under different conditions).

Catalysts	BET surface area[a] (m^2/g)	Cumulative pore volume[b] (cm^3/g)	Average pore diameter[c] (nm)
Ti–P-773	48.2	0.120	4.6
Ti–P-873	35.9	0.109	4.9
Ti–P-973	20.1	0.098	5.2
Ti–S-773	36.3	0.096	4.9
Ti–S-873	25.9	0.073	5.3
Ti–S-973	11.7	0.051	5.4
TiZr–P-773	124	0.234	4.3
TiZr–P-873	101	0.217	4.6
Zr–P-973	76.3	0.210	4.6
Zr–S-773	95.2	0.147	4.6
Zr–S-873	73.9	0.110	5.1
Zr–S-973	54.0	0.079	5.3
TiZr–P-773 (Ti/Zr = 1/1)	198	0.394	2.5
TiZr–P-873 (Ti/Zr = 1/1)	187	0.391	2.5
TiZr–P-973 (Ti/Zr = 1/1)	165	0.382	2.7
TiZr–S-773 (Ti/Zr = 1/1)	163	0.259	3.3
TiZr–S-873 (Ti/Zr = 1/1)	149	0.217	3.9
TiZr–S-973 (Ti/Zr = 1/1)	119	0.194	4.2
TiZr–M-773 (Ti/Zr = 1/1)	121	0.201	3.8
TiZr–M-873 (Ti/Zr = 1/1)	109	0.155	4.4
TiZr–M-973 (Ti/Zr = 1/1)	97.4	0.150	4.9
TiZr–P-873 (Ti/Zr = 3/1)	109	0.181	3.9
TiZr–P-873 (Ti/Zr = 1/3)	130	0.271	4.3

[a] Error of measurement = ±5%.
[b] BJH desorption cumulative volume of pores between 1.7 and 300 nm diameter.
[c] BJH desorption average pore diameter.

Table 2
Acid–base properties of TiO_2, ZrO_2 and TiO_2–ZrO_2 (prepared by various methods and treated under different conditions).

Catalysts	Amount of acid site (μmol/g)	Density of acid site (μmol/m^2)	Amount of base site (μmol/g)	Density of base site (μmol/m^2)
Ti–P-773	161	3.34	84	1.74
Ti–P-873	108	3.00	86	2.39
Ti–P-973	59.1	2.94	92	4.58
Ti–S-773	70.7	1.95	84	2.32
Ti–S-873	47.3	1.83	87	3.37
Ti–S-973	18.0	1.54	88	7.51
Zr–P-773	232	1.87	129	1.04
Zr–P-873	177	1.75	145	1.44
Zr–P-973	119	1.56	166	2.19
Zr–S-773	171	1.80	138	1.45
Zr–S-873	119	1.61	149	2.02
Zr–S-973	62.1	1.15	170	3.14
TiZr–P-773 (Ti/Zr = 1/1)	692	3.49	697	3.52
TiZr–P-873 (Ti/Zr = 1/1)	645	3.45	712	3.81
TiZr–P-973 (Ti/Zr = 1/1)	554	3.35	806	4.89
TiZr–S-773 (Ti/Zr = 1/1)	471	2.89	654	4.01
TiZr–S-873 (Ti/Zr = 1/1)	393	2.64	672	4.51
TiZr–S-973 (Ti/Zr = 1/1)	301	2.53	687	5.78
TiZr–M-773 (Ti/Zr = 1/1)	216	1.79	215	1.78
TiZr–M-873 (Ti/Zr = 1/1)	183	1.68	219	2.01
TiZr–M-973 (Ti/Zr = 1/1)	137	1.41	226	2.33
TiZr–P-873 (Ti/Zr = 3/1)	309	2.84	84	1.74
TiZr–P-873 (Ti/Zr = 1/3)	256	1.97	86	2.39

observed from the catalyst calcined at 873 K; the use of lower calcinations temperature (773 K) resulted in the low reaction reactivity, whereas the catalyst calcined at higher temperature (973 and 1073 K) was also found inactive (due to the reducing of catalyst acidity at high calcinations temperature). According to the XRD patterns of TiO_2–ZrO_2, the phase of TiO_2–ZrO_2 turns from amorphous to crystalline phase at 873 K; hence this revealed the impact of catalyst phase formation on its reaction reactivity (the crystalline phase is the active one for the interested reactions). It can also be seen from the studies that the phase TiO_2 and ZrO_2 also affected its reaction reactivity i.e. TiO_2 calcined at low temperature of 773 K (mainly anatase phase) showed better reactivity than that calcined at higher temperature (slight formation of rutile phase detected); this result is in good agreement with the results reported by Watanabe et al. (2005a,b) who indicated that anatase–TiO_2 showed better dehydration reactivity than rutile–TiO_2. As for ZrO_2, we found that the catalyst with larger portion of tetragonal phase (compared to monoclinic phase) shows greater reactivities toward hydrolysis and dehydration.

4. Conclusions

The reaction of lignocellulosic biomass under HCW condition at 573 K efficiently produced furfural and HMF. In the presence of TiO_2–ZrO_2, high product yields can be achieved due to the

promotion of hydrolysis, isomerization and dehydration reactions. The catalysts prepared by (co-) precipitation gained higher reactivity than those prepared by sol–gel and physical mixing due to their greater acidity. Furthermore, the catalyst calcination temperature also made strong impact on its reactivity with regard to the portion of phase formation (i.e. anatase/rutile for TiO_2, monoclinic/tetragonal for ZrO_2 and amorphous/crystalline for TiO_2–ZrO_2), which strongly affected the acidity–basicity and the reactivity of catalysts.

Acknowledgement

The financial support from The Thailand Research Fund (TRF) throughout this project is gratefully acknowledged.

References

Aida, T.M., Watanabe, M., Aizawa, Y., Iida, T., Levy, C., Sue, K., Inomata, H., 2007. Dehydration of D-glucose in high temperature water at pressures up to 80 MPa. J. Supercrit. Fluids 40, 381–388.

Ando, H., Ohba, H., Sakaki, T., Takamine, K., Kamino, Y., Moriwaki, S., Bakalova, R., Uemura, Y., Hatate, Y., 2004. Hot-compressed-water decomposed products from bamboo manifest a selective cytotoxicity against acute lymphoblastic leukemia cells. Toxicol. In Vitro 18, 765–771.

Asghari, F.S., Yoshida, H., 2006. Dehydration of fructose to 5-hydroxymethylfurfural in sub-critical water over heterogeneous zirconium phosphate catalysts. Carbohydr. Res. 341, 2379–2387.

Bicker, M., Hirth, J., Vogel, H., 2003. Dehydration of fructose to 5-hydroxymethylfurfural in sub- and supercritical acetone. Green Chem. 5, 280–284.

Bower, S., Wickramasinghe, R., Nagle, N.J., Schell, D.J., 2008. Modeling sucrose hydrolysis in dilute sulfuric acid solutions at pretreatment conditions for lignocellulosic biomass. Bioresour. Technol. 99, 7354–7362.

Cheng, H., Zhu, X., Zhu, C., Qian, J., Zhu, N., Zhao, L., Chen, J., 2008. Hydrolysis technology of biomass waste to produce amino acids in sub-critical water. Bioresour. Technol. 99, 3337–3341.

Huber, G.W., Chheda, J.N., Barrett, C.J., Dumesic, J.A., 2005. Production of liquid alkanes by aqueous-phase processing of biomass-derived carbohydrates. Science 308, 1446–1450.

Kabyemela, B.M., Malaluan, R.M., Adschiri, T., Arai, K., 1997. Kinetics of glucose epimerization and decomposition in subcritical and supercritical water. Ind. Eng. Chem. Res. 36, 1552–1558.

Karimi, K., Kheradmandinia, S., Taherzadeh, M.J., 2006. Conversion of rice straw to sugars by dilute-acid hydrolysis. Biomass Bioenergy 30, 247–253.

Laopaiboon, P., Thani, A., Leelavatcharamas, V., Laopaiboon, L., 2010. Acid hydrolysis of sugarcane bagasse for lactic acid production. Bioresour. Technol. 101, 1036–1043.

Maniriquez, M.E., Lopez, T., Gomez, R., Navarrete, J., 2004. Preparation of TiO_2–ZrO_2 mixed oxides with controlled acid–basic properties. J. Mol. Catal. A 220, 229–237.

Minowa, T., Inoue, S., 1999. Hydrogen production from biomass by catalytic gasification in hot compressed water. Renew. Energy 16, 1114–1117.

Moreau, C., Durand, R., Roux, A., Tichit, D., 2000. Isomerization of glucose into fructose in the presence of cation-exchanged zeolites and hydrotalcites. Appl. Catal. A 193, 257–264.

Sasaki, M., Goto, K., Tajima, K., Adschiri, T., Arai, K., 2002. Rapid and selective retro–aldol condensation of glucose to glycolaldehyde in supercritical water. Green Chem. 4, 285–287.

Sasaki, M., Takahashi, K., Haneda, Y., Satoh, H., Sasaki, A., Narumi, A., Satoh, T., Kakuchi, T., Kaga, H., 2008. Thermochemical transformation of glucose to 1,6-anhydroglucose in high-temperature steam. Carbohydr. Res. 343, 848–854.

Sun, Y., Cheng, J., 2002. Hydrolysis of lignocellulosic materials for ethanol production: a review. Bioresour. Technol. 83, 1–11.

Thomsen, M.H., Thygesen, A., Thomsen, A.B., 2008. Hydrothermal treatment of wheat straw at pilot plant scale using a three-step reactor system aiming at high hemicellulose recovery, high cellulose digestibility and low lignin hydrolysis. Bioresour. Technol. 99, 4221–4228.

Tomishige, K., Ikeda, Y., Sakaihori, T., Fujimoto, K., 2000. Catalytic properties and structure of zirconia catalysts for direct synthesis of dimethyl carbonate from methanol and carbon dioxide. J. Catal. 192, 355–362.

Vázquez, M., Oliva, M., Téllez-Luis, S.J., Ramírez, J.A., 2007. Hydrolysis of sorghum straw using phosphoric acid: evaluation of furfural production. Bioresour. Technol. 98, 3053–3060.

Watanabe, M., Aizawa, Y., Iida, T., Aida, T.M., Levy, C., Sue, K., Inomata, H., 2005a. Glucose reactions with acid and base catalysts in hot compressed water at 473 K. Carbohydr. Res. 340, 1925–1930.

Watanabe, M., Aizawa, Y., Iida, T., Nishimura, R., Inomata, H., 2005b. Catalytic glucose and fructose conversions with TiO_2 and ZrO_2 in water at 473 K: relationship between reactivity and acid–base property determined by TPD measurement. Appl. Catal. A 295, 150–156.

Weil, J.R., Dien, B., Bothast, R., Hendrickson, R., Mosier, N.S., Ladisch, M.C., 2002. Removal of fermentation inhibitors formed during pretreatment of biomass by polymeric adsorbents. Ind. Eng. Chem. Res. 41, 6132–6138.

Yang, B.Y., Montgomery, R., 1996. Alkaline degradation of glucose: effect of initial concentration of reactants. Carbohydr. Res. 280, 27–45.

Yat, S.C., Berger, A., Shonnard, D.R., 2008. Kinetic characterization for dilute sulfuric acid hydrolysis of timber varieties and switchgrass. Bioresour. Technol. 99, 3855–3863.

Zhang, Z., Zhao, Z.K., 2010. Microwave-assisted conversion of lignocellulosic biomass into furans in ionic liquid. Bioresour. Technol. 101, 1111–1114.

Bioresource Technology 101 (2010) 8416–8423

Contents lists available at ScienceDirect

Bioresource Technology

journal homepage: www.elsevier.com/locate/biortech

Synthesis of methyl esters from relevant palm products in near-critical methanol with modified-zirconia catalysts

N. Laosiripojana [a,*], W. Kiatkittipong [b], W. Sutthisripok [c], S. Assabumrungrat [d]

[a] The Joint Graduate School of Energy and Environment, King Mongkut's University of Technology Thonburi, Thailand
[b] Department of Chemical Engineering, Faculty of Engineering and Industrial Technology, Silpakorn University, Nakhon Pathom 73000, Thailand
[c] Department of Mining and Materials Engineering, Faculty of Engineering, Prince of Songkla University, Songkhla, Thailand
[d] Department of Chemical Engineering, Faculty of Engineering, Chulalongkorn University, Bangkok 10330, Thailand

ARTICLE INFO

Article history:
Received 4 March 2010
Received in revised form 24 May 2010
Accepted 25 May 2010
Available online 25 June 2010

Keywords:
Transesterification
Esterification
Tungsten zirconia
Palm oil

ABSTRACT

The transesterification and esterification of palm products i.e. crude palm oil (CPO), refined palm oil (RPO) and palm fatty acid distillate (PFAD) under near-critical methanol in the presence of synthesized SO_4–ZrO_2, WO_3–ZrO_2 and TiO_2–ZrO_2 (with various sulfur- and tungsten loadings, Ti/Zr ratios, and calcination temperatures) were studied. Among them, the reaction of RPO with 20%WO_3–ZrO_2 (calcined at 800 °C) enhanced the highest fatty acid methyl ester (FAME) yield with greatest stability after several reaction cycles; furthermore, it required shorter time, lower temperature and less amount of methanol compared to the reactions without catalyst. These benefits were related to the high acid-site density and tetragonal phase formation of synthesized WO_3–ZrO_2. For further improvement, the addition of toluene as co-solvent considerably reduced the requirement of methanol to maximize FAME yield, while the addition of molecular sieve along with catalyst significantly increased FAME yield from PFAD and CPO due to the inhibition of hydrolysis reaction.

1. Introduction

Biodiesel or methyl ester is known as a promising renewable fuel to replace petroleum-based oil in transportation section. It can be efficiently produced from the transesterification of vegetable oil and/or animal fat with short chain alcohols (e.g. methanol). Currently, palm oil is the major feedstock for biodiesel production in Thailand due to its availability and good conversion efficiency. Typically, crude palm oil (CPO) contains high amount of free fatty acids (FFAs), which easily converts to soap during the transesterification reaction and consequently reduces the overall process performance (Zallaikah et al., 2005). To avoid this formation, most of FFAs in CPO must be treated or removed (as called palm fatty acid distilled or PFAD); and the treated palm oil after PFAD removal is called refined palm oil (RPO), which can be efficiently converted to biodiesel via transesterification reaction. It is noted that the conversion of PFAD to fatty acid methyl ester (FAME) via esterification reaction is a good procedure to reduce the production cost of biodiesel and consequently to make biodiesel enable to compete economically with petroleum-based fuels.

Theoretically, both transesterification and esterification reactions require catalyst to activate the reaction. The typical catalysts for these reactions are the homogeneous alkali- and/or acid-based catalysts (e.g. NaOH, H_2SO_4); nevertheless, the major limitation of homogeneous catalyzed reactions is the difficulty for catalyst recovery and treatment, which causes large amount of wastewater and increase the overall cost of the process. In addition, according to the technical report of local palm oil refinery industries, the acid-catalyzed esterification process with H_2SO_4 seems to be unsuitable due to the massive corrosion in several system equipments. As an alternative procedure, heterogeneous catalyst has widely been reported to overcome these problems due to its easily separate and recover from the process (Kiss et al., 2006). Previously, several solid catalysts have been investigated for transesterification and esterification reactions (Furuta et al., 2004; Lopez et al., 2005; Kiss et al., 2006; Kim et al., 2010; Sun et al., 2010). Among them, sulfated zirconia (SO_4–ZrO_2) has been known to give high activity and selectivity for transesterification and esterification of several vegetable oils and fatty acids (Lopez et al., 2005; Kiss et al., 2006; Garcia et al., 2008); this catalyst can also be applied in several important industrial processes e.g. hydrocarbon isomerization and alkylation (Tanabe and Holderich, 1999). Apart from SO_4–ZrO_2, other zirconia-based catalysts e.g. TiO_2–ZrO_2 and WO_3–ZrO_2 have also been of interest to researchers for several acid- and base-catalyzed reactions. TiO_2–ZrO_2 is known to have bifunctionality for both acidity and basicity properties which benefits for acid- and base-catalyzed reactions e.g. hydrolysis and

* Corresponding author. Tel.: +66 662 872 9014; fax: +66 662 872 6736.
E-mail address: navadol_l@jgsee.kmutt.ac.th (N. Laosiripojana).

0960-8524/$ - see front matter © 2010 Elsevier Ltd. All rights reserved.
doi:10.1016/j.biortech.2010.05.076

isomerization, while WO_3–ZrO_2 was also reported to active for transesterification and esterification reactions under specific conditions (Furuta et al., 2004; Lopez et al., 2005; Rao et al., 2006).

Alternative to the catalytic processes, Saka and Kusdiana (2001) proposed a method of biodiesel production via non-catalytic transesterification of vegetable oils in supercritical methanol. According to this process, the reaction takes place in a shorter time and the diffusive problem can be eliminated since the reactants form homogeneous phase in supercritical state. Furthermore, feedstock with high FFA content can be efficiently used in this process and the catalyst removal step can be eliminated. However, major disadvantages of this method are the requirement of high operating temperature, pressure and methanol to reactant ratio, which result in high energy consumption and high cost of production. In order to overcome these barriers, several approaches have been investigated i.e. the addition of appropriate solid catalyst which allows the supercritical reaction to be carried out under milder conditions e.g. near-critical condition) (Demirbas, 2007) and the addition of co-solvent along with the feed (Kasim et al., 2009).

In the present work, we aimed to study the transesterification and esterification of relevant palm products i.e. CPO, RPO and PFAD under near-critical methanol in the presence of three synthesized zirconia-based catalysts i.e. SO_4–ZrO_2, TiO_2–ZrO_2 and WO_3–ZrO_2. The effects of catalyst preparing conditions i.e. sulfate and tungsten loadings, Ti/Zr molar ratio, and calcination temperature on the catalyst performance were intensively studied; and the physical characteristics of these synthesized catalysts, i.e. acidity–basicity properties, phase formation and catalyst surface properties were analyzed in order to relate these properties with the catalytic reactivity. Then, the beneficial of these catalysts on the reaction performance in terms of reaction reactivity, reaction time, temperature and amount of alcohol requirements were investigated. In addition, the effect of co-solvent adding on reaction performance was studied by introducing three promising co-solvents (i.e. toluene, benzene and hexane) along with the reactants to the system. Lastly, since it is known that the formation of water during the esterification reaction could strongly inhibit the yield of FAME production, the effect of water removal i.e. as feedstock pre-treatment prior the reaction and during the reaction were studied by adding molecular sieve (as water sorbent) to the reactants. From all studies, the suitable catalyst, type of co-solvent, process to treat water in the system, and the optimum operating conditions for converting CPO, RPO and PFAD to biodiesel were eventually determined.

2. Experimental

2.1. Chemicals

CPO, RPO and PFAD samples used in this study were obtained from Pathum Vegetable Oil, Co. Ltd. (Thailand). PFAD consists of 93.2 wt.% free fatty acid (FFA) (45.6% palmitic, 33.3% oleic, 7.7% linoleic, 3.8% stearic, 1.0% myristic, 0.6% tetracosenoic, 0.3% linolenic, 0.3% ecosanoic, 0.2% ecosenoic, and 0.2% palmitoleic acid) and the rest elements are triglycerides, diglycerides (DG), monoglycerides (MG) and traces of impurities, whereas CPO contains 7 wt.% FFA (43.5% palmitic, 39.8% oleic, 10.2% linoleic, 4.3% stearic). Methyl ester standards (i.e. methyl palmitate, methyl stearate and methyl oleate) were obtained from Wako Chemicals (USA). Commercial grade methanol (95%) and analytical grade hexane, toluene, and benzene (99.9%) ware purchased from Fisher scientific (UK) and commercial grade 3 Å molecular sieve was supplied from Fluka, Buchs (Switzerland).

2.2. Catalyst preparation and characterization

SO_4–ZrO_2 and WO_3–ZrO_2 were prepared by incipient wetness impregnation of sulfuric acid or ammonium metatungstate over zirconium oxide (ZrO_2). Regarding the preparation of ZrO_2, a solution of zirconyl chloride ($ZrOCl_2$) precursor (0.1 M) was slowly dropped into a well-stirred precipitating solution of ammonium hydroxide (NH_4OH) at room temperature. The solution was controlled at pH of 11. The obtained precipitate was removed, and then washed with deionized water and ethanol. Then, the solid sample was dried overnight at 110 °C and calcined at 500 °C for 6 h. SO_4–ZrO_2 and WO_3–ZrO_2 were then prepared by immersing of synthesized ZrO_2 in 0.1 mol l^{-1} of H_2SO_4 and/or ammonium metatungstate at 70 °C for 30 min, then dried overnight at 110 °C and calcined at three different temperatures (500, 600 and 700 °C for SO_4–ZrO_2 and 700, 800 and 900 °C for WO_3–ZrO_2) for 3 h. It is noted that three different amounts of sulfuric acid (providing sulfur contents of 0.75, 1.8 and 2.5 wt.%) and ammonium metatungstate (providing tungsten weight contents of 10, 20 and 30 wt.%) were applied in the present work. For TiO_2–ZrO_2, this catalyst (with Ti/Zr molar ratios of 1/3, 1/1, and 3/1) was prepared by co-precipitation method. In detail, a mixture of zirconium and titanium salt precursors (i.e. zirconyl chloride ($ZrOCl_2$) and titanium chloride ($TiCl_4$) (0.15 M)) was slowly dropped into a well-stirred precipitating solution of ammonium hydroxide (NH_4OH) (2.5 wt.%) at room temperature. The solution was controlled at pH of 11. The obtained precipitate was removed, and then washed with deionized water until Cl^- was not detected by a silver nitrate ($AgNO_3$) solution. Then, the solid sample was dried overnight at 110 °C and calcined at three different temperatures (i.e. 500 °C, 600 °C and 700 °C) under continuous air flow for 6 h with a temperature ramping rate of 10 °C min^{-1}.

After preparation, these synthesized catalysts (with the average particle size of 100–150 μm) were characterized by several techniques. The measurements of BET surface area, cumulative pore volume and average pore diameter were performed by N_2 physisorption technique using Micromeritics ASAP 2020 surface area and porosity analyzer. The XRD patterns of powder were performed by X-ray diffractometer, in which the crystallite size was estimated from line broadening according to the Scherrer equation. NH_3- and CO_2-TPD were used to determine the acid–base properties of catalysts. TPD experiments were carried out using a flow apparatus. The catalyst sample (0.1 g) was treated at 500 °C in helium flow for 1 h and then saturated with 15% NH_3/He mixture or pure CO_2 flow after cooling to 100 °C. After purging with helium, the sample was heated to 650 °C in helium flow. The amount of acid–base sites on the catalyst surface was calculated from the desorption amount of NH_3 and CO_2, which was determined by measuring the areas of the desorption profiles obtained from the Chemisorption System analyzer.

2.3. Study of transesterification and esterification reactions in near-critical methanol

A batch type stainless steel reactor with a vertical shaker was applied to study the transesterification and esterification reactions in the present work. It is noted that Type-K thermocouple was placed into the annular space between the reactor and the furnace; furthermore, another Type-K thermocouple was inserted at the inner side of the reactor in order to re-check the possible temperature gradient. Prior to the experiment, the temperature of the heating furnace at the location of the furnace adjacent to the reactor was controlled at 200–300 °C. To carry out the reaction, palm feedstock (i.e. CPO, RPO and PFAD) was mixed with methanol at a specific molar ratio of 6:1–42:1 (methanol to CPO or RPO) and 3:1–18:1 (methanol to PFAD) and the solid catalyst was then

added in the reactants at the concentration range of 0–1 wt.%. The reactor was placed in the furnace and reached to the desired reaction temperature approximately 15 min (heating time), at which point the reaction was allowed to continue for a period of 0–15 min. It is noted that the shaker was turned on when the reactor temperature reached its setting point in order to minimize the occurring of the reaction during heating up period.

The effect of co-solvent on the reaction performance was studied by adding toluene, benzene and hexane (10% v/v) along with the feed before charging the solution to the reactor. Regarding the effect of water content on the reaction performance, the experiments were carried out by (1) adding molecular sieve to dehydrate the reactant (CPO, RPO and PFAD) before filtering out from the reactant prior the reaction and (2) adding molecular sieve to dehydrate the mixture (of reactant and products) during the reaction. After the reaction, the reactor was placed into a water bath to stop the reaction. The product was separated into three phases i.e. phase of methyl ester, phase of glycerol (or water), and phase of solid catalyst. FAME analysis was carried out using GC (Shimadzu 2010 model) with a flame ionization detector (FID) in which 1 μl of the sample was injected into column. The GC consists of a capillary column (DB-WAX, Carbowax 20 M, 30 m, 0.32 mm ID, 0.25 μm). The injector, detector, and column temperatures were set at 250, 260 and 200 °C, respectively. Pressure was 64.1 kPa and linear velocity was 25 cm s^{-1}. The carrier gas was helium and the make-up gas was nitrogen. The sample was prepared by adding 0.05 ml of FAME to 5 ml of *n*-hexane and methyl heptadecanoate was used as an internal standard. It is noted that the FAME yield was calculated as the total weight of FAME production to the weight of palm reactant introduced to the system.

3. Results and discussion

As described, SO_4–ZrO_2, TiO_2–ZrO_2 and WO_3–ZrO_2 catalysts were synthesized at various preparation conditions and tested for transesterification and esterification of CPO, RPO and PFAD in near-critical methanol condition. Here, the synthesized SO_4–ZrO_2, TiO_2–ZrO_2 and WO_3–ZrO_2 were denoted as SZ, TZ, and WZ. SZ catalysts prepared by loading the sulfur contents of 0.75%, 1.8%, and 2.5% and calcined at 500 °C were denoted as 0.75SZ-500, 1.8SZ-500, and 2.5SZ-500. TZ catalysts with Ti/Zr ratios of 1/3, 1/1 and 3/1 and calcined at 500 °C were donated as 1/3TZ-500, 1/1TZ-500 and 3/1TZ-500. Lastly, WZ catalysts prepared by loading WO_3 of 10%, 20% and 30% and calcined at 800 °C were donated as 10WZ-800, 20WZ-800 and 30WZ-800.

3.1. Catalyst characterization

The specific surface area, cumulative pore volume, average pore diameter and pore size distribution of all synthesized catalysts, determined by N_2 physisorption using Micromeritics ASAP 2020 surface area and porosity analyzer, are summarized in Table 1. It can be seen that the specific surface area of SO_4–ZrO_2 increased when the sulfur was loaded up to 1.8%, then the surface area slightly decreased when the sulfur loading content was 2.5%. The abrupt decrease in surface area with higher sulfur contents could be correlated with the alteration of crystal structure and sulfate migration into the bulk phase of the solid. It should be noted that, by loading sulfur over zirconia, the catalyst exhibited smaller crystallite sizes, which caused the increase in the cumulative pore volume, and the reduction of the average pore diameter. As for WO_3–ZrO_2, the specific surface area was also found to increase with increasing tungsten loading content, which could be due to the reducing of ZrO_2 sintering rate by WO_3 adding as reported by Iglesia et al. (1993). It can also be seen from Table 1 that the specific surface area and cumulative pore volume of SO_4–ZrO_2 considerably decrease with increasing calcination temperature, whereas those of WO_3–ZrO_2 also decrease but with the lower rate due to the preventing of ZrO_2 sintering by WO_3 as mentioned above. For TiO_2–ZrO_2, the BET results indicated that TiO_2–ZrO_2 with Ti/Zr molar ratio of 1/1 shows the greatest specific surface area. Similar to SO_4–ZrO_2 and WO_3–ZrO_2, the specific surface area and cumulative pore volume of TiO_2–ZrO_2 linearly decreased with increasing calcination temperature, whereas the average pore diameter increased.

Table 1
N_2 Physisorption results of SO_4–ZrO_2, WO_3–ZrO_2 and TiO_2–ZrO_2 prepared from different conditions.

Catalysts	BET surface area[a] (m^2/g)	Cumulative pore volume[b] (cm^3/g)	Average pore diameter[c] (nm)
0.75SZ-500	228	0.321	3.9
1.8SZ-500	243	0.390	3.6
2.5SZ-500	237	0.354	3.8
1.8SZ-600	179	0.314	4.0
1.8SZ-700	113	0.254	4.4
20WZ-700	121	0.293	4.1
10WZ-800	91	0.157	4.0
20WZ-800	95	0.193	3.8
30WZ-800	103	0.221	3.8
20WZ-900	78	0.112	4.3
1/1TZ-500	198	0.394	2.5
3/1TZ-500	175	0.385	2.6
1/3TZ-500	189	0.392	2.5
1/1TZ-600	187	0.391	2.5
1/1TZ-700	165	0.382	2.7

[a] Error of measurement ±5%.
[b] BJH desorption cumulative volume of pores between 1.7 and 300 nm diameter.
[c] BJH desorption average pore diameter.

According to the XRD measurement, it was found that all SO_4–ZrO_2 and WO_3–ZrO_2 catalysts contain both tetragonal and monoclinic phases with various contents depending on the preparation condition. Table 2 presents the contents of both phases for these catalysts, which were calculated from the areas of corresponding XRD characteristic peaks. The results revealed that the average crystal size and the fraction of monoclinic phase for SO_4–ZrO_2 decreased when the sulfur loading content increased from 0% to 0.75% and 1.8%, then they slightly increased when the sulfur loading content was 2.5%. For WO_3–ZrO_2, the fraction of tetragonal phase increased with increasing tungsten loading; in addition, the formation of triclinic phase WO_3 was also detected at high WO_3 loadings. It can also be seen that the crystal size in monoclinic phase and the fraction of monoclinic phase for both SO_4–ZrO_2 and

Table 2
Catalyst characteristics obtained from XRD measurement.

Catalysts	Phase	Average crystal size (nm)	Crystal size (nm)[a]		% Monoclinic phase[a]
			M[b]	T[c]	
0.75SZ-500	*M*, *T*	8.1	8.3	4.2	66.3
1.8SZ-500	*M*, *T*	7.8	8.1	4.0	62.9
2.5SZ-500	*M*, *T*	7.9	8.1	3.9	63.4
1.8SZ-600	*M*, *T*	8.2	8.2	4.3	65.0
1.8SZ-700	*M*, *T*	8.7	8.5	4.7	68.7
20WZ-700	*M*, *T*	8.4	8.9	4.7	50.3
10WZ-800	*M*, *T*	9.7	9.9	5.3	53.8
20WZ-800	*M*, *T*	9.5	9.7	5.1	51.4
30WZ-800	*M*, *T*	9.4	9.6	5.1	51.2
20WZ-900	*M*, *T*	10.3	10.5	5.9	57.6

[a] Based on XRD line broadening.
[b] Monoclinic phase in ZrO_2.
[c] Tetragonal phase in ZrO_2.

WO_3–ZrO_2 increased with increasing calcination temperature. For TiO_2–ZrO_2, the main phase observed from XRD over this catalyst is $TiZrO_4$ (as amorphous phase) when calcined at 500 °C and turns to be crystalline at higher calcination temperature (>500 °C).

Lastly, NH_3- and CO_2-TPD techniques were used to measure the acid–base properties of the catalysts. The amounts of acid and base sites, which were calculated from the area below curves of these TPD profiles, are listed in Table 3. Along with these values, the distribution of acid and base site on the catalyst surface (namely the density of acid and base site; μmol m^{-2}) is also given in the table since this parameter is important indicator to determine the catalytic reactivity of acid and base reactions (Maniriquez et al., 2004; Tomishige et al., 2000). According to the studies over SO_4–ZrO_2, the amount and density of acid sites increased with increased percents of sulfur contents. Differently for WO_3–ZrO_2, the density of acid sites increased with increased percents of tungsten content in ZrO_2 up to 20% of tungsten content; then it decreased with more tungsten loadings (30%). Considering the base sites, the amount of base sites for both SO_4–ZrO_2 and WO_3–ZrO_2 catalysts increased proportional to the sulfur and tungsten contents in ZrO_2. By increasing the calcination temperature, the amounts of acid and base sites for both catalysts decreased. Nevertheless, it was found that the densities of acid and base sites for SO_4–ZrO_2 decreased with increasing calcination temperature (from 500 °C to 600 and 700 °C), whereas they increased with increasing calcination temperature from 700 °C to 800 °C for WO_3–ZrO_2 before dropped down at higher calcination temperature (900 °C). It can also be noticed that, at the same calcination temperature (700 °C), the amount and density of acid sites for WO_3–ZrO_2 are slightly higher than those of SO_4–ZrO_2. For TiO_2–ZrO_2, the catalyst with Ti/Zr molar ratio of 1/1 showed the greater amounts and densities of acid sites compared to other two ratios (3/1 and 1/3). In addition, the calcination temperature was found to affect the acidity–basicity properties of TiO_2–ZrO_2; the amount and density of acid sites decreased with increasing calcination temperature, whereas those of base sites increased with increasing calcination temperature.

3.2. Catalyst reactivity toward transesterification/esterification in near-critical methanol

The catalytic reactivities toward transesterification and esterification of CPO, RPO and PFAD were firstly tested at 250 °C with the reaction time of 10 min with and without the presence of three different catalysts. Fig. 1 shows the yield of FAME production from these reactions; it can be seen that the FAME yield from the reaction of RPO is the highest, whereas that from the reaction of PFAD is relatively lower than other two feedstocks. In addition, in the presence of catalyst, the FAME yields are significantly higher than those without catalyst, particularly for WO_3–ZrO_2 and SO_4–ZrO_2 catalysts. The reusability of these solid catalysts was also carried out by washed and dried the separated catalysts from the solution before re-testing their reactivities at the same operating conditions. As also shown in Fig. 1, the reactivities of spent WO_3–ZrO_2 and TiO_2–ZrO_2 are almost identical to the fresh one indicated their well-reusable; this highlights the great benefit of these modified zirconia-based catalysts. In contrast, for SO_4–ZrO_2, significant deactivation was observed form the reused catalyst. According to the characterizations over the spent catalysts after these reaction cycles, insignificant changes (i.e. the catalyst specific surface area, the phase formation and the acid–base properties) were observed over WO_3–ZrO_2 and TiO_2–ZrO_2. Nevertheless, regarding the elemental analysis study, high percentage of sulfur losing (48%) were observed for SO_4–ZrO_2 after five reaction cycles (the sulfur content decreased from 1.8% to 1.07%, 1.03%, 0.92%, 0.88% and 0.86% after the first to fifth reaction cycles, respectively). In addition, according to the NH_3-TPD study over the spent SO_4–ZrO_2, the density of acid sites after fifth reaction cycle decreased from 3.02 μmol/m^2 to 1.48 μmol/m^2. These results clearly explain the high deactivation of SO_4–ZrO_2, from which mainly relates to the sulfur leaching. It has also been widely reported that the sulfur leaching from the catalyst as well as the poisoning and pore filling during the process are the main barriers of SO_4–ZrO_2 catalyst (Lopez et al., 2008; Corma, 1997; Kiss et al., 2006).

Importantly, we found that the catalyst preparation condition (i.e. sulfate and tungsten loading contents, Ti/Zr molar ratio, and the catalyst calcination temperature) strongly affects the reaction reactivity, as shown in Fig. 2. Among all types of catalyst, 20WZ-800 is the most active one providing the FAME yields of 91.3%, 94.1% and 81.0% from CPO, RPO and PFAD, respectively. For SZ-based and TZ-based catalysts, 1.8SZ-500 and 1/1TZ-500 are the most active catalyst in their own groups. It can be seen from this figure that the loading of too high sulfur and tungsten contents (2.5SZ and 30WZ) caused a slight negative effect on the catalytic activity. The inhibitory effect for SO_4–ZrO_2 could be due to the agglomeration of the active SO_4^{2-} phase and/or the cover of basic sites by the exceeded SO_4^{2-}, which results in lower the surface areas of active components and eventually the catalytic activity as reported by Xie et al., 2007, whereas the negative effect for WO_3–ZrO_2 can be explained by the acid–base properties of catalyst, according to NH_3- and CO_2-TPD results. As seen in Table 3, although the amount of acid sites for 30WZ is higher than that of 10WZ and 20WZ, the density of acid sites for 20WZ is greater than that of 10WZ and 30WZ. We therefore suggest here that the acid-site density is important indicator than the amount of acid site to judge the catalyst reactivity toward our interest reactions. In the case of TiO_2–ZrO_2, the high reactivity of 1/1TZ could be due to the higher specific surface area, the amount and the density of acid sites for this catalyst compared to 1/3TZ and 3/1TZ. It is noted that although the amount and the density of acid sites for TiO_2–ZrO_2 catalysts are relatively higher than those of WO_3–ZrO_2 and SO_4–ZrO_2, the catalyst reactivities toward these reactions are obviously lower. This implies the influence of other parameters that affect the reactivity toward transesterification and esterification reactions apart from catalyst acid–base properties.

It can be seen from Fig. 2 that the calcination temperature showed significant impact on the catalyst reactivity. At high calcination temperature (700 °C), the reactivities of SO_4–ZrO_2 and TiO_2–ZrO_2 considerably decreased; this can be explained by the decreases of catalyst specific surface area and the amount of acid

Table 3
Results from NH_3- and CO_2-TPD measurements of SO_4–ZrO_2, WO_3–ZrO_2 and TiO_2–ZrO_2 prepared from different conditions.

Catalysts	Total sites (μmol/g)		Density of sites (μmol/m^2)	
	Acid sites[a]	Base sites[b]	Acid sites	Base sites
0.75SZ-500	677.2	47.9	2.97	0.21
1.8SZ-500	733.9	70.5	3.02	0.29
2.5SZ-500	734.7	78.2	3.10	0.33
1.8SZ-600	524.5	43.0	2.93	0.24
1.8SZ-700	305.1	19.2	2.70	0.17
20WZ-700	330.3	42.9	2.73	0.35
10WZ-800	263.1	31.8	2.89	0.34
20WZ-800	280.2	35.5	2.95	0.37
30WZ-800	286.3	37.2	2.75	0.36
20WZ-900	219.2	21.4	2.81	0.27
1/1TZ-500	692	697	3.49	3.52
3/1TZ-500	594	708	3.39	4.04
1/3TZ-500	653	703	3.45	3.71
1/1TZ-600	645	712	3.45	3.81
1/1TZ-700	554	806	3.35	4.89

[a] From NH_3-TPD.
[b] From CO_2-TPD.

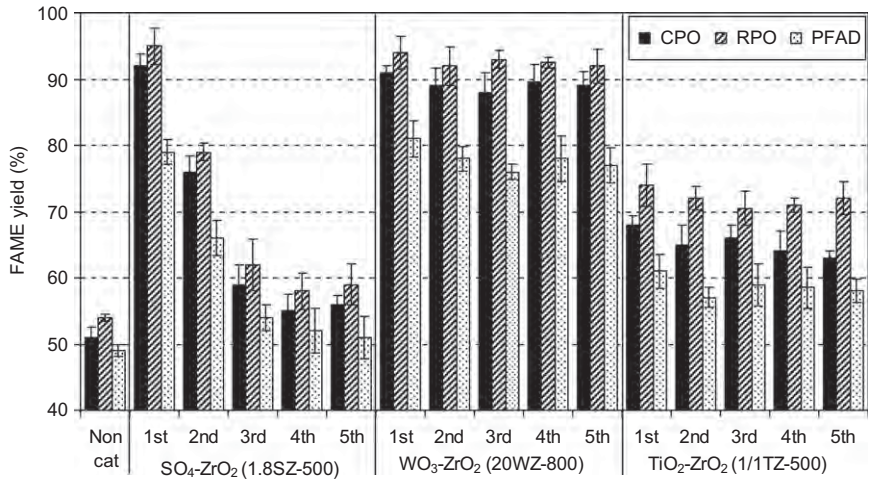

Fig. 1. Yield of FAME production (in five reaction cycles) from the transesterification and esterification of CPO, RPO and PFAD with and without the presence of three selected catalysts at 250 °C with the reaction time of 10 min and methanol to feedstock molar ratios of 24:1 (for CPO and RPO) and 18:1 (for PFAD).

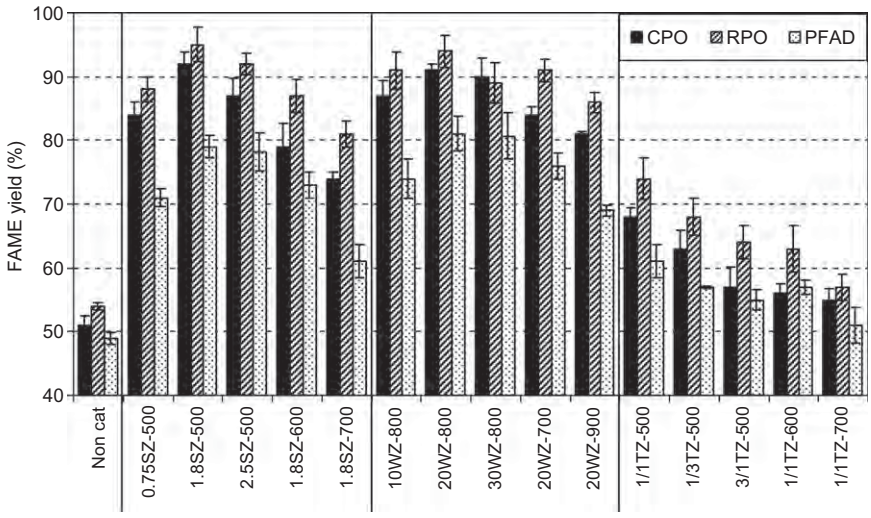

Fig. 2. Effect of catalyst preparing condition on the yield of FAME production from the transesterification and esterification of CPO, RPO and PFAD at 250 °C with the reaction time of 10 min and methanol to feedstock molar ratios of 24:1 (for CPO and RPO) and 18:1 (for PFAD).

sites at high calcination temperature. Furthermore, it can be noticed from the XRD studies that the crystalline structure of catalysts calcined at different temperatures also closely related to the catalyst reactivity. As seen in Table 2, the percentage of tetragonal phase for SO_4–ZrO_2 is in the same trend as the reaction rate; and it seems that the presence of tetragonal phase render to increase the reactivity for the interested reactions. In the case of TiO_2–ZrO_2, the best reactivity was observed from the catalyst calcined at 500 °C. According to the XRD studies, the phase of TiO_2–ZrO_2 turns from amorphous to crystalline phase above 500 °C; hence, this suggests that TiO_2–ZrO_2 with amorphous phase is more active than crystalline phase. Importantly, for WO_3–ZrO_2, it was found that the catalyst calcined at 800 °C achieved higher reactivity than those calcined at 700 °C and 900 °C. This result is in good agreement with Lopez et al. (2008) who suggested that the presence of polymeric tungsten species (at the calcination temperature of 800 °C) along with the tetragonal form of ZrO_2 support promote the reactivity of toward the acid- and alkali-catalyzed reactions. We summarized from our studies that the catalyst acid–base properties and the phase formation play an important role on the reactivity toward transesterification and esterification reactions under near-critical methanol condition.

3.3. Effect of operating conditions on the reaction reactivity

Based on the above results, 20WZ-800 was selected for further studies in order to determine the optimum operating conditions that maximize the yield of FAME production from CPO, RPO and PFAD. Firstly, the effect of reaction time on the FAME yield was determined by varying the reaction time from 0 to 90 min (using the reaction temperature of 250 °C and methanol to reactant molar ratios of 24:1 for CPO and RPO and 6:1 for PFAD). As shown in Fig. 3, it was found that the FAME yield increases with increasing the reaction time until 10 min for the transesterification of CPO and RPO and around 1 min for the esterification of PFAD, providing the FAME yields of 91.3%, 94.1% and 81.0%, respectively. At the longer reaction time (up to 90 min), the yields remained constant or slightly decreased in some cases, which could be due to thermal decomposition (Xie et al., 2006). Hence, we indicate that the suitable reaction time for the reactions of CPO and RPO was at 10 min, whereas that of PFAD was at 1 min. For comparison, the reactions without catalyst were also studied. As also shown in Fig. 3, the transesterification and the esterification reactions require 1 h and 30 min, respectively, to maximize the FAME yield; in addition, the maximum yields of FAME production are relatively lower than

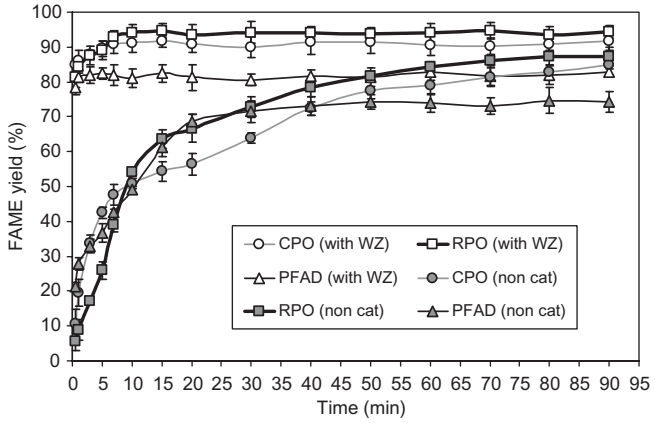

Fig. 3. Effect of reaction time on the yield of FAME production from the transesterification and esterification of CPO, RPO and PFAD with and without the presence of 20WZ-800 catalyst at 250 °C with the methanol to feedstock molar ratios of 24:1 (for CPO and RPO) and 18:1 (for PFAD).

those achieved from the reactions with 20WZ-800. It is noted according to our experiment that although we minimized the occurring of the reaction during the heating up period by shaking the reactor at the setting temperature, the reaction could still occurs due to the presence of catalyst along with the reactants and that causes the shorten reaction time requirement to complete the reaction. Hence, the effect of reaction time will be further investigated in the large-scale stirred reactor with the movable catalyst basket after this pre-screening catalyst work.

Then, the effect of reaction temperature on the yield of FAME production was carried out by varying the reaction temperature from 200 to 300 °C. The results in Fig. 4 indicate that, in the presence of WO_3–ZrO_2, the yields of FAME production increase with increasing the reaction temperature from 200 to 250 °C for all reactions; above that temperature, the FAME yields are relatively constant. In contrast, without catalyst, the FAME yields from these reactions continue increased (from 51.2% (CPO), 54.1% (RPO), and 49.4% (PFAD) at 250 °C to 81.5% (CPO), 88.6% (RPO), and 72.7% (PFAD) at 300 °C). It can be seen that even at the reaction temperature as high as 300 °C, the FAME yields from these reactions are relatively lower than those from the reactions in the presence of WO_3–ZrO_2 at 250 °C. Therefore, apart from the beneficial in term of shorter reaction time, the lower reaction temperature is another advantage of WO_3–ZrO_2 adding for these reactions.

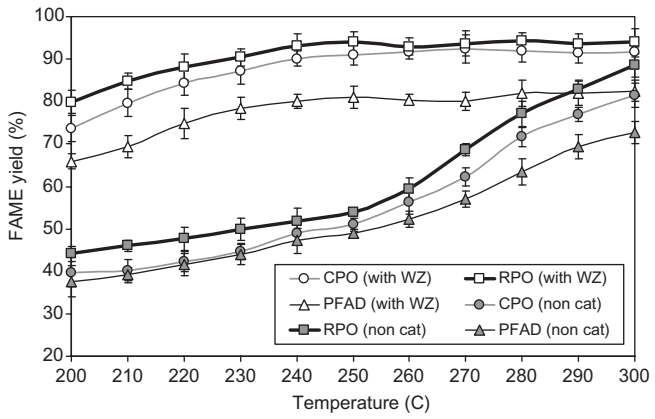

Fig. 4. Effect of reaction temperature on the yield of FAME production from the transesterification and esterification of CPO, RPO and PFAD with and without the presence of 20WZ-800 catalyst at the reaction time of 10 min and methanol to feedstock molar ratios of 24:1 (for CPO and RPO) and 18:1 (for PFAD).

The effect of methanol to reactant molar ratio on the yield of FAME production was also determined. According to the typical transesterification, three moles of alcohol and one mole of triglyceride are required to produce three moles of fatty acid ester and one mole of glycerol. As for esterification, it requires one mole of alcohol and fatty acid to produce one mole of fatty acid ester and water. Practically, excess amount of alcohol is always applied in order to shift the equilibrium to the right-hand side. However, the use of too high amount of alcohol could also increase the cost of FAME and/or biodiesel production. In this study, the effect of methanol to reactant molar ratio was determined by varying the ratio between 6:1 to 42:1 for the transesterification of CPO and RPO and 3:1 to 18:1 for the esterification of PFAD. Fig. 5 shows the effect of this molar ratio on the yield of FAME production after 10 min reaction time. Clearly, the yield increased with increasing methanol to reactant molar ratio (from 47.7% to 91.3% and 52.9% to 94.1% as the molar ratio increase from 6:1 to 24:1 for the transesterification of CPO and RPO, respectively, and from 67.3% to 81.0% as the molar ratio increase from 3:1 to 6:1 for the esterification of PFAD). Upon those molar ratios, the reaction rates seem to be unaffected by the methanol content. Therefore, the optimum molar ratio of methanol to reactants for the transesterification of CPO and RPO and the esterification of PFAD in near-critical methanol were 24:1 and 6:1, respectively. For comparison, these reactions without catalyst were also carried out and it was found that the transesterification of CPO and RPO required methanol to reactant molar ratios more than 39:1, while the esterification of PFAD required the ratio of 15:1 to reach the same levels of FAME yield. Hence, another great benefit of WO_3–ZrO_2 is that it can significantly reduce the requirement of excess methanol to complete the reaction. We concluded from all experiments that the optimum conditions that maximize the yield of FAME production from the transesterification of CPO and RPO in the presence of WO_3–ZrO_2 are at 250 °C with the reaction time of 10 min and methanol to reactant molar ratio of 24:1, while those for the esterification of PFAD are at 250 °C with the reaction time of 1 min and methanol to PFAD molar ratio of 6:1. It is noted that the effect of catalyst to reactants mass ratio on the reaction rates was also studied and we found that the optimum mass ratio of catalyst to reactant for both transesterification and esterification under near-critical methanol seems to be 0.5 %.

3.4. Reactions in the presence of co-solvents

Previously, it has been reported that the additional of suitable co-solvent could improve the performance of transesterification

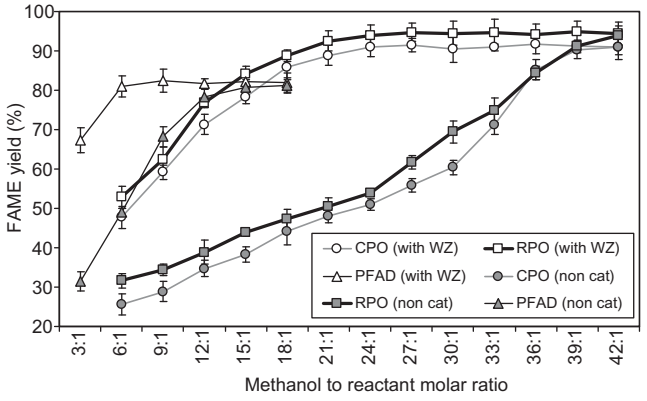

Fig. 5. Effect of methanol to feedstock molar ratio on the yield of FAME production from the transesterification and esterification of CPO, RPO and PFAD with and without the presence of 20WZ-800 catalyst at 250 °C with the reaction time of 10 min.

Table 4
Effect of co-solvent adding on the yield of FAME production from the reactions of CPO, RPO and PFAD in the presence of 20WZ-800 at various methanol to feedstock molar ratios (at 250 °C with the reaction time of 10 min).

Feedstock	Methanol to feedstock ratio	FAME production yield (%)			
		No co-solvent	With hexane	With benzene	With toluene
CPO	6:1	47.7 (±2.7)	45.4 (±1.9)	49.6 (±2.5)	54.7 (±0.8)
	12:1	71.3 (±2.4)	68.3 (±2.1)	74.7 (±1.8)	78.9 (±2.3)
	18:1	85.9 (±3.1)	81.4 (±2.0)	87.2 (±2.1)	91.5 (±1.7)
	24:1	91.0 (±2.4)	88.7 (±0.4)	92.2 (±1.4)	93.9 (±2.0)
RPO	6:1	52.9 (±2.8)	49.9 (±1.3)	55.6 (±2.1)	58.8 (±3.1)
	12:1	76.9 (±1.2)	74.5 (±3.4)	79.3 (±1.9)	82.7 (±2.3)
	18:1	88.7 (±1.5)	84.7 (±2.4)	90.9 (±2.7)	94.0 (±1.4)
	24:1	94.1 (±2.5)	91.2 (±1.8)	94.7 (±0.7)	95.5 (±1.8)
PFAD	3:1	67.3 (±3.1)	64.3 (±2.8)	71.2 (±2.2)	75.4 (±2.0)
	6:1	81.0 (±2.7)	77.9 (±2.3)	84.7 (±1.8)	87.7 (±1.9)
	9:1	82.4 (±2.9)	79.0 (±1.4)	86.1 (±2.1)	90.3 (±0.8)
	12:1	81.6 (±1.4)	80.1 (±0.8)	87.4 (±2.3)	90.2 (±1.3)

reaction by reducing the amount of methanol required for the reaction; hence, the effect of co-solvent adding (i.e. hexane, benzene and toluene) was also evaluated in the present work by adding 10% v/v of these solvents in palm feedstocks. These non-polar solvents were chosen regarding to their high solubility in oil compounds. The enhancing effect of co-solvent adding in the reaction medium at different methanol to reactant molar ratios is shown in Table 4. Clearly, the FAME yields increase when toluene and benzene were added particularly at low methanol to reactant molar ratio, whereas they slightly decrease when hexane was added. In the presence of toluene, more than 90% yields of FAME production can be obtained from the reactions of CPO, RPO and PFAD using methanol to reactant molar ratio of 18:1 (for CPO and RPO) and 9:1 (for PFAD), whereas these reactions without toluene adding required methanol to reactant molar ratio of 24:1 to achieve that range of FAME yields. It is noted that the reaction improvement with additions of benzene and toluene could possibly be due to the fact that benzene and toluene are good solvents for vegetable oil and both are miscible with methanol (Krisnangkura and Simamaharnnop, 1992), therefore these solvents could help the mixing of methanol with oil in reactor. The inhibitory effect of hexane could be due to the low solubility of this solvent in methanol, hence it acts as an antisolvent and reduced the biodiesel production yield.

3.5. Effect of water on the reaction reactivity

It is well established that the presence of water provides negative effect on the alkali- and acid-catalyzed reactions, since water interferes with the catalyst and reduces catalyst performance (Komers and Stloukal, 2001). For the alkaline-catalyzed process, the conversion was reported to reduce slightly when some water was presented in the system. As for acid-catalyzed reaction, only as little as 0.1% of water added to the reaction could lead to 6% reduction of the production yield (Canakci and VanGerpen, 1999). According to the transesterification in supercritical methanol, Kusdiana and Saka (2001) demonstrated that in the presence of water up to 30% w/w triglycerides still transesterified to methyl ester efficiently with very minimal loss in conversion. For the esterification in supercritical methanol, Kusdiana and Saka (2004) reported approximately 2–5% reduction in conversion of oleic acid to methyl oleate in the presence of water (up to 30%) at 350 °C with the oleic acid to methanol molar ratio of 1.0:42.0.

In this study, the effect of water on the reaction performance were carried out by 2 methods: (1) pre-treatment of feedstock prior the reaction by adding molecular sieve to dehydrate the reactants (CPO, RPO and PFAD) before filtering out and (2) adding the molecular sieve along with reactants to the system to dehydrate the mixture of reactant and products during the reaction. As shown in Fig. 6, it can be seen that uses of molecular sieve by both methods shows insignificant effect on the transesterification of RPO but led to improvement in FAME yields for CPO and PFAD (particularly for PFAD at low methanol to PFAD ratios using method (2), which

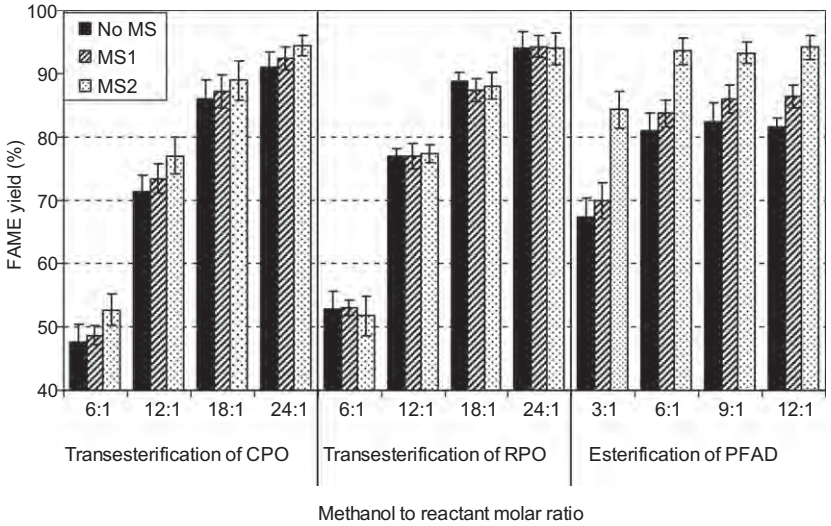

Fig. 6. Effect of molecular sieve adding (MS1: for pre-treatment of feedstock before filtering out prior the reaction; MS2: adding along with reactants to the system) on the yield of FAME production from the transesterification and esterification of CPO, RPO and PFAD at various methanol to feedstock molar ratios in the presence of 20WZ-800 at 250 °C with the reaction time of 10 min.

achieved 21.9% increasing of FAME yield). Water is known to affect biodiesel synthesis by favoring hydrolysis of triacylglycerol and ester products from transesterification and esterification reactions (Yamane et al., 1989; Anthonsen and Sjursens, 2000; Shah and Gupta, 2007). In this study where dried feedstocks were used (by method 1), the occurring of hydrolysis reaction is inhibited and results in the higher FAME yield achievements. The insignificant effect for the reaction of RPO could be due to its low water content after refined process and no water formation during the reaction. According to method 2, the positive effect of molecular sieve adding on the FAME yield is due to the continuous removal of water generated from the esterification of free fatty acids in PFAD and CPO (which also contains a high proportion of free fatty acids). The continuous dehydration prevents an increase of water activity in the reaction and thus results in remarked improved FAME yields from feedstocks containing high free fatty acid content. These results suggest that, in order to maximize the yield of FAME production from PFAD, care must be taken to remove water before and/or during the reaction.

4. Conclusions

WO_3–ZrO_2 enables to catalyze the transesterification of CPO and RPO and the esterification of PFAD under near-critical methanol with high FAME yield and good stability achievements after several reaction cycles. The reactions requires shorter time, lower temperature and less amount of methanol compared to the reactions without catalyst, which is proven to relate with the high acid-site density and tetragonal phase formation of the catalyst. The addition of toluene as co-solvent reduces the methanol requirement to maximize FAME yield, while the addition of molecular sieve significantly increases FAME yield from PFAD and CPO due to the inhibition of hydrolysis reaction.

Acknowledgement

The financial support from The Thailand Research Fund (TRF) throughout this project is gratefully acknowledged.

References

Anthonsen, T., Sjursens, B.J., 2000. Importance of water activity for enzymes catalysis in non-aqueous organic systems. In: Gupta, M.N. (Ed.), Methods in Non-aqueous Enzymology. Birkhauser Verlag, Basel, pp. 14–35.

Canakci, M., VanGerpen, J.H., 1999. Biodiesel production via acid catalysis. Trans. ASAE 42, 1203–1210.

Corma, A., 1997. Solid acid catalysts. Curr. Opin. Solid State Mater. Sci. 2, 63–75.

Demirbas, A., 2007. Biodiesel from sunflower oil in supercritical methanol with calcium oxide. Energy Convers. Manage. 48, 937–941.

Furuta, S., Matsuhashi, H., Arata, K., 2004. Biodiesel fuel production with solid super acid catalyst in fixed bad reactor under atmospheric pressure. Catal. Commun. 5, 721–723.

Garcia, C.M., Teixeira, S., Marciniuk, L.L., Schuchardt, U., 2008. Transesterification of soybean oil catalyzed by sulfated zirconia. Bioresour. Technol. 99, 6608–6613.

Iglesia, E., Soled, S.L., Kramer, G.M., 1993. Isomerization of alkanes on sulfated zirconia: promotion by Pt and by adamantly hydride transfer species. J. Catal. 144, 238–253.

Kasim, N.S., Tsai, T.H., Gunawan, S., Ju, Y.H., 2009. Biodiesel production from rice bran oil and supercritical methanol. Bioresour. Technol. 100, 2399–2403.

Kim, M., Yan, S., Salley, S.O., Ng, K.Y.S., 2010. Competitive transesterification of soybean oil with mixed methanol/ethanol over heterogeneous catalysts. Bioresour. Technol. 101, 4409–4414.

Kiss, A.A., Omota, F., Dimian, A.C., Rothenberg, G., 2006. The heterogeneous advantage: biodiesel by catalytic reactive distillation. Top. Catal. 40, 141–150.

Komers, J.M., Stloukal, R., 2001. Biodiesel from rapeseed oil, methanol and KOH. 2. Composition of solution of KOH in methanol as reaction partner of oil. Eur. J. Lipid Sci. Technol. 103, 359–362.

Krisnangkura, K., Simamaharnnop, R., 1992. Continuous transmethylation of palm oil in an organic solvent. JAOCA 69, 166–169.

Kusdiana, D., Saka, S., 2001. Kinetics of transesterification in rapeseed oil to biodiesel fuel as treated in supercritical methanol. Fuel 80, 693–698.

Kusdiana, D., Saka, S., 2004. Effects of water on biodiesel fuel production by supercritical methanol treatment. Bioresour. Technol. 91, 289–295.

Lopez, D.E., Goodwin Jr., J.G., Bruce, D.A., Lotero, E., 2005. Transesterification of triacetin with methanol on solid acid and base catalysts. Appl. Catal. A 295, 97–105.

Lopez, D.E., Goodwin Jr., J.G., Bruce, D.A., Furuta, S., 2008. Esterification and transesterification using modified-zirconia catalysts. Appl. Catal. A 339, 76–83.

Maniriquez, M.E., Lopez, T., Gomez, R., Navarrete, J., 2004. Preparation of TiO_2–ZrO_2 mixed oxides with controlled acid-basic properties. J. Mol. Catal. A 220, 229–237.

Rao, K.N., Sridhar, A., Lee, A.F., Tavener, S.J., Young, N.A., Wilson, K., 2006. Zirconium phosphate supported tungsten oxide solid acid catalysts for the esterification of palmitic acid. Green Chem. 8, 790–797.

Saka, S., Kusdiana, D., 2001. Biodiesel fuel from rapeseed oil as prepared in supercritical methanol. Fuel 80, 225–231.

Shah, S., Gupta, M.N., 2007. Lipase catalyzed preparation of biodiesel from Jatropha oil in a solvent free system. Process Biochem. 42, 409–414.

Sun, H., Ding, Y., Duan, J., Zhang, Q., Wang, Z., Lou, H., Zheng, X., 2010. Transesterification of sunflower oil to biodiesel on ZrO_2 supported La_2O_3 catalyst. Bioresour. Technol. 101, 953–958.

Tanabe, K., Holderich, W.F., 1999. Industrial application of solid acid–base catalysts. Appl. Catal. 181, 399–434.

Tomishige, K., Ikeda, Y., Sakaihori, T., Fujimoto, K., 2000. Catalytic properties and structure of zirconia catalysts for direct synthesis of dimethyl carbonate from methanol and carbon dioxide. J. Catal. 192, 355–362.

Xie, W., Huang, X., Li, H., 2007. Soybean oil methyl esters preparation using NaX zeolites loaded with KOH as a heterogeneous catalyst. Bioresour. Technol. 98, 936–939.

Xie, W., Peng, H., Chen, L., 2006. Transesterification of soybean oil catalyzed by potassium loaded on alumina as a solid-base catalyst. Appl. Catal. A 300, 67–74.

Yamane, T., Kojima, Y., Ichiryu, T., Nagata, M., Shimizu, S., 1989. Intramolecular esterification by lipase powder in microaqueous benzene: effect of moisture content. Biotechnol. Bioeng. 34, 838–843.

Zallaikah, S., Lai, C., Vali, S.R., Ju, Y.H., 2005. A two-step acid-catalyzed process for the production of biodiesel from rice bran oil. Bioresour. Technol. 96, 1889–1896.

INTERNATIONAL JOURNAL OF HYDROGEN ENERGY 35 (2010) 6747–6756

Available at www.sciencedirect.com

ScienceDirect

journal homepage: www.elsevier.com/locate/he

Reactivity of Ce-ZrO_2 (doped with La-, Gd-, Nb-, and Sm-) toward partial oxidation of liquefied petroleum gas: Its application for sequential partial oxidation/steam reforming

N. Laosiripojana [a,*], W. Sutthisripok [b], P. Kim-Lohsoontorn [c], S. Assabumrungrat [d]

[a] The Joint Graduate School of Energy and Environment, King Mongkut's University of Technology Thonburi, Bangkok, 10140, Thailand
[b] Department of Mining and Materials Engineering, Prince of Songkla University, Songkhla, Thailand
[c] Department of Chemical Engineering, Mahidol University, Nakorn Pathom 73170, Thailand
[d] Center of Excellence in Catalysis and Catalytic Reaction Engineering, Department of Chemical Engineering, Faculty of Engineering, Chulalongkorn University, Bangkok 10330, Thailand

ARTICLE INFO

Article history:
Received 4 March 2010
Received in revised form
11 April 2010
Accepted 15 April 2010
Available online 23 May 2010

Keywords:
Liquefied petroleum gas
Hydrogen
Ce-ZrO_2
Partial oxidation

ABSTRACT

Ce-ZrO_2 was found to have useful partial oxidation activity under moderate temperatures. It converted liquefied petroleum gas (LPG) to H_2, CH_4, CO and CO_2 with small amounts of C_2H_6 and C_2H_4 formations depending on the operating temperature and provided significantly greater resistance toward carbon deposition compared to conventional Ni/Al_2O_3. The doping of La, Sm and Gd over Ce-ZrO_2 considerably improved catalytic reactivity, whereas Nb-doping reduced its reactivity. It was found that the impact of doping element is strongly related to the degrees of oxygen storage capacity (OSC) and/or lattice oxygen (O_O^x) of materials. Among all catalysts, La-doped Ce-ZrO_2 was observed to have highest OSC value and was the most active catalyst. Above 850 °C with inlet LPG/O_2 molar ratio of 1.0/1.0, the main products from the reaction over La-doped Ce-ZrO_2 were H_2, CH_4, CO, and CO_2.

Practical application was then proposed by applying La-doped Ce-ZrO_2 as primary oxidative catalyst for sequential partial oxidation/steam reforming of LPG (by using Ni/Al_2O_3 as the steam reforming catalyst). At 850 °C, this coupling pattern offered high H_2 yield (87.0–91.4%) without any hydrocarbons left in the products indicating the complete conversion of LPG to syngas. H_2 yield from this system was almost identical to that observed from the typical autothermal reforming over Rh/Al_2O_3; hence it could efficiently replace the requirement of expensive noble metal catalysts to reform LPG properly.

1. Introduction

Hydrogen-rich fuel is a major fuel for Solid Oxide Fuel Cell (SOFC), which can be produced readily from the reactions of several hydrocarbon fuels i.e. methane, methanol, ethanol, liquefied petroleum gas (LPG), gasoline and other oil derivatives with oxygen-containing co-reactant i.e. oxygen, steam, and carbon dioxide. Partial oxidation and steam reforming as well as the combination of both reactions (as called autothermal reforming) have been known as feasible processes to produce hydrogen-rich fuel from several hydrocarbons [1,2]. Steam reforming is probably the most common

* Corresponding author.
E-mail address: navadol_l@jgsee.kmutt.ac.th (N. Laosiripojana).
0360-3199/$ – see front matter © 2010 Professor T. Nejat Veziroglu. Published by Elsevier Ltd. All rights reserved.
doi:10.1016/j.ijhydene.2010.04.095

method for producing hydrogen in chemical process industry [1], however, it has a disadvantage of slow start-up, which makes it more suitable for a stationary system rather than for a mobile system [2]. Recently, catalytic partial oxidation [3–6] and autothermal reforming [7,8] appear to have attracted much interest. Partial oxidation consists of sub-stoichiometric oxidation of hydrocarbons, while autothermal reforming integrates partial oxidation with steam reforming. Theoretically, both partial oxidation and autothermal reforming offer significant lower energy requirement and higher gas-space velocity than steam reforming reaction [9].

Focusing on fuel selection, among above hydrocarbon fuels, liquefied petroleum gas (LPG) is one of the good candidates for applying as a primary fuel for SOFC particularly in remote areas where pipeline natural gas is not available due to its easy transported and enable to store on-site [10,11], In Japan, LPG and kerosene are promising alternative fuels for H_2 production along with natural gas due to their cost effective and easy distribution [12]. Typically, LPG is a mixture of C_3H_8 and C_4H_{10} (with various ratios depending on its source) that exist as liquids under modest pressures at ambient temperatures [13]. For instance, the composition of LPG from Australian LPG Association ranges from pure C_3H_8 to a 40:60 mixture of C_3H_8 and C_4H_{10} [14], whereas the composition of LPG from PTT Company (Thailand) is 60% C_3H_8 and 40% C_4H_{10}. Previously, most of studies over the reforming and relevant reactions of LPG have been carried out over noble metal catalysts (e.g. Rh, Ru, and Pt) on oxide supports [15–21]. The main products from the reforming of LPG are known to be H_2, CO, and CO_2; nevertheless, the formations of C_2H_6, C_2H_4, and CH_4 are also generally observed due to the decomposition of LPG and methanation reactions. These formations particularly C_2H_6 and C_2H_4 are the major difficulty for converting of LPG to hydrogen-rich gas since these elements easily decomposes to carbon species at moderate temperature and eventually deposits on the surface of catalyst and/or anode material of SOFC, which considerably degrades the reactivity of catalyst and SOFC anode.

This work is aimed at the development of a catalyst for partial oxidation of LPG, which provides high stability and activity at such a high temperature (700–900 °C) for later application as an in-stack reforming of SOFC (IR-SOFC). Although Pt, Rh and Ru have been reported to provide high activity for the reforming and relevant reactions with excellent resistant to the carbon formation [22,23], the current prices of these metals are very high and the availability of some precious metals i.e. Ru was too low to have a major impact on the total reforming catalyst market [24]. In view of these economical considerations, an alternative catalyst was developed and studied instead. Ceria and doped ceria with Gd, Nb, La, and Sm have been reported as a catalyst in a wide variety of reactions involving oxidation or partial oxidation of hydrocarbons (e.g. automotive catalysis). A high oxygen mobility [25], high oxygen storage capacity [26], strong interaction with the supported metal (strong metal–support interaction) [27] and the modifiable ability [28] render these materials very interesting for catalysis. Importantly, ceria-based materials have been reported to have reactivity toward the decomposition of CH_4 at such a high temperature (800–1000 °C) with greater resistance toward carbon deposition compared to conventional metallic catalysts. The addition of ZrO_2 to ceria, as Ce-ZrO_2, has been reported to improve the oxygen storage capacity, redox property, thermal stability and catalytic activity of ceria [29–31]. This high oxygen storage capacity was associated with enhanced reducibility of cerium (IV) in Ce-ZrO_2, which is a consequence of the high O^{2-} mobility inside the fluorite lattice. Due to the high thermal stability of this material, Ce-ZrO_2 would be a good candidate to be used as an in-stack reforming of SOFC.

In the present work, the reactivity toward the partial oxidation of LPG over Ce-ZrO_2 (at various Ce/Zr ratios), and doped Ce-ZrO_2 with Gd, Nb, La, and Sm was studied in order to determine the suitable material for this reaction and to investigate the benefit of these element (i.e. Gd, Nb, La, and Sm) doping; it is noted that the partial oxidation over Ni/Al_2O_3 was also carried out for comparison. The influences of inlet O_2/LPG molar ratio and temperature on the product compositions and the amount of carbon formation over these catalysts were determined. Lastly, an alternative concept to maximize the yield of H_2 production from LPG by applying sequential partial oxidation/steam reforming operation and using ceria-based material as primary oxidative catalyst was proposed and compared to the typical autothermal reforming over Rh/Al_2O_3; detail of this study is explained in Section 3.5.

2. Experimental

2.1. Catalyst preparation and characterization

Ce-ZrO_2 was chosen as a based catalyst in the present work. This material with different Ce/Zr molar ratios was prepared by co-precipitation of $Ce(NO_3)_3$ and $Zr(NO_3)_4$ in the presence of 0.1 M cetyltrimethylammonium bromide solution (from Aldrich) as a cationic surfactant. We previously reported that the preparation of ceria-based materials by cationic surfactant-assisted method can provide materials with high surface area and good stability after thermal treatment [32]. The achievement of high surface area material from this preparation technique is due to the interaction of hydrous oxide with cationic surfactants under basic condition [33], while the high thermal stability are due to the incorporation of surfactants during preparation which reduces the interfacial energy and eventually decreases the surface tension of water contained in the pores; this incorporation reduces the shrinkage and collapse of the catalyst during heating up, which consequently help the catalyst maintaining high surface area after calcinations [33].

The ratio between $Ce(NO_3)_3$ and $Zr(NO_3)_4$ was altered to achieve Ce/Zr molar ratios of 1/3, 1/1 and 3/1, while the molar ratio of (([Ce]+[Zr])/[cetyltrimethylammonium bromide]) was kept constant at 0.8. The solid solution was formed by the slow mixing of this metal salt solution with 0.4 M of urea. After preparation, the precipitate was filtered and washed with deionised water and ethanol to prevent an agglomeration of the particles. It was dried overnight in an oven at 110 °C, and then calcined in air at 900 °C for 6 h. As for the synthesis of doped Ce-ZrO_2 with Gd, Nb, La, and Sm, these materials were prepared by mixing $Ce(NO_3)_3$ and $Zr(NO_3)_4$ with $RE(NO_3)_x$ (Re = Gd, Nb, La, and Sm) to achieve the RE ratio in the material of 0.1; $RE_{0.1}$-$CeZrO_2$.

Ni/Al_2O_3 and Rh/Al_2O_3 (5 wt% Ni and Rh) were prepared by impregnating γ-Al_2O_3 with $Ni(NO_3)_2$ and $Rh(NO_3)_2$ solutions (from Aldrich). The catalysts were calcined at 900 °C and reduced with 10%H_2 in helium at 500 °C for 6 h before use. After reduction, these catalysts were characterized with several physicochemical methods i.e. the weight contents of Ni were determined by X-ray fluorescence (XRF) analysis, the reducibility and dispersion percentages of metal were measured from temperature-programmed reduction (TPR) with 5% H_2 in helium and temperature-programmed desorption (TPD), while the catalyst specific surface areas were obtained from BET measurements. All physicochemical properties of the synthesized Ni/Al_2O_3 and Rh/Al_2O_3 are presented in Table 1.

2.2. *Apparatus and procedures*

An experimental system was designed and constructed as shown elsewhere [34]. The feed gases including the components of interest (e.g. LPG, H_2O from the evaporator, and O_2) and the carrier gas (helium) were introduced to the reaction section, in which a 10-mm diameter quartz reactor was mounted vertically inside a furnace. The contents of desulpherized LPG used in this work are 60% C_3H_8 and 40% C_4H_{10} based on the compositions of LPG from PTT Company (Thailand). The inlet LPG concentration was kept constant at 5 kPa (C_3H_8/C_4H_{10} ratio of 0.6/0.4), while the inlet O_2 and H_2O concentrations were varied depending on the inlet O_2/LPG molar ratio requirement for each experiment. A Type-K thermocouple was placed into the annular space between the reactor and the furnace. This thermocouple was mounted on the tubular reactor in close contact with the catalyst bed to minimize the temperature difference between the catalyst bed and the thermocouple. Another Type-K thermocouple was inserted in the middle of the quartz tube in order to re-check the possible temperature gradient; this inner-system thermocouple is covered with small closed-end quartz rod to prevent the catalytic reactivity of thermocouple during reaction. The recorded values showed that the maximum temperature fluctuation during the reaction was always ±1.0 °C or less from the temperature specified for the reaction. Catalysts with the total weight of 500 mg were loaded in the quartz reactor. Based on the results from our previous studies, in order to avoid any limitations by intra-particle diffusion, the total gas flow rate was kept constant at 1000 $cm^3\,min^{-1}$ under a constant residence time of 5×10^{-4} g min cm^{-3} in all experiments.

After the reactions, the exit gas mixture was transferred via trace-heated lines to Porapak Q column Shimadzu 14B gas chromatograph (GC) and mass spectrometer (MS). The GC was applied in order to investigate the partial oxidation and reforming reactivities at steady-state condition. The reactivity was defined in terms of conversion and product distribution. The yield of H_2 production (S_{H2}) was calculated by the hydrogen balance, defined as the molar fraction of H_2 produced to the total hydrogen in the products. Distributions of other by-product selectivities (e.g. S_{CO}, S_{CO2}, S_{CH4}, S_{C2H6}, and S_{C2H4}) were calculated by the carbon balance, defined as the ratios of the product moles to the consumed moles of hydrocarbon, accounting for stoichiometry; this information was presented in term of (relative) fraction of these by-product components, which are summed to 100%. The MS was applied for the transient carbon formation experiment using Temperature-programmed Oxidation (TPO) technique. The TPO was carried out after exposure in the reforming of LPG by introducing 10% O_2 in He (with the flow rate of 100 $cm^3\,min^{-1}$) into the system, after being purged with He. The amount of carbon formation was determined by measuring the CO and CO_2 yields from the TPO results. Furthermore, the amount of carbon deposition was confirmed by the calculation of carbon balance in the system. The amount of carbon deposited on the surface of catalyst is theoretically equal to the difference between the inlet carbon containing components (LPG) and the outlet carbon containing components (CO, CO_2, CH_4, C_2H_6, and C_2H_4).

Table 1 – Physicochemical properties of Ni/Al_2O_3 and Rh/Al_2O_3 after reduction.

Catalyst	Metal-load[a] (wt.%)	BET surface area ($m^2\,g^{-1}$)	Metal-dispersion[c] (%)	Metal-reducibility[b] (%)
Ni/Al2O3	4.9	40	92.1	4.87
Rh/Al2O3	5.1	42	94.8	5.04

a Measured from X-ray fluorescence analysis.
b Measured from temperature-programmed reduction (TPR) with 5%hydrogen.
c Measured from temperature-programmed desorption (TPD) of hydrogen after TPR measurement.

3. Results and discussion

3.1. *Homogenous (non-catalytic) partial oxidation*

Before studying the catalyst performance, homogeneous (non-catalytic) partial oxidation of LPG was investigated. Feed stream consisting $C_3H_8/C_4H_{10}/O_2$ at a molar ratio of 0.6/0.4/1.0 was introduced to the system without packing of catalyst, while the temperature increased from ambient to 900 °C. Fig. 1

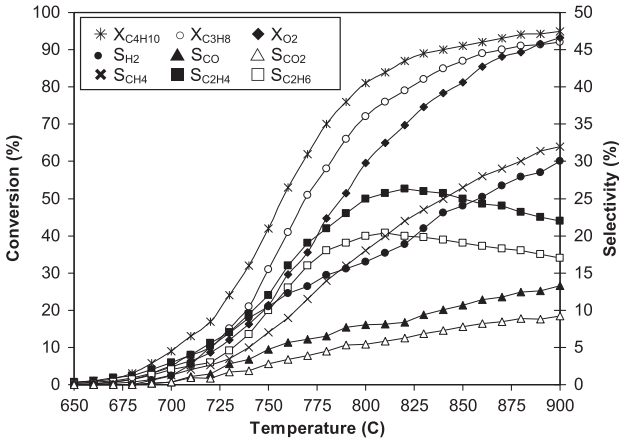

Fig. 1 – Homogeneous (in the absence of catalyst) partial oxidation of LPG (with $C_3H_8/C_4H_{10}/O_2$ molar ratio of 0.6/0.4/1.5).

shows the conversions of C_3H_8 and C_4H_{10} as well as all product distribution at several temperatures. It can be seen that both C_3H_8 and C_4H_{10} were converted to CH_4, C_2H_6, C_2H_4, and H_2 at the temperature above 650 °C. These components were formed via the homogeneous decomposition of C_3H_8 and C_4H_{10}. CO and CO_2 also occurred at slightly higher temperature indicating the homogeneous oxidation of inlet O_2 with hydrocarbons presented in the system. Furthermore, noticeable amount of carbon was also detected in the blank reactor after exposure for 10 h.

3.2. *Reactivity of Ce-ZrO_2 and Ni/Al_2O_3 toward partial oxidation of LPG*

The partial oxidation of LPG over Ce-ZrO_2 with different Ce/Zr ratios (1/3, 1/1, and 3/1) and Ni/Al_2O_3 was preliminary studied at 850 °C by introducing LPG and O_2 with $C_3H_8/C_4H_{10}/O_2$ molar ratios of 0.6/0.4/1.0 to the catalytic reactor. Fig. 2(a)–(d) shows the variations in conversion and product distribution (%) with time (under the period of 48 h) over these catalysts. For all catalysts, the conversions of C_3H_8, C_4H_{10} and O_2 were always closed to 100%. Regarding the product distribution, apart from the productions of H_2, CO, and CO_2, significant amounts of CH_4, C_2H_4, and C_2H_6 were also detected from these catalysts. The production of CO_2 indicates the contribution of the water-gas shift at this high temperature, while the presence of gaseous hydrocarbons (i.e. CH_4, C_2H_4, and C_2H_6) comes from the decomposition of C_3H_8 and C_4H_{10} (Eqs. (1)–(4)).

$$C_4H_{10} \rightarrow C_2H_6 + C_2H_4 \quad (1)$$

$$C_3H_8 \rightarrow 3/2(C_2H_4) + H_2 \quad (2)$$

$$C_2H_6 \rightarrow C_2H_4 + H_2 \quad (3)$$

$$C_2H_4 \Leftrightarrow CH_4 + C \quad (4)$$

Compared between these catalysts, Ce-ZrO_2 with Ce/Zr ratio of 3/1 presents the highest H_2 yield (~78%) with considerably lower formations of CH_4, C_2H_4, and C_2H_6. As for Ni/Al_2O_3, unstable profiles of all gaseous products were observed; the decreases in H_2, CO and CO_2 productions and increases in hydrocarbon (i.e. CH_4, C_2H_4 and C_2H_6) formations

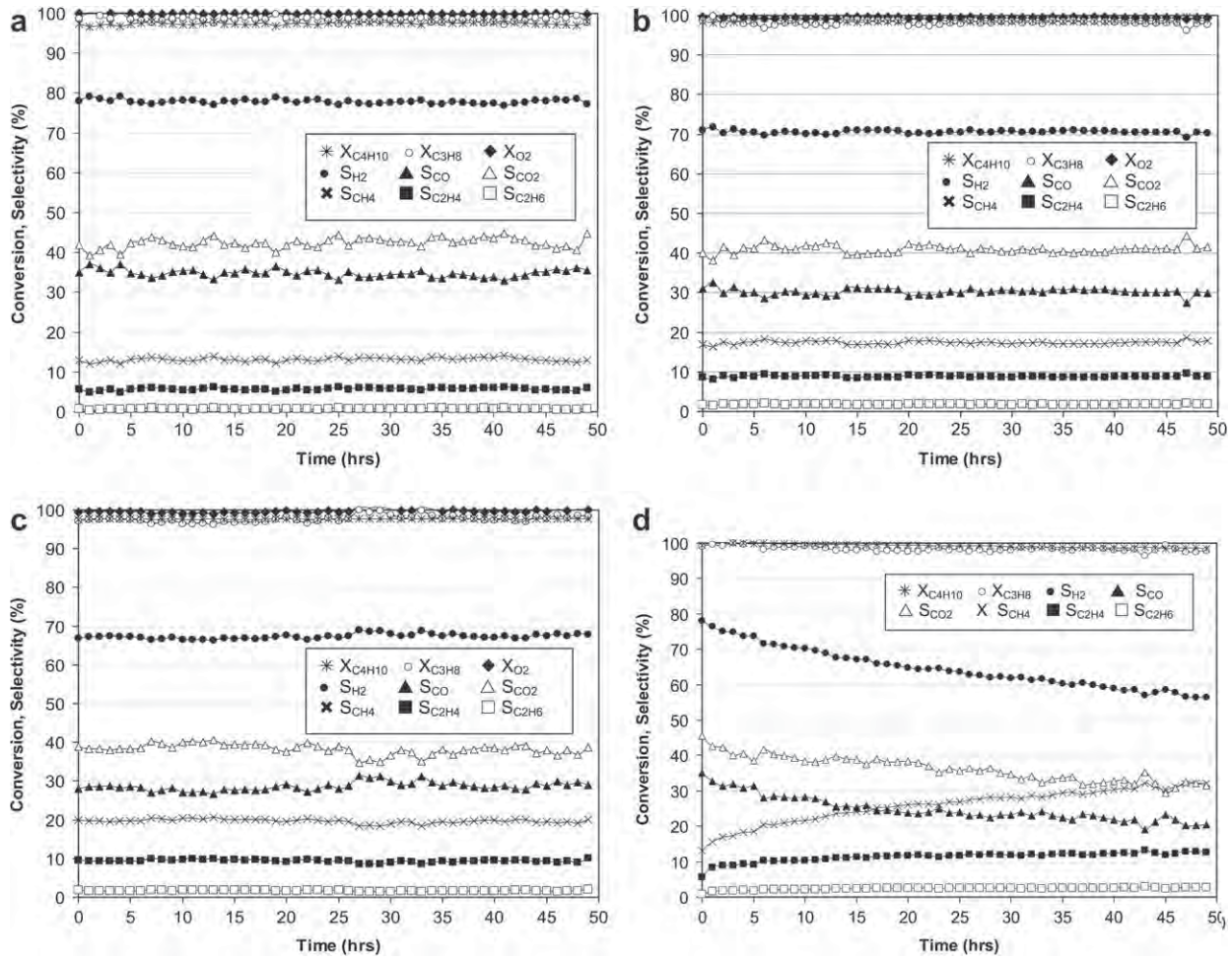

Fig. 2 – (a) Variations in conversions and product compositions with time from the partial oxidation of LPG at 850 °C over Ce-ZrO_2 (Ce/Zr molar ratio of 3/1). (b) Variations in conversions and product compositions with time from the partial oxidation of LPG at 850 °C over Ce-ZrO_2 (Ce/Zr molar ratio of 1/1). (c) Variations in conversions and product compositions with time from the partial oxidation of LPG at 850 °C over Ce-ZrO_2 (Ce/Zr molar ratio of 1/3). (d) Variations in conversions and product compositions with time from the partial oxidation of LPG at 850 °C over Ni/Al_2O_3.

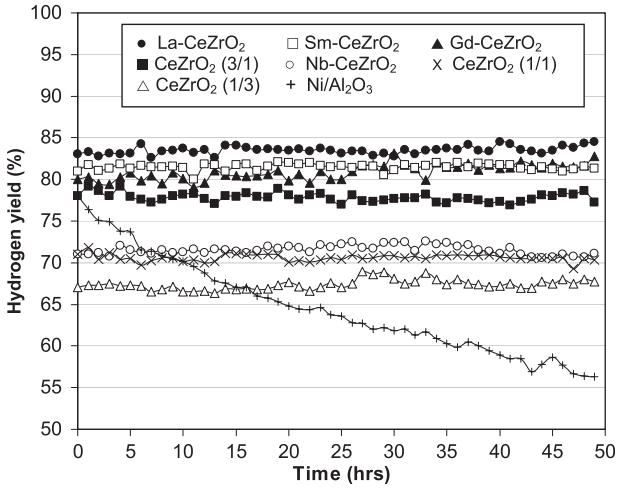

Fig. 3 – Variations in H_2 yield with time from the partial oxidation of LPG at 850 °C over doping Ce-ZrO_2 with Sm-, Gd-, La-, and Nb compared to undoped Ce-ZrO_2 and Ni/Al_2O_3.

with time are related to the rapid formation of carbon species on the surface of catalyst. After purging in helium, the post-reaction TPO experiments were carried out by introducing of 10% O_2 in helium to determine the amount of carbon formation occurred in the system (by measuring the CO and CO_2 yields). Small amount of carbon was detected on the surface of Ce-ZrO_2 (between 1.2 and 2.7 mmol g_{cat}^{-1}), whereas significantly higher amount of carbon was found over Ni/Al_2O_3 ($\sim 4.8 \pm 0.07$ mmol g_{cat}^{-1}); this indicates the greater resistance toward carbon deposition of ceria-based catalysts. It is noted that this amount of carbon deposited was ensured by calculating the carbon balance of the system. Regarding the calculations, the molar amount of carbon deposited per gram of Ni/Al_2O_3 was 4.76 mmol g^{-1}, which is in good agreement with the value observed from the TPO. Regarding these experimental results, Ce-ZrO_2 with a Ce/Zr ratio of 3/1 was selected for further investigations.

3.3. *Reactivity of doped Ce-ZrO_2 (with Gd, Nb, La, and Sm) toward partial oxidation of LPG*

The partial oxidation of LPG over doped Ce-ZrO_2 (Ce/Zr ratio of 3/1) with Gd, Nb, La, and Sm was then studied at the same conditions as those of Ce-ZrO_2 in Section 3.2 (850 °C with C_3H_8/C_4H_{10}/O_2 molar ratio of 0.6/0.4/1.0). As seen in Fig. 3 and Table 2, the doping of La, Gd, and Sm improve the partial oxidation reactivity whereas the doping of Nb slightly reduce the catalyst reactivity. The low activity by Nb-doping could be due to the strong segregation of Nb from ceria surface, as previously suggested by Ramírez-Cabrera et al. [35]. Among them, La-doped Ce-ZrO_2 has the highest H_2 production with considerably lowest CH_4, C_2H_4, and C_2H_6 formations. The post-reaction TPO experiment and the calculation of carbon balance also indicated that La-doped Ce-ZrO_2 provided the greatest resistance toward carbon formation, Table 2; thus this catalyst was selected for further studies i.e. the effects of inlet O_2 content and temperature.

The effect of inlet O_2 content was carried out by feeding LPG and O_2 with several C_3H_8/C_4H_{10}/O_2 molar ratios (between 0.6/0.4/0.5, 0.6/0.4/0.75, 0.6/0.4/1.0, 0.6/0.4/1.25, and 0.6/0.4/1.5) to the catalytic reactor at 850 °C. After exposure for 10 h at each condition, H_2 yield and the distribution of other by-products (i.e. C_2H_6, C_2H_4, CH_4, CO, and CO_2) were compared as shown in Fig. 4. It can be seen that the yield of H_2 and the distribution of CO increased with increasing O_2 content until the inlet C_3H_8/C_4H_{10}/O_2 molar ratio reached 1.0. On the contrary, these products gradually decreased when O_2 content were higher, whereas the distribution of CO_2 (and the detecting of H_2O at the outlet) grew up significantly; this is mainly due to the combustion of H_2 and CO by excess O_2. With increasing O_2 content, the presences of C_2H_6 and C_2H_4 decreased dramatically and closed to 0.0 when the inlet C_3H_8/C_4H_{10}/O_2 molar ratio reached 0.6/0.4/1.5. The dependence of the O_2 content on CH_4 production was non-monotonic, CH_4 increased when the inlet C_3H_8/C_4H_{10}/O_2 molar ratio changed from 0.6/0.4/0.5 to 0.6/0.4/1.0, then it slightly decreased at higher O_2 content. The decreasing of C_2H_6 and C_2H_4 and the nonlinear change for CH_4 with increasing O_2 content are due to the decomposition of C_2H_6 and C_2H_4 to CH_4 at low inlet O_2 concentration and further reforming of CH_4 at higher O_2 content.

The effect of temperature was then determined by varying the reactor temperatures from 750 to 950 °C while keeping C_3H_8/C_4H_{10}/O_2 molar ratio at 0.6/0.4/1.0. It was observed that H_2 and CO increased with increasing temperature, whereas CO_2 decreased. Some amount of C_2H_6 and C_2H_4 occurred at low temperature but considerably decreased with increasing temperature, Fig. 5. The decrease of CO_2 is due to the influence of reverse water-gas shift reaction ($CO_2 + H_2 \rightarrow CO + H_2O$), whereas the increases of CO and H_2 come from the partial

Table 2 – Product distribution and degree of carbon formation after exposure in partial oxidation of LPG at 850 °C with C_3H_8/C_4H_{10}/O_2 molar ratio of 0.6/0.4/1.0 for 48 h.

Catalyst	Product distribution (%)						Carbon formation (mmol g_{cat}^{-1})
	SH_2	SCO_2	SCO	SCH4	SC_2H_4	SC_2H_6	
La-doped Ce-ZrO_2	84.6	40.2	37.2	19.8	2.6	0.2	0.4
Sm-doped Ce-ZrO_2	81.3	44.0	35.9	15.2	4.7	0.2	0.9
Gd-doped Ce-ZrO_2	80.1	44.9	36.1	14.5	4.0	0.5	0.9
Ce-ZrO_2 (Ce/Zr = 3/1)	77.2	44.7	35.6	12.9	6.0	0.8	1.2
Nb-doped Ce-ZrO_2	71.1	42.0	29.1	17.5	9.3	2.1	3.1
Ce-ZrO_2 (Ce/Zr = 1/1)	70.3	41.6	29.8	17.9	8.9	1.8	2.5
Ce-ZrO_2 (Ce/Zr = 1/3)	67.7	38.7	29.0	20.1	10.1	2.1	2.7

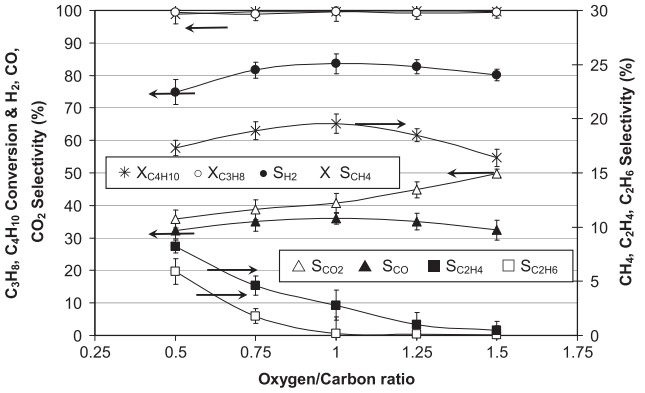

Fig. 4 – Effect of inlet O_2/carbon molar ratio on conversions and product compositions from the partial oxidation of LPG at 850 °C over La-doped Ce-ZrO_2.

oxidation of C_2H_6 and C_2H_4 at higher temperature. It is noted that the amount of carbon formation on the surface of La-doped Ce-ZrO_2 after exposure in the partial oxidation at several inlet conditions (several $C_3H_8/C_4H_{10}/O_2$ molar ratios and operating temperatures) was also determined by the post-reaction temperature-programmed oxidation (TPO) experiments. Only few degree of carbon formation was detected even at low $C_3H_8/C_4H_{10}/O_2$ molar ratio and at low temperature (750 °C), Table 3, indicating the excellent resistance toward carbon deposition of La-doped Ce-ZrO_2.

3.4. *Oxygen storage capacity (OSC) measurement*

It is known that oxygen storage capacity (OSC) is an important property of ceria-based material. In this study, the degrees of OSC for undoped Ce-ZrO_2 (Ce/Zr ratios of 3/1, 1/1 and 1/3) and doped Ce-ZrO_2 (Ce/Zr ratio of 3/1) with Gd, Nb, La, and Sm were investigated using reduction measurement (R-1), which was performed by purging the catalysts with 5%H_2 in helium at 900 °C. The amount of H_2 uptake is correlated to the amount of O_2 stored in the catalysts. As shown in Fig. 6, among Ce-ZrO_2 catalysts, the amount of H_2 uptakes from Ce-ZrO_2 (Ce/Zr ratio of 3/1) is higher than other Ce-ZrO_2, which indicates its

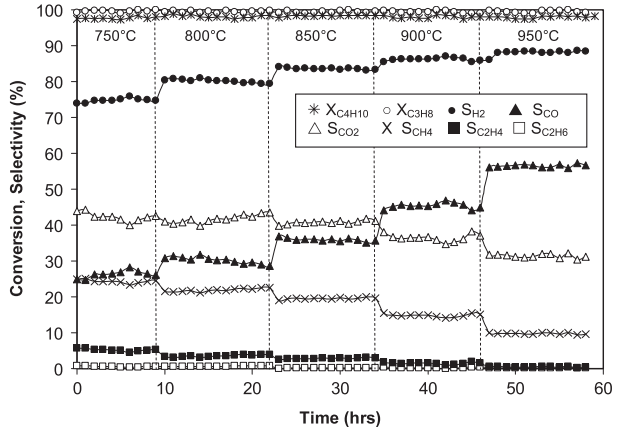

Fig. 5 – Effect of temperature on conversions and product compositions from the partial oxidation of LPG over La-doped Ce-ZrO_2 ($C_3H_8/C_4H_{10}/O_2$ molar ratio of 0.6/0.4/1.0).

Table 3 – Effects of temperature and oxygen/carbon molar ratio on the degrees of carbon formation over La-doped Ce-ZrO_2 after exposure in partial oxidation of LPG.

Catalyst	Temperature (°C)	Oxygen/carbon Molar ratio	Carbon formation (mmol $gcat^{-1}$)
La-doped Ce-ZrO_2	850	0.5	0.8
	850	0.75	0.6
	850	1.0	0.4
	850	1.25	0.3
	850	1.5	0.4
La-doped Ce-ZrO_2	750	1.0	1.4
	800	1.0	1.1
	900	1.0	0.2
	950	1.0	0.1

strongest OSC; this result is in good agreement with several reports from the literature [36–38]. In addition, La-doped Ce-ZrO_2 (with Ce/Zr ratio of 3/1) exhibits significantly higher H_2 uptakes than other catalysts, suggesting the increasing of OSC with the doping of La. After purged with He, the OSC reversibility was then determined by applying oxidation measurement ($O_x - 1$) following with second time reduction measurement (R-2). The amounts of O_2 chemisorbed and H_2 uptakes (from R-1 and R-2) are calculated and summarized in Table 4. Clearly, H_2 uptakes from R-2 are almost identical to those from R-1 for all materials, indicating the reversibility of OSC for these synthesized ceria-based materials.

The results from Sections 3.2 and 3.3 indicate that the partial oxidation reactivity and the resistance toward carbon deposition of ceria-based materials are strongly related to the degree of their OSC. It has been widely reported that at moderate temperature, the lattice oxygen (O_O^x) at CeO_2

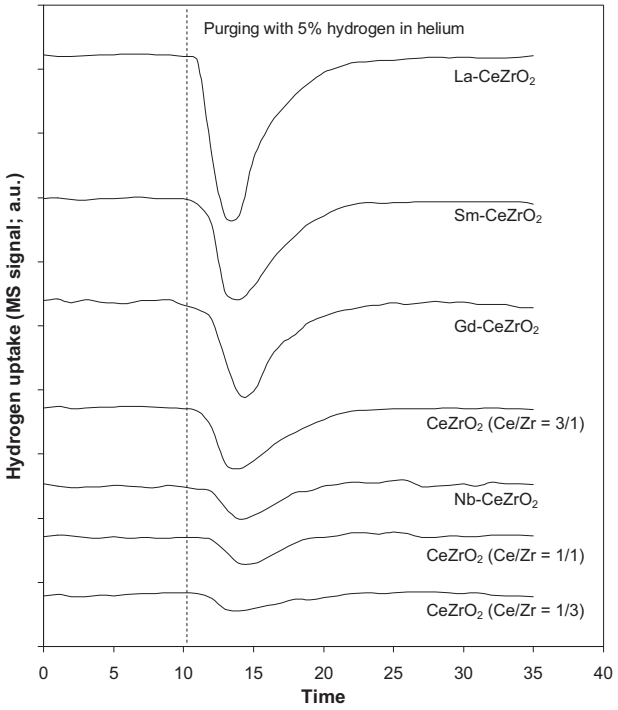

Fig. 6 – Reduction measurement (R-1) of several ceria-based catalysts.

Table 4 – Results of R-1, $O_x - 1$ and R-2 analyses of fresh catalysts.

Catalyst	Total H_2 uptake from R-1 (μmol/gcat)	Total O_2 uptake from $O_x - 1$ (μmol/gcat)	Total H_2 uptake from R-2 (μmol/gcat)
La-doped Ce-ZrO_2	6872	3436	6859
Sm-doped Ce-ZrO_2	5418	2716	5417
Gd-doped Ce-ZrO_2	5411	2705	5407
Ce-ZrO_2 (Ce/Zr = 3/1)	5234	2637	5232
Nb-doped Ce-ZrO_2	3707	1844	3701
Ce-ZrO_2 (Ce/Zr = 1/1)	3695	1853	3690
Ce-ZrO_2 (Ce/Zr = 1/3)	2884	1479	2872

surface can oxidize gaseous hydrocarbons (e.g. CH_4 [32]). By using these ceria as partial oxidation catalyst, the gas–solid reactions between hydrocarbons present in the system (i.e. CH_4, C_2H_4, and C_2H_6) and O_O^x takes place at the ceria surface forming CO and H_2 from which the formation of carbon is thermodynamically unfavorable. Previously, we have proposed the redox mechanism to explain the reforming behavior of ceria-based catalysts by indicating that the reforming reaction mechanism involves the reaction between CH_4, or an intermediate surface hydrocarbon species, and O_O^x at the ceria-based material surface [32]. During reaction, the isothermal reaction rate reaches steady-state where co-reactant (i.e. H_2O and CO_2) provides a continuing source of oxygen. We also proposed that the controlling step is the reaction of CH_4 with ceria, and that O_O^x is replenished by a significantly more facile surface reaction of ceria with H_2O or CO_2. Therefore, we here suggested that the reaction pathway for the partial oxidation of LPG over these ceria involves the reaction between absorbed hydrocarbons (forming intermediate surface hydrocarbon species) with the lattice oxygen (O_O^x) at ceria surface, as illustrated schematically below.

C_nH_m adsorption

$$C_nH_m + (n+m)^* \rightarrow (CH_x^*) + (H^*) \rightarrow n(C^*) + m(H^*) \quad (5)$$

Co-reactant (O_2) adsorption

$$O_2 + 2^* \Leftrightarrow 2O^* \quad (6)$$

Redox reactions of lattice oxygen (O_O^x) with C* and O*

$$C^* + O_O^x \rightarrow CO^* + V_O^{\bullet\bullet} + 2e' \quad (7)$$

$$V_O^{\bullet\bullet} + 2e' + O^* \Leftrightarrow O_O^x + ^* \quad (8)$$

Desorption of products (CO and H_2)

$$CO^* \Leftrightarrow CO + ^* \quad (9)$$

$$2(H^*) \Leftrightarrow H_2 + 2^* \quad (10)$$

Using the Kroger–Vink notation, $V_O^{\bullet\bullet}$ denotes as an oxygen vacancy with an effective charge 2^+, and e′ is an electron which can either be more or less localized on a cerium ion or delocalized in a conduction band. * is the surface active site of ceria-based materials. During the reactions, hydrocarbons adsorbed on * forming intermediate surface hydrocarbon species (CH_x*) (Eq. (5)) and later reacted with O_O^x (Eq. (7)). The steady-state rate is due to the continuous supply of the oxygen source by oxygen that reacted with the reduced-state catalyst to recover O_O^x (Eqs. (6) and (8)). It is noted that, according to our previous studies, * can be considered as unique site or same site as O_O^x [32]. During the reaction, hydrocarbons adsorbed on either unique site or O_O^x whereas O_2 is always reacted with the catalyst reduced site.

3.5. *Sequential partial oxidation/steam reforming as autothermal operation*

As observed, the partial oxidation of LPG over La-doped Ce-ZrO_2 provided higher reactivity than other ceria-based catalysts with greater resistance toward carbon deposition compared to conventional Ni/Al_2O_3. Nevertheless, some formation of CH_4 remains observed even above 950 °C indicating the incomplete conversion of LPG to syngas (CO and H_2). Thus, an alternative concept to maximize the yield of H_2 from LPG was proposed by applying sequential partial oxidation/steam reforming operation and using La-doped Ce-ZrO_2 as primary oxidative catalyst. In detail, the reforming reactor was designed as an annular reactor (made from ceramic), as shown in Fig. 7. La-doped Ce-ZrO_2 (with the weight of 200 mg) was packed at the inner side of this annular reactor, where

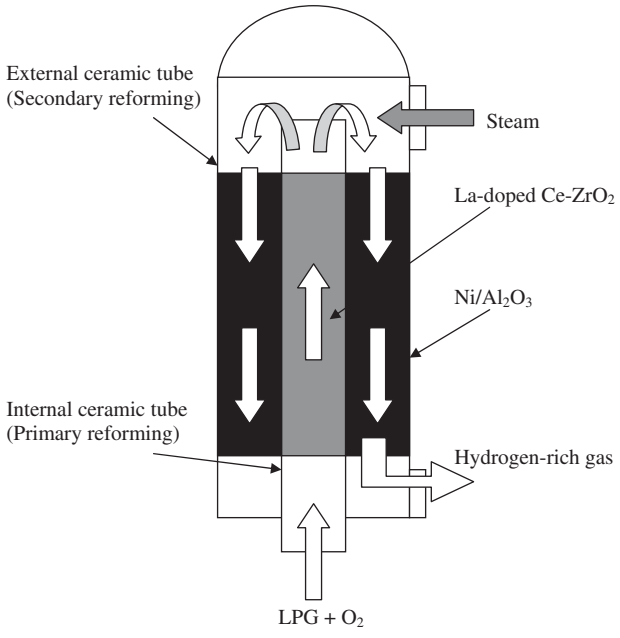

Fig. 7 – Configuration of catalytic testing unit with sequential partial oxidation/steam reforming.

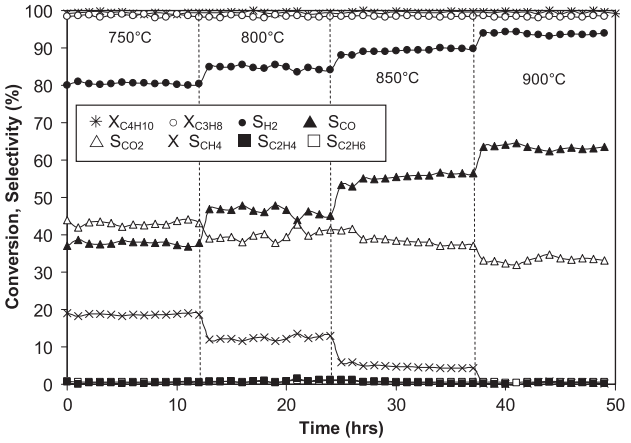

Fig. 8 – Effect of temperature on the conversions and product compositions from the sequential partial oxidation/steam reforming of LPG.

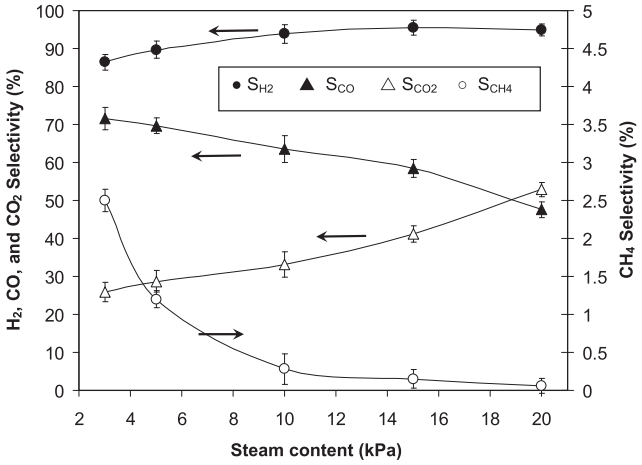

Fig. 9 – Effect of inlet H_2O/carbon molar ratio on product compositions from the sequential partial oxidation/steam reforming of LPG at 850 °C (with O_2/carbon molar ratio at 1.0).

LPG and O_2 were introduced and the partial oxidation reaction took place. At the end of this inner tube, all gas components flowed backward and instantly mixed with steam (diluted in helium) from the external source before passing through the secondary bed at the outer side of this annular reactor, where Ni/Al_2O_3 (with the weight of 300 mg) was packed. For this experiment, the total gas flow rate was kept constant at 1000 $cm^3\,min^{-1}$ under a constant residence time of 5×10^{-4} g $min\,cm^{-3}$. According to this design, the aims of La-doped Ce-ZrO_2 are to convert all high hydrocarbons i.e. C_4H_{10}, C_3H_8, C_2H_6, and C_2H_4 to CH_4, CO, CO_2, and H_2 (and technically supply heat to the secondary steam reforming part), whereas Ni/Al_2O_3 is applied to convert all CH_4 left from the first section and maximize the yield of H_2 production.

According to the test, the feed to inner tube was C_3H_8/C_4H_{10}/O_2 with molar ratio of 0.6/0.4/1.0; and at the exit of the inner tube, 10 kPa H_2O was added. Fig. 8 presents the yield of H_2 and other product distribution over this configuration at several temperatures (750–900 °C). It can be seen that H_2 and CO increased with increasing temperature, whereas the trends of CO_2, CH_4, C_2H_6 and C_2H_4 decreased. The conversions of LPG and O_2 were always 100% whereas that of H_2O was around 80–85%. Above 900 °C, the main products from this system were H_2, CO and CO_2 without the formation of hydrocarbons. At the same operating conditions, H_2 produced from this configuration is significantly higher than that observed from the partial oxidation over La-doped Ce-ZrO_2. Furthermore, according to the TPO testing over spent catalysts, the amount of carbon deposition observed on the surface of Ni/Al_2O_3 was relatively low compared to that observed from the partial oxidation of LPG (~2.4 mmol g_{cat}^{-1} at 850 °C).

The influence of inlet H_2O content on the yield of H_2 and other product distribution from this coupling configuration were also studied by changing the inlet H_2O content from 3 to 20 kPa as represented in Fig. 9. It was found that H_2 and CO_2 increased with increasing inlet H_2O concentration, whereas CO and CH_4 decreased. The changes of H_2, CO and CO_2 are related to the influence of higher water-gas shift reaction ($CO + H_2O \rightarrow CO_2 + H_2$), while the decreasing of CH_4 could be due to the promotion of steam reforming rate by excess H_2O to generate more CO and H_2. At 850 °C with inlet C_3H_8/C_4H_{10}/O_2 molar ratio of 0.6/0.4/1.0, the highest H_2 yield of 91.4% can be achieved by introducing inlet H_2O content of 15 kPa.

Lastly, the performance of this reactor configuration was compared with that of the conventional autothermal reforming over Rh/Al_2O_3. Rh-based catalyst was selected since it has been widely reported to be one of the most active catalysts for reforming and relevant reactions; even through the Rh cost is relatively high compared to other metals. The tests were carried out by feeding LPG and O_2 along with H_2O to the quartz reactor at 900 °C where 500 mg of Rh/Al_2O_3 was packed. The inlet C_3H_8/C_4H_{10}/H_2O/O_2 molar ratios were varied from 0.6/0.4/4.0/0.5 to 0.6/0.4/4.0/1.25 in order to identify the most suitable ratio, which provided the highest H_2 yield with

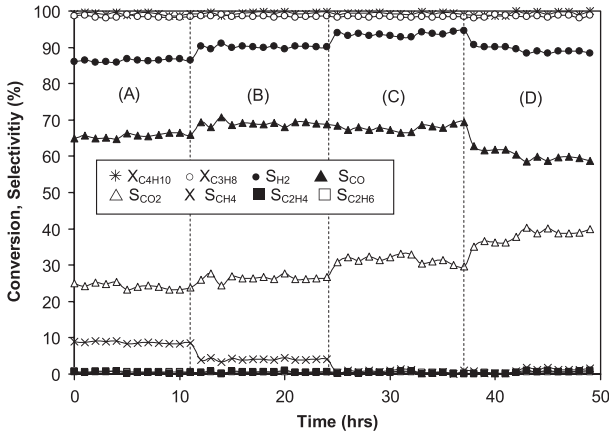

Fig 10 – The variations in conversions and product compositions with time from the autothermal reforming of LPG over Rh/Al_2O_3 at 850 °C with the inlet O_2/H_2O/carbon molar ratios of 0.0/7.0/1.0 (A), 0.2/7.0/1.0 (B), 0.4/7.0/1.0 (C), and 0.6/7.0/1.0 (D).

lower degree of carbon deposition. As shown in Fig. 10, the suitable $C_3H_8/C_4H_{10}/H_2O/O_2$ molar ratio that provided the highest H_2 yield (94.5%) is 0.6/0.4/4.0/1.0. Compared to the coupling of partial oxidation/steam reforming over La-doped Ce-ZrO_2 and Ni/Al_2O_3, the yield of H_2 from both systems are in the same range indicated the possible replacement of expensive noble metal catalysts with this combination pattern.

4. Conclusion

Ce-ZrO_2 was found to have useful LPG partial oxidation activity with excellent resistance toward carbon deposition under moderate temperature. Doping of La, Sm and Gd over Ce-ZrO_2 promoted its catalytic reactivity, whereas the doping of Nb slightly reduced the partial oxidation reactivity. Among La-, Sm- and Gd-doping, La-doped Ce-ZrO_2 was the most active catalyst. At temperature above 850 °C with inlet LPG/O_2 molar ratio of 1.0/1.0, the main products from the partial oxidation of La-doped Ce-ZrO_2 were H_2, CH_4, CO, and CO_2. By applying this catalyst as pre-oxidative catalyst for sequential partial oxidation/steam reforming system, excellent performance comparable to the autothermal reforming over Rh/Al_2O_3 can be achieved.

Acknowledgement

The financial support from Thailand Research Fund (TRF) throughout this project is gratefully acknowledged.

REFERENCES

[1] Ahmed S, Krumpelt M. Hydrogen from hydrocarbon fuels for fuel cells. Int J Hydrogen Energy 2001;26:291–301.
[2] Seo Y-S, Shirley A, Kolaczkowski ST. Evaluation of thermodynamically favourable operating conditions for production of hydrogen in three different reforming technologies. J Power Sources 2002;108:213–5.
[3] Kumar Shashi, Kumar Surendra, Prajapati Jitendra K. Hydrogen production by partial oxidation of methane: modeling and simulation. Int J Hydrogen Energy 2009;34: 6655–68.
[4] Corbo Pasquale, Migliardini Fortunato. Hydrogen production by catalytic partial oxidation of methane and propane on Ni and Pt catalysts. Int J Hydrogen Energy 2007;32:55–66.
[5] Nguyen BNT, Leclerc CA. Catalytic partial oxidation of methyl acetate as a model to investigate the conversion of methyl esters to hydrogen. Int J Hydrogen Energy 2008;33: 1295–303.
[6] Al-Hamamre Z, Voß S, Trimis D. Hydrogen production by thermal partial oxidation of hydrocarbon fuels in porous media based reformer. Int J Hydrogen Energy 2009;34:827–32.
[7] Simeone M, Salemme L, Scognamiglio D, Allouis C, Volpicelli G. Effect of water addition and stoichiometry variations on temperature profiles in an autothermal methane reforming reactor with Ni catalyst. Int J Hydrogen Energy 2008;33:1252–61.
[8] Qi Aidu, Wang Shudong, Ni Changjun, Wu Diyong. Autothermal reforming of gasoline on Rh-based monolithic catalysts. Int J Hydrogen Energy 2007;32:981–91.
[9] Recupero V, Pino L, Leonardo RD, Lagana M, Maggio G. Hydrogen generator, via catalytic partial oxidation of methane for fuel cells. J Power Sources 1998;71:208–14.
[10] Kikuchi R, Iwasa Y, Takeguchi T, Eguchi K. Partial oxidation of CH_4 and C_3H_8 over hexaaluminate-type oxides. Appl Catal A Gen 2005;281:61–7.
[11] Fukunaga T, Katsuno H, Matsumoto H, Takahashi O, Arai Y. Development of kerosene fuel processing system for PEFC. Catal Today 2003;84:197–200.
[12] Takenaka S, Kawashima K, Matsune H, Kishida M. Production of CO-free hydrogen through the decomposition of LPG and kerosene over Ni-based catalysts. Appl Catal A Gen 2007;321:165–74.
[13] Falkiner RJ. Liquefied petroleum gas. Glen Burnie, MD: ASTM International; 2003.
[14] Pino L, Vita A, Cipitì F, Laganà M, Recupero V. Performance of Pt/CeO_2 catalyst for propane oxidative steam reforming. Appl Catal A 2006;306:68–77.
[15] Ahmed K, Gamman J, Föger K. Demonstration of LPG-fueled solid oxide fuel cell systems. Solid State Ionics 2002;152–153:485–92.
[16] Suzuki T, Iwanami H, Iwamoto O, Kitahara T. Pre-reforming of liquefied petroleum gas on supported ruthenium catalyst. Int J Hydrogen Energy 2001;26:935–40.
[17] Avci AK, Trimm DL, Aksoylu AE, Önsan ZI. Ignition characteristics of Pt, Ni and Pt–Ni catalysts used for autothermal fuel processing. Catal Lett; 88: p. 17–22.
[18] Ghenciu AF. Review of fuel processing catalysts for hydrogen production in PEM fuel cell systems. Curr Opinion Solid State Mater Sci 2002;6:389–99.
[19] Rampe T, Heinzel A, Vogel B. Hydrogen generation from biogenic and fossil fuels by autothermal reforming. J Power Sources 2000;86:536–41.
[20] Joensen F, Rostrup-Nielsen JR. Conversion of hydrocarbons and alcohols for fuel cells. J Power Sources 2002;105:195–201.
[21] Recupero V, Pino L, Vita A, Cipitı F, Cordaro M, Laganà M. Development of a LPG fuel processor for PEFC systems: laboratory scale evaluation of autothermal reforming and preferential oxidation subunits. Int J Hydrogen Energy 2005; 30:963–71.
[22] Mattos LV, Rodino E, Resasco DE, Possos FB, Noronha FB. Partial oxidation and CO_2 reforming of methane on Pt/Al_2O_3, Pt/ZrO_2, and Pt/Ce-ZrO_2 catalysts. Fuel Process Technol 2003; 83:147–61.
[23] Roh HS, Jun KW, Park SE. Methane-reforming reactions over Ni/Ce-ZrO_2/θ-Al_2O_3 catalysts. Appl Catal A 2003;251:275–83.
[24] Rostrup-Nielsen JR, Bak-Hansen JH. CO_2-reforming of methane over transition metals. J Catal 1993;144:38–49.
[25] Fornasiero P, Balducci G, Monte RD, Kaspar J, Sergo V, Gubitosa G, et al. Modification of the redox behaviour of CeO_2 induced by structural doping with ZrO_2. J Catal 1996;164:173–83.
[26] Imamura S, Shono M, Okamoto N, Hamada R, Ishida S. Effect of cerium on the mobility of oxygen on manganese oxides. Appl Catal A 1996;142:279–88.
[27] Fan L, Fujimoto K. Reaction mechanism of methanol synthesis from carbon dioxide and hydrogen on ceria-supported palladium catalysts with SMSI effect. J Catal 1997; 172:238–42.
[28] Pijolat M, Prin M, Soustelle M. Thermal stability of doped ceria-experimental and modeling. J Chem Soc Faraday Trans 1995;91:3941–8.
[29] Balducci G, Kaspar J, Fornasiero P, Graziani M, Islam MS. Surface and reduction energetics of the CeO_2–ZrO_2 catalysts. J Phys Chem B 1998;102:557–61.
[30] Fornasiero P, Dimonte R, Rao GR, Kaspar J, Meriani S, Trovarelli A, et al. Rh-Loaded CeO_2–ZrO_2 solid-solutions as

highly efficient oxygen exchangers: dependence of the reduction behavior and the oxygen storage capacity on the structural-properties. J Catal 1995;151:168–77.
[31] Yao MH, Baird RJ, Kunz FW, Hoost TE. An XRD and TEM investigation of the structure of alumina-supported ceria–zirconia. J Catal 1997;166:67–74.
[32] Laosiripojana N, Assabumrungrat S. Catalytic dry reforming of methane over high surface area ceria. Appl Catal B 2005; 60:107–16.
[33] Terribile D, Trovarelli A, Llorca J, Leitenburg C, Dolcetti G. The preparation of high surface area CeO_2–ZrO_2 mixed oxides by a surfactant-assisted approach. Catal Today 1998;43:79–88.
[34] Laosiripojana N, Assabumrungrat S. Hydrogen production from steam and autothermal reforming of LPG over high surface area ceria. J Power Sources 2006;158:1348–57.
[35] Ramírez-Cabrera E, Laosiripojana N, Atkinson A, Chadwick D. Methane conversion over Nb-doped ceria. Catal Today 2003;78:433–8.
[36] Deshmukh Subodh S, Zhang Minghui, Kovalchuk Vladimir I, d'Itri Julie L. Effect of SO_2 on CO and C_3H_6 oxidation over CeO_2 and $Ce_{0.75}Zr_{0.25}O_2$. Appl. Catal. B 2003;45:135–45.
[37] Laosiripojana N, Assabumrungrat S. Kinetic dependencies and reaction pathways in hydrocarbon and oxyhydrocarbon conversions catalyzed by ceria-based materials. Appl Catal B 2008;82:103–13.
[38] Singh Preetam, Hegde MS. Controlled synthesis of nanocrystalline CeO_2 and $Ce_{1-x}M_xO_{2-\delta}$ (M = Zr, Y, Ti, Pr and Fe) solid solutions by the hydrothermal method: structure and oxygen storage capacity. J Solid State Chem 2008;181: 3248–56.

Process Biochemistry 45 (2010) 829–834

Contents lists available at ScienceDirect

Process Biochemistry

journal homepage: www.elsevier.com/locate/procbio

Biocatalytic ethanolysis of palm oil for biodiesel production using microcrystalline lipase in *tert*-butanol system

Marisa Raita [a], Verawat Champreda [b,*], Navadol Laosiripojana [a]

[a] *Joint Graduate School for Energy and Environment (JGSEE), King Mongkut's University of Technology Thonburi, Bangmod, Bangkok 10140, Thailand*
[b] *Enzyme Technology Laboratory, National Center for Genetic Engineering and Biotechnology, 113 Thailand Science Park, Paholyothin Road, Klong Luang, Pathumthani 12120, Thailand*

ARTICLE INFO

Article history:
Received 2 October 2009
Received in revised form 24 December 2009
Accepted 1 February 2010

Keywords:
Biodiesel
Ethanolysis
Lipase
Palm oil
Protein-coated microcrystals

ABSTRACT

Biocatalytic synthesis is a promising environmentally friendly process for the production of biodiesel, a sustainable alternative fuel from renewable plant resources. In order to develop an economical heterogeneous biocatalyst, protein-coated microcrystals (PCMCs) were prepared from a commercial enzyme preparation from a recombinant *Aspergillus* strain expressing *Thermomyces lanuginosus* lipase and used for synthesis of biodiesel from palm olein by ethanolysis. Reaction parameters, including catalyst loading, temperature, and oil/alcohol molar ratio have been systematically optimized. Addition of *tert*-butanol was found to markedly increase the biocatalyst activity and stability resulting in improved product yield. Optimized reactions (20%, w/w PCMC-lipase to triacylglycerol and 1:4 fatty acid equivalence/ethanol molar ratio) led to the production of alkyl esters from palm olein at 89.9% yield on molar basis after incubation at 45 °C for 24 h in the presence of *tert*-butanol at a 1:1 molar ratio to triacylglycerol. Crude palm oil and palm fatty acid distillate were also efficiently converted to biodiesel with 82.1 and 75.5% yield, respectively, with continual dehydration by molecular sieving. Operational stability of PCMC-lipase could be improved by treatment with *tert*-butanol allowing recycling of the biocatalyst for at least 8 consecutive batches with only slight reduction in activity. This work thus shows a promising approach for biodiesel synthesis with microcrystalline lipase which could be further developed for cost-efficient industrial production of biodiesel.

1. Introduction

Biodiesel is an alternative fuel for diesel engines from renewable resources. Currently, several approaches have been used for the synthesis of biodiesel, including chemocatalytic, thermocatalytic and biocatalytic methods [1–3]. As an alternative to the conventional alkali-catalyzed transesterification process currently used in industry, the biocatalytic process has been studied as an environmentally friendly approach for biodiesel synthesis under mild conditions employing lipase biocatalysts, and has gained increasing commercial interest [4]. This method has many advantages for the synthesis of alkyl esters, including easy recovery of glycerol, ability to convert free fatty acids to esters, which allows complete conversion of glycerides with high free fatty acid content, and no requirement for subsequent wastewater treatment [5]. The enzymatic approach has been used for the synthesis of biodiesel from various vegetable oils, such as soybean oil [6], rice bran oil [7], sunflower oil [8], palm oil [9], waste edible oil [5] and acid oil [10]. Lipases from different microbial origins e.g. *Candida antarctica* [11], *Pseudomonas cepacia* [12], *Muchor miehei* [13] and *Thermomyces lanuginosus* [14] have been employed as biocatalysts in biodiesel synthesis. In addition to purified lipase enzymes, whole cells of *Rhizopus oryzae* expressing lipase have been employed as a biocatalyst for synthesis of biodiesel from various feedstocks [15]. However, the main drawback of the enzymatic approach is the high cost and low stability of biocatalysts. Further improvement of enzymatic processes for biodiesel production has thus been focused on the cost reduction for lipases and improvement of the enzyme's operational time and reusability, which would benefit the commercialization of the biocatalytic process.

Immobilization is considered as a potential approach for optimizing the operational performance of enzymes in industrial processes, especially for non-aqueous systems. Several approaches have been used for immobilization of lipases for biodiesel synthesis, including adsorption [16], entrapment [12], and

Abbreviations: EtOH, ethanol; FA, fatty acid; FAEE, fatty acid ethyl ester; PCMCs, protein-coated microcrystals; TAG, triacylglycerol; *t*-BuOH, *tert*-butanol.

* Corresponding author. Tel.: +66 2564 6700x3473; fax: +66 2564 6707.
E-mail address: verawat@biotec.or.th (V. Champreda).

1359-5113/$ – see front matter © 2010 Elsevier Ltd. All rights reserved.
doi:10.1016/j.procbio.2010.02.002

covalent immobilization on a carrier [17] as well as carrier-free immobilization e.g. cross-linked enzyme aggregates (CLEAs) [18] and cross-linked enzyme crystals (CLECs) [19]. Protein-coated microcrystals (PCMCs) have been reported as an alternative biocatalyst design with great potential for catalysis in non-aqueous systems e.g. biodiesel synthesis and kinetic resolution of enantiomers in organic solvents [20,21]. PCMCs are characterized as a uniform enzyme layer on the surface of micron-sized salt crystals, which can be prepared by co-precipitation of enzyme and salt in an organic solvent. PCMCs possess several advantages over existing immobilization methods, including a low mass-transfer limitation, high catalytic performance, improved stability and reusability, and low preparation cost [22,23]. The use of PCMC-lipase has recently been demonstrated for synthesis of biodiesel from local feedstocks e.g. jatropha oil [22] and Mahua oil [23]. Here, the optimization of PCMC-lipase on biodiesel synthesis from palm oil (*Elaeis guineensis*), one of the most important energy crops in tropical regions with ethanol is reported. Both feedstocks are considered major renewable bio-products in Thailand and Southeast Asian countries. This would provide an attractive alternative for biocatalytic production of biodiesel for future development of green energy industry.

2. Materials and methods

2.1. Materials

Refined edible grade palm oil (palm olein; RPO) was obtained from a local market. Crude palm oil (CPO) and palm fatty acid distillate (PFAD) were obtained from the Pathum Vegetable Oil, Co. Ltd. (Pathumthani, Thailand). Liquid lipase from a genetically modified *Aspergillus* sp., DELIP 50L (50 KLU/g) was supplied by Flexo Research, Pathumthani, Thailand (1 KLU is defined as the amount of enzyme liberating 1 mmole of titratable butyric acid from tributyrin in 1 min). Novozymes® 435 (immobilized *C. antarctica* lipase B) and Lipolase 100T (granulated silica immobilized *T. lanuginosus* lipase) were from Novozymes (Bagsvaerd, Denmark). Chemicals and reagents were analytical grade and obtained from major chemical companies. All reagents were dehydrated with 3 Å molecular sieve (Fluka, Buchs, Switzerland) before use.

2.2. Lipase activity assay

Lipase activity was assayed based on hydrolysis of *p*-nitrophenyl palmitate [24]. The standard reaction (100 μl) contained 50 mM sodium phosphate buffer, pH 8, 2.5 mM of *p*-nitrophenyl palmitate and an appropriate dilution of the enzyme. The reaction was incubated at 45 °C for 15 min and terminated by addition of 100 μl of 0.2 M $NaCO_3$. The formation of *p*-nitrophenolate was determined by measuring the absorbance at 405 nm. Control reactions with no enzyme were included in all experiments to subtract the appropriate values for non-enzymatic hydrolysis of substrates from the results. One unit of the enzyme activity was defined as the amount of enzyme catalyzing the release of 1 μmole *p*-nitrophenolate/min under the standard experimental conditions used.

2.3. Preparation of PCMC-lipase

PCMC-lipase was prepared based on the method modified from Shah et al. [22]. Commercial lipase preparation DELIP 50L (192 ml) was clarified by centrifugation (12,000 × *g*, 10 min) and pre-concentrated (3×, to 64 ml) using ultrafiltration on a Minimate tangential flow filtration system using a Minimate TFF capsule with 10 kDa MWCO membrane (Pall, Easthills, NY, USA). Saturated solution of potassium sulphate (96 ml) was added to the concentrated lipase solution (64 ml). This combined mixture was then added drop-wise to a stirring vial (150 rpm) containing 420 ml of acetone. The precipitate obtained was centrifuged at 2200 × *g* for 5 min to remove acetone. The precipitate was then washed three times with 25 ml of acetone. The air-dried precipitate (0.48 g from initial concentrated lipase of 1 ml) exhibiting 0.35 IU/g lipase activity based on *p*-nitrophenyl palmitate assay [24] was used as the biocatalyst in this study.

2.4. Lipase-catalyzed transesterification (biodiesel synthesis)

For the optimized reaction, palm oil (500 mg) and ethanol were reacted in the molar ratio of 1:4 (FA/EtOH) in the presence of *tert*-butanol at 1:1 molar ratio (TAG/*t*-BuOH). PCMC-lipase was added to 20% (w/w) based on TAG in the reaction and incubated at 45 °C on a vertical rotator. Samples were withdrawn at time intervals. The samples (2 μl) were diluted with hexane (10 μl) and mixed with lauric acid methyl ester (5 μl) as an internal standard. The amount of esters formed was then determined by gas chromatography. The conversion yield (%) is the amount of alkyl esters converted from triglycerides on a molar basis. For reusability study, the biocatalyst was recovered by centrifugation, washed with 1 ml of acetone or *tert*-butanol twice, and air-dried before use in the next batch.

2.5. Gas chromatography analysis of alkyl esters

The alkyl esters were analyzed by gas chromatography on a Shimadzu 2010, equipped with a flame ionization detector (Shimadzu, Kyoto, Japan) and a polyethylene glycol capillary column (Carbowax 20M, 30 m × 0.32 mm, Agilent Technologies, Santa Clara, CA). The column oven temperature was at 200 °C, with injector and detector temperatures at 250 and 260 °C, respectively. Helium was used as the carrier gas at a constant pressure of 64.1 kPa with linear velocity at 25 cm/s. The amount of FAEE and FAME were determined based on the standard curves using the corresponding esters. The reactions were done in triplicate and standard deviations were reported for all experimental results.

2.6. Scanning electron microscopy analysis

The structure and morphology of the PCMC-lipase were analyzed by scanning electron microscope (SEM) using a JSM-6301F Scanning Electron Microscope (JEOL, Tokyo, Japan. The samples were dried and coated with gold for analysis. An electron beam energy of 5 kV was used for analysis.

3. Results and discussion

3.1. Synthesis of PCMC-lipase

In this study, PCMC-lipase was prepared from a crude commercial lipase preparation DELIP 50L from a genetically modified *Aspergillus* sp. LC/MS/MS analysis revealed that the lipase origin was from a thermophilic fungus *T.* (*Humicola*) *lanuginosus* (data not shown). Lipase preparations from *T. lanuginosus* have been used in biodiesel synthesis with high efficiency [14,25–27]. The 3× concentrated enzyme in solution showed high hydrolysis activity towards *p*-nitrophenyl palmitate with volumetric activity of 0.27 IU/ml. Preliminary study using this liquid lipase preparation showed high efficiency on transesterification of purified palm olein. This enzyme was thus suitable for preparation as a PCMC conjugate.

Preliminary optimization of K_2SO_4 concentration showed that salt equivalent to 0.6× of saturated concentration was optimal for PCMC-lipase preparation (data not shown). The physical characteristics of PCMC-lipase were examined using SEM. The biocatalysts are formed as an aggregate of crystals and had a variable size distribution (10–50 μm in diameter). The surface of PCMC-lipase was rough with tiny pores distributed on the catalyst surface and was physically different to that reported previously (Fig. 1). The overall surface of PCMC-lipase was different to the K_2SO_4 salt control of which showed rectangular crystal structure similar to that previously reported [22]. The surface characteristics of PCMC-lipase are suggestive of enzyme molecule aggregation on the salt crystals. PCMC-lipase was found to be sensitive to free water in the reaction. Pre-dehydration of the reaction components by molecular sieving was found to increase the catalytic activity and stability, resulting in an increased product yield of approximately 20% under the optimized conditions (data not shown). Control reaction using molecular sieve with no PCMC-lipase resulted in no detectable product under the same reaction conditions. A similar observation was reported in the previous study on application of PCMCs in non-aqueous synthesis reaction [22].

3.2. Effects of reaction parameters on biodiesel synthesis

Initial trials on analyzing the catalytic reactivity of the biocatalyst and operational conditions for biodiesel synthesis started with the optimization of biocatalyst loading (5–30%, w/w based on TAG) in the presence of *tert*-butanol (molar ratio of 1:1 TAG/*t*-BuOH) using ethanol or methanol as the nucleophile. PCMC-lipase loading at 20% (w/w) based on TAG was found to be optimal,

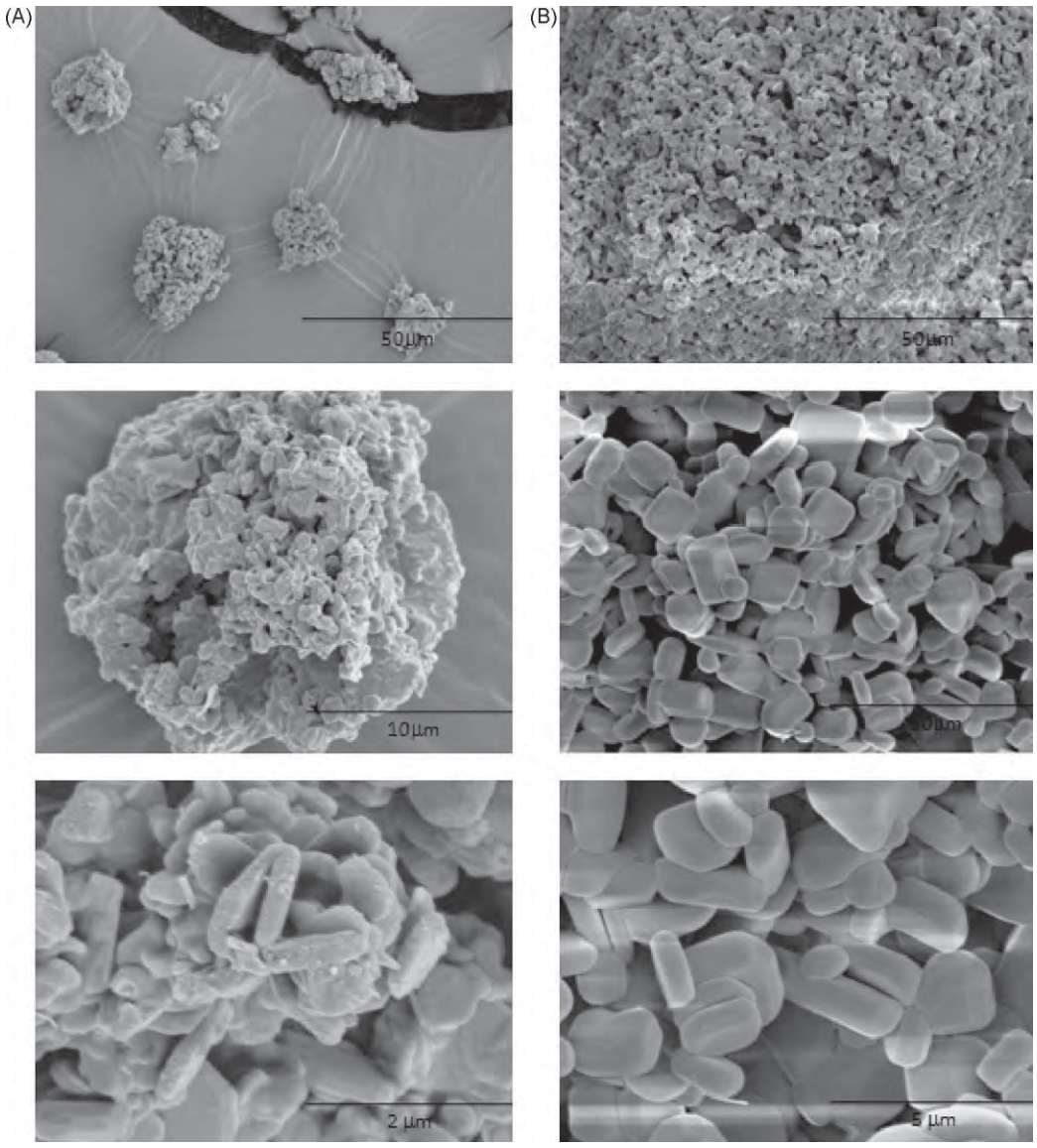

Fig. 1. SEM analysis of PCMC-lipase. (A) PCMC-lipase and (B) K_2SO_4 crystals control, no lipase added.

with a sharp increase in FAEE yield during the first 12 h leading to 89.9% conversion yield of FAEE with ethanol in the presence of *tert*-butanol after 24 h incubation at 45 °C (Fig. 2). The biocatalyst loading was in the same range (4–50%) as those previously reported using different forms of immobilized lipase [22,27,28]. The biocatalyst reactivity towards methanolysis was investigated by varying the biocatalyst loading under the same reaction conditions. Much lower yields were obtained with methanol at all enzyme loadings, with a maximal yield of 32.1% after incubation for 24 h in the presence of *tert*-butanol (Fig. 3). The greater FAEE yield for lipase biocatalysis in ethanol is likely due to ethanol's lower nucleophile induced deactivation of lipase and the use of ethanol has been found to be more facile for enzymatic biodiesel synthesis in many cases [27,29]. Lipases from different microbial origins have been reported to have different sensitivities towards nucleophile induced deactivation [27], and fungal lipases, including *T. lanuginosus* lipase, have been reported to be inactive towards biodiesel synthesis using methanolysis under certain conditions [27,30].

The effects of key reaction parameters on synthesis of FAEE were further investigated systematically by varying one reaction

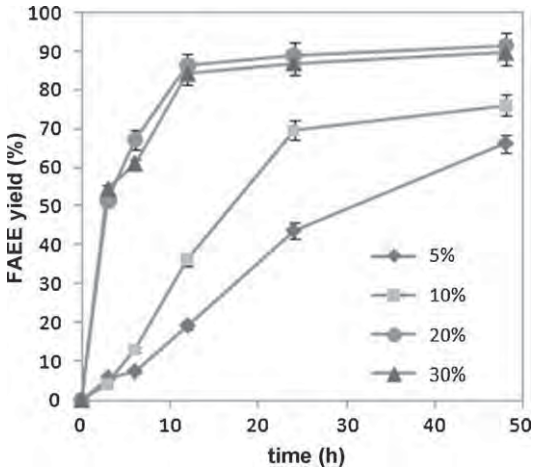

Fig. 2. Biocatalytic synthesis of biodiesel using PCMC-lipase. The reactions contained 500 mg of palm olein, 1:4 FA/EtOH molar ratio, in the presence of 1:1 TAG/*t*-BuOH molar ratio with varying amount of PCMC-lipase (5–30%, w/w based on TAG) and incubated at 45 °C for 48 h.

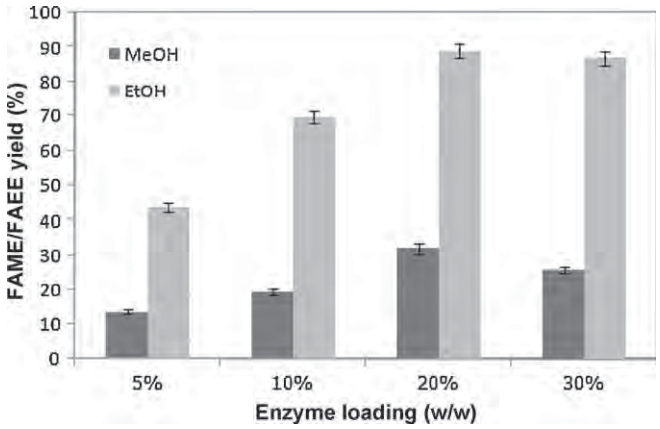

Fig. 3. Reactivity of PCMC-lipase on biodiesel synthesis using different nucleophiles. The reactions contained 500 mg of palm olein, 1:4 FA/alcohol (ethanol or methanol) molar ratio, in the presence of 1:1 TAG/*t*-BuOH molar ratio with varying amount of PCMC-lipase (5–30%, w/w based on TAG) and incubated at 45 °C for 24 h.

parameter at a time. The conversion rate on transesterification of TAG increased with increasing temperature from 30 to 45 °C, with the optimal temperature for the PCMC-catalyzed ethanolysis reaction at 45 °C leading to 88.9% FAEE yield (Fig. 4A). The lower yield at 50 °C (67.1%) suggested thermal inactivation of lipase at this temperature. In lipase-catalyzed biodiesel synthesis, yield is controlled by temperature-related phenomena, namely (i) the temperature dependence of enzyme catalysis rate; (ii) the increase on solubility of reactants at higher temperatures, and (iii) the increase in nucleophile induced deactivation of lipase at higher temperature [27]. The optimal reaction temperature at 45 °C for PCMC-lipase in this study is higher than some of that previously reported for different immobilized lipases [31]. High optimal temperatures are advantageous for transesterification of oil feedstock with high saturated fatty acid content in the form of TAG.

The effect of molar ratio of FA equivalence in TAG to nucleophile is shown in Fig. 4B. Increasing the FA/EtOH molar ratio from 1:2 to 1:4 led to an increase in FAEE yields from 62.7 to 88.9%, whereas higher ratios (1:6 and 1:8) led to lower product yields. The FA/EtOH molar ratio at 1:4 was thus optimal for ethanolysis using PCMC-lipase. The nucleophile (ethanol) has been reported to exert opposing effects on reaction, involving (i) a deactivation effect on the biocatalyst and (ii) an enhancing effect on reaction kinetics by facilitating the formation of a homogenous suspension of the biocatalysts and reactants [27]. Deactivation of lipases at high FA/EtOH molar ratios is caused by contact of the lipases with the immiscible polar organic phase, which is formed by incomplete solubility of alcohol as well as glycerol in the oil phase [5]. The deactivation effect by lower molecular weight alcohol i.e. methanol is greater than ethanol [27]. The optimal FA/EtOH ratio in this study is comparable to some previous reports of biodiesel synthesis from different vegetable oils using methanol and ethanol as a nucleophile with various immobilized lipases [9,12].

The enhancing effect of *tert*-butanol in the reaction medium at different molar ratios is shown in Fig. 4C. The TAG/*t*-BuOH molar ratio was found to be optimal at 1:1, which is similar to a previous study using commercial immobilized lipases [31]. Addition of *tert*-butanol to the reaction mixture leads to increased catalytic activity and operational stability of lipases, resulting in increasing conversion yields from reactions using either methanol or ethanol [31,32]. Pretreatment of immobilized lipase deactivated by methanol with *tert*-butanol also led to regeneration of enzyme activity [33]. The activation and stabilization of lipases could be due to the effects of *tert*-butanol on lipase stabilization from the nucleophile inactivation by linear low molecular weight alcohols

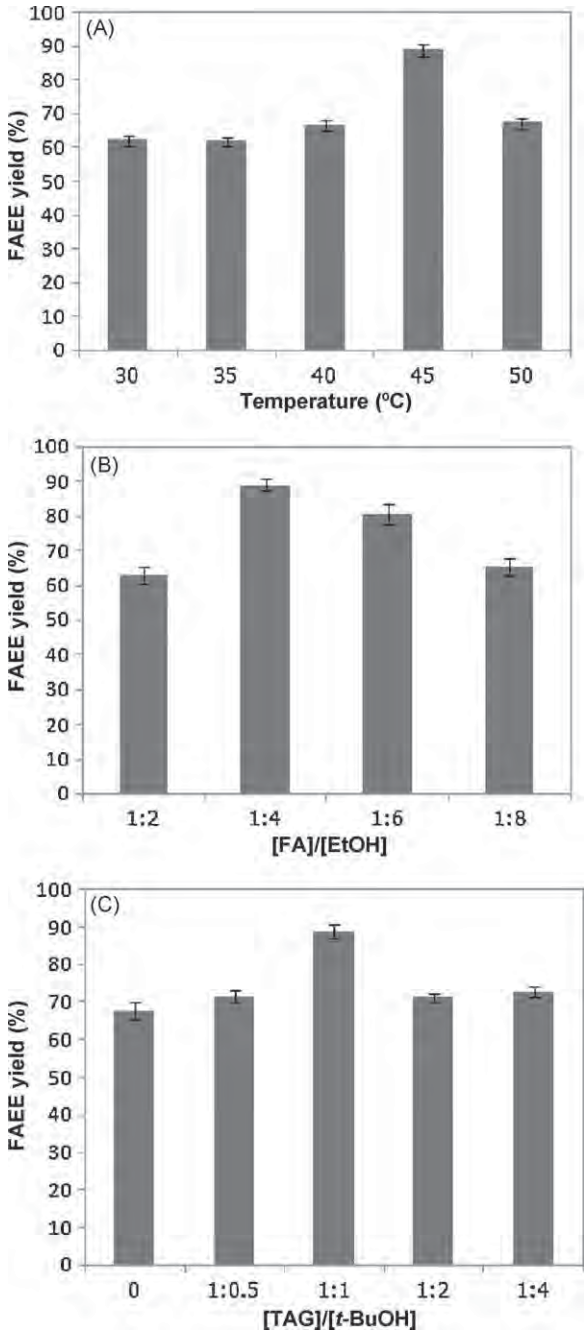

Fig. 4. Effects of reaction parameters on FAEE synthesis. The reactions contained 500 mg of palm olein as the substrate with 20% (w/w based on TAG) PCMC-lipase with varying reaction parameters of which the standard conditions contained (or otherwise indicated) 1:4 FA/EtOH, and 1:1 TAG/*t*-BuOH molar ratio. The reactions were incubated at 45 °C for 24 h. (A) Effects of temperature; (B) effects of different FA/EtOH molar ratio; (C) effects of TAG/*t*-BuOH molar ratio.

and removal of the by-product, glycerol from the enzyme surface. The activation effects of *tert*-butanol have been previously shown for different forms of immobilized lipases and whole-cell biocatalyst [15,31,34]. To our knowledge, this study is the first to demonstrate the catalysis and stability enhancing effects of *tert*-butanol for lipase immobilized in protein-coated microcrystal form on the biodiesel synthesis reaction.

The potential of PCMC-lipase on biodiesel synthesis was compared with other types of immobilized lipases under the same enzyme loading (20%) and reaction conditions. The yield of FAEE using PCMC-lipase prepared from pre-concentrated DELIP

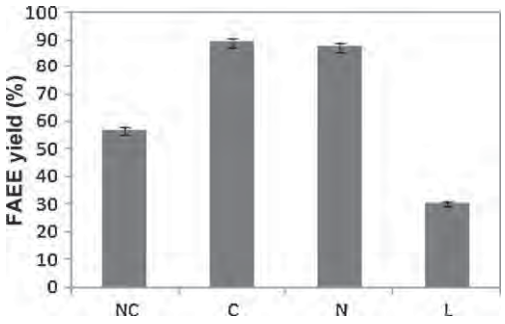

Fig. 5. Comparison of FAEE synthesis using different immobilized lipases. The reactions contained 500 mg of palm olein, 1:4 FA/EtOH molar ratio, in the presence of 1:1 TAG/*t*-BuOH molar ratio, and 20% (w/w based on TAG) PCMC-lipase. The reactions were incubated at 45 °C for 24 h. NC: PCMC prepared from non-concentrated DELIP 50L; C: PCMC prepared from concentrated DELIP 50L; N: Novozyme® 435; L: Lipolase 100T.

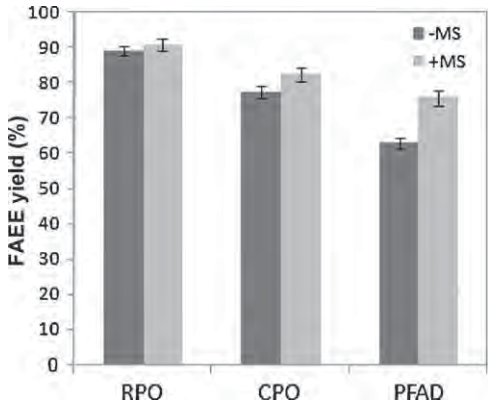

Fig. 6. Synthesis of FAEE from different feedstocks. The reactions contained 500 mg of palm oil feedstock as the substrate and 1:4 FA/EtOH molar ratio, with 20% (w/w based on TAG) PCMC-lipase in the presence of 1:1 TAG/*t*-BuOH molar ratio. The reactions were incubated at 45 °C for 24 h. RPO: refined palm olein; CPO: crude palm oil; PFAD: palm fatty acid distillate; −MS: no molecular sieve; +MS: molecular sieve.

50L lipase (0.27 IU/ml) was comparable to that using the widely used immobilized *C. antarctica* lipase (Novozyme® 435) (87.2% FAEE yield), which were both markedly higher than Lipolase 100T (30.2%), and from non-concentrated DELIP 50L (0.10 IU/ml; 56.4%) (Fig. 5). The high conversion yields thus demonstrated the potential of PCMCs prepared from *T. lanuginosus* lipase as an economical heterogeneous biocatalyst for ethanolysis biodiesel production.

Application of PCMC-lipase on ethanolysis of different industrial palm oil feedstocks, including crude palm oil, and palm fatty acid distillate was studied in comparison to the refined palm olein under the optimized reaction conditions (Fig. 6). Stearin fraction was completely solubilized at the optimal reaction temperature (45 °C) and could be efficiently converted to FAEE using PCMC-lipase. The composition of different feedstock for industrial biodiesel production is shown in Table 1. The highest product yield was obtained using refined palm olein (88.9%), while slightly

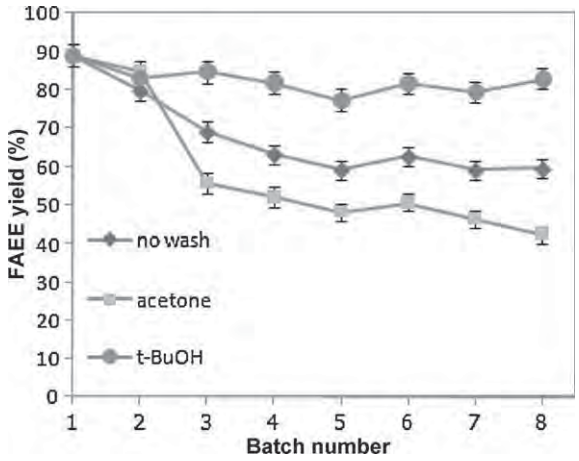

Fig. 7. Stability of PCMC-lipase in consecutive batch reactions. PCMC-lipase was reused in consecutive batch reactions with or without organic solvent treatment. The reactions contained 500 mg of palm olein and 1:4 FA/EtOH molar ratio, with 20% (w/w based on TAG) of PCMC-lipase in the presence of *tert*-butanol (1:1 TAG/*t*-BuOH) molar ratio. The reactions were incubated at 45 °C for 24 h. PCMC-lipase was treated by washing with 1 ml of the solvent twice before using in the consecutive batch.

slower yields were obtained from crude palm oil (77.0%) and palm fatty acid distillate (62.5%). Addition of molecular sieve (30%, w/w to oil) to the reaction showed no significant effect to ethanolysis of refined palm olein but led to significant improvement in product yields for crude palm oil and palm fatty acid distillate (82.1% and 75.5%, respectively, in the presence of molecular sieve). In addition to the sensitivity of PCMC biocatalysts to free water as mentioned above, water is known to affect biodiesel synthesis by favoring hydrolysis of TAG over transesterification and also on the alkyl ester products [35–37]. In this study where dried feedstocks were used as reactants, the effect of molecular sieving on increasing FAEE yield is due to the continuous removal of free water generated from esterification of free fatty acids in the feedstock, which can be seen clearly for the palm fatty acid distillate and crude palm oil, which contain a high proportion of free fatty acids. The continuous dehydration prevents an increase of free water in the reaction and thus results in remarked improved FAEE yields from feedstocks containing high free fatty acid content [31]. The maximal FAEE conversion yield under the optimized reaction conditions in this study is comparable to previous studies using palm oil with conventional immobilized lipases [9,28] or other oils using alternative biocatalyst forms, including CLEAs and PCMCs [18,22]. The conversion yield using the one-step lipase-catalyzed reaction in this study was also markedly higher than that reported by Matassoli et al. [38] on ethanolysis of crude palm oil using stepwise addition of methanol.

3.3. Reusability of PCMC-lipase

The reusability of PCMC-lipase was studied by analyzing the conversion efficiency after consecutive batch cycles under the optimal reaction conditions (Fig. 7). PCMC-lipase stability de-

Table 1
Composition of different feedstocks from palm oil industry for biodiesel production.

Feedstock	Free fatty acid content (%)	Composition of fatty acid (%)				
		Palmitic	Oleic	Linoleic	Stearic	Others
Refined palm olein (RPO)	0	39.8	42.5	11.2	4.4	2.1
Crude palm oil (CPO)	7.0	43.5	39.8	10.2	4.3	2.2
Palm fatty acid distillate (PFAD)	93.2	47.1	35.7	9.3	4.5	3.4

creased sharply after the first batch in the absence of *tert*-butanol in the reaction medium (data not shown). Addition of *tert*-butanol at 1:1 TAG/*t*-BuOH molar ratio in the reaction medium markedly improved the biocatalyst operational stability; however decreases in FAEE yields in subsequent batch cycles were still observed. A significant drop in FAEE yield was seen during the first two batches, which then stabilized with the average product yield of 63.3–59.1% for batches 4–8. Trial on PCMC treatment by washing with acetone [37] after each batch reaction led to deterioration in the biocatalyst's catalytic stability, resulting in marked drop of FAEE yield to 42.6% in batch 8. Treatment of the PCMC-lipase with *tert*-butanol wash resulted in remarkable improvement on catalytic stability. This allowed the reusability of the biocatalyst for at least 8 consecutive cycles with a slight decrease in FAEE yield with the final product yield in the range of 77.5–84.8% for batch cycles 2–8. Comparable product yields (79.5–86.2%) for reusability were obtained using Novozyme® 435 under the same conditions in the presence of 1:1 TAG/*t*-BuOH molar ratio. The stabilization mechanism of *tert*-butanol on lipases immobilized in PCMCs and other immobilization forms has been described as discussed above. The result thus suggested the importance of using *tert*-butanol as the reaction medium and for biocatalyst treatment in further process development.

4. Conclusion

Biocatalytic synthesis is considered a promising approach for biodiesel production with its key advantages over the conventional chemical catalyzed reactions. Immobilization of lipase in PCMCs offers a cost-effective approach for preparation of an active and stable biocatalyst for using in non-aqueous biodiesel synthesis reaction. In this study, biodiesel was produced at high yields from various feedstocks from the palm oil industry using the ethanolysis reaction with PCMC-lipase. An enhancing effect of *tert*-butanol on catalysis and stability of the protein-coated microcrystal lipase biocatalysts were also demonstrated. Both palm oil and ethanol are important renewable feedstocks and are widely available in Thailand as well as many other tropical countries. There is thus potential for the development of the completely "green biodiesel" production process and further development of PCMC-lipase for industrial application in biodiesel production.

Acknowledgements

This project was supported by a research grant from the Thailand Research Fund. Manuscript proofreading by Dr. Philip James Shaw is appreciated.

References

[1] Ma F, Hanna MA. Biodiesel production: a review. Bioresour Technol 1999;70:1–15.
[2] Singh V, Solanki K, Gupta MN. Process optimization for biodiesel production. Recent Pat Biotechnol 2008;2:130–43.
[3] Van Gerpen J. Biodiesel processing and production. Fuel Process Technol 2005;86(10):1097–107.
[4] Robles-Medina A, González-Morino PA, Esteban-Cerdán L, Molina-Grima E. Biocatalysis: towards ever greener biodiesel production. Biotechnol Adv 2009;27:398–408.
[5] Shimada Y, Watanabe Y, Sugihara A, Tominaga Y. Enzymatic alcoholysis for biodiesel fuel production and application of the reaction to oil processing. J Mol Catal B Enzym 2002;17:133–42.
[6] Du W, Xu Y, Liu D, Zeng J. Comparative study on lipase catalyzed transformation of soybean oil for biodiesel production with different acyl acceptors. J Mol Catal B Enzym 2004;30:125–9.
[7] Lai CC, Zullaikah S, Vali RR, Ju YH. Lipase-catalyzed production of biodiesel from rice bran oil. J Chem Technol Biotechnol 2005;80:331–7.
[8] Oliveira AC, Rosa MF. Enzymatic transesterification of sunflower oil in an aqueous-oil biphasic system. J Am Oil Chem Soc 2006;83:21–5.
[9] Moreira ABR, Perez VH, Zanin GM, de Castro HF. Biodiesel synthesis by enzymatic transesterification of palm oil with ethanol using lipases from several sources immobilized on silica-PVA composite. Energy Fuels 2007;21:3689–94.
[10] Watanabe Y, Pinsirodom P, Nagao T, Yamauchi A, Kobayashi T, Nishida Y, et al. Conversion of acid oil by-produced in vegetable oil refining to biodiesel fuel by immobilized *Candida antarctica* lipase. J Mol Catal B Enzym 2004;44:94–105.
[11] Samukawa T, Kaieda M, Matsumoto T, Ban K, Kondo A, Shimada Y, et al. Pretreatment of immobilized *Candida antarctica* lipase for biodiesel production from plant oil. J Biosci Bioeng 2000;90180–3.
[12] Noureddini H, Gao X, Philkana RS. Immobilized *Pseudomonas cepacia* lipase for biodiesel fuel production from soybean oil. Bioresour Technol 2005;96:769–77.
[13] Akoh CC, Chang S-W, Lee G-C, Shaw J-F. Enzymatic approach to biodiesel production. J Agric Food Chem 2008;55:8995–9005.
[14] Du W, Xu YY, Liu DH, Li Z. Study on acyl migration in immobilized lipozyme TL-catalyzed transesterification of soybean oil for biodiesel production. J Mol Catal B Enzym 2005;37:68–71.
[15] Li L, Du W, Liu D. *Rhizopus oryzae* IFO 4697 whole cell catalyzed methanolysis of crude and acidified rapeseed oils for biodiesel production in tert-butanol system. Process Biochem 2007;43:1481–5.
[16] Gao Y, Tan TW, Nie KL, Wang F. Immobilization of lipase on macroporous resin and its application in synthesis of biodiesel in low aqueous media. Chin J Biotechnol 2006;22:114–8.
[17] Talukder MMR, Puah SM, Wu JC, Won CJ, Chow Y. Lipase-catalyzed methanolysis of palm oil in presence and absence of organic solvent for production of biodiesel. Biocatal Biotransform 2006;24:257–62.
[18] Shah S, Sharma A, Gupta MN. Preparation of cross-linked enzyme aggregates by using bovine serum albumin as a proteic feeder. Appl Anal Chem 2006;351:207–13.
[19] Lee TS, Vaghjiani JD, Lye GJ, Turner MK. A systematic approach to the large-scale production of protein crystals. Enzyme Microb Technol 2000;26:582–92.
[20] Kreiner M, Moore BD, Parker MC. Enzyme-coated micro-crystals: a 1-step method for high activity biocatalyst preparation. Chem Commun 2001;12:1096–7.
[21] Kreiner M, Amorim Fernandes JF, O'Farrell N, Halling PJ, Parker M-C. Stability of protein-coated microcrystals in organic solvents. J Mol Cat B Enzym 2005;33:65–72.
[22] Shah S, Sharma A, Varandani D, Mehta B, Gupta MN. A high performance lipase preparation: characterization and atomic force microscopy. J Nanosci Nanotechnol 2007;7:2157–60.
[23] Kumari V, Shah S, Gupta MN. Preparation of biodiesel by lipase-catalyzed transesterification of high free fatty acid containing oil from *Madhuca indica*. Energy Fuels 2007;21:368–72.
[24] Gilham D, Lehner R. Techniques to measure lipase and esterase activity in vitro. Methods 2005;36:139–47.
[25] Wang Y, Wu H, Zong MH. Improvement of biodiesel production by lipozyme TL IM-catalyzed methanolysis using response surface methodology and acyl migration enhancer. Bioresour Technol 2008;99:7232–7.
[26] Al-Zuhair S. Production of biodiesel by lipase-catalyzed transesterification of vegetable oils: a kinetics study. Biotechnol Prog 2005;21:1442–8.
[27] Hernández-Mártin E, Otero C. Different enzyme requirements for the synthesis of biodiesel: Novozym® 435 and Lipozyme® TL IM. Bioresour Technol 2008;99:277–86.
[28] Halim SFA, Kamaruddin HA. Catalytic studies of lipase on FAME production from waste cooking palm oil in a *tert*-butanol system. Process Biochem 2008;43:1436–9.
[29] Abigor RP, Vadia P, Foglia T, Hass M, Jones J, Okefa E, et al. Lipase catalyzed production of biodiesel fuel from some Nigerian lauric oils. Biochem Soc Trans 2000;28:979–81.
[30] Salis A, Pinna M, Monduzzi M, Solinaz V. Comparison among immobilized lipases on macroporous polypropylene toward biodiesel synthesis. J Mol Cat B Enzym 2008;54:19–26.
[31] Li LL, Du W, Liu DH. Lipase-catalyzed transesterification of rapeseed oils for biodiesel production with a novel organic solvent as the reaction medium. J Mol Catal B Enzym 2006;43:58–62.
[32] Royon D, Daz M, Ellenrieder G, Locatelli S. Enzymatic production of biodiesel from cotton seed oil using *t*-butanol as a solvent. Bioresour Technol 2007;98:648–53.
[33] Chen J-W, Wu W-T. Regeneration of immobilized *Candida antarctica* lipase for transesterification. J Biosci Bioeng 2003;95:466–9.
[34] Du W, Liu D, Li L, Dai D. Mechanism exploration during lipase-mediated methanolysis of renewable oils for biodiesel production in a *tert*-butanol system. Biotechnol Prog 2007;23:1087–90.
[35] Yamane T, Kojima Y, Ichiryu T, Nagata M, Shimizu S. Intramolecular esterification by lipase powder in microaqueous benzene: effect of moisture content. Biotechnol Bioeng 1989;34:838–43.
[36] Anthonsen T, Sjursens BJ. Importance of water activity for enzymes catalysis in non-aqueous organic systems. In: Gupta MN, editor. Methods in non-aqueous enzymology. Basel: Birkhauser Verlag; 2000. p. 14–35.
[37] Shah S, Gupta MN. Lipase catalyzed preparation of biodiesel from jatropha oil in a solvent free system. Process Biochem 2007;42:409–14.
[38] Matassoli AL, Corrêa IN, Portilho MF, Veloso CO, Langone MA. Enzymatic synthesis of biodiesel via alcohol lysis of palm oil. Appl Biochem Biotechnol 2009;1–3:347–55.

Fuel 89 (2010) 2873–2880

Contents lists available at ScienceDirect

Fuel

journal homepage: www.elsevier.com/locate/fuel

Reactions of C_5 and C_6-sugars, cellulose, and lignocellulose under hot compressed water (HCW) in the presence of heterogeneous acid catalysts

A. Chareonlimkun [a], V. Champreda [b], A. Shotipruk [c], N. Laosiripojana [a,*]

[a] The Joint Graduate School of Energy and Environment, King Mongkut's University of Technology Thonburi, Thailand
[b] National Center for Genetic Engineering and Biotechnology (BIOTEC), Pathumthani, Thailand
[c] Department of Chemical Engineering, Faculty of Engineering, Chulalongkorn University, Thailand

ARTICLE INFO

Article history:
Received 21 October 2009
Received in revised form 28 January 2010
Accepted 8 March 2010
Available online 17 March 2010

Keywords:
Lignocellulosic biomass
Sugar
Furfural
Hot compressed water

ABSTRACT

The benefit of TiO_2, ZrO_2 and SO_4–ZrO_2 on the reactions of C_5-sugar (xylose), C_6-sugar (glucose), cellulose, and lignocellulose was studied in hot compressed water (HCW) at 473–673 K with an aim to produce furfural and 5-hydroxymethylfurfural (HMF). TiO_2 and SO_4–ZrO_2 were found to active for hydrolysis and dehydration reactions producing high furfural and HMF yields with less by-products (i.e. glucose, fructose, xylose, and 1,6-anhydroglucose (AHG)) formation, whereas ZrO_2 was highly active for isomerization reaction; thus significant amount of fructose was observed in the liquid product.

Importantly, it was also found that the starting salt precursor, the sulfur-doping content (for SO_4–ZrO_2) and the calcination temperature strongly affected the catalyst reactivity. Catalysts prepared from the chloride-based precursors (i.e. $ZrOCl_2$ and $TiCl_4$) gained higher reactivity compared to those prepared from nitrate-based precursors (i.e. $ZrO(NO_3)_2$ and $TiO(NO_3)_2$) due to their greater acidity, according to the NH_3- and CO_2-TPD studies. For SO_4–ZrO_2, among the catalyst with sulfur contents of 0.75%, 1.8% and 2.5%, SO_4–ZrO_2 with 1.8% sulfur content presented the highest acidity and reactivity toward hydrolysis and dehydration reactions. It is noted that the suitable calcination temperature for all catalysts was at 773 K; the XRD patterns revealed that different portions of phase formation was observed over catalysts with different calcination temperatures i.e. anatase/rutile for TiO_2 and monoclinic/tetragonal for ZrO_2 and SO_4–ZrO_2; the portion of these phase formations obviously affected the acidity–basicity of catalyst and thus the catalyst reactivity.

1. Introduction

Biorefinery is a promising industry for production of energy and chemicals from lignocellulosic plant biomass with major advantages on environment and feedstock sustainability in comparison to the current petrochemical-based processes [1]. Lignocellulosic biomass is the most abundant renewable carbon resource which is considered carbon–neutral and can be processed by thermo-chemo-catalytic or biocatalytic conversion approaches in biorefineries. Potential biomass such as agricultural residues and herbaceous energy crops consists mainly of three different types of biopolymers i.e. cellulose (35–50%), hemicellulose (25–30%) and lignin (25–30%), which are associated with each other [2]. Degradation of the polysaccharide constituents i.e. cellulose and hemicelluloses results in the generation of hexose and pentose sugars which could be used as versatile starting materials for further conversion to a range of value-added products.

Hydrothermal conversion using hot compressed water (HCW) is an attractive approach for processing of sugars and lignocellulosic feedstock due to its advantages on environmental friendliness and potential on reaction control through use of water density [3–5]. Chemical reactions in HCW can be enhanced by water which can act as solvent, reactant and catalyst in the systems. Thermocatalytic processes based on HCW have been developed for production of various chemicals. Among potential commodity chemicals in biorefinery, furfural-based compounds (5-hydroxymethylfurfural, furfural and their derivatives) hold a key position in biomass-derived intermediates due to their applications in several chemical, petrochemical and energy processes. They have been widely utilized as chemical intermediates, solvents, and as sustainable substitutes for petroleum-based building blocks used in production of fine chemicals and plastics [6]. Recently, Huber et al. reported a novel process for conversion of biomass-derived compounds into liquid alkane biofuel using solid base catalysts in HCW [7]. The important primary step in their process is the conversion of sugar-based compounds to furfural and HMF via dehydration reaction, in which these intermediates are later converted to alkane-based fuel via aldol condensation and hydrogenation reactions in

* Corresponding author. Tel.: +66 2 8729014; fax: +66 2 8726736.
E-mail address: navadol_l@jgsee.kmutt.ac.th (N. Laosiripojana).

0016-2361/$ - see front matter © 2010 Elsevier Ltd. All rights reserved.
doi:10.1016/j.fuel.2010.03.015

the presences of acetone and hydrogen. Hence, the production of HMF and furfural from lignocellulosic materials is currently of great interest for research and application.

The development of HCW-based process for production of furfural-based compounds has received increasing attention as the alternative approach for the conventional reaction from biomass which requires the use of strong acids and organic solvents [8]. Several research and development on the production of HMF and furfural from sugar- or carbohydrate-based feedstock via HCW, subcritical water and supercritical water technologies have been reported [9–19]. For instance, Watanabe et al. studied the hydrolysis of glucose in HCW in the presence of acid and alkali homogenous catalysts [9], in which the effects of H_2SO_4 on enhancement of HMF formation via dehydration reaction and NaOH on endorsement of the glucose isomerization to fructose were reported. Asghari et al. studied acid-catalyzed production of HMF from D-fructose in subcritical water condition and found that the production of HMF could be greatly increased by the presence of H_3PO_4 [10]. Although the effects of homogenous catalysts on product yield improvement has been clearly demonstrated; however, the use of homogenous catalysts led to difficulties in catalyst recovery, product contamination, and solvent recycle as well as increasing cost on waste water treatment. Recently, a few literatures have proposed the use of heterogeneous acid-based catalysts for dehydration reaction with the advantages on simple catalyst separation and recovery. Watanabe et al. studied dehydration of glucose in the presence of solid TiO_2 and ZrO_2 and indicated that ZrO_2 catalyzed the isomerization reaction, whereas anatase–TiO_2 promoted both dehydration and isomerization reactions [11]. They also proposed that catalytic activity of each reaction strongly depends on the acidity and basidity of catalysts. Thus this emphasizes the potential on development of catalytic HCW processes with heterogeneous catalysts for production of furfural-based compounds from biomass-derived feedstock.

Regarding the reaction of lignocellulosic biomass in HCW, the material can be efficiently converted to sugar-based compounds via hydrolysis reaction under various conditions [20–26]. Karimi et al. studied the hydrolysis of rice straw to sugars in the presence of H_2SO_4 [20], while Sasaki et al. investigated the hydrolysis of cellulose in subcritical and supercritical water at 563–673 K and 25 MPa [21]. In addition, Ando et al. studied decomposition behavior of several biomasses under HCW conditions and found that hemicelluloses started to decompose at the temperature above 453 K, while cellulose decomposed above 503 K, while most lignin could be extracted at low temperature and flowed out with the decomposed products of hemicellulose [22]. Furthermore, Minowa et al. studied the cellulose decomposition under HCW condition in the presence of alkali and nickel catalysts [23]; and revealed that alkali inhibited the char formation, whereas nickel catalyzed the steam reforming and methanation reactions.

In the present work, we aimed at the study of hydrolysis and dehydration reactions to produce HMF and furfural from sugar-, cellulose-, and lignocellulosic-based materials under HCW condition. Here, the benefits of adding heterogeneous catalysts i.e. TiO_2, ZrO_2 and sulfated zirconia (SO_4–ZrO_2) on the reaction reactivities were determined. TiO_2 and ZrO_2 were previously reported to have activity toward the dehydration of sugars [9,11], while SO_4–ZrO_2 is one of the promising acid catalyst for various reactions. The effects of catalyst starting salt precursors (i.e. chloride-based precursor and nitrate-based precursor) and calcination temperature on the catalytic reactivity were also studied since several researchers indicated the significant impact of salt precursor type and calcination temperature on the catalytic reactivity of these oxide-based materials. The hydrolysis and dehydration of sugar-based compounds (i.e. glucose, fructose, and xylose), cellulose and lignocellulosic biomass (i.e. sugarcane bagasse) in the presence of these synthesized catalysts were compared at various temperatures to determine the suitable operating conditions for enhancing maximum yield of HMF and furfural productions. Lastly the physical characteristics of these synthesized catalysts, i.e. acid–base properties and surface properties were also carried out in order to relate these properties with the type of starting salt precursor, calcination temperature and catalytic performance. This work thus provides a basis for further development of an environmental friendly HCW process for production of the potential furfural-based compounds for industrial application.

2. Experimental

2.1. Chemicals and materials

Glucose, xylose, cellulose, and xylan (representative for hemicellulose) were supplied from Aldrich and Ajax Finechem; whereas sugarcane bagasse (with the percentages of cellulose, hemicellulose, and lignin of 0.44:0.29:0.20) was used in the present work. Before undergoes the reaction testing, sugarcane bagasse was ground with a ball-milling to become fine particle with the average particle size less than 75 μm.

2.2. Catalyst preparation and characterization

Zirconia (ZrO_2) was synthesized via the precipitation method. A solution of zirconium salt precursors i.e. zirconyl chloride ($ZrOCl_2$) or zirconyl nitrate ($ZrO(NO_3)_2$) (0.15 M) was slowly dropped into a well-stirred precipitating solution of ammonium hydroxide (NH_4OH) (2.5 wt.%) at room temperature. The solution was controlled at pH of 11. The obtained precipitate was removed, and then washed with deionized water until Cl^- was not detected by a silver nitrate ($AgNO_3$) solution. Then, the solid sample was dried overnight at 383 K and calcined under continuous air flow for 6 h. Similarly, titania (TiO_2) was also prepared by precipitation of either titanium chloride ($TiCl_4$) or titanium nitrate ($TiO(NO_3)_2$) and treated under the same procedures as those of ZrO_2. It is noted that the calcination temperature was varied from 773, 873 and 973 K in order to determine its impact on the catalyst performance. Sulfated zirconia (SO_4–ZrO_2) catalyst was prepared from the wet impregnation of H_2SO_4 over ZrO_2, synthesized via precipitation of $ZrOCl_2$ and $ZrO(NO_3)_2$. The selected ZrO_2 was immersed in 0.1 mol l^{-1} of H_2SO_4 at 343 K for 30 min, then dried overnight at 383 K and calcined at two different temperatures (773 and 973 K) for 3 h. It is noted that various amounts of sulfuric acid (providing actual sulfur contents after calcination of 0.75%, 1.8% and 2.5%) were doped.

After treatment, several characterizations i.e. BET, XRD and TPD were performed. BET measurements was carried out by N_2 physisorption technique using Micromeritics ASAP 2020 surface area and porosity analyzer to determine the specific surface area, cumulative pore volume and average pore diameter of material. The X-ray diffraction (XRD) patterns of powder were analyzed by X-ray diffractometer. Temperature-programmed desorption techniques with ammonia and carbon dioxide (NH_3- and CO_2-TPD) were applied to determine the acid–base properties of catalysts using a flow apparatus, in which the catalyst sample was treated at 773 K in helium and then saturated with 15% NH_3/He mixture or pure CO_2 flow after cooling to 373 K. After purging with helium, the sample was heated to 923 K under helium and the amount of acid–base sites on the catalyst surface was calculated by measuring the areas of the desorption profiles of NH_3 and CO_2 using the Chemisorption System analyzer.

2.3. Catalyst testing toward hydrolysis and dehydration reactions

Hydrolysis and dehydration reactions were carried out in a 0.5 inch diameter stainless steel reactor placing vertically inside tubular furnace. For the base condition, 0.1 g of sample was mixed with 1 cm^3 of water (with and without the presence of 0.1 g catalyst) and N_2 was loaded to raise the reactor pressure up to 2.5 MPa before placing the reactor in the furnace. A Type-K thermocouple was placed into the annular space between the reactor and furnace with close contact to the catalyst bed to minimize the temperature difference between the furnace temperature and reaction temperature). The reaction temperature was varied from 473 to 523, 573, 623, and 673 K, while the pressure inside the reactor was measured by a pressure transducer (Kyowa, PGM-500 KD) connected to the reactor. After the reaction time was reached, the reactor was quenched in a water bath to stop the reaction and the products were removed for further analyses. In the present work, the quantification and identification of gaseous and liquid products were conducted by GC-TCD (Shimadzu GC-14B) and HPLC (equipped with a Dionex PDA-100 photodiode array detector with a Shodex RSpak KC-811 of 8.0 mm ID × 300 mm column). It is noted that, according to the measurement of total carbon amount in the water solution after reaction, the TOC (total organic carbon) values for all experiments were in the range of 3–10% depending the reaction temperature and type of feedstock. This revealed that the quantity of gaseous products from the reactions were considerably less than that of liquid products; hence we here reported the results and discussion only for the liquid products from the reactions. The yields of liquid product were calculated by the carbon balance, defined as the ratios of the amount of carbon atom in the specified product to the amount of carbon atom in the reactants. In this study, we focus on the hydrolysis and dehydration reactions; therefore, the possible product species i.e. glucose, fructose, xylose, furfural, HMF and 1,6-anhydroglucose (AHG) were quantified.

3. Results and discussion

The reactions of C_5 and C_6-sugars, cellulose, and lignocellulose in the presence of various catalysts i.e. TiO_2, ZrO_2, and SO_4–ZrO_2 prepared from nitrate and chloride precursors and treated under different conditions were studied. The synthesized TiO_2 and ZrO_2 prepared from nitrate and chloride precursors were denoted as Ti–N, Ti–Cl, Zr–N, and Zr–Cl, whereas SO_4–ZrO_2 catalysts prepared by using various sulfur contents of 0.75%, 1.8%, and 2.5% were denoted as 0.75SZ, 1.8SZ, and 2.5SZ. The catalysts calcined at 773, 873 and 973 K were denoted as Ti–N-773, Ti–N-873, and Ti–N-973.

3.1. Catalyst characterizations

The physical characteristics of all synthesized catalysts i.e. acid–base properties and surface properties were determined by using XRD, BET and NH_3- and CO_2-TPD; the results of these characterizations are summarized in Tables 1–3. According to the XRD measurements, the main phase observed for TiO_2 calcined at 773 K (from both $TiCl_4$ and $TiO(NO_3)_2$) was anatase crystalline phase; nevertheless, rutile phase was also detected along with anatase crystalline phase when the calcination temperature increased to 973 K. As for ZrO_2 and SO_4–ZrO_2, the XRD pattern indicated the containing of both tetragonal and monoclinic phases with various contents depending on the preparation procedure; we found that the crystal size in monoclinic phase and the fraction of monoclinic phase increased considerably with increasing calcination temperature, whereas tetragonal phase decreased (Table 1). As for SO_4–ZrO_2, the results revealed that the average crystal size and the fraction of monoclinic phase decreased when the sulfur loading content increased from 0% to 0.75% and 1.8%, then they slightly increased when the sulfur loading content was 2.5%.

Table 1
Catalyst characteristics obtained from XRD measurement.

Catalysts	Phase	Average crystal size (nm)	Crystal size (nm)[a]		% Monoclinic phase[a]
			M[b]	T[c]	
Zr–N-773	M, T	9.2	10.0	5.2	74.9
Zr–N-873	M, T	9.7	10.4	5.4	77.3
Zr–N-973	M, T	10.3	11.0	5.5	80.5
Zr–Cl-773	M, T	8.3	8.5	4.4	69.2
Zr–Cl-873	M, T	8.5	8.8	4.3	74.1
Zr–Cl-973	M, T	8.9	9.4	4.7	78.0
0.75SZ-773	M, T	8.1	8.3	4.2	66.3
1.8SZ-773	M, T	7.8	8.1	4.0	62.9
2.5SZ-773	M, T	7.9	8.1	3.9	63.4
0.75SZ-873	M, T	8.8	8.6	4.5	69.9
1.8SZ-873	M, T	8.2	8.2	4.3	65.0
2.5SZ-873	M, T	8.3	8.4	4.3	66.4
0.75SZ-973	M, T	9.5	8.9	4.8	71.4
1.8SZ-973	M, T	8.7	8.5	4.7	68.7
2.5SZ-973	M, T	8.9	8.5	4.5	69.9

[a] Based on XRD line broadening.
[b] Monoclinic phase in ZrO_2.
[c] Tetragonal phase in ZrO_2.

Table 2
N_2 physisorption results of TiO_2, ZrO_2 and SO_4–ZrO_2 (prepared from different precursors and treated under different conditions).

Catalysts	BET surface area[a] (m^2/g)	Cumulative pore volume[b] (cm^3/g)	Average pore diameter[c] (nm)
Ti–N-773	38.1	0.098	4.9
Ti–N-873	27.9	0.081	5.1
Ti–N-973	12.0	0.069	5.4
Ti–Cl-773	48.2	0.120	4.6
Ti–Cl-873	35.9	0.109	4.9
Ti–Cl-973	20.1	0.098	5.2
Zr–N-773	103	0.161	4.5
Zr–N-873	76.4	0.139	5.0
Zr–N-973	60.2	0.092	5.2
Zr–Cl-773	124	0.234	4.3
Zr–Cl-873	101	0.217	4.6
Zr–Cl-973	76.3	0.210	4.6
0.75SZ-773	228	0.321	3.9
1.8SZ-773	243	0.390	3.6
2.5SZ-773	237	0.354	3.8
0.75SZ-873	153	0.261	4.2
1.8SZ-873	179	0.314	4.0
2.5SZ-873	171	0.290	4.2
0.75SZ-973	102	0.221	4.7
1.8SZ-973	113	0.254	4.4
2.5SZ-973	109	0.228	4.5

[a] Error of measurement = ±5%.
[b] BJH desorption cumulative volume of pores between 1.7 and 300 nm diameter.
[c] BJH desorption average pore diameter.

The BET measurements are given in Table 2, the results indicated that TiO_2 and ZrO_2 prepared from chloride-based precursors show greater specific surface area than those prepared from nitrate-based precursors. It can also be seen that the calcination temperature significantly affect the specific surface area, cumulative pore volume and average pore diameter of catalysts; the specific surface area and cumulative pore volume linearly decreased with increasing calcination temperature, whereas the average pore diameter dramatically increased. As for SO_4–ZrO_2, the specific surface area increased when the sulfur was loaded up to 1.8%, then the surface area slightly decreased when the sulfur loading content

Table 3
Results from NH_3- and CO_2-TPD measurements of TiO_2, ZrO_2 and SO_4–ZrO_2 (prepared from different precursors and treated under different conditions).

Catalysts	Total sites (μmole/g)		Density of sites (μmol/m^2)	
	Acid sites[a]	Base sites[b]	Acid sites	Base sites
Ti–N-773	77.0	78.1	2.02	2.05
Ti–N-873	51.9	61.1	1.86	2.19
Ti–N-973	19.1	28.4	1.59	2.37
Ti–Cl-773	161.0	83.9	3.34	1.74
Ti–Cl-873	107.7	85.8	3.00	2.39
Ti–Cl-973	59.1	92.1	2.94	4.58
Zr–N-773	178.2	134.9	1.73	1.31
Zr–N-873	126.1	113.8	1.65	1.49
Zr–N-973	84.3	98.1	1.40	1.63
Zr–Cl-773	231.9	129.0	1.87	1.04
Zr–Cl-873	176.8	145.4	1.75	1.44
Zr–Cl-973	119.0	167.1	1.56	2.19
0.75SZ-773	677.2	47.9	2.97	0.21
1.8SZ-773	733.9	70.5	3.02	0.29
2.5SZ-773	734.7	78.2	3.10	0.33
0.75SZ-873	434.5	23.0	2.84	0.15
1.8SZ-873	524.5	43.0	2.93	0.24
2.5SZ-873	519.8	49.6	3.04	0.29
0.75SZ-973	270.3	3.1	2.65	0.03
1.8SZ-973	305.1	19.2	2.70	0.17
2.5SZ-973	298.7	24.0	2.74	0.22

[a] From NH_3-TPD.
[b] From CO_2-TPD.

was 2.5%. The abrupt decrease in surface area with higher sulfur contents could be correlated with the alteration of crystal structure and sulfate migration into the bulk phase of the solid. It should be noted that, by loading sulfur over zirconia, the catalyst exhibited smaller crystallite sizes, which caused the increase in the cumulative pore volume, and the reduction of the average pore diameter. Considering pore size distribution of sulfated zirconia catalysts, no significant change was observed for those regarding pore size distribution.

Lastly, NH_3- and CO_2-TPD techniques were used to measure the acid–base properties of the catalysts; the amounts of acid and base sites, which were calculated from the area below curves of these TPD profiles, are listed in Table 3. Along with these values, the distribution of acid and base site on the catalyst surface (namely the density of acid and base site; μmol m^{-2}) and the strength of acid and base sites (the top peak of TPD spectra) are also given in the table since these parameters are important indicators to determine the catalytic reactivity of acid and base reactions [27,28]. Among all catalysts, TiO_2 prepared from $TiCl_4$ shows the greatest amounts and densities for both acid and base sites; in addition, the highest peaks of NH_3- and CO_2-TPD spectra for this catalyst was relatively lower than other catalysts indicated that its weak acid and base sites. It should be noted that the calcination temperature and preparation procedure also affect the acid–base properties of catalysts; the amount of acid sites decreased with increasing the calcination temperature whereas the base sites increased for all catalysts. According to the results of SO_4–ZrO_2, the amount of acid sites increased with increased percents of sulfur content in ZrO_2 up to 1.8% of sulfur content, and then decreased with more sulfur loading (2.5%). Considering the base sites, the amount of base sites decreased proportional to the sulfur content in ZrO_2 and the percent of tetragonal phase in catalysts.

3.2. C_5 and C_6-based sugar reactions under HCW condition

The reactions of glucose and xylose were studied under HCW condition with and without adding of solid catalysts. It was found that the main products from the glucose reaction were fructose, furfural, HMF and AHG indicated the occurring of dehydration and isomerization reactions, whereas the only product from the xylose reaction was furfural. HMF, furfural (and AHG as by-product) are produced from the dehydration of glucose (C_6-sugar), whereas only furfural can be produced from the dehydration of xylose (C_5-sugar). The presence of fructose in the product comes from the isomerization of glucose, while the further dehydration of fructose also results in HMF and furfural production. The conversion and yields of these liquid products from the reaction at various conditions are shown in Fig. 1(a)–(c), whereas the effect of reaction temperature was also studied by varying the temperature from 473 to 673 K as shown in Fig. 2. It is noted that the conversions and product yield reported in all figures are the average values from 3 to 5 runs of experiments (with the error in the range of ±1.3–2.5% in all experiments). It can be seen that the highest yield of liquid products can be achieved at the reaction temperature of 523 K for all catalysts. At this temperature, the presence of catalyst makes significant impact on the yield and selectivity of products; furthermore, the type of catalyst, salt precursor and calcination temperature also strongly affect the catalyst performance. Clearly, all catalysts prepared from chloride-based precursors showed higher reactivity than those prepared from nitrate-based precursors; in addition, the catalyst reactivity decreased steadily with increasing calcination temperature. Among them, TiO_2 (prepared from the precipitation of $TiCl_4$ and calcined at 773 K) was the most active one in terms of sugar conversion, total product yields and HMF-furfural selectivities, whereas the reaction with ZrO_2 (prepared from the precipitation of $ZrO(NO_3)_2$ and calcined at 973 K) provided the greatest amount of fructose in the product indicated the promotion of isomerization reaction by this catalyst. As for SO_4–ZrO_2, the catalyst prepared by the wet impregnation of H_2SO_4 (with sulfur content of 1.8%) over ZrO_2 synthesized from the precipitation of $ZrOCl_2$ and calcined at 773 K showed the greatest dehydration reactivity; nevertheless, its reactivity was relatively less than TiO_2.

These results can be explained based on the characterization results in Section 3.1 that the catalyst reactivity, phase formation and acidity–basicity properties are closely related. According to the TPD studies, TiO_2 (from the precipitation of $TiCl_4$) was observed to have higher acid site density and weaker acid site than TiO_2 (from the precipitation of $TiO(NO_3)_2$)), SO_4–ZrO_2 and ZrO_2; and this catalyst also gained the highest dehydration reactivity. Importantly, although SO_4–ZrO_2 has higher amount of acid site than TiO_2, its acid site density is lower. Hence, it can be revealed from the studies that the acid site density is more important indicator than the amount of acid site to judge the catalyst reactivity toward dehydration reaction. It is noted that the acidity of all catalysts decreased with increasing temperature, thus the dehydration reactivities of catalysts calcined at low temperature (773 K) is greater than those calcined at higher temperatures. In contrast, the strong promotion of isomerization reaction by ZrO_2 prepared from the precipitation of $ZrO(NO_3)_2$ with high calcination temperature could be due to the highest amount of base site observed over this catalyst. In addition to the acidity–basicity properties, the phase of catalyst also closely related to its reaction reactivity i.e. TiO_2 calcined at low temperature of 773 K (mainly anatase phase) showed better reactivity than that calcined at higher temperature (slight formation of rutile phase detected); this result is in good agreement with the results reported by Watanabe et al. [9,11] who indicated that anatase–TiO_2 showed better dehydration reactivity than rutile–TiO_2. As for ZrO_2, the catalyst with larger portion of monoclinic phase shows greater isomerization reactivity.

It is noted that the high HMF and furfural productions with low AHG and fructose formations observed over TiO_2 could be due to the strong isomerization of glucose to fructose following with the

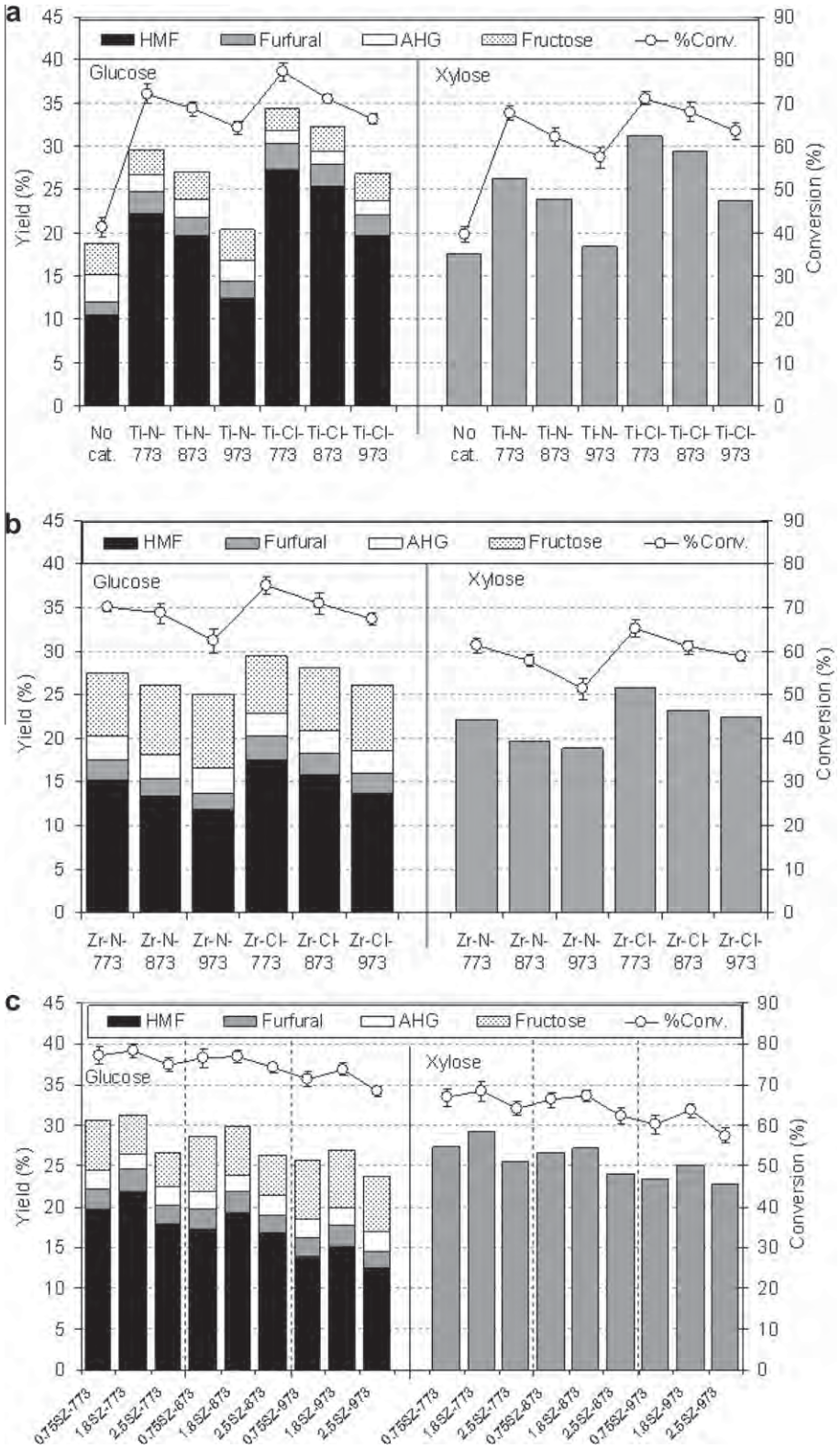

Fig. 1. Conversions and yield of liquid products from the reactions of glucose and xylose at 523 K and 5 min in the presence of (a) TiO_2, (b) ZrO_2 and (c) SO_4–ZrO_2 (prepared from different precursors and treated under different conditions).

rapid dehydration of fructose to HMF by this catalysts since TiO_2 was also found to have high base site density and weak base site comparable to ZrO_2, according to the TPD measurements. To prove this clarification, the experiments with various reaction times (1, 2, 3, 4, and 5 min) were carried out, Fig. 3. It was found that initially within the first 1–2 min, high amount of fructose was observed; but it decreased with increasing reaction time, whereas the yield of HMF increased rapidly with increasing reaction time before reaching steady state value at 5 min. This implies the benefit of TiO_2 as bifunctional catalyst for both acid and base reactions.

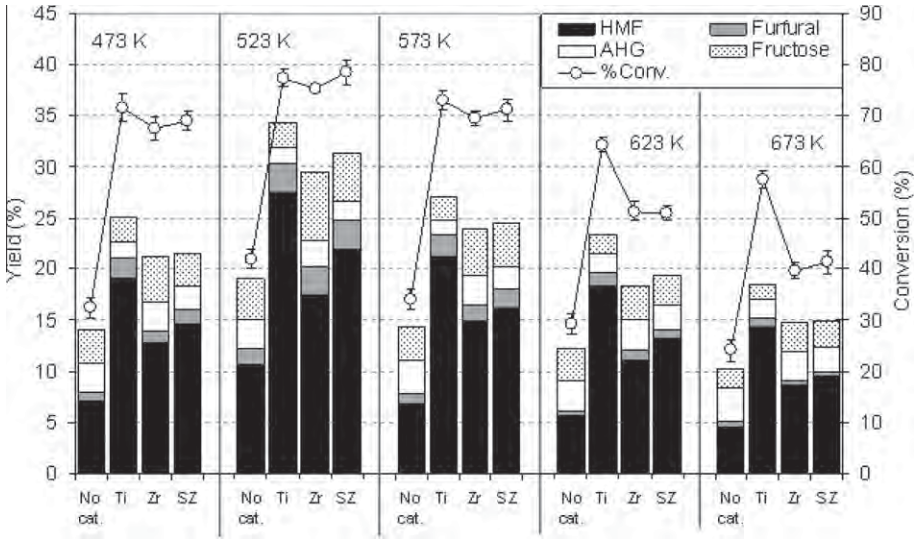

Fig. 2. Effect of reaction temperature (473–673 K) on the conversion and yield of liquid products from the reaction of glucose with and without the presence of catalysts.

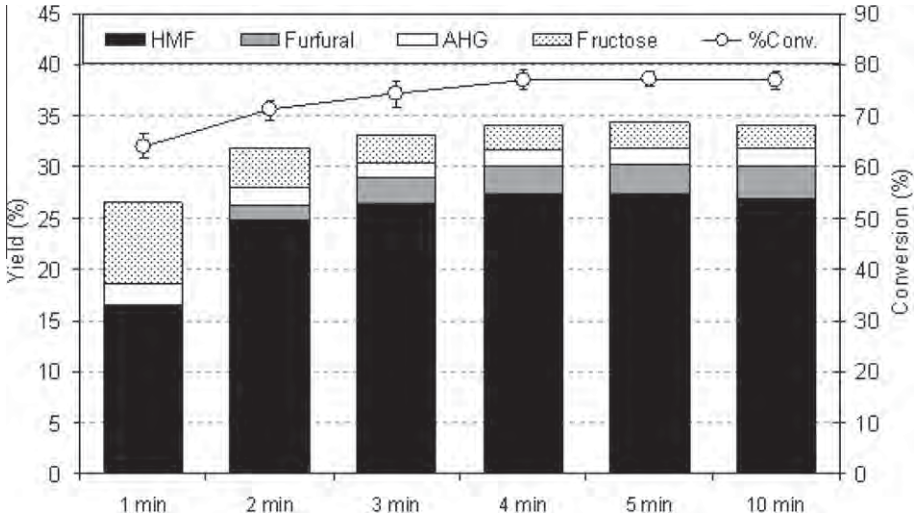

Fig. 3. Effect of reaction time (1–5 min) on the conversion and yield of liquid products from the reaction of glucose at 523 K in the presence of TiO_2.

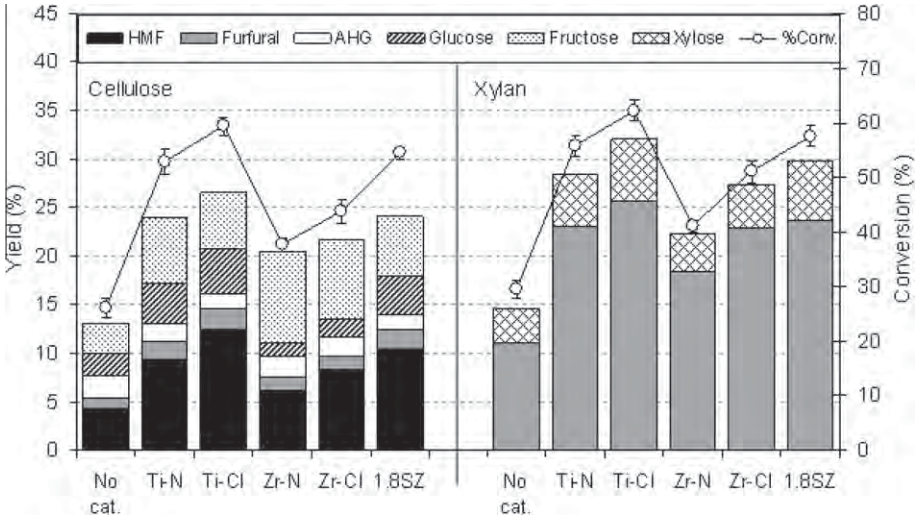

Fig. 4. Conversions and yield of liquid products from the reactions of cellulose and xylan at 523 K and 5 min in the presence of various catalysts.

3.3. Cellulose, hemicellulose and lignocellulose reactions under HCW condition

As the next step, to investigate the occurring of hydrolysis reaction simultaneously with dehydration reaction, the reactions of cellulose and xylan (as hemicellulose) were studied. Fig. 4 shows the conversion and product yield from the reaction in the presence of all three catalysts over cellulose and xylan, respectively. Clearly, the main product from the conversion of cellulose is HMF with some amounts of glucose, fructose, furfural and AHG also observed in the liquid product. In contrast, the main product from the conversion of xylan is only furfural with small amount of xylose detected in the product. Similar to glucose and xylose reactions, the most active catalyst for the reactions of cellulose and xylan is TiO_2. Theoretically, it is known that the main product from the hydrolysis of cellulose is glucose, while the presence of fructose in the product comes from the further isomerization of glucose. As for the hydrolysis of xylan, xylose is the only product from the reaction, which is further converted to furfural via dehydration reaction.

In the present work, the reaction of lignocellulose was also investigated; and sugarcane bagasse was selected as lignocellulose material in this study. Fig. 5 shows the product yields from this reaction over several catalysts. It can be seen that, similar to the reaction of cellulose, the main products from the reaction were glucose, fructose, xylose, furfural, HMF and AHG indicated the occurring of hydrolysis, isomerization and dehydration reactions. The main difference between cellulose and lignocellulose reactions is the higher portion of furfural production from lignocellulose reaction, which is mainly due to the hydrolysis and dehydration of hemicellulose present in sugarcane bagasse (29%). Lastly, the reusability of solid catalysts was also carried out. After separated from water solution, all remaining solids were washed and the catalyst was separated from the solid residues by filtering. It is noted that in our studies the particle size of synthesized catalysts were controlled (by sieving) to be in the range of 150–200 μm, which was larger than the solid reactants (with the average particle size less than 75 μm). After separated, the catalyst was dried before re-testing the reaction at the same operating conditions. As shown in Fig. 6, the reactivities of spent TiO_2 and ZrO_2 are almost identical

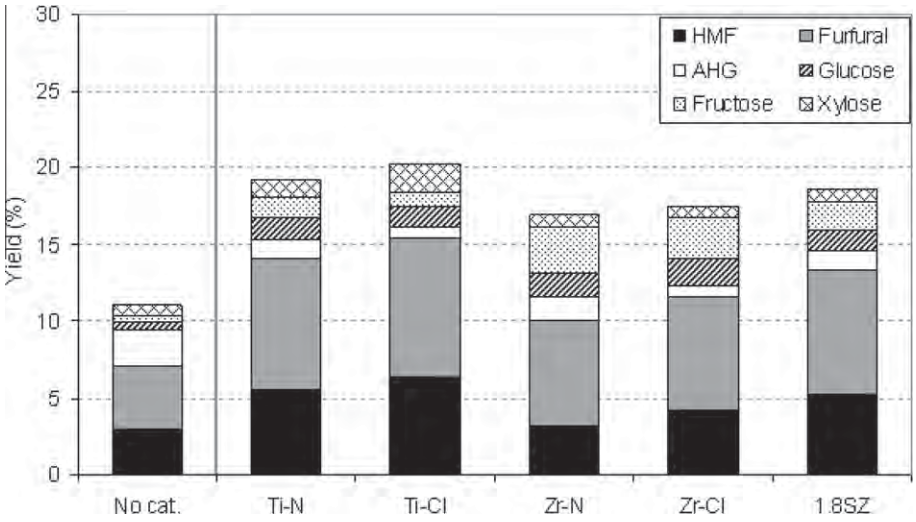

Fig. 5. Yield of liquid products from the reaction of sugarcane bagasse at 523 K and 5 min with and without the presence of catalysts.

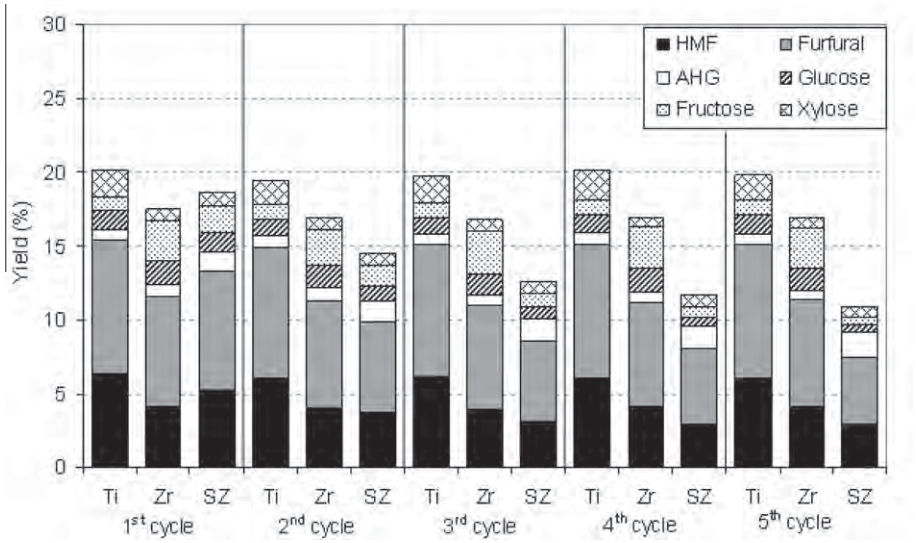

Fig. 6. Reusability testing of TiO_2, ZrO_2 and SO_4–ZrO_2 toward the reaction of sugarcane bagasse at 523 K.

to the fresh one indicated its well-reusable; this highlights the great benefit of these heterogeneous oxide-based catalyst compared to the typical homogeneous catalysts (e.g. H_2SO_4). Nevertheless, significant deactivation was observed over the reused SO_4–ZrO_2, which could be due to the sulfur leaching from the catalyst during the reaction. Thus, TiO_2 (prepared by chloride-based precursor) would be a good candidate for hydrolysis/dehydration of lignocellulosic biomass ahead of ZrO_2 and SO_4–ZrO_2 in terms of product yield, selectivity toward HMF and furfural productions, and its reusability.

4. Conclusion

Under HCW operation at 553 K, the presence of TiO_2 and SO_4–ZrO_2 promoted the hydrolysis and dehydration of C_5-sugar (xylose), C_6-sugar (glucose), cellulose, and lignocellulose to furfural and HMF with less by-products (i.e. glucose, fructose, xylose, and 1,6-anhydroglucose (AHG)) formation, whereas ZrO_2 strongly promoted the isomerization reaction; thus significant amount of fructose was observed in the liquid product. It was also observed that the starting salt precursor, the sulfur-doping content (for SO_4–ZrO_2) and the calcination temperature strongly affected the catalyst reactivity. Catalysts prepared from the chloride-based precursors gained higher reactivity compared to those prepared from nitrate-based precursors. For SO_4–ZrO_2, SO_4–ZrO_2 with 1.8% sulfur content presented the highest reactivity. The suitable calcination temperature for all catalysts was at 773 K; the XRD patterns revealed that different portions of phase formation was observed over catalysts with different calcination temperatures and this strongly affected the acidity–basicity properties and thus the reactivity of catalyst.

Acknowledgement

The financial support from The Thailand Research Fund (TRF) and Science and Technology Postgraduate Education and Research Development Office (PERDO) throughout this project is gratefully acknowledged.

References

[1] Kamm B, Kamm M. Principles of biorefineries. Appl Microbiol Biotechnol 2004;64:137–45.
[2] Ragauskas AJ, Williams CK, Davison BH, Britovsek G, Cairney J, Eckert CA, et al. The path forward for biofuels and biomaterials. Science 2006;311:484–9.
[3] Akiya N, Savage PE. Roles of water for chemical reactions in high temperature water. Chem Rev 2002;102:2725–50.
[4] Hashaikeh R, Fang Z, Butler IS, Hawari J, Kozinski JA. Hydrothermal dissolution of willow in hot compressed water as a model for biomass conversion. Fuel 2007;86:1614–22.
[5] Wahyudiono Sasaki M, Goto M. Conversion of biomass model compound under hydrothermal conditions using batch reactor. Fuel 2009;88:1656–64.
[6] Weil JR, Dien B, Bothast R, Hendrickson R, Mosier NS, Ladisch MC. Removal of fermentation inhibitors formed during pretreatment of biomass by polymeric adsorbents. Ind Eng Chem Res 2002;41:6132–8.
[7] Huber GW, Chheda JN, Barrett CJ, Dumesic JA. Production of liquid alkanes by aqueous-phase processing of biomass-derived carbohydrates. Science 2005;308:1446–50.
[8] Kuster BFM. 5-Hydroxymethylfurfural (HMF): a review focusing on its manufacture. Starch/Stärke 1990;42:314–21.
[9] Watanabe M, Aizawa Y, Iida T, Aida TM, Levy C, Sue K, et al. Glucose reactions with acid and base catalysts in hot compressed water at 473 K. Carbohydr Res 2005;340:1925–30.
[10] Asghari FS, Yoshida H. Dehydration of fructose to 5-hydroxymethylfurfural in sub-critical water over heterogeneous zirconium phosphate catalysts. Carbohydr Res 2006;341:2379–87.
[11] Watanabe M, Aizawa Y, Iida T, Nishimura R, Inomata H. Catalytic glucose and fructose conversions with TiO_2 and ZrO_2 in water at 473 K: relationship between reactivity and acid–base property determined by TPD measurement. Appl Catal A 2005;295:150–6.
[12] Bicker M, Hirth J, Vogel H. Dehydration of fructose to 5-hydroxymethylfurfural in sub- and supercritical acetone. Green Chem 2003;5:280–4.
[13] Aida TM, Watanabe M, Aizawa Y, Iida T, Levy C, Sue K, et al. Dehydration of D-glucose in high temperature water at pressures up to 80 MPa. J Supercritic Fluid 2007;40:381–8.
[14] Yat SC, Berger A, Shonnard DR. Kinetic characterization for dilute sulfuric acid hydrolysis of timber varieties and switchgrass. Bioresour Technol 2008;99:3855–63.
[15] Kabyemela BM, Adschiri T, Malaluan RM, Arai K. Glucose and fructose decomposition in subcritical and supercritical water: detailed reaction pathway, mechanisms, and kinetics. Ind Eng Chem Res 1999;38:2888–95.
[16] Yang BY, Montgomery R. Alkaline degradation of glucose: effect of initial concentration of reactants. Carbohydr Res 1996;280:27–45.
[17] Kabyemela BM, Malaluan RM, Adschiri T, Arai K. Kinetics of glucose epimerization and decomposition in subcritical and supercritical water. Ind Eng Chem Res 1997;36:1552–8.
[18] Moreau C, Durand R, Roux A, Tichit D. Isomerization of glucose into fructose in the presence of cation-exchanged zeolites and hydrotalcites. Appl Catal A 2000;193:257–64.
[19] Sasaki M, Goto K, Tajima K, Adschiri T, Arai K. Rapid and selective retro-aldol condensation of glucose to glycolaldehyde in supercritical water. Green Chem 2002;4:285–7.
[20] Karimi K, Kheradmandinia S, Taherzadeh MJ. Conversion of rice straw to sugars by dilute-acid hydrolysis. Biomass Bioenerg 2006;30:247–53.
[21] Sasaki M, Takahashi K, Haneda Y, Satoh H, Sasaki A, Narumi A, et al. Thermochemical transformation of glucose to 1,6-anhydroglucose in high-temperature steam. Carbohydr Res 2008;343:848–54.
[22] Ando H, Ohba H, Sakaki T, Takamine K, Kamino Y, Moriwaki S, et al. Hot-compressed-water decomposed products from bamboo manifest a selective cytotoxicity against acute lymphoblastic leukemia cells. Toxicol in Vitro 2004;18:765–71.
[23] Minowa T, Inoue S. Hydrogen production from biomass by catalytic gasification in hot compressed water. Renew Energ 1999;16:1114–7.
[24] Cheng H, Zhu X, Zhu C, Qian J, Zhu N, Zhao L, et al. Hydrolysis technology of biomass waste to produce amino acids in sub-critical water. Bioresour Technol 2008;99:3337–41.
[25] Sun Y, Cheng J. Hydrolysis of lignocellulosic materials for ethanol production: a review. Bioresour Technol 2002;83:1–11.
[26] Thomsen MH, Thygesen A, Thomsen AB. Hydrothermal treatment of wheat straw at pilot plant scale using a three-step reactor system aiming at high hemicellulose recovery, high cellulose digestibility and low lignin hydrolysis. Bioresour Technol 2008;99:4221–8.
[27] Maniriquez ME, Lopez T, Gomez R, Navarrete J. Preparation of TiO_2–ZrO_2 mixed oxides with controlled acid–basic properties. J Mol Catal A 2004;220:229–37.
[28] Tomishige K, Ikeda Y, Sakaihori T, Fujimoto K. Catalytic properties and structure of zirconia catalysts for direct synthesis of dimethyl carbonate from methanol and carbon dioxide. J Catal 2000;192:355–62.

Fuel Processing Technology 91 (2010) 1510–1516

Contents lists available at ScienceDirect

Fuel Processing Technology

journal homepage: www.elsevier.com/locate/fuproc

Esterification of industrial-grade palm fatty acid distillate over modified ZrO_2 (with WO_3–, SO_4 –and TiO_2–): Effects of co-solvent adding and water removal

P. Mongkolbovornkij [a], V. Champreda [b], W. Sutthisripok [c], N. Laosiripojana [a,*]

[a] The Joint Graduate School of Energy and Environment, King Mongkut's University of Technology Thonburi, Thailand
[b] National Center for Genetic Enginnering and Biotechnology (BIOTEC), Pathumthani, Thailand
[c] Department of Mining and Materials Engineering, Prince of Songkla University, Songkhla, Thailand

ARTICLE INFO

Article history:
Received 4 March 2010
Received in revised form 13 May 2010
Accepted 25 May 2010

Keywords:
Esterification
Sulfated zirconia
Tungsten zirconia
Palm fatty acid distillate

ABSTRACT

The esterification of palm fatty acid distillate (PFAD), a by-product from palm oil industry, in the presence of three modified zirconia-based catalysts i.e. SO_4–ZrO_2, WO_3–ZrO_2 and TiO_2–ZrO_2 (with several sulfur- and tungsten-loading contents, Ti/Zr molar ratios, and calcination temperatures) was studied. It was found that, among all synthesized catalysts, the reaction in the presence of SO_4–ZrO_2 and WO_3–ZrO_2 (with 1.8%SO_4 calcined at 500 °C and/or 20%WO_3 calcined at 800 °C) enhances relatively high fatty acid methyl ester (FAME) yield (84.9–93.7%), which was proven to relate with the high acid site density and specific surface area as well as the formation of tetragonal phase over these catalysts. The greater benefit of WO_3–ZrO_2 over SO_4–ZrO_2 was its high stability after several reaction cycles, whereas significant deactivation was detected over SO_4–ZrO_2 due to the leaching of sulfur from catalyst. For further improvement, the addition of toluene as co-solvent was found to increase the FAME yield along with reduce the requirement of methanol to PFAD molar ratio (while maintains the FAME yield above 90%). Furthermore, it was observed that the presence of water in the feed considerably lower the FAME yield due to the catalyst surface interfering by water and the further hydrolysis of FAME back to fatty acids. We proposed here that the negative effect can be considerably minimized by adding molecular sieve to remove water from the feed and/or during the reaction.

1. Introduction

Biodiesel is known as one of the promising renewable fuels for petroleum-based fuel substitution, which can be efficiently produced from the tranesterification of vegetable oil or animal fat with short chain alcohols. Currently, palm oil is the major feedstock for biodiesel production in Thailand due to its availability and good conversion efficiency. Typically, crude palm oil (CPO) contains high amount of free fatty acids (FFAs), which easily converts to soap during the transesterification reaction and consequently reduces the overall process performance [1]. To avoid this formation, most of FFAs in CPO must be firstly treated or removed (as called palm fatty acid distilled or PFAD). Recently, some researchers have suggested that the conversion of PFAD to fatty acid methyl ester (FAME) via esterification reaction is a good procedure to reduce the production cost of biodiesel and consequently to make biodiesel enable to compete economically with petroleum-based fuel.

Typically, the esterification reaction is an acid-catalyzed process, in which the conventional acid-catalysts are sulfuric acid and hydrochloric acid. Nevertheless, the major limitation of homogeneous acid-catalyzed reaction is the difficulty for catalyst recovery and/or treatment; hence, extensive washing is usually required to remove all acid compounds from the product causing large amount of wastewater and consequently increase the overall cost of process. Furthermore, according to the technical report of local palm oil refinery industries, the acid-catalyzed esterification process with H_2SO_4 seems to be unsuitable due to the massive corrosion in several system equipments. As an alternative procedure, heterogeneous catalyst has widely been reported to overcome these problems due to its easily separate and recover from the process [2]. Recently, several literatures have proposed the use of various heterogeneous catalysts for both transesterification and esterification reactions [2–5]. Among solid catalysts, sulfated zirconia (SO_4–ZrO_2) have been known to give high activity and selectivity for transesterification and esterification of several vegetable oils and fatty acids; this catalyst is also of interest in several other industrial processes, such as hydrocarbon isomerization and alkylation [6]. Apart from SO_4–ZrO_2, recently other zirconia-based catalysts e.g. TiO_2–ZrO_2 and WO_3–ZrO_2 have also been of interest to researchers for several chemical reactions. TiO_2–ZrO_2 is known to have bifunctionality for both acidity and basicity properties which benefits for acid- and base-catalyzed reactions e.g. hydrolysis and isomerization. For WO_3–ZrO_2, this catalyst was also reported to active for transesterification and esterification reactions under specific conditions [3,4,7].

* Corresponding author. Tel.: +66 2 872 9014; fax: +66 2 872 6736.
E-mail address: navadol_l@jgsee.kmutt.ac.th (N. Laosiripojana).

0378-3820/$ – see front matter © 2010 Elsevier B.V. All rights reserved.
doi:10.1016/j.fuproc.2010.05.030

In the present work, we aimed to study the esterification of PFAD in the presence of three zirconia-based catalysts i.e. SO_4–ZrO_2, TiO_2–ZrO_2 and WO_3–ZrO_2. The effects of catalyst preparing conditions i.e. sulfate and tungsten loadings, Ti/Zr molar ratio, and calcination temperature on the catalyst performance were intensively studied. The physical characteristics of these synthesized catalysts, i.e. acidity-basicity properties, phase formation and catalyst surface properties were tested by Temperature-programmed desorption techniques with ammonia and carbon dioxide (NH_3- and CO_2-TPD), X-ray diffraction (XRD) and N2 physisorption in order to relate these properties with the catalytic reactivity. Then, the beneficial of these catalysts on the esterification reaction in terms of reaction reactivity, reaction time, temperature and amount of alcohol requirements were investigated at various operating conditions. In addition, since it is known that the formation of water during the esterification reaction could strongly inhibit the yield of FAME production due to the occurring of hydrolysis reaction, the effect of water content in the system on the reaction performance was carried out by: (1) adding water along with the reactant to the system, (2) adding molecular sieve (as water sorbent) to dehydrate PFAD before filtering out from the reactant prior the reaction and (3) adding the molecular sieve along with the reactants to dehydrate the components during the reaction. Lastly, the effect of co-solvent adding (i.e. hexane, benzene and toluene) on the yield of FAME production was evaluated in the present work.

2. Experimental

2.1. Chemicals

PFAD sample used in this study was provided by Patum Vegetable Oil Co. Ltd, Thailand. It consists of 93.5 wt.% free fatty acid (FFA) (44.8% palmitic, 35.6% oleic, 7.9% linoleic, 3.0% stearic, 1.2% myristic, 0.5% tetracosenoic, 0.2% linolenic, 0.1% ecosanoic, 0.1% ecosenoic, and 0.1% palmitoleic acid) and the rest elements are triglycerides, diglycerides (DG), monoglycerides (MG) and traces of impurities. Methyl ester standard (methyl palmitate, methyl stearate and methyl oleate) were obtained from Wako Chemicals, USA. Commercial grade methanol (95%) and analytical grade hexane (99.9%) ware purchased from Fisher scientific, UK.

2.2. Preparation of catalysts

SO_4–ZrO_2 and WO_3–ZrO_2 were prepared by the incipient wetness impregnation of sulfuric acid or ammonium metatungstate over zirconium oxide (ZrO_2), synthesized via precipitation method. For the preparation of ZrO_2, a solution of zirconyl chloride ($ZrOCl_2$) precursor (0.1 M) was slowly dropped into a well-stirred precipitating solution of ammonium hydroxide (NH_4OH) at room temperature. The solution was controlled at pH of 11. The obtained precipitate was removed, and then washed with deionized water and ethanol. Then, the solid sample was dried overnight at 110 °C and calcined at 500 °C for 6 h. SO_4–ZrO_2 and WO_3–ZrO_2 were then prepared by immersing of synthesized ZrO_2 in 0.1 mol l^{-1} of H_2SO_4 or ammonium metatungstate at 70 °C for 30 min, then dried overnight at 110 °C and calcined at three different temperatures (500, 600 and 700 °C for SO_4–ZrO_2 and 700, 800 and 900 °C for WO_3–ZrO_2) for 3 h. It is noted that three different amounts of sulfuric acid (providing sulfur contents of 0.75, 1.8 and 2.5 wt.%) and ammonium metatungstate (providing tungsten weight contents of 10, 20 and 30 wt.%) were applied in the present work.

For TiO_2–ZrO_2, this catalyst (with Ti/Zr molar ratios of 1/3, 1/1, and 3/1) was prepared by co-precipitation method. In detail, a mixture of zirconium and titanium salt precursors (i.e. zirconyl chloride ($ZrOCl_2$) and titanium chloride ($TiCl_4$) (0.15 M)) was slowly dropped into a well-stirred precipitating solution of ammonium hydroxide (NH_4OH) (2.5 wt.%) at room temperature. The solution was controlled at pH of 11. The obtained precipitate was removed, and then washed with deionized water until Cl^- was not detected by a silver nitrate ($AgNO_3$) solution. Then, the solid sample was dried overnight at 110 °C and calcined at three different temperatures (i.e. 500 °C, 600 °C and 700 °C) under continuous air flow for 6 h with a temperature ramping rate of 10 °C min^{-1}.

2.3. Catalyst characterizations

Measurements of BET surface area, cumulative pore volume and average pore diameter were performed by N2 physisorption technique using Micromeritics ASAP 2020 surface area and porosity analyzer. The XRD patterns of powder were performed by X-ray diffractometer, in which the crystallite size was estimated from line broadening according to the Scherrer equation. The characteristic peaks at $2\theta = 28.2^o$ and 31.5^o for (-111) and (111) reflexes were represented to the monoclinic phase in ZrO_2, while that at $2\theta = 30.2^o$ for the (111) reflex in the XRD patterns was the tetragonal phase in ZrO_2. The percents of tetragonal and monoclinic phases were calculated by a comparison of the areas for the characteristic peaks of the monoclinic phase and the tetragonal phase using means of the Gaussian areas ($h \times w$), where h and w are the height and half-height width of the corresponding XRD characteristic peak.

NH_3- and CO_2-TPD were used to determine the acid-base properties of catalysts. TPD experiments were carried out using a flow apparatus. The catalyst sample (0.1 g) was treated at 500 °C in helium flow for 1 h and then saturated with 15% NH_3/He mixture or pure CO_2 flow after cooling to 100 °C. After purging with helium, the sample was heated to 650 °C in helium flow. The amount of acid-base sites on the catalyst surface was calculated from the desorption amount of NH_3 and CO_2. It was determined by measuring the areas of the desorption profiles obtained from the Chemisorption System analyzer.

2.4. Study of esterification reaction

A batch type reactor was applied to study the esterification reaction in the present work. PFAD was firstly melted at 60 °C and mixed with methanol (with PFAD to methanol molar ratios of 3:1–9:1). 50 g of mixture was charged into the vessel that was connected with a condenser and the catalyst was added to the mixture with the concentration range of 0.25–1.5 wt.%. The reaction was then taken place under specified reaction times (20–360 min) and temperatures (60–90 °C). After reaction, the product was cooled down and separated into three phases. The upper phase was methyl ester, the middle phase was water and methanol, and the lower phase was solid catalyst. Water was removed from the product by a separatory funnel, whereas methanol was removed by evaporation. Lastly, methyl ester product was neutralized by washing repeatedly with water in a separatory funnel and the remaining water was finally removed by a rotary evaporator.

The effect of water content on the reaction performance was studied by three sets of experiments. In the first experiment, water was added along with PFAD and methanol (with the content of 0–30 wt.%) at selected conditions. For the second and third experiments, various amounts of commercial grade molecular sieve (2–10 wt.%; from Fluka, Buchs, Switzerland) was either added to dehydrate PFAD before filtering out from the reactant prior the reaction or added along with the reactants to dehydrate the components during the reaction. The yield of FAME productions from these studies were compared to that from the base condition without water or molecular sieve adding. As for the effect of co-solvent on the reaction performance, it was studied by adding toluene, benzene and hexane (10% v/v) along with the feed before charging to the reactor.

2.5. Product analysis

The fatty acid methyl esters (FAMEs) analysis was carried out using GC (Shimadzu 2010 model) with a flame ionization detector (FID) in which one microliter of the sample was injected into column. The GC consists of a capillary column (DB-WAX, Carbowax 20 M, 30 m, 0.32 mm ID, 0.25 μm). The injector, detector, and column temperatures were set at 250, 260 and 200 °C respectively. Pressure was 64.1 kPa and linear velocity was 25 cm s^{-1}. The carrier gas was helium and the make-up gas was nitrogen. The sample was prepared by adding 0.05 ml of FAMEs to 5 ml of n-hexane and methyl heptadecanoate was used as an internal standard.

3. Results and discussion

As described, SO_4–ZrO_2, TiO_2–ZrO_2 and WO_3–ZrO_2 catalysts were synthesized at various preparation conditions and tested for esterification of PFAD. Here, the synthesized SO_4–ZrO_2, TiO_2–ZrO_2 and WO_3–ZrO_2 calcined at 700 °C were denoted as SZ-700, and WZ-700. SZ catalysts prepared by loading the sulfur contents of 0.75, 1.8, and 2.5% and calcined at 500 °C were denoted as 0.75SZ-500, 1.8SZ-500, and 2.5SZ-500. TZ catalysts with Ti/Zr ratios of 1/3, 1/1 and 3/1 and calcined at 500 °C were donated as 1/3TZ-500, 1/1TZ-500 and 3/1TZ-500. Lastly, WZ catalysts prepared by loading WO_3 of 10, 20 and 30% and calcined at 800 °C were donated as 10WZ-800, 20WZ-800 and 30WZ-800.

3.1. Catalyst characterization

The specific surface area, cumulative pore volume, average pore diameter and pore size distribution of all synthesized catalysts, determined by N_2 physisorption using Micromeritics ASAP 2020 surface area and porosity analyzer, are summarized in Table 1. It can be seen that the specific surface area of SO_4–ZrO_2 increased when the sulfur was loaded up to 1.8%, then the surface area slightly decreased when the sulfur loading content was 2.5%. The abrupt decrease in surface area with higher sulfur contents could be correlated with the alteration of crystal structure and sulfate migration into the bulk phase of the solid. It should be noted that, by loading sulfur over zirconia, the catalyst exhibited smaller crystallite sizes, which caused the increase in the cumulative pore volume, and the reduction of the average pore diameter. Considering pore size distribution of SO_4–ZrO_2, no significant change was observed for those regarding pore size distribution. As for WO_3–ZrO_2, the specific surface area was also found to increase with increasing tungsten loading content, which could be due to the reducing of ZrO_2 sintering rate by WO_3 adding as reported by Iglesia et al [8]. It can also be seen from Table 1 that the specific surface area and cumulative pore volume of SO_4–ZrO_2 considerably decrease with increasing calcination temperature, whereas those of WO_3–ZrO_2 also decrease but with the lower rate (even at the higher calcination temperatures); this also proves the high resistance of ZrO_2 sintering by WO_3 loading. For TiO_2–ZrO_2, the BET results indicated that TiO_2–ZrO_2 with Ti/Zr molar ratio of 1/1 shows the greatest specific surface area. Nevertheless, the specific surface area and cumulative pore volume linearly decreased with increasing calcination temperature, whereas the average pore diameter dramatically increased.

According to the XRD measurement, all SO_4–ZrO_2 and WO_3–ZrO_2 catalysts contain both tetragonal and monoclinic phases with various contents depending on the preparation condition. Table 2 presents the contents of both phases for these catalysts, which were calculated from the areas of corresponding XRD characteristic peaks as described earlier. The results revealed that the average crystal size and the fraction of monoclinic phase for SO_4–ZrO_2 decreased when the sulfur loading content increased from 0% to 0.75% and 1.8%, then they slightly increased when the sulfur loading content was 2.5%. For WO_3–ZrO_2, the fraction of tetragonal phase increased with increasing tungsten loading; in addition, the formation of triclinic phase WO_3 was also detected at high WO_3 loading (30%), Fig. 1. It can also be seen that the crystal size in monoclinic phase and the fraction of monoclinic phase for both SO_4–ZrO_2 and WO_3–ZrO_2 increased with increasing calcination temperature, Fig. 1. For TiO_2–ZrO_2, the main phase observed from XRD over this catalyst is $TiZrO_4$ (as amorphous phase when calcined at 500 °C and turns to be crystalline at higher calcination temperature, Fig. 1).

3.2. Catalytic reactivity toward esterification of PFAD

The catalytic activities toward esterification of PFAD were firstly tested at 80 °C with the reaction time of 180 min. Fig. 2 shows the reaction reactivity of each catalyst in term of FAME yield; it can be seen that among all catalysts 1.8SZ-500 and 20WZ-800 are the highly active catalysts providing the product yields of 93.7 and 84.9%. From the figure, it is clear that sulfate and tungsten loading contents, Ti/Zr molar ratio, and the catalyst calcination temperature strongly affect the catalyst performance toward this reaction. The loading of too high sulfur and tungsten contents (2.5SZ and 30WZ) caused a slight negative effect on the catalytic activity. The inhibitory effect for SO_4–ZrO_2 could be due to the agglomeration of the active SO_4^{2-}phase and/or the cover of basic sites by the exceeded SO_4^{2-}, which results in lower the surface areas of active components and eventually the catalytic activity as reported by Xie et al., 2007 [9,10]. For WO_3–ZrO_2,

Table 1
N_2 Physisorption results of SO_4–ZrO_2, WO_3–ZrO_2 and TiO_2–ZrO_2 prepared from different conditions [3].

Catalysts	BET surface area[a] (m^2/g)	Cumulative pore volume[b] (cm^3/g)	Average pore diameter[c] (nm)
0.75SZ-500	228	0.321	3.9
1.8SZ-500	243	0.390	3.6
2.5SZ-500	237	0.354	3.8
1.8SZ-600	179	0.314	4.0
1.8SZ-700	113	0.254	4.4
20WZ-700	121	0.293	4.1
10WZ-800	91	0.157	4.0
20WZ-800	95	0.193	3.8
30WZ-800	103	0.221	3.8
20WZ-900	78	0.112	4.3
1/1TZ-500	198	0.394	2.5
3/1TZ-500	175	0.385	2.6
1/3TZ-500	189	0.392	2.5
1/1TZ-600	187	0.391	2.5
1/1TZ-700	165	0.382	2.7

[a] Error of measurement = ±5%.
[b] BJH desorption cumulative volume of pores between 1.7 and 300 nm diameter.
[c] BJH desorption average pore diameter.

Table 2
Catalyst characteristics obtained from XRD measurement [3].

Catalysts	Phase	Average crystal size (nm)	Crystal size (nm)[a]		% monoclinic phase[a]
			M[b]	T[c]	
0.75SZ-500	M, T	8.1	8.3	4.2	66.3
1.8SZ-500	M,T	7.8	8.1	4.0	62.9
2.5SZ-500	M, T	7.9	8.1	3.9	63.4
1.8SZ-600	M,T	8.2	8.2	4.3	65.0
1.8SZ-700	M, T	8.7	8.5	4.7	68.7
20WZ-700	M, T	8.4	8.9	4.7	50.3
10WZ-800	M, T	9.7	9.9	5.3	53.8
20WZ-800	M, T	9.5	9.7	5.1	51.4
30WZ-800	M, T	9.4	9.6	5.1	51.2
20WZ-900	M, T	10.3	10.5	5.9	57.6

[a] Based on XRD line broadening.
[b] Monoclinic phase in ZrO_2.
[c] Tetragonal phase in ZrO_2.

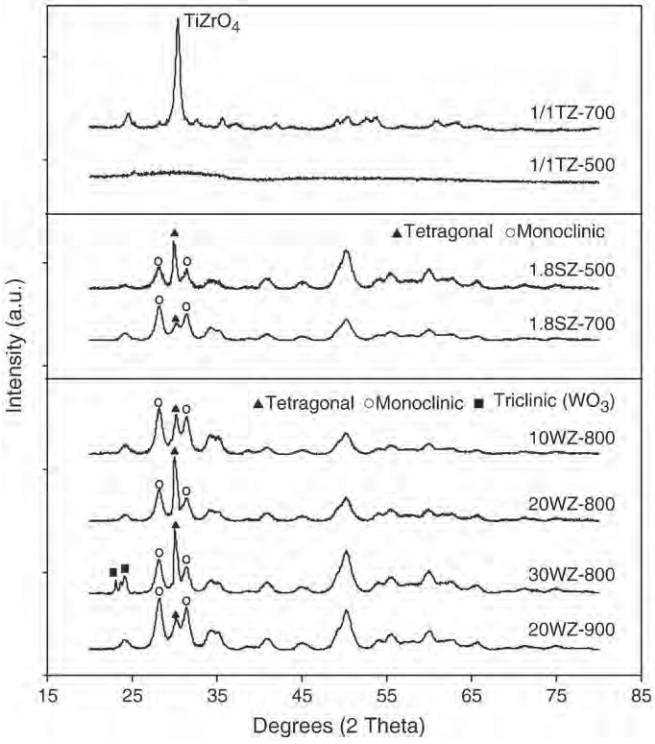

Fig. 1. XRD patterns of three catalysts synthesized at various conditions.

the negative effect can be explained by the acid-base properties of the catalyst from NH_3- and CO_2-TPD testing. The amounts of acid and base sites, which were calculated from the area below curves of these TPD profiles, are listed in Table 3. Along with these values, the distribution of acid and base site on the catalyst surface (namely the density of acid and base site; $\mu mol\ m^{-2}$) is also given in the table since this parameter is important indicator to determine the catalytic reactivity of acid and base reactions [11,12]. According to the TPD studies over SO_4–ZrO_2, the amount and density of acid sites increased with increased percents of sulfur contents. Differently for WO_3–ZrO_2, the amount and density of acid sites increased with increased percents of tungsten content in ZrO_2 up to 20% of tungsten content (20WZ); then they decreased with more tungsten loadings (30WZ). We therefore suggest that the acid site density is important indicator to judge the catalyst reactivity toward the acid-catalyzed esterification reaction.

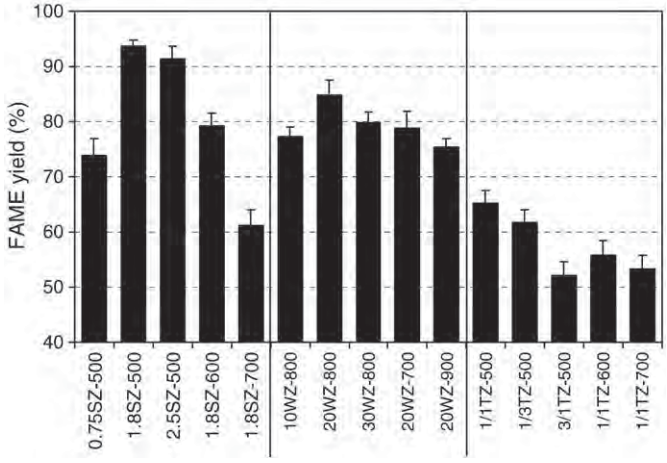

Fig. 2. Effect of catalyst preparing condition on the yield of FAME production from the esterification of PFAD at 80 °C with the reaction time of 120 min and methanol to PFAD molar ratio of 6:1.

Table 3
Results from NH_3- and CO_2-TPD measurements of SO_4–ZrO_2 and WO_3–ZrO_2 prepared by different conditions [3].

Catalysts	Total sites (μmol/g)		Density of sites (μmol/m^2)	
	Acid sites[a]	Base sites[b]	Acid sites	Base sites
0.75SZ-500	677.2	47.9	2.97	0.21
1.8SZ-500	733.9	70.5	3.02	0.29
2.5SZ-500	734.7	78.2	3.10	0.33
1.8SZ-600	524.5	43.0	2.93	0.24
1.8SZ-700	305.1	19.2	2.70	0.17
20WZ-700	330.3	42.9	2.73	0.35
10WZ-800	263.1	31.8	2.89	0.34
20WZ-800	280.2	35.5	2.95	0.37
30WZ-800	286.3	37.2	2.75	0.36
20WZ-900	219.2	21.4	2.81	0.27
1/1TZ-500	692	697	3.49	3.52
3/1TZ-500	594	708	3.39	4.04
1/3TZ-500	653	703	3.45	3.71
1/1TZ-600	645	712	3.45	3.81
1/1TZ-700	554	806	3.35	4.89

[a] From NH_3-TPD.
[b] From CO_2-TPD.

It is noted that the calcination temperature also showed significant impact on the catalyst reactivity. At high calcination temperature (700 °C), the reactivity of SO_4–ZrO_2 considerably decreased, which is mainly due to the loss of sulfur species from SO_4–ZrO_2 as well as the decreases in catalyst specific surface area and the amount of acid sites during the high calcination temperature. According to the elemental analysis, the sulfur content in SO_4–ZrO_2 decreased from 1.8% to 1.78%, 1.73% and 1.57% when calcined at 500, 600 and 700 °C, respectively. In addition, the crystalline structure of catalyst also closely related to the catalyst reactivity. As seen in Table 2, the percentage of tetragonal phase for SO_4–ZrO_2 is in the same trend as the reaction rate; hence, we suggest that the presence of tetragonal phase render to increase the reactivity of these catalysts. In the case of WO_3–ZrO_2, it was found that the catalyst calcined at 800 °C achieved higher reactivity than those calcined at 700 °C and 900 °C. This result is in good agreement with Ramu et al. [13] and Lopez et al. [14] who suggested that the presence of polymeric tungsten species (at the calcination temperature of 800 °C) along with the tetragonal form of ZrO_2 support promote the reactivity of toward the transesterification and esterification reactions. In the case of TiO_2–ZrO_2, the high reactivity of 1/1TZ-500 could be due to its relatively high specific surface area as well as its amorphous phase formation. According to the XRD studies, the phase of TiO_2–ZrO_2 turns from amorphous to crystalline phase above 500 °C; this revealed the impact of catalyst phase formation on its reaction reactivity (the amorphous phase is more active than crystalline phase for the interested reactions).

3.3. Effect of operating conditions on the esterification of PFAD

Based on the above results, it can be seen that 1.8SZ-500 and 20WZ-800 were highly active among all catalysts tested, hence both catalysts were selected for optimizing the operating conditions to maximize the yield of FAME production. Firstly, the effects of catalyst to PFAD mass ratio and reaction time on the reaction rate was studied by varying the mass ratio of catalyst to PFAD from 0–1.5 % and varying the reaction time from 20 to 360 min. As seen in Fig. 3 (a) and (b), the yield of FAME production increases considerably with increasing the catalyst to PFAD mass ratio from 0.25 to 1.0% for 1.8SZ-500 and from 0.25 to 0.5% for 20WZ-800. Upon these points, it slightly decreases which could be due to the reverse of reactions near equilibrium condition. Regarding the effect of reaction time, the results in Fig. 3 (a) and (b) indicate that the reaction rates increase with increased reaction time, providing the yield of FAME production of 93.7% at 180 min for 1.8SZ-500 and 84.9% at 120 min for 20WZ-800. After that, the yield of FAME almost remained constant. Hence, the optimum

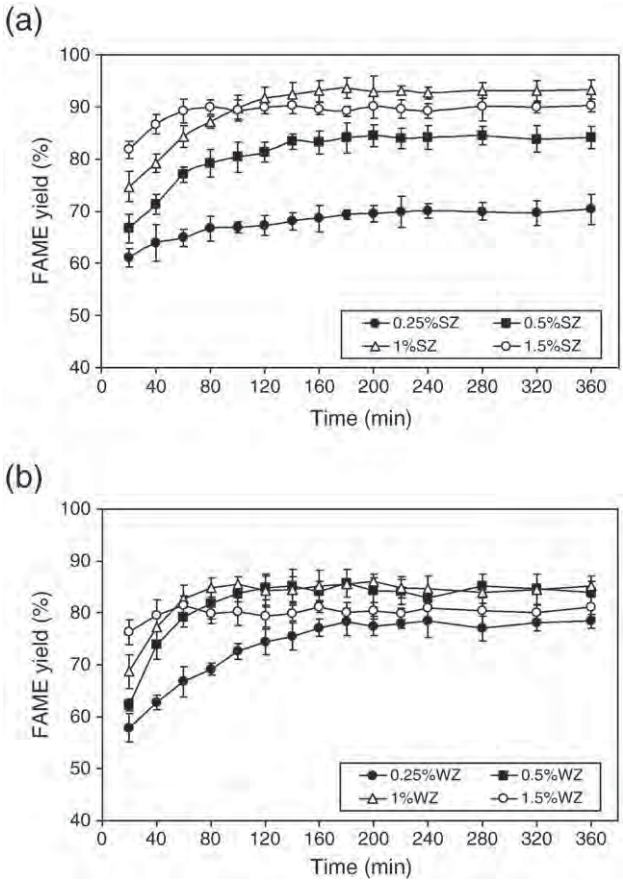

Fig. 3. Effect of reaction time on the yield of FAME production from the esterification of PFAD with various amounts of (a) 1.8SZ-500 and (b) 20WZ-800 at 80 °C with the methanol to PFAD molar ratios of 6:1.

mass ratios of 1.8SZ-500 to PFAD and 20WZ-800 to PFAD for the esterification of PFAD seem to be at 1.0 and 0.5%, while the reaction times for 1.8SZ-500 and 20WZ-800 are 180 and 120 min respectively.

As the next step, the effect of methanol to PFAD molar ratio on the yield of FAME production at various reaction temperatures was determined. Theoretically the esterification reaction requires one mole of alcohol and fatty acid to produce one mole of fatty acid ester and water; nevertheless, excess amount of alcohol is practically applied in order to shift the equilibrium to the right-hand side. However, the use of too high amount of alcohol could also increase the cost of FAMEs and/or biodiesel production; hence the optimization of required alcohol must be intensively considered. Fig. 4 shows the effect of methanol to PFAD molar ratio (between 3:1 to 9:1) on the yield of FAME production at the reaction temperature from 60 to 90 °C. It can be seen that the FAME yield significantly increases with increasing the reaction temperature and the methanol to PFAD molar ratio, particularly at low methanol to PFAD ratio (from 3:1 to 5:1 for 1.8SZ-500 and from 3:1 to 6:1 for 20WZ-800). Upon those molar ratios, the methanol to PFAD molar ratio shows slight positive effect on the reaction rate. According to the effect of reaction temperature, the results indicate that the yield of FAME production considerably increases with increasing the reaction temperature from 60 to 80 °C; above that temperature, the FAME yield insignificantly increases, particularly when the high methanol to PFAD molar ratio is applied.

3.4. Reusability testing

The reusability of SZ, WZ and TZ catalysts was also carried out. After separated from the solution, the catalysts were washed and dried before re-testing the reaction for 5 cycles at the same operating conditions. As shown in Fig. 5, the reactivities of spent WO_3–ZrO_2 and TiO_2–ZrO_2 are almost identical to the fresh one indicated its well-reusable over this reaction, whereas significant deactivation was observed over the reused SO_4–ZrO_2. According to the elemental analysis of the catalysts after each reaction cycle, high percentage of sulfur losing (44%) were observed for SO_4–ZrO_2 after five reaction cycles (the sulfur content decreased from 1.8% to 1.24%, 1.19%, 1.11%, 1.03% and 1.0% after the first to fifth reaction cycles respectively), whereas lower percentage of tungsten losing (9%) was found for WO_3–ZrO_2 (tungsten content decreased from 20% to 19.1%, 18.8%, 18.3%, 18.2% and 18.2% after the first to fifth reaction cycles). As for TiO_2–ZrO_2, insignificant change of Ti–Zr content was observed after five reaction cycles. These results clearly explain the low deactivations of WO_3–ZrO_2 and TiO_2–ZrO_2 compared to SO_4–ZrO_2, from which the high activity losing after several reaction cycles is due to the sulfur leaching. It has been widely reported that the sulfur leaching from the

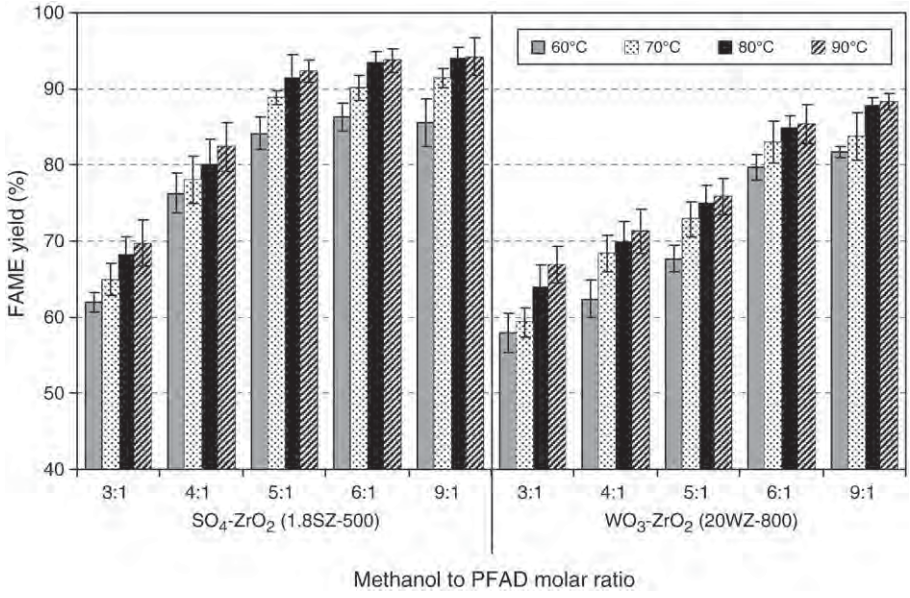

Fig. 4. Effect of methanol to PFAD molar ratio on the yield of FAME production from the esterification of PFAD in the presence of 1.8SZ-500 (1 wt.%) and 20WZ-800 (0.5 wt.%) at 80 °C with the reaction time of 120 min.

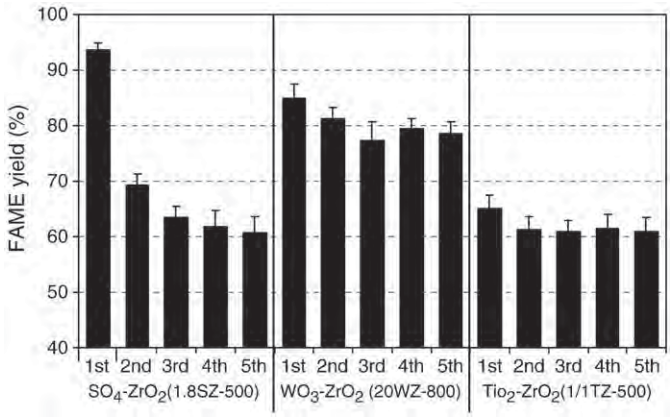

Fig. 5. Reusability testing (in 5 reaction cycles) of 1.8SZ-500 (1 wt.%), 20WZ-800 (0.5 wt.%) and 1/1TZ-500 (1 wt.%) toward the esterification of PFAD at 80 °C with the reaction time of 120 min and methanol to PFAD molar ratios of 6:1.

catalyst as well as the poisoning and pore filling during the process are the main barriers of SO_4–ZrO_2 [2,14,15]. Lopez et al. [14] also indicated that the high electronegative sulfate ions can be lost from the catalyst during the reaction with alcohol. In addition, the catalyst deactivation can also be due to the side blockage by adsorbed intermediates or product species that were considerably more polar than the original reagents [4], and/or carbon deposition [16]. Considering the benefit in terms of reactivity and stability, WO_3–ZrO_2 would be a good candidate for esterification of PFAD ahead of SO_4–ZrO_2 and TiO_2–ZrO_2; this catalyst was then selected for further studies.

3.5. Effect of co-solvent adding on the esterification of PFAD with WO_3–ZrO_2

The effect of co-solvent adding (i.e. hexane, benzene and toluene) was also evaluated in the present work by adding 10% v/v of these solvents in the reactant prior the reaction. The enhancing effect of co-solvent adding in the reaction medium at different methanol to reactant molar ratios is shown in Fig. 6. Clearly, the presences of toluene and benzene can increase the FAME yield along with reduce the requirement of methanol to PFAD molar ratio to maintain the FAME yield above 90%, whereas the presence of hexane shows slight inhibitory effect. In the presence of toluene, the FAME yield of 90.3% can be obtained at the methanol to reactant molar ratio of 5:1, whereas the reaction without toluene adding required methanol to reactant molar ratio of 9:1 to reach the maximum FAME yield of 87.7%. It is noted that the reaction improvement with addition of benzene and toluene could possibly be due to the fact that benzene and toluene are good solvents for vegetable oil and both are miscible with methanol [17], therefore these solvents could help the mixing of methanol with oil in reactor. The inhibitory effect of hexane could be due to the low solubility of this solvent in methanol, hence it acts as an antisolvent and reduced the biodiesel production yield.

3.6. Effect of water content on the esterification of PFAD with WO_3–ZrO_2

It is well established that the presence of water provides negative effect on the acid-catalyzed reactions, since water interferes with the catalyst and reduces catalyst performance [18]. In addition, the presence of water during the esterification reaction could result in the occurring of hydrolysis reaction, which eventually reduces the FAME production yield. Hence, in this study, the effect of water adding (between 0–30%) on the esterification of PFAD was determined at various methanol to PFAD molar ratios (using the reaction temperature of 80 °C, reaction time of 120 min, mass ratio of 20WZ-800 to PFAD of 0.5%). The result in Fig. 7(a) indicates that the presence of water indeed lowered the yield of FAME produced, particularly when the low methanol to PFAD molar ratio is applied. In the presence of 30% water, the FAME yield decreased by 9% when the methanol to PFAD ratio of 9:1 was used, but dramatically reduced by 34% when the methanol to PFAD ratio of 3:1 was applied. It is noted that, at prolong reaction time employed (180 min) in the presence of 30% water, the yields of FAME continuously reduced to 13.4 and 37.2% when the methanol to PFAD ratios of 9:1 and 3:1 were used, respectively. This could be due to the further reaction of water with FAME by hydrolysis reaction, which converts FAME back to fatty acids.

As another approach, the esterification of PFAD after pre-treatment with molecular sieve (Method 1: M1) and in the presence of molecular sieve (Method 2: M2) was studied. It can be seen from Fig. 7(b) that uses of molecular sieve led to improvement in FAME yield, particularly for the reaction in the presence of molecular sieve (M2). By adding 10 wt.% of molecular sieve along with 20WZ-800, the yield of FAME production can be increased from 87.7% to 93.4%.

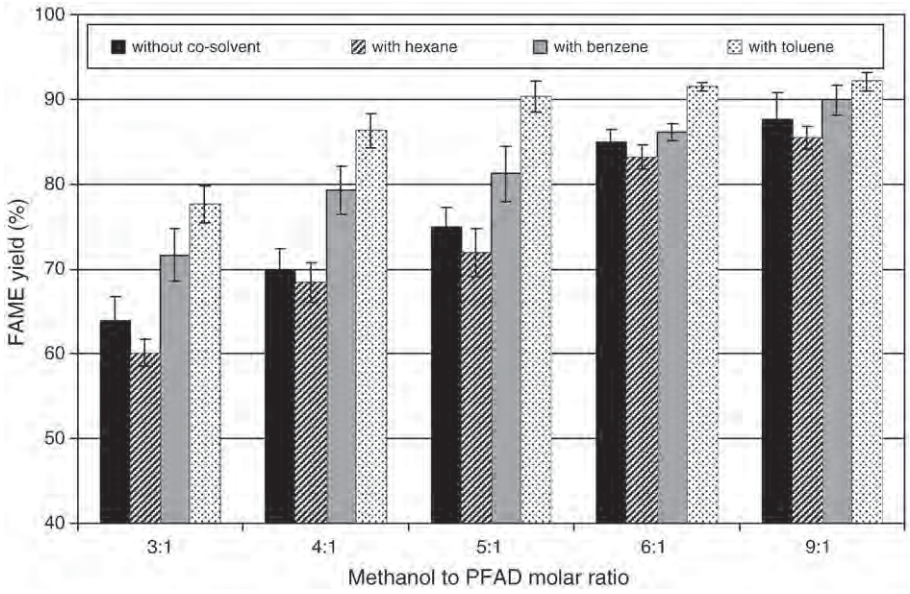

Fig. 6. Effect of co-solvent adding on the yield of FAME production from the esterification of PFAD in the presence of 20WZ-800 (0.5 wt.%) at various methanol to PFAD molar ratios (at 80 °C with the reaction time of 120 min).

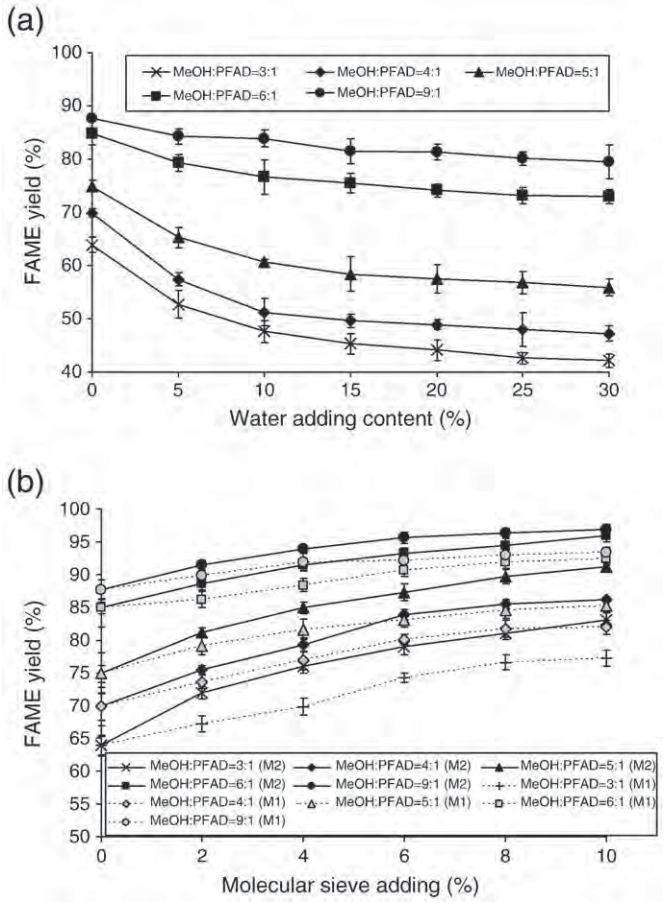

Fig. 7. Effect of water content (a) and molecular sieve adding (b) (M1: for pre-treatment of PFAD before filtering out prior the reaction; M2: adding along with reactants to the system) on the yield of FAME production from the esterification of PFAD in the presence of 20WZ-800 at various methanol to PFAD molar ratios at 80 °C with the reaction time of 120 min.

Theoretically, water is known to affect biodiesel synthesis by favoring hydrolysis of ester products from esterification reaction [19–21]. In this study where dried feedstocks were used, the occurring of hydrolysis reaction can be inhibited and results in the higher FAME yield achievements. Furthermore, in the presence of molecular sieve, considerable increase of FAME yield can be achieved due to the continuous removal of water generated from the esterification of PFAD, which prevents the surface interfering of WO_3–ZrO_2 by water as well as inhibit the occurring of hydrolysis reaction. These results suggest that, in order to maximize the yield of FAME production from PFAD, care must be taken to remove water before and/or during the reaction.

4. Conclusion

FAME could be efficiently produced from the esterification of PFAD in the presence of SO_4–ZrO_2 and WO_3–ZrO_2 (with 1.8%SO_4 calcined at 500 °C or 20%WO_3 calcined at 800 °C); the catalyst characterizations indicated that the good reactivity of these catalysts was related to their high acid site density and specific surface area as well as the formation of tetragonal phase. The major benefit of WO_3–ZrO_2 compared to SO_4–ZrO_2 was the excellent reusability of WO_3–ZrO_2 after several reaction cycles, whereas significant deactivation was observed over SO_4–ZrO_2 due to the leaching of sulfur from catalyst. We found that the addition of toluene (10% v/v) as co-solvent can increase the yield of FAME production as well as reduce the requirement of methanol to PFAD. Furthermore, the presence of water in the feed considerably lower the FAME yield; we suggested that this negative effect can be minimized by adding molecular sieve (10 wt.%) along with solid catalyst to remove water from the feed and/or during the reaction.

Acknowledgement

The financial support from The Thailand Research Fund (TRF) throughout this project is gratefully acknowledged.

References

[1] S. Zallaikah, C. Lai, S.R. Vali, Y.H. Ju, A two-step acid-catalyzed process for the production of biodiesel from rice bran oil, Bioresour. Technol. 96 (2005) 1889–1896.
[2] A.A. Kiss, F. Omota, A.C. Dimian, G. Rothenberg, The heterogeneous advantage: biodiesel by catalytic reactive distillation, Top. Catal. 40 (2006) 141–150.
[3] N. Laosiripojana, W. Kiatkittipong, W. Sutthisripok, S. Assabumrungrat, Synthesis of methyl esters from relevant palm products in near-critical methanol with modified-zirconia catalysts, Bioresour. Technol. 101 (2010) 8416–8423.
[4] D.E. Lopez, J.G. Goodwin Jr., D.A. Bruce, E. Lotero, Transesterification of triacetin with methanol on solid acid and base catalysts, Appl. Catal. A 295 (2005) 97–105.
[5] Qing Shu, Qiang Zhang, Xu. Guanghui, Zeeshan Nawaz, Dezheng Wang, Jinfu Wang, Synthesis of biodiesel from cottonseed oil and methanol using a carbon-based solid acid catalyst, Fuel Proc. Tech. 90 (2009) 102–108.
[6] K. Tanabe, W.F. Holderich, Industrial application of solid acid-base catalysts, Appl. Catal. 181 (1999) 399–434.
[7] K.N. Rao, A. Sridhar, A.F. Lee, S.J. Tavener, N.A. Young, K. Wilson, Zirconium phosphate supported tungsten oxide solid acid catalysts for the esterification of palmitic acid, Green Chem. 8 (2006) 790–797.
[8] E. Iglesia, S.L. Soled, G.M. Kramer, Isomerization of alkanes on sulfated zirconia: promotion by Pt and by adamantly hydride transfer species, J. Cat. 144 (1993) 238–253.
[9] W. Xie, X. Huang, H. Li, Soybean oil methyl esters preparation using NaX zeolites loaded with KOH as a heterogeneous catalyst, Bioresour. Technol. 98 (2007) 936–939.
[10] W. Xie, H. Peng, L. Chen, Transesterification of soybean oil catalyzed by potassium loaded on alumina as a solid-base catalyst, Appl. Catal. A 300 (2006) 67–74.
[11] M.E. Maniriquez, T. Lopez, R. Gomez, J. Navarrete, Preparation of TiO_2–ZrO_2 mixed oxides with controlled acid–basic properties, J. Mol. Catal. A. 220 (2004) 229–237.
[12] K. Tomishige, Y. Ikeda, T. Sakaihori, K. Fujimoto, Catalytic properties and structure of zirconia catalysts for direct synthesis of dimethyl carbonate from methanol and carbon dioxide, J. Catal 192 (2000) 355–362.
[13] S. Ramu, N. Lingaiah, B.L.A.P. Devi, R.B.N. Prasad, I. Suryanarayana, P.S. Sai Prasad, Esterification of palmitic acid with methanol over tungsten oxide supported on zirconia solid acid catalysts: effect of method of preparation of the catalyst on its structural stability and reactivity, Appl. Catal. A 276 (2004) 163–168.
[14] D.E. Lopez, J.G. Goodwin Jr., D.A. Bruce, S. Furuta, Esterification and transesterification using modified-zirconia catalysts, Appl. Catal. A 339 (2008) 76–83.
[15] A. Corma, Solid acid catalysts, Curr. Opin. Solid State Mater. Sci. 2 (1997) 63–75.
[16] K. Suwannakarn, E. Lotero, J.G. Goodwin Jr., C. Lu, Stability of sulfated zirconia and the nature of the catalytically active species in the transesterification of triglycerides, J. Catal. 255 (2008) 279–286.
[17] K. Krisnangkura, R. Simamaharnnop, Continuous transmethylation of palm oil in an organic solvent, JAOCA 69 (1992) 166–169.
[18] J.M. Komers, R. Stloukal, Biodiesel from rapeseed oil, methanol and KOH. 2. Composition of solution of KOH in methanol as reaction partner of oil, Eur. J. Lipid Sci. Tech. 103 (2001) 359–362.
[19] T. Yamane, Y. Kojima, T. Ichiryu, M. Nagata, S. Shimizu, Intramolecular esterification by lipase powder in microaqueous benzene: effect of moisture content, Biotechnol. Bioeng. 34 (1989) 838–843.
[20] T. Anthonsen, B.J. Sjursens, Importance of water activity for enzymes catalysis in non-aqueous organic systems, in: M.N. Gupta (Ed.), Methods in non-aqueous enzymology, Birkhauser Verlag, Basel, 2000, pp. 14–35.
[21] S. Shah, M.N. Gupta, Lipase catalyzed preparation of biodiesel from Jatropha oil in a solvent feee system, Proc Biochem. 42 (2007) 409–414.

Chemical Vapor Deposition

DOI: 10.1002/cvde.201006857

Full Paper

Fabrication of $La_{0.8}Sr_{0.2}CrO_3$-based Perovskite Film via Flame-Assisted Vapor Deposition for H_2 Production by Reforming**

By *Mayuree Sansernnivet*, *Navadol Laosiripojana*, *Suttichai Assabumrungrat*, and *Sumittra Charojrochkul**

Flame-assisted vapor deposition (FAVD) has a principle similar to conventional CVD in which a film is deposited from a vapor phase. It is a simple and cost-effective technique as it is operated in an open atmosphere. The microstructure of the deposited films is controlled by varying the processing parameters. In our research, an oxide film of lanthanum chromite perovskite-based ($La_{0.8}Sr_{0.2}CrO_3$) material is fabricated, using the FAVD technique, on a stainless steel substrate (SS430) for an application in solid oxide fuel cells (SOFC). The precursor solution for $La_{0.8}Sr_{0.2}CrO_3$ film is prepared from metal nitrate compounds with a concentration in the range 0.0125 – 0.0500 M. Dense and porous films are fabricated, depending on various processing parameters such as fuel to water ratio, air pressure, flow rate of a precursor, and the distance between the spray nozzle and the substrate. The effect of various processing parameters on the microstructure and phase formation of the deposited film are investigated using scanning electron microscopy (SEM) and X-ray diffraction (XRD). The deposition temperature resulting from the total heat of combustion from the combination of all the deposition parameters is very important in determining the properties of the films. According to the SEM images, a small particle size on the nanometer scale is found at high deposition temperature. On the other hand, the particles are connected into a dense film at low deposition temperatures. The main phase of $LaCrO_3$ is found in all deposition temperatures (temp range). For hydrogen production, the methane steam reforming over the porous film of $La_{0.8}Sr_{0.2}CrO_3$ at 900 °C is investigated. Under specific operating conditions (low inlet H_2O/CH_4 ratio), its catalytic reactivity is comparable to metallic-based catalysts but with less inlet steam required.

Keywords: FAVD, Lanthanum chromite ($La_{0.8}Sr_{0.2}CrO_3$), Methane steam reforming, Perovskite, Solid oxide fuel cells

1. Introduction

Lanthanum chromite-based perovskite ($LaCrO_3$) has been widely recognized as a promising interconnect material for SOFCs.[1–3] It has recently been found to be useful in other applications such as catalytic combustion of methane,[4] and SOFC anode materials,[5] however different properties are desired to serve as each functional part in SOFCs. The synthesis methods and fabrication routes are known to have an effect on the microstructure which also affects properties of materials. Many techniques, such as electrochemical vapor deposition (EVD),[6] CVD,[7] and physical vapor deposition (PVD),[8] have been used to fabricate SOFC components. These vapor processing methods are generally very expensive because they require complex reactors or vacuum systems. To reduce the cost of fabrication, FAVD has been introduced to deposit films as it requires a simple apparatus and is performed in an open atmosphere. Preliminary work showed the potential of this technique in depositing porous lanthanum strontium manganese oxide (LSM) as a cathode for SOFCs.[9] The microstructure of the film can be controlled by varying the processing parameters, resulting in dense or porous film deposition. The aim of this research is to study the effect of processing parameters on the microstructure and phase formation in the deposited films. The effects of processing parameters, i.e., the ratio of ethanol to water in the precursor, air pressure, precursor flow rate, and the distance between the air atomizer and the substrate, were studied. The effect of various processing parameters on film microstructure and phase formation of the deposited film were investigated using scanning electron microscope (SEM) and X-ray diffraction (XRD), respectively. For hydrogen production, the methane steam reforming over the optimized porous film of $La_{0.8}Sr_{0.2}CrO_3$ at 900 °C was investigated.

[*] Dr. S. Charojrochkul
National Metal and Materials Technology Center
Pathumthani (Thailand)
E-mail: sumittrc@mtec.or.th

M. Sansernnivet, Prof. N. Laosiripojana
The Joint Graduate School of Energy and Environment, KMUTT
Bangkok (Thailand)

Prof. S. Assabumrungrat
Department of Chemical Engineering, Chulalongkorn University
Bangkok (Thailand)

[**] This research is supported by Thailand Graduate Institute of Science and Technology Scholarship (TGIST) under the grant No.TG-33-20-51-062M from National Science and Technology Development Agency (NSTDA), Thailand Research Fund (TRF), and National Metal and Materials Technology Center (MTEC). Mr.Wittaya Wongklang is greatly acknowledged for setting up the FAVD apparatus.

2. Results and Discussion

2.1. Effect of Ethanol/Water Ratio in the Precursor Solution

Four different ratios of ethanol to water were studied (i.e., 85:15, 80:20, 75:25, and 70:30 v/v), while the other parameters were kept constant. The processing conditions are shown in Table 1. The following are the detailed results obtained from each condition. At the highest ethanol/water ratio investigated (85:15 v/v), the deposition temperature was in the range 850 – 900 °C. The morphology of the obtained surface is shown in Figure 1(a-1). According to the SEM image, the characteristic of the films seemed to be porous, containing relatively large particles (0.15 – 1.00 μm) compared to those of other specimens. In addition, the cross-section view in Figure 1(a-2) shows that the thickness of the film is about 5 μm and it is not smooth. At a slightly lower ethanol/water ratio of 80:20 v/v, the deposition temperature was in the range 820 – 845 °C. In terms of morphology, agglomeration of particles was observed. The particle size and shape were not uniform, as in Figure 1(b-2). The thickness of the film was about 10 μm. The higher ratio of ethanol to water yields a greater amount of total heat generation of the system from the combustion of ethanol than a lower ratio of ethanol to water which results in higher deposition temperature.

At the ethanol/water ratio of 75:25 v/v, the deposition temperature and the morphology were found to be similar to those observed with the ratio of 80:20 v/v, however the film was thicker, as in Figure 1(c-2). At the lowest ethanol/water ratio of 70:30 v/v, the deposition temperature was reduced to 620 – 720 °C. The size of particle ranged from 0.2 to 3.0 μm. The resulting film was found to be the most dense and the thickest compared to those using higher ethanol/water ratios, as illustrated in Figure 1(d-1) and Figure 1(d-2). The microstructures of films obtained from various ethanol/water ratios agreed with those proposed earlier.[9] For high ethanol/water ratios, the nucleation of particles occurs prior to reaching the surface of the substrate, resulting in an agglomeration of particles or porous films, while for the low ethanol/water ratios, heterogeneous deposition takes place at the vicinity of the substrate, resulting in a dense film.[11]

When the ethanol/water ratio was decreased further, from 70:30 v/v to 50:50 v/v, the deposited film did not adhere well to the substrate and was rather flaky.

From these studies, it can be seen that the ethanol/water ratio has an effect on the deposition temperature during reaction. A higher deposition temperature was obtained by increasing the ethanol/water ratio. In addition, the variations of the ethanol to water ratio also showed an impact on the morphology of the deposited films. It was observed that the lower the ratio of ethanol to water, the denser the films become.

2.2. Effect of Air Pressure

In this study, the air pressure was varied between 15 and 30 psi. Under the lowest pressure, 15 psi, the deposition temperature was in the range 700 – 770 °C, and a moderately dense film was produced, as shown in Figure 2(a-1). In addition, the range of deposition temperature was broad and the shape of the combustion flame during the deposition was very thin such that it did not cover the whole surface of the substrate. Figures 2(b-1) and 2(c-1) show the porous films with fine particles (2 – 5 μm in size) which were formed when the air pressures were set at 20 psi and 25 psi. The deposition temperature was 740 – 780 °C and 740 – 760 °C, respectively.

Under the highest air pressure, 30 psi, the particles were packed into a very dense film of joined particles, as shown in Figure 2(d-1). The deposition temperature for this condition was reduced to 475 – 510 °C. Furthermore, the film thicknesses, as investigated from the cross-sectional images of specimens shown in Figure 2, were estimated to be 12, 8, 7, and 33 μm when the air pressures were at 15, 20, 25, and 30 psi, respectively. A high air pressure results in low deposition temperature, while the particles become more connected as the deposition becomes more heterogeneous than in the lower air pressure condition.[10,11]

2.3. Effect of Flow Rate of Precursor

In this study, four different flow rates of precursor were examined; 7, 13, 17, and 25 mL min^{-1}. SEM images of surface area and cross-section of deposited films using these flow rates are shown in Figure 3. At the lowest flow rate of 7 mL min^{-1}, the resulting film seemed to be porous, containing particles in the range 0.1 – 7.0 μm. The deposition temperature was low, in the range 470 – 510 °C. It was

Table 1. Experimental conditions of FAVD processing parameters.

Parameter variation	Ethanol/deionized water [v/v]	Air pressure [psi]	Flow rate of precursor [mL min^{-1}]	Distance between air atomiser and substrate [cm]
Ethanol/deionized water	85:15,80:20,75:25,70:30	20	13	13
Air pressure	75:25	15,20,25,30	13	13
Flow rate of precursor	75:25	20	7,13,17,25	13
Distance between air atomiser and substrate	75:25	20	13	10,13,15,17

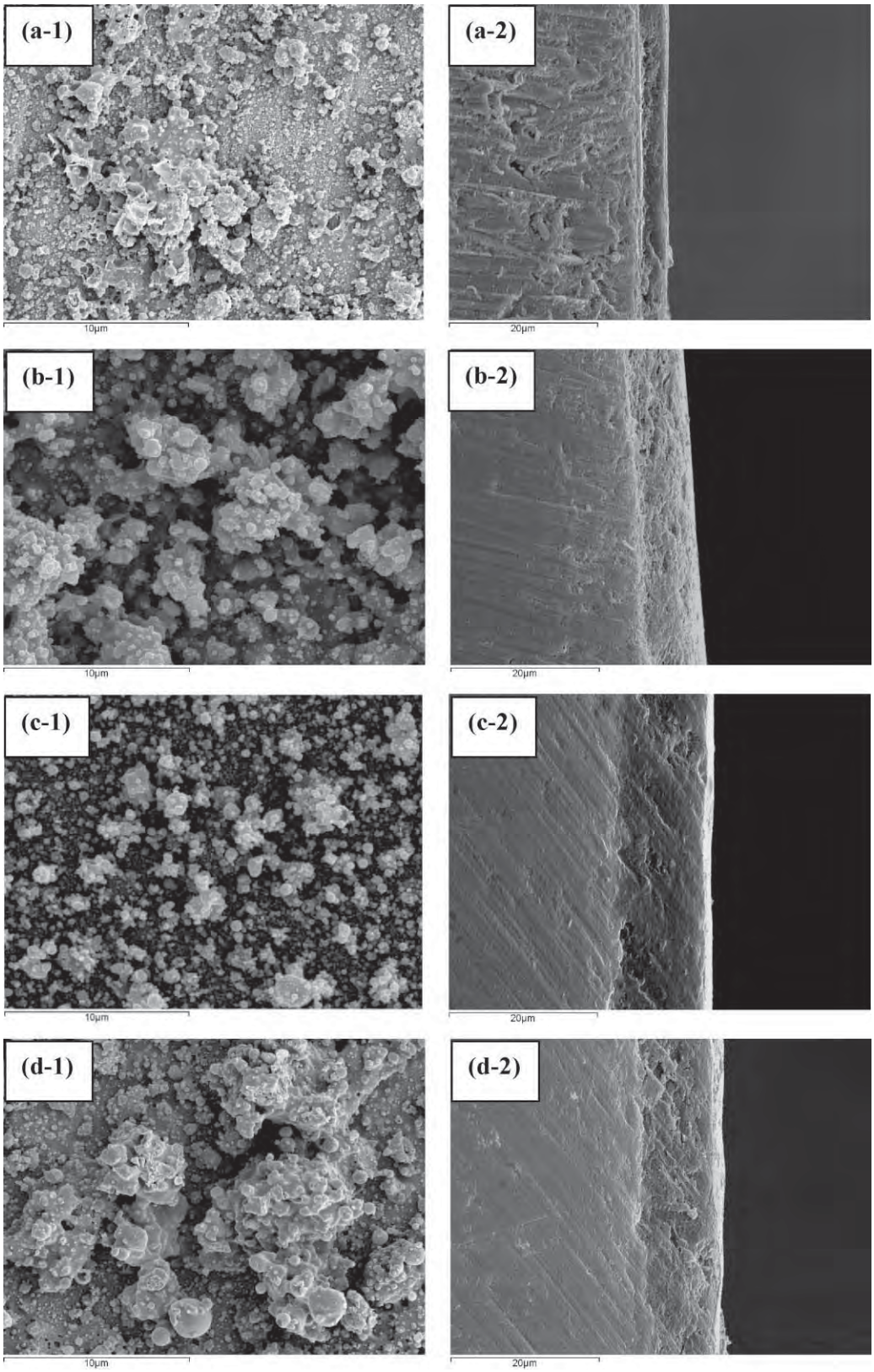

Fig. 1. SEM images of (1) surface morphology and (2) cross-section of films deposited at various ratios of ethanol/water; a) 85:15, b) 80:20, c) 75:25, and d) 70:30 v/v.

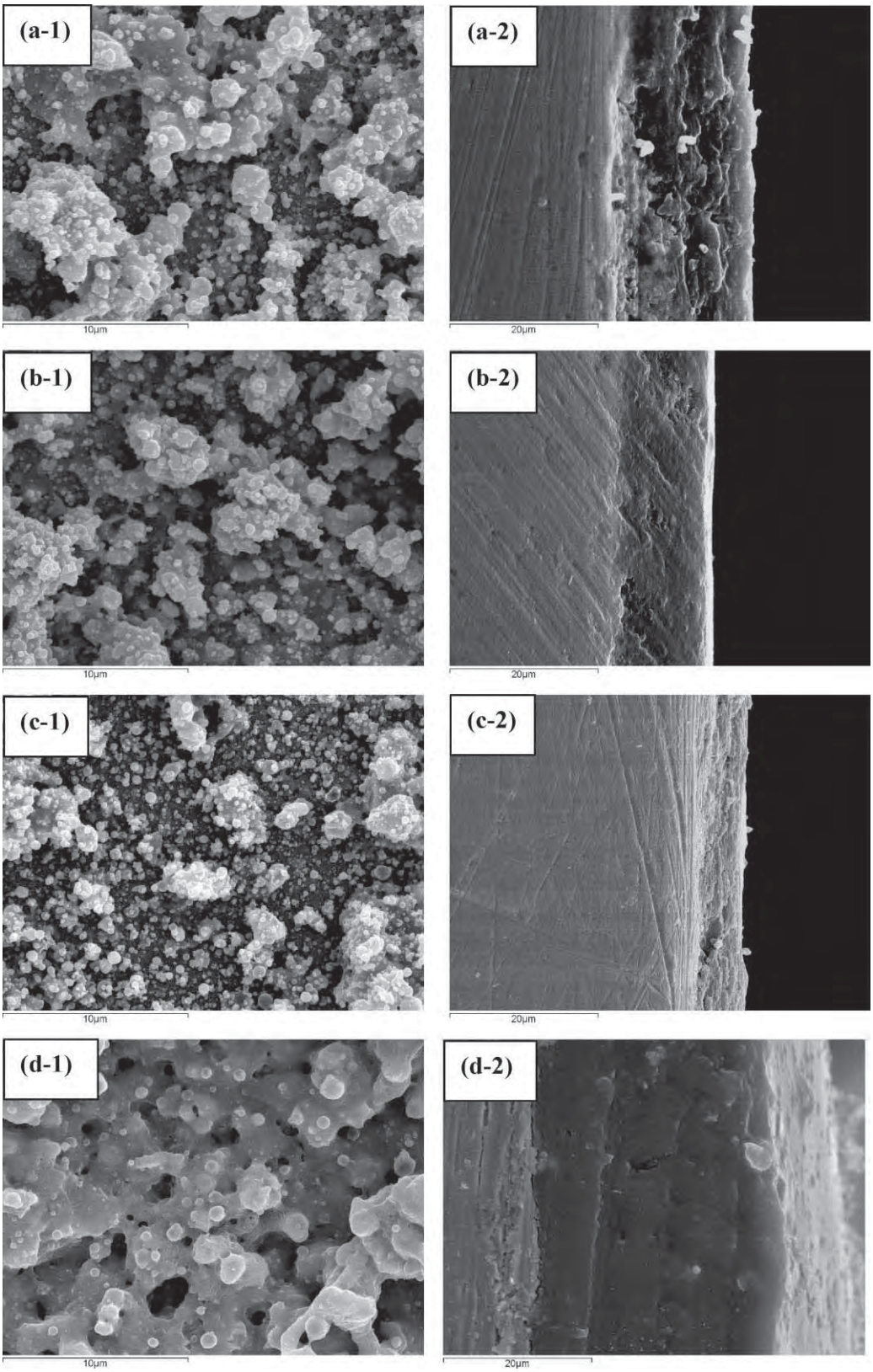

Fig. 2. SEM images of (1) surface morphology and (2) cross-section of films under various air pressures; a) 15 psi, b) 20 psi, c) 25 psi, and d) 30 psi.

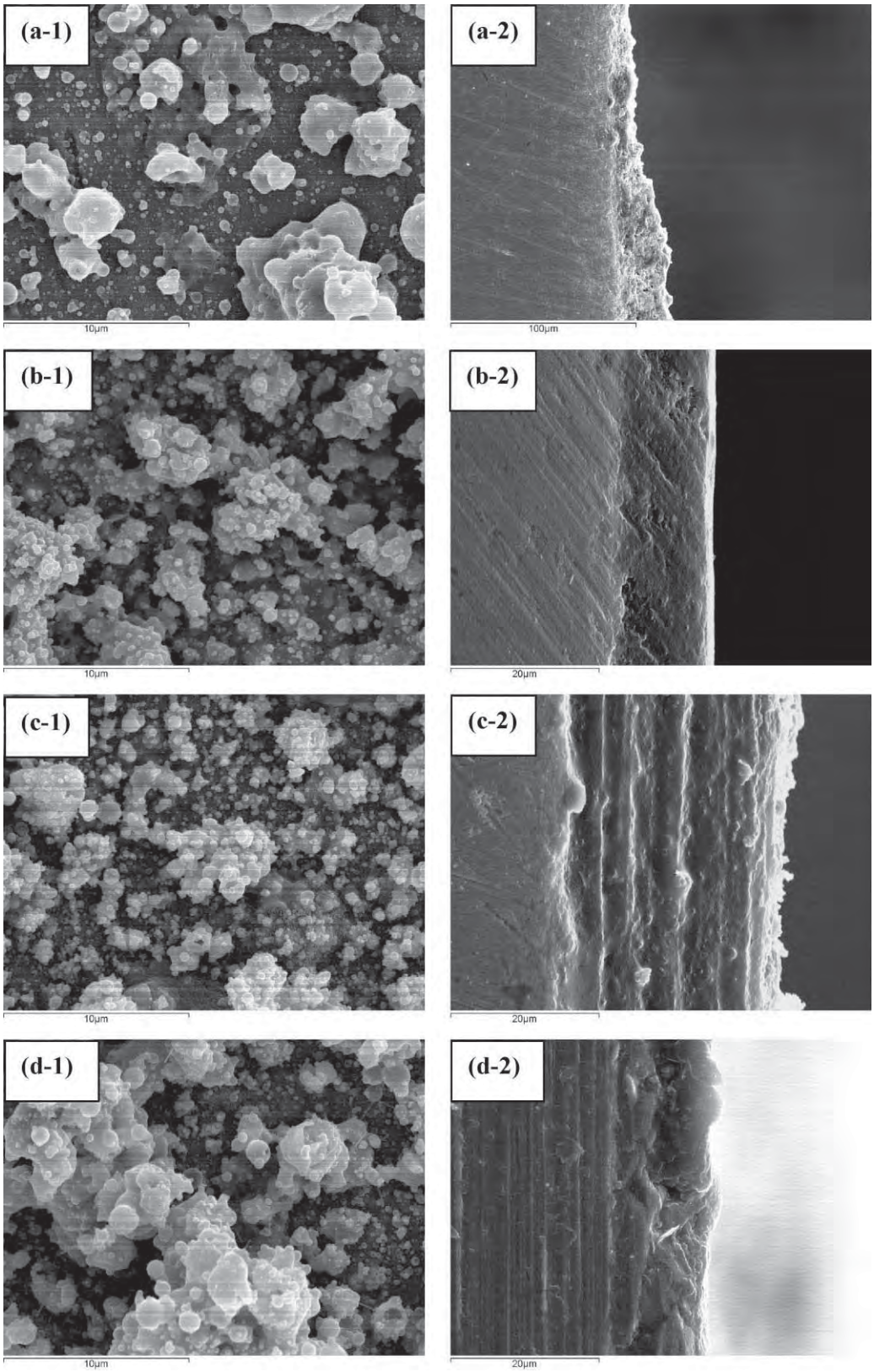

Fig. 3. SEM images of (1) surface morphology and (2) cross-section of films deposited at different flow rates of precursor; a) 7 mL min^{-1}, b) 13 mL min^{-1}, c) 17 mL min^{-1}, and d) 25 mL min^{-1}.

observed that the flame did not cover the substrate during the deposition process due to a limited precursor feeding. This was confirmed in Figure 3(a-2) with a small amount of coating on the specimen. The thickness was less than 20 μm.

For the medium flow rates of 13 and 17 mL min^{-1}, the microstructure images of films displayed similar morphology of agglomerate particles combined into dense films of heterogeneous deposition,[11] as shown in Figures 3(b-1) and 3(c-1), respectively. Nevertheless, the thickness of films obtained with these medium flow rates of precursor was found to be different. The film produced at the flow rate of 13 mL min^{-1} gave a significantly thinner film than that produced at 17 mL min^{-1}, as shown in Figures 3(b-2) and 3(c-2), respectively.

At the highest precursor flow rate of 25 mL min^{-1}, the deposition temperature was at 730 – 880 °C. The microstructure of film produced at high flow rate exhibited a greater amount of particles than those at lower flow rate, as this deposition is mainly a homogeneous nucleation.[11] At high flow rate of precursor, the particles were combined into a dense film as shown in Figure 3(d-1). Nonetheless, the film thickness from the highest flow rate was found to be quite low, as seen in Figure 3(d-2). This might be caused by the shape of flame during reaction, being quite extensive due to a large amount of precursor solution being fed. It was observed that the diameter of the flame on the substrate was about 10 cm which was spread out from the area of coating surface in some depositions.

Although the high flow rate of precursor resulted in dense film morphology, the comparison of SEM images between that of high precursor flow rate and that of high air pressure deposition (Fig. 3(d-2)) indicated that the precursor flow rate did not have as much influence as the air pressure on the microstructure. This might be due to the difference in temperature observed during both depositions.

2.4. Effect of Distance Between Air Atomizer and Substrate

The effect of the distance between the air atomizer and the substrate on the deposited film was investigated by varying the distance in the range 10 – 17 cm. Films produced at the shortest distance, 10 cm, are shown in Figure 4(a-1) and (a-2). The fine particles were agglomerated and thus resulted in the most dense film when compared with other deposition distances in this study. This showed the distance for heterogeneous deposition.[11] The deposition temperature was monitored to vary in a narrow range 650 – 690 °C while the shape of combustion flame during deposition was observed to cover the whole substrate. Furthermore, there seemed to be a significant difference in the corresponding film thickness obtained using the deposition distance of 10 and 15 cm, as shown in Figures 4(a-2) and (c-2). In addition, for the distance of 15 cm, a porous film was deposited containing particles of various sizes between 0.1 and 8.5 μm, as illustrated in Figure 4(c-1).

By using the longest distance, 17 cm, the deposition temperature was observed to range from 550 – 580 °C, which was considerably lower than the other deposition distances. This could be due to the distance between the air atomizer and the substrate being too far. It might encourage the vaporization of combusted gases into the atmosphere prior to deposition onto the substrate. The morphology of this film appeared to be neither uniform nor porous, with the corresponding particle sizes ranging widely. From Figure 4(d-2), the resulting film thickness for this deposition distance can be seen to be the thinnest compared to other, shorter distances.

Under these conditions, the low deposition temperature was observed when using the following combination of conditions; low ethanol/water ratio, high air pressure, high flow rate of precursor and moderate distance between air atomizer and substrate. The deposition temperature was varied in the range 470 – 550 °C. It was observed that during deposition the combustion flame reached the substrate with little splashing. The combustion reaction was found to have an effect on the microstructure as shown schematically in Figure 5. The heterogeneous reaction results in a dense film coating as the thermal environment has the major influence on the microstructure of deposited films.[11] On the other hand, a porous film of lanthanum chromite could be deposited at high temperature using the following combination of conditions; high ethanol/water ratio, moderate air pressure, medium flow rate of precursor, and short distance between air atomizer and substrate. The deposition temperature was varied in the quite high temperature range 760 – 900 °C. It was observed that, during deposition, the shape of the combustion flame reached the substrate with broad splashing, larger than 4 cm in diameter, as shown in Figure 6. The high ratio of fuel to water leads to high temperature reaction in which the precursor was combusted and reacted readily before deposition onto the substrate. As a result, the deposited film consisted of an agglomeration of very fine particles, a combination of homogenous nucleation and heterogeneous deposition.[11]

2.5. Effect of Deposition Temperature on the Phase Formation

The common factor observed in all of the conditions mentioned above was that the variation of processing parameters obviously affected the deposition temperature. The effect of deposition temperature is actually a result of the combustion process of each set of combined parameters. Several combinations of processing parameters (ratio of ethanol to water, flow rate of precursor, distance between the air atomizer and substrate, and air pressure) tend to result in the same combustion process and deposition temperature. The phase formation is then directly affected

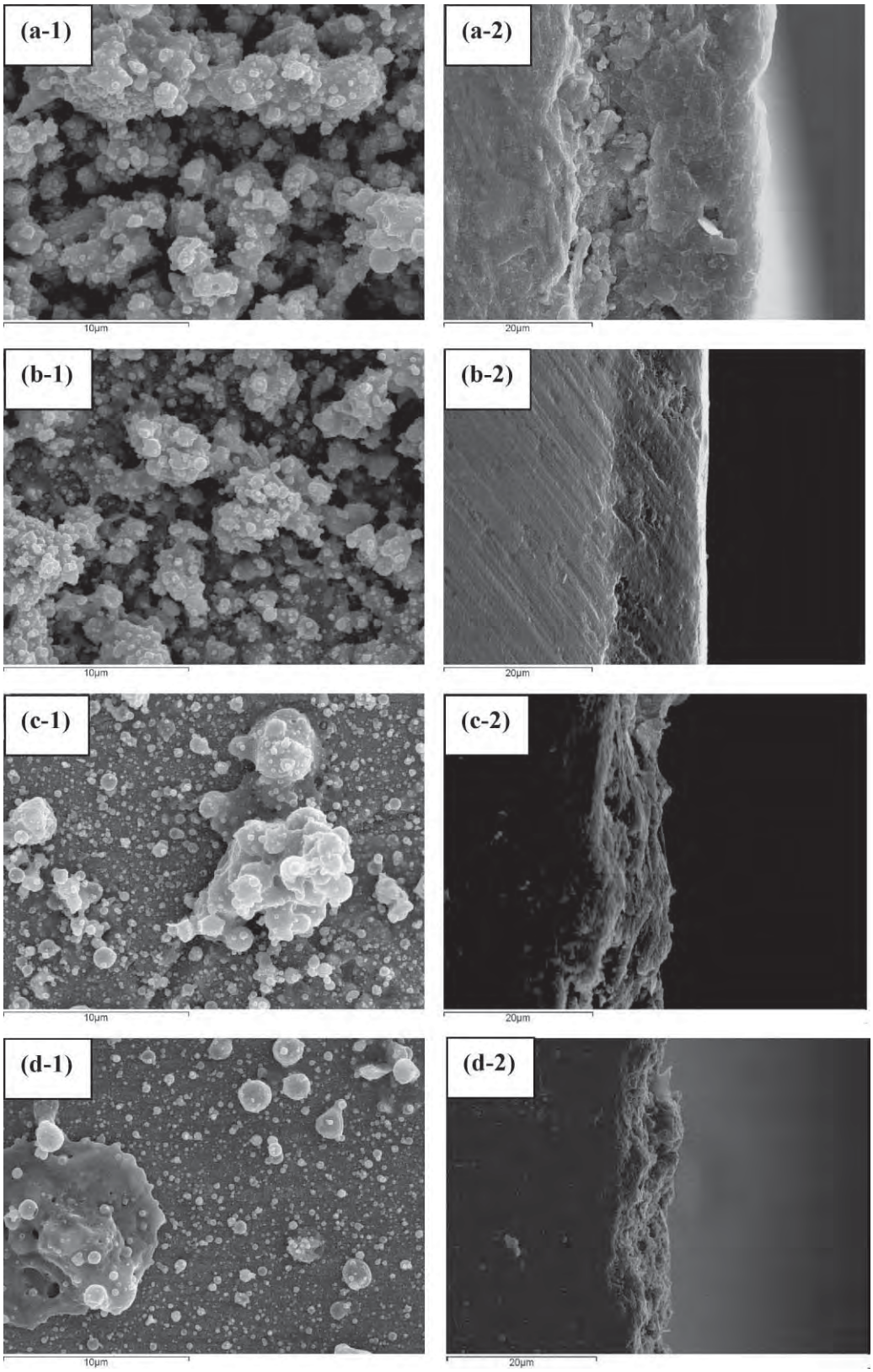

Fig. 4. SEM images of (1) surface morphology and (2) cross-section of film depositions at various distances between the air atomizer and the substrate; a) 10 cm, b) 13 cm, c) 15 cm, and d) 17 cm.

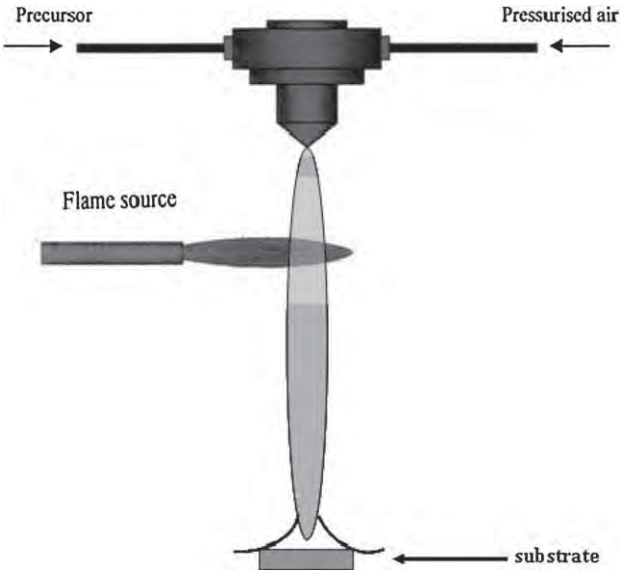

Fig. 5. A sketch of combustion reaction at low deposition temperature.

by the combustion process which is represented by the deposition temperature. It was, therefore, fundamental that the correlation between the deposition temperature and the presenting phase formation was determined. The phase formation of the samples were investigated using XRD. The deposition temperature was varied from 470 °C to 900 °C. From the XRD pattern shown in Figure 7, $La_{0.8}Sr_{0.2}CrO_3$ was the main phase found in all deposition temperature ranges, as indicated, between $LaCrO_3$ and $La_{0.75}Sr_{0.25}CrO_3$. At low deposition temperatures, 470 – 580 °C, the XRD pattern showed lower intensity and high background noise,

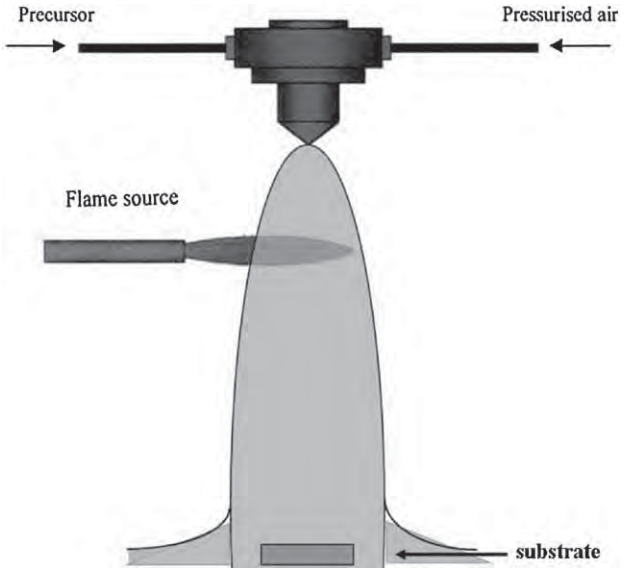

Fig. 6. A sketch of combustion reaction at high deposition temperature.

due to its low crystallization. These peaks still show the $La_{0.8}Sr_{0.2}CrO_3$ as a main phase, $SrCrO_4$ as a secondary phase, and a small peak of Cr phase, however the secondary phase of $SrCrO_4$ was not present at higher deposition temperatures. $SrCrO_4$ has a lower melting point than $LaSrCrO_3$.[12,13] This second phase of $SrCrO_4$ was reported by Yokokawa et al.[13] to co-occur with even a small amount of non-stoichiometry of lanthanum chromite. The unreacted Sr^{2+} then forms $SrCrO_4$.[15] The absence of $SrCrO_4$ at higher deposition temperatures might be caused by a complete combustion reaction to form $La_{0.8}Sr_{0.2}CrO_3$, as the combustion and deposition occur simultaneously and rapidly, compared with a slow sintering process. The XRD pattern for the medium deposition temperature range 640 – 780 °C showed a higher intensity than that observed in the low deposition temperature range. The XRD pattern of the film that was deposited at a medium temperature range mainly consisted of $La_{0.8}Sr_{0.2}CrO_3$, while tiny peaks of Cr phase were also detected. In the high deposition temperature range, 800 – 900 °C, the highest intensity peaks were obtained. The corresponding phase formation exhibited a similar pattern to that observed in the medium deposition temperature range, apart from an absence of Cr phase peaks. This Cr phase was probably from the substrate as 430 stainless steels were used and combined with a too thin coating. Nevertheless, none of the XRD patterns mentioned above exhibited the chromium oxide phase (Cr_2O_3), as reported by Lu et al.,[16] which reduced the reaction with the cathode material and also decreased the performance of the cell for use as an interconnector.

2.6. Reactivity of LaCrO3 in the Steam Reforming of Methane

Lanthanum chromite-based ($La_{0.8}Sr_{0.2}CrO_3$) porous film deposited with the fixed processing conditions of air pressure at 20 psi, 75:25 ethanol/water, 13 mL min^{-1} flow rate of precursor, and 13 cm distance between the air atomizer and substrate, as shown in Figure 2b, was selected for studying the capability as a potential catalyst in steam reforming of methane at 900 °C which may be used as a hydrogen generator or an anode material for SOFCs. The feed was a mixture of CH_4 and steam in nitrogen with the inlet molar H_2O/CH_4 ratios of 0.3, 0.5, 0.75, 1.0, and 3.0. It is noted that the ratio of 3.0 is a typical value employed in steam reforming of methane, and the effect of low inlet molar H_2O/CH_4 ratio on the reaction activity was investigated in the present work. After 10 h of operation, $La_{0.8}Sr_{0.2}CrO_3$ porous film exhibited high stability with slight deactivation in methane conversion (the deactivations from the steam reforming testing are in the range 4.2 – 7.9%, depending on the inlet molar ratio of H_2O/CH_4 applied). Figure 8 shows the CH_4 conversion under steady-state conditions (after 10 h of operation) from the steam reforming over this film.

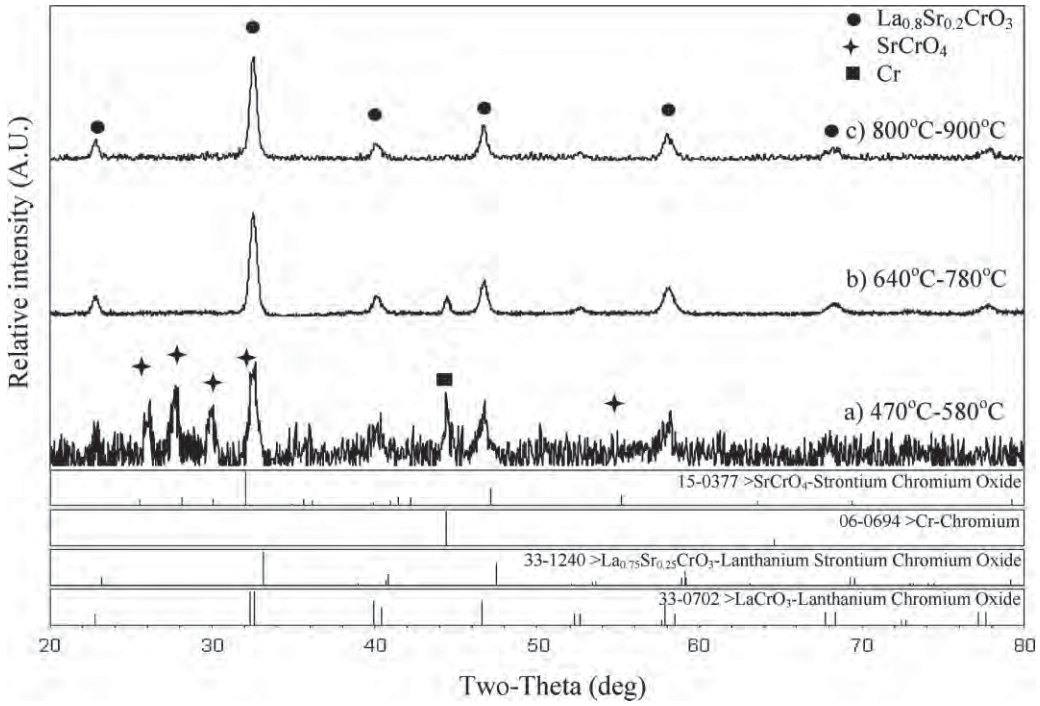

Fig. 7. XRD patterns of deposited films at various deposition temperatures from 470 – 900 °C.

It can be seen that the conversion is strongly affected by the concentration of H_2O. With the inlet ratio of H_2O/CH_4 at 0.3, the conversion was relatively low. Nevertheless, when the inlet ratio of H_2O/CH_4 was raised to 0.75, the methane conversion was dramatically increased to 67.3%; this value is in the same range as that obtained from the steam reforming over conventional Ni/Al_2O_3 catalyst (65.4% CH_4 conversion). At higher H_2O/CH_4 ratios (from 0.75 to 1.0), the methane conversion was considerably decreased, but beyond these ratios (H_2O/CH_4 ratio of 3.0), the inlet H_2O content showed insignificant influence on the methane conversion. It is noted that the main products from the reaction were H_2 and CO with some CO_2 formation, indicating the influence of the water/gas shift (WGS)reaction (Fig. 9). Based on the measured concentrations of reactants and products during the reforming, the approach to WGS equilibrium condition (η_{WGS}) in the range of temperature studied (850 – 1000 °C) is always close to 1.0, indicating that the WGS reaction is at equilibrium. At 900 °C, the highest H_2 production can be achieved at the inlet H_2O/CH_4 molar ratio of 0.75, which is in good agreement with the reforming result in Figure 8.

Two possible reforming mechanisms in the methane steam reforming over $La_{0.8}Sr_{0.2}CrO_3$ are proposed, depending on the applied operating conditions. Under the operating conditions of high H_2O/CH_4 ratios, the oxygen non-stoichiometry value (δ) of $La_{0.8}Sr_{0.2}CrO_{3-\delta}$ is theoretically close to 0 and the material behaves like oxide-based

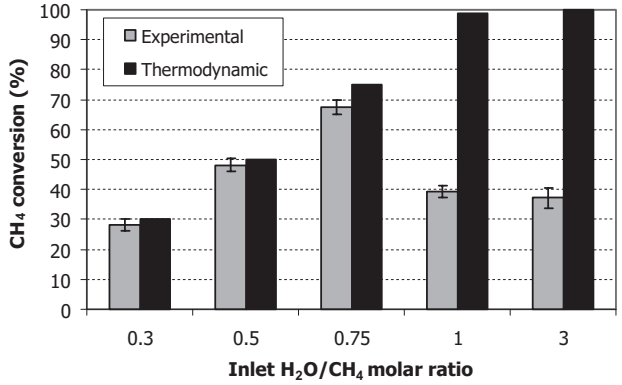

Fig. 8. Steam reforming of methane at 900 °C at various concentrations of methane feeding for porous films.

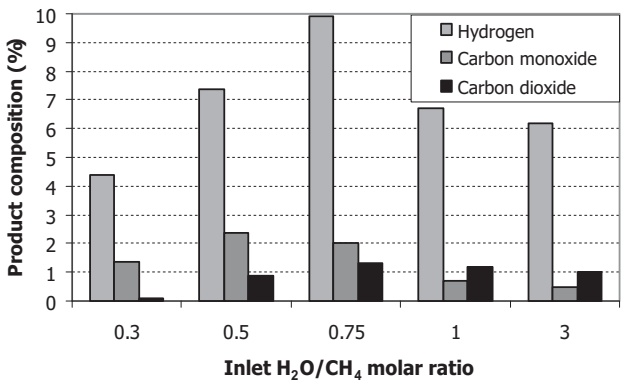

Fig. 9. Product composition from the steam reforming of methane at 900 °C at various concentrations of methane feeding for porous films.

catalysts (e.g., ceria-based catalysts). The redox mechanism was previously proposed to explain the steam reforming behavior of ceria-based catalysts;[16] the studies provided the evidence that the sole kinetically relevant elementary step is the reaction of intermediate surface hydrocarbon species with the lattice oxygen on the surface of the catalyst. In addition, that oxygen is replenished by the oxygen supplied from H_2O. On the other hand, under the operating conditions of low H_2O/CH_4 (0.5) ratio, the δ value of $La_{0.8}Sr_{0.2}CrO_{3-\delta}$ increases and the material behaves more like metallic-based catalysts.[17,18] Its high reforming reactivity, comparable to the metallic-based Ni/Al_2O_3, under this reaction regime provides the practical evidence for this claim. Recently, the steam and dry reforming of methane over perovskite-based $La_{0.8}Sr_{0.2}Cr_{0.9}Ni_{0.1}O_3$ powder was reported, and its reforming mechanism showed the same trend as the film-based catalyst in this work,[16] from which the catalyst behaves like an oxide-based catalyst at high co-reactant/CH_4 ratio, whereas it tends to behave more like a metallic-based catalyst at low co-reactant/CH_4 ratios, resulting in the high reforming reactivity. A dense $La_{0.8}Sr_{0.2}CrO_3$ deposition film was also tested instead of the porous film, resulting in much worse reforming activity than that of the porous film.

3. Conclusion

The FAVD technique has been demonstrated to accomplish the deposition of both dense and porous films on 430 stainless steel (SS430). The deposition temperature was related to the shape of the flame during the combustion reaction, which was very important in determining the properties of the films. In this research, dense films of lanthanum strontium chromite could be deposited at low temperature using the following condition; the ethanol/water ratio of 70:30 v/v, air pressure of 30 psi, 13 mL min^{-1} flow rate of precursor, 13 cm distance between the air atomizer and substrate. The high density of the film is suitable for use as an interconnector material in SOFCs. Conversely, the porous film could be fabricated at high temperature deposition under the following conditions; the ethanol/water ratio of 85:15 v/v, air pressure at 25 psi, 17 mL min^{-1} flow rate of precursor, 13 cm distance between the air atomizer and substrate. The porous film containing rather small particles is appropriate for use as a catalyst for internal reforming of SOFCs. The phase of $LaSrCrO_3$ was detected in all depositions with no chromium oxide phase. Lanthanum chromite-based material has good potential for hydrogen production via a steam reforming reaction. Under specific operating conditions (low inlet ratio of H_2O/CH_4), its catalytic reactivity is comparable to metallic-based catalysts but with less inlet steam required. It is noted that the requirement of lower inlet steam content is a major benefit of this material since the concerns over water management in the system (e.g., reformer and SOFC system) are minimal.

4. Experimental

Precursor Preparation: The precursor solution contained nitrate compounds of $La(NO_3)_3{\cdot}6H_2O$ 99.9%, $Cr(NO_3)_3{\cdot}9H_2O$ 98.5%, and $Sr(NO_3)_2$ (99.0% supplied by Alfa Aesar). They were mixed together to a required stoichiometric composition of 0.8:1:0.2 by mole and dissolved in de-ionized water to obtain the aqueous precursor with the concentration of 0.0125 M. Then ethanol (ACS 99.9%) was added to increase the inflammability of the solution. The ratio of ethanol to water was varied from 70:30 v/v to 85:15 v/v.

Specimen Preparation and Characterization: The films were deposited using an FAVD technique onto a 430 stainless steel substrate (SS430). SS430 consists of Fe (80.3 wt.-%), Cr (17 wt.-%), Mn (1.0 wt.-%), Ni (0.50 wt.-%), Si (1.0 wt.-%), C (0.12 wt.-%), P (0.04 wt.-%), and S (0.03 wt.-%). SS430 substrates (10 mm × 10 mm × 2 mm) were cut from a large sheet 1 mm thick, cleaned with detergent, and ultrasonicated in de-ionized water for 10 min prior to the deposition. The FAVD technique was performed in an open atmosphere. The precursor solutions were fed through the air atomizer to produce the atomized droplets which were sprayed across a flame source where the decomposition and combustion occur. The temperature of reaction was measured using a type K thermocouple at the surface of the substrate right in the combustion zone. The accuracy of this thermocouple is ± 1 °C. The oxide film was then deposited onto the substrate which was being heated on a hotplate. More details of the FAVD technique may be found in our previous literature[9,19].

XRD analysis (Cu Kα, JEOL JDX-3530) was performed to examine the crystal structure and phase formation of the prepared specimens. The deposited films were examined in the range $2\theta = 20 - 80$ with a goniometer scanning speed of 2 ° per min. The surface morphology and thickness of lanthanum chromite films were investigated using a secondary electron mode in a SEM (JEOL JSM-6310F).

Catalytic Steam Reforming of Methane: To investigate the methane steam reforming, an experimental reactor system was constructed. The feed gases, including the components of interest such as CH_4, H_2O, and He, were introduced to the reaction section in which a quartz reactor was mounted vertically inside a furnace. The catalyst was loaded into the quartz reactor, which was packed with a small amount of quartz wool to prevent the catalyst from moving. A type K thermocouple was placed into the annular space between the reactor and the furnace. This thermocouple was mounted on the tubular reactor in close contact with the catalyst bed to minimize the temperature difference between the catalyst bed and the thermocouple. To investigate the stability of materials under the real steam reforming conditions, the catalyst, lanthanum chromite, was operated at room temperature to 200 °C in a nitrogen atmosphere until the steady-state system was reached. After that, the temperature was increased to 900 °C at the rate of 20 °C min^{-1} in the atmosphere of 2 – 10% CH_4/N_2 and steam. The overall feeding rate was 100 mL min^{-1}. After the reactions, the product gases were transferred via trace-heated lines to the analysis section using gas chromatography (GC SHIMADZU GC-148).

Received: June 28, 2010
Revised: October 1, 2010

[1] N. Q. Minh, T. Takahashi, *Science and Technology of Ceramic Fuel Cells*, Elsevier, New York **1995.**

[2] H. U. Anderson, M. M. Nasrallah, B. K. Flandermeyer, A. K. Agarwal, *J. Solid State Chem.* **1985**, *56*, 325.

[3] J. W. Fergus, *Solid State Ionics* **2004**, *171*, 1.

[4] T. Caillot, P. Gélin, J. Dailly, G. Gauthier, C. Cayron, J. Laurencin, *Catalysis Today* **2007**, *128*, 264.

[5] J. Sfeir, P. A. Buffat, P. Mockli, N. Xanthopoulos, R. Vasquez, H. J. Mathieu, J. V. Herle, T. K. Ravindranathan, *J. Catalysis* **2001**, *202*, 229.

[6] R. J. Bratton, P. Reichner, L. W. Montgomery, Fuel Cell Seminar Abstracts, presented at the University of Nottingham, UK **1986.**

[7] Y. B. Kim, S. G. Yoon, H. G. J. Kim, *Electrochem. Soc.* **1992**, *139*, 2559.

[8] E. S. Thiele, L. S. Wang, T. O. Wang, S. A. J. Barnett, *J. Vac. Sci. Technol.* **1991**, *9*, 3054.

[9] S. Charojrochkul, K. L. Choy, B. C. H. Steele, *J. Eur. Ceram. Soc.* **2004**, *24*, 2515.

[10] K. L. Choy, S. Charojrochkul, B. C. H. Steele, *Solid State Ionics* **1997**, *96*, 49.

[11] J. C. Viguié, J. Spitz, *J. Electrochem. Soc.* **1975**, *122*, 585.

[12] T. Negas, R. S. Roth, *J. Res. Natl. Bur. Stand, Sect. A* **1996**, *73*(4), 433.

[13] Z. Phanek, *Silikaty 1981, 25, 169, quoted in Phase Diagrams for Ceramists, Vol. VI, Fig. 6691*, The American Ceramic Society, 1987.

[14] H. Yokokawa, N. Sakai, T. Kawada, M. Dokiya, *J. Electrochem. Soc.* **1991**, *138*(4), 1018.

[15] M. Mori, N. M. Sammes, *Solid State Ionics* **2002,** *146* (3–4), 301.

[16] Z. Lu, J. Zhu, Y. Pan, N. Wu, A. Ignatiev, *J. Power Sources* **2008**, *178*, 282.

[17] C. Chettapongsaphan, S. Charojrochkul, S. Assabumrungrat, N. Laosiripojana, *Appl. Catal. A* **2010**, *386*, 194.

[18] J. Wei, E. Iglesia, *J. Catalysis* **2004**, *225*, 116.

[19] G. Pudmich, B. A. Boukamp, M. Gonzalez-Cuenca, W. Jungen, W. Zipprich, F. Tietz, *Solid State Ionics* **2000**, *135*, 433.

Catalytic Steam and Autothermal Reforming of Used Lubricating Oil (ULO) over Rh- and Ni-Based Catalysts

U. Wetwatana,[†] P. Kim-Lohsoontorn,[‡] S. Assabumrungrat,[§] and N. Laosiripojana*,[||]

The Sirindhorn International Thai-German Graduate School of Engineering, King Mongkut's University of Technology North Bangkok, Bangkok, Thailand, Department of Chemical Engineering, Faculty of Engineering, Mahidol University, Bangkok, Thailand, Department of Chemical Engineering, Faculty of Engineering, Chulalongkorn University, Bangkok, Thailand, and The Joint Graduate School of Energy and Environment, King Mongkut's University of Technology Thonburi, Bangkok, Thailand

The steam reforming of used lubricating oil (ULO) over Ni- and Rh-based catalysts supported by Ce-ZrO_2 and Al_2O_3 is studied in the present work. Among all catalysts, Rh/Ce-ZrO_2 (5 wt % Rh) provides relatively higher reforming reactivity (in terms of ULO conversion and H_2 yield) with excellent resistance toward carbon deposition compared to the other three catalysts. At 850 °C after exposure in the steam reforming condition for 72 h, H_2 yield of 78.1% can be achieved from the reaction over Rh/Ce-ZrO_2. For Ni/Ce-ZrO_2 and Ni/Al_2O_3, significant deactivations with time are detected and H_2 yields of 55.3−58.7% are achieved after exposure for 72 h; in addition, considerable amounts of C_2H_4, C_2H_6 and C_3H_6 are also found in the product along with H_2, CO, CO_2, and CH_4. The effect of O_2 addition was further studied over Ni/Ce-ZrO_2 and Ni/Al_2O_3. It was found that this addition significantly reduces the degree of carbon deposition as well as promoting the conversion of hydrocarbons to CO and H_2. At a suitable amount of O_2, a high H_2 yield comparable to that of steam reforming over Rh-based catalysts can be achieved. Nevertheless, it must be noted that introducing too high an O_2 content resulted in lower H_2 production due to the combustion of H_2 and ULO by O_2 addition.

Introduction

Hydrogen-rich gas or synthesis gas is one of the promising clean fuels for the near future. Currently, the main existing process for synthesis gas production is catalytic steam reforming and partial oxidation of various hydrocarbons, e.g., natural gas, ethanol, methanol, and oils. Nevertheless, the use of these hydrocarbon feedstocks for hydrogen production always faces high competition for utilization with several applications, e.g., for petrochemical feedstock or for transportation fuel. On this basis, the production of hydrogen from wastes has great benefit in terms of energy and environmental aspects. Used lubricating oil (ULO) is known as an important hazardous waste that currently is generated in amounts more than 35 million tons from the industrial sector a year. It is one of the most serious materials for humans and the environment due to its toxicity and difficulty in management. It is classified as "F list designates", which is hazardous wastes from certain common industrial or manufacturing processes (wastes from nonspecific sources). Polychlorinated biphenyls (PCBs) and polycyclic aromatic hydrocarbons (PAHs) are main components in ULO; these compounds are highly toxic when released to the environment or contaminated in water, causing the obstruction of sunlight and oxygen from the atmosphere to water which consequently results in the harm to aquatic life. Considering these toxicities to the environment, the catalytic treatment of ULO to produce hydrogen would be a great promising technology for clean fuel generation and environmental treatment.

Recently, catalytic steam reforming of several hydrocarbons and oxygenated hydrocarbons, e.g., natural gas, LPG, methanol, acetic acid, ethanol, acetone, phenol, or cresol, has been widely investigated. In addition, in recent years, many researchers have also investigated the addition of oxygen together with steam in a single process, called autothermal reforming. By this combination, exothermic heat from the partial oxidation can directly supply the energy required for the endothermic steam reforming reaction. Therefore, it is considered to be thermally self-sustaining and consequently more attractive than steam reforming. However, the main disadvantage of this reaction is the lower production of synthesis gas (H_2 and CO) from this reaction compared to steam reforming. Currently, the general process for the production of hydrogen and synthesis gas is based on the steam reforming reaction using nickel-based catalyst. It is noted that worldwide efforts are in progress to explore a novel catalyst with higher activity and stability for the reforming reactions. Various precious metals such as Pt, Rh, and Ru have been reported to be active for the reforming reactions and resistant to the carbon formation. However, the current prices of these metals are very high for commercial uses, and the availability of some precious metals such as ruthenium was too low to have a major impact on the total reforming catalyst market. It should also be noted that selection of catalyst support material is an important issue as there was evidence that metal catalysts are not very active when supported on inert oxides.[1] Various supports have been investigated, for example, α-Al_2O_3, γ-Al_2O_3, and γ-Al_2O_3 with alkali metal oxide and rare earth metal oxide, $CaAl_2O_4$ and Ce-ZrO_2. A promising catalyst system for the reforming reactions appeared to be a metal on Ce-ZrO_2 support, where the metal can be Ni, Pt, or Pd.[2–9]

The aim of the present work is to develop the reforming catalysts that can convert ULO to hydrogen with high reforming activity and great resistance toward carbon formation. For economy, Ni was applied as a catalyst rather than precious metals such as Pt, Rh, and Ru, although it is more sensitive to carbon formation. Ni/Ce-ZrO_2 was selected as primary catalyst; its reforming performances were compared to conventional Ni/Al_2O_3. In addition, for comparison, Rh/Ce-ZrO_2 and Rh/Al_2O_3

* To whom correspondence should be addressed. Tel.: +66 2 8729014. Fax: +66 2 8726736. E-mail: navadol_l@jgsee.kmutt.ac.th.
[†] King Mongkut's University of Technology North Bangkok.
[‡] Mahidol University.
[§] Chulalongkorn University.
[||] King Mongkut's University of Technology Thonburi.

10.1021/ie1004288
Published on Web 06/25/2010

Table 1. Physical Properties of Synthesized Catalysts

catalyst	specific surface area (m^2g^{-1})	metal loading (%wt)	catalyst reducibility (%)	metal dispersion (%)
$Rh/Ce\text{-}ZrO_2$	36.7	5.0	89.4	4.2
Rh/Al_2O_3	42.3	4.9	94.5	4.4
$Ni/Ce\text{-}ZrO_2$	38.1	5.1	91.3	4.8
Ni/Al_2O_3	45.0	5.0	94.9	4.9

were also tested as the reforming catalysts; their steam and autothermal reforming reactivity were carried out compared to Ni-based catalysts.

Experimental Methodology

Catalyst Preparations and Characterizations. $Ce_{1-x}Zr_xO_2$ was prepared by coprecipitation of cerium nitrate ($Ce(NO_3)_3 \cdot H_2O$), and zirconium oxychloride ($ZrOCl_2 \cdot H_2O$) (from Aldrich). It should be noted according to our previous publication[10] that $Ce_{1-x}Zr_xO_2$ with Ce/Zr molar ratio of 3/1 showed the best performance in terms of steam reforming activity and stability, therefore, the ratio between each metal salt that provides nominal Ce/Zr molar ratio of 3/1 was used in the present work. The starting solution was prepared by mixing 0.1 M of metal salt solution with 0.4 M of urea at a 2 to 1 volumetric ratio. This solution was stirred by magnetic stirring (100 rpm) for 3 h, and the precipitate was filtered and washed with deionized water and ethanol to prevent an agglomeration of the particles. The precipitate was dried overnight in an oven at 110 °C, and then calcined in air at 900 °C for 6 h.

$Rh/Ce\text{-}ZrO_2$ and $Ni/Ce\text{-}ZrO_2$ were prepared by dry impregnating $Ce\text{-}ZrO_2$ with $Rh(NO_3)_2$ and $Ni(NO_3)_2$ solutions (from Aldrich). The catalyst was reduced with $10\%H_2/Ar$ at 500 °C for 6 h before use. For comparison, Rh/Al_2O_3 and Ni/Al_2O_3 were also prepared by impregnating γ-Al_2O_3 (from Aldrich) with $Rh(NO_3)_2$ and $Ni(NO_3)_2$. After reduction, the XRD study indicated the formation of crystalline phase over these synthesized catalysts. Furthermore, these catalysts were characterized with various physicochemical methods. The weight contents of Rh and Ni were determined by X-ray fluorescence (XRF) analysis. The reducibility percentage of rhodium was measured and calculated from the degree of H_2 uptake from the temperature-programmed reduction (TPR) test using 5% H_2 with a total flow rate of 100 cm^3 min^{-1} and temperature from room temperature to 500 °C, whereas the dispersion percentage of rhodium was identified from the volumetric H_2 chemisorption measurement using a chemisorption analyzer. The catalyst specific surface areas were obtained from BET measurement. All physicochemical properties of the synthesized catalysts are presented in Table 1.

According to these characterization results, the metal loadings are closed to 5 wt % as initially prepared, which indicates insignificant loss of metals during preparation. Furthermore, high catalyst reducibility and metal dispersion can be achieved for all synthesized catalysts. It is noted that the catalyst reducibility and metal dispersion are known to be important parameters for determining the catalyst activity; the good catalyst should have a high portion of reduced-form metal (i.e., Ni and Rh) compared to oxidized-form metal (i.e., NiO and RhO) as well as high dispersion of these metals on the surface of the support.

Apparatus and Procedures. To investigate the steam reforming of ULO and its associated reactions, an experimental reactor system was constructed. It is noted that the compositions of ULO used in the present work are 82.8% C, 15.2% H, 0.9% N, 0.53% O, and 0.57% S according to the ultimate analysis. The feed gases including the components of interest such as ULO, H_2O, helium, and O_2 were introduced to the reaction section, in which an 8-mm i.d. and 40-cm length quartz reactor was mounted vertically inside a furnace. The catalyst was loaded in the quartz reactor, which was packed with a small amount of quartz wool to prevent the catalyst from moving. Regarding the results in our previous publications,[10,11] to avoid any limitations by external mass transfer, the total gas flow was 1000 cm^3 min^{-1} under a constant residence time of 5×10^{-4} g min cm^{-3} in all experiments. A Type-K thermocouple was placed into the annular space between the reactor and the furnace. This thermocouple was mounted on the tubular reactor in close contact with the catalyst bed to minimize the temperature difference between the catalyst bed and the thermocouple. Another Type-K thermocouple was inserted in the middle of the quartz tube to recheck the possible temperature gradient, especially when O_2 was added along with ULO and H_2O as the autothermal reforming. The record showed that the maximum temperature fluctuation during the reaction never exceeded ±1.90 °C from the temperature specified for the reaction. After the reactions, the exit gas mixture was transferred via trace-heated lines to the analysis section, which consisted of a Porapak Q column Shimadzu 14B gas chromatograph (GC) and a mass spectrometer (MS).

To study the formation of carbon species on catalyst surface, temperature programmed oxidation (TPO) was applied by introducing 10% O_2 in helium, after purging the system with helium. The operating temperature increased from 100 to 1000 °C at a rate of 20 °C min^{-1}. The amounts of carbon formation (mmol g_{cat}^{-1}) on the surface of catalysts were determined by measuring the CO and CO_2 yields from the TPO results (using Microcal Origin Software). In the present work, the reactivity was defined in terms of conversion and product distribution. The yield of H_2 production was calculated by hydrogen balance, defined as molar fraction of H_2 produced to total H_2 in the products. Distributions of other byproduct selectivities (e.g., CO, CO_2, CH_4, C_2H_4, C_2H_6, and C_3H_6) were calculated by carbon balance, defined as ratios of each mole of product to the moles of hydrocarbons in the product gas, accounting for stoichiometry; this information was presented in terms of (relative) fractions of these byproduct components, which are summed to 100%.

Results and Discussions

Reactivity toward the Steam Reforming of ULO. The catalytic steam reforming reactions over several catalysts were carried out under atmospheric pressure at 850 °C with H_2O/C ratio of 3. Figure 1 shows conversion of ULO (calculated by the carbon balance assumption), H_2 production, and carbon formation of all the catalysts after exposure in the steam reforming condition for 72 h.

It can be seen that the initial conversion for all catalysts is above 90%, while H_2 yields are in the ranges of 71.6−72.4% and 82.9−84.3% over Ni- and Rh-based catalysts, respectively. After 72 h of operation, H_2 yields drop by 19−22% over Ni-based catalysts and 7−10% over Rh-based catalysts. The deactivation is mainly related to the formation of carbon species on the surface of catalysts. After exposure to ULO steam reforming for 72 h, coke formation was investigated by TPO

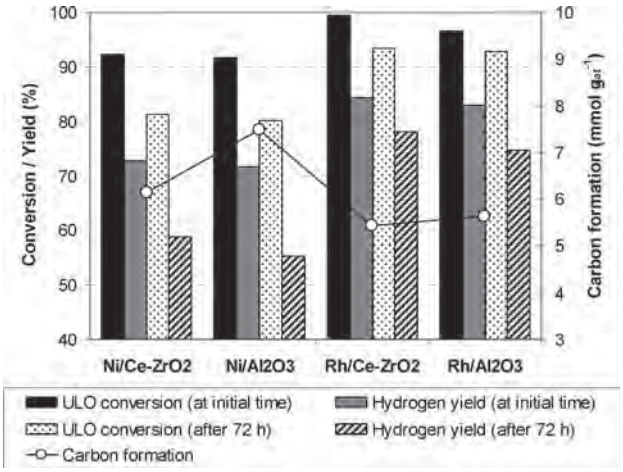

Figure 1. Effect of catalysts on ULO conversion, H_2 % yield, and carbon formation after exposure under steam reforming at 850 °C (with H_2O/C ratio of 3 for 72 h).

Table 2. Gaseous Byproduct Selectivities from the Steam Reforming of ULO at 850 °C (With H_2O/C Ratio of 3 for 72 h)

	gaseous byproduct selectivities (%)					
catalyst	CO	CO_2	CH_4	C_2H_4	C_2H_6	C_3H_6
$Rh/CeZrO_2$	21.7	37.9	32.2	6.5	3.9	2.8
Rh/Al_2O_3	23.9	32.6	27.4	14.4	4.1	2.6
$Ni/Ce\text{-}ZrO_2$	19.2	29.7	23.3	24.1	5.3	3.4
Ni/Al_2O_3	19.3	28.3	21.5	24.8	7.2	3.9

and was found to occur in all cases. The results show that $Rh/Ce\text{-}ZrO_2$ gave the best carbon formation resistance toward steam reforming whereas Ni/Al_2O_3 gave the least resistance (5.4 and 7.5 mmol/g-catalyst, respectively). Considering the gaseous product distribution, along with H_2 generated, CO and CO_2 as well as the light hydrocarbons (i.e., CH_4, C_2H_4, C_2H_6, and C_3H_6) were also observed in the product gas with different contents depending on the catalyst used, as presented in Table 2. It can be seen that relatively higher formation of hydrocarbons with less production of H_2, CO, and CO_2 was observed from Ni-based catalysts, particularly Ni/Al_2O_3, compared to Rh-based catalysts.

According to the mechanistic viewpoint, the overall reactions involved in the steam reforming of ULO are complex. At such a high operating temperature, the thermal decomposition of ULO takes place producing several gaseous products as well as coke from the following reaction:

$$C_xH_yO_z \rightarrow \text{gases}(H_2, CO, CO_2, C_nH_m) + \text{coke} \quad (1)$$

When steam is introduced, the catalytic steam reforming of hydrocarbons (C_nH_m) occurs along with some side-reactions (e.g., water gas shift reaction and methanation).

$$C_nH_m + nH_2O \rightarrow nCO + (n + 0.5\,m)H_2 \quad (2)$$

$$nCO + nH_2O \rightarrow nCO_2 + nH_2 \quad (3)$$

$$nCO + 3nH_2 \rightarrow nCH_4 + nH_2O \quad (4)$$

$$nCO_2 + 4nH_2 \rightarrow nCH_4 + 2nH_2O \quad (5)$$

The generations of saturated and unsaturated C_{2+} hydrocarbons (e.g., ethylene and ethane) are the major difficulties for the catalytic steam reforming, as these components act as very strong promoters for carbon formation. Based on these studies, it can be indicated that Rh-based catalysts efficiently convert

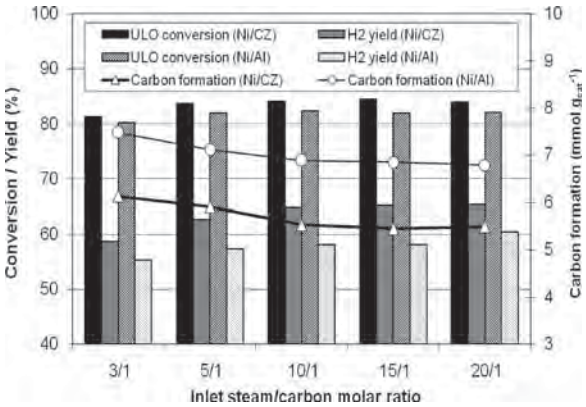

Figure 2. Effect of steam to carbon ratio over $Ni-Al_2O_3$ and $Ni-Ce/ZrO_2$ toward steam reforming at 850 °C in terms of ULO conversion, H_2 % yield, and carbon formation

ULO to H_2 with less formation of hydrocarbon byproduct compared to Ni-based catalysts. Rh is well-known as the most active catalyst toward several types of steam reforming reactions and also exhibits the highest resistance toward deactivation by carbon formation.[12] On comparison of supports, it was found that Ce/ZrO_2 gave higher ULO conversion and higher H_2 % yield compared to Al_2O_3 due to its higher oxygen storage capacity (OSC).[13] It is noted according to our studies that the OSC values over $Rh/Ce\text{-}ZrO_2$ and $Ni/Ce\text{-}ZrO_2$ (determined by the TPR) are 2539−2572 μmol g_{cat}^{-1}, which are close to the OSC of $Ce\text{-}ZrO_2$ (2649 μmol g_{cat}^{-1}). In general, $Ce\text{-}ZrO_2$ and Rh render better coke resistance; the former provides higher OSC, which is crucial for combustion of deposited coke, while the latter is well known to provide high resistance toward carbon formation during the reforming of hydrocarbons.

Effect of Steam to Carbon Ratio. The steam to carbon (H_2O/C) ratio was varied in the range of 3:1 to 20:1 to investigate its effect on catalytic performance over $Ni-Al_2O_3$ and $Ni-Ce/ZrO_2$. The H_2O/C ratio was maintained at ratios of 3, 5, 10, 15, and 20. Again, ULO conversion, H_2 production, and carbon deposition after exposure were observed over Ni-doped catalysts toward steam reforming of ULO at 850 °C under atmospheric pressure as shown in Figure 2. For both catalysts, the result shows that higher amounts of steam help to improve catalyst performance to a small degree. However, there was no significant difference for ULO conversions at all ratios of H_2O/C to produce 80−85% conversion. H_2 production was found to increase significantly with increasing H_2O/C ratio for both catalysts. This is presumably due to more H_2O molecules in the feed reactant stoichiometrically. Nevertheless, the amount of H_2 production at H_2O/C ratios higher than 10 showed no increase.

It was found that carbon formation decreases with increasing steam to carbon ratio. It might well be possible that increased quantities of oxygen were available. Among the same catalysts, the carbon formation started to drop and remained constant at steam to carbon ratios higher than 10 indicating that excess steam beyond this ratio did not improve coke resistance to ULO steam reforming. The optimal steam to carbon ratio for ULO steam reforming over $Ni-Al_2O_3$ and $Ni-Ce/ZrO_2$ is 10. At the same steam to carbon ratio, $Ni-Ce/ZrO_2$ showed better performance compared to $Ni-Al_2O_3$ regarding ULO conversion, H_2 % yield, and coke resistance possibly due to its higher OSC. It should be noted that the use of high H_2O/C ratio strongly affected the CO and CO_2 selectivities. The production of CO_2 increased gradually with increasing this ratio, whereas the production of CO decreased, which is mainly due to the effect

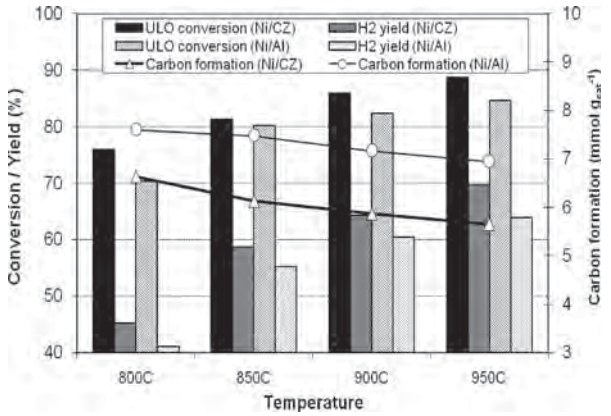

Figure 3. Effect of temperature over Ni−Al_2O_3 and Ni−Ce/ZrO_2 toward steam reforming (with H_2O/C ratio of 3) in terms of ULO conversion, H_2 % yield, and carbon formation

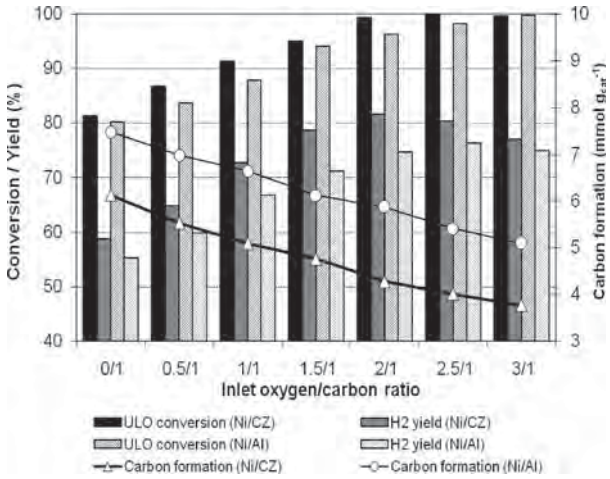

Figure 4. Effect of O_2 inlet to carbon ratio over Ni−Al_2O_3 and Ni−Ce/ZrO_2 toward steam reforming at 850 °C (with H_2O/C ratio of 3) in terms of ULO conversion, H_2 % yield, and carbon formation

of water gas shift reaction. Nevertheless, the H_2O/C ratio shows only slight impact on the CH_4, C_2H_4, C_2H_6, and C_3H_6 selectivities; significant amounts of these hydrocarbons remain even by using the inlet H_2O/C ratio of 20.

Effect of Temperature. The effects of operating temperatures on ULO steam reforming were studied over Ni-doped catalysts. The temperature was kept constant at 800, 850, 900, and 950 °C. Figure 3 shows ULO conversion, H_2 production, and carbon deposition after exposure of Ni−Ce/ZrO_2 and Ni−Al_2O_3 at different temperatures to ULO steam reforming. Both catalysts show some ULO conversion and H_2 % yields at low temperature. For instance, at 800 °C, ULO conversions of Ni−Ce/ZrO_2 and Ni−Al_2O_3 are 76 and 70, while their H_2 productions are 45 and 41% yield, respectively. Higher operating temperature improved ULO conversion and H_2 production. At temperature higher than 900 °C, the ULO conversions for both catalysts are higher than 80%. There is a large improvement in H_2 productions also as they turn out to be higher than 60% yield. The highest ULO conversion and H_2 % yield occurred in both catalysts at 950 °C. Carbon formation was found to decrease on increasing the temperature for both catalysts. The lowest carbon formation for both catalysts was detected at 950 °C at 5.7 and 7.0 mmol/g, respectively.

Apart from the benefits in terms of H_2 yield production improvement and carbon formation reduction, the use of high operating temperature also reduced the formation of hydrocarbons in the product gas. By increasing the operating temperature from 850 to 950 °C, the CH_4, C_2H_4, C_2H_6, and C_3H_6 selectivities from the steam reforming over Ni/Ce-ZrO_2 decreased from 23.3%, 24.1%, 5.3%, and 3.4% to 22.1%, 16.3%, 1.9%, and 0.1%, respectively. This is mainly due to the higher conversion of these hydrocarbons to H_2, CO, and CO_2 at high operating temperature.

Effect of Oxygen Addition. Lastly, the dependence of oxygen on the yield of hydrogen production over Ni/Ce-ZrO_2 was tested, as shown in Figure 4.

Figure 4 illustrates the effect of O_2 inlet to carbon ratio on ULO conversion, H_2 % yield, and carbon deposition of Ni-doped catalyst systems. It can be seen that the amount of carbon deposition linearly decreases with increasing O_2 adding content; nevertheless, the effect of oxygen addition on hydrogen yield is nonmonotonic. Hydrogen production yield was observed to increase with increasing O_2 partial pressures until a ratio of 2:1 and 2.5:1 was reached for Ni−Ce/ZrO_2 and Ni−Al_2O_3, respectively. Above that ratio, oxygen was found to negatively affect the hydrogen yield. At low O_2 addition, O_2 adding helps oxidizing the surface carbon species; hence, the steam reforming can occur efficiently and H_2 yield increases with increasing O_2 addition content. Nevertheless, by adding too much O_2, H_2 yield oppositely decreases, which could be due to the oxidation of ULO as well as H_2 to H_2O. Importantly, by adding O_2 along with the feed, the formation of hydrocarbons in the product gas can be reduced considerably. By adding O_2 at the inlet O_2/C ratio of 2, the CH_4, C_2H_4, C_2H_6, and C_3H_6 selectivities from the steam reforming over Ni/Ce-ZrO_2 decreased to 15.3%, 2.1%, 0.2%, and 0%, which could be due to the prevention of ULO thermal decomposition by adding O_2.

Conclusions

Rh/Ce-ZrO_2 exhibits excellent reactivity toward the steam reforming of ULO in terms of its high H_2 yield and a high resistance toward carbon deposition. It is predicted that Ce-ZrO_2 support plays an important role in improving the reforming performance due to its high oxygen storage capacity (OSC). Addition of O_2 with ULO and H_2O can reduce the degree of carbon deposition and promote the conversions of CH_4, C_2H_4, and C_2H_6 to CO and H_2. The major consideration was the suitable co-fed reactant/ULO ratio since the presence of too high an O_2 concentration could reduce the yield of H_2 production.

Acknowledgment

The financial support from The Thailand Research Fund (TRF) throughout this project is gratefully acknowledged.

Literature Cited

(1) Wang, X.; Gorte, R. J. A study of steam reforming of hydrocarbon fuels on Pd/ceria. *Appl. Catal., A* **2002**, *224*, 209.

(2) Martínez-Arias, A.; Coronado, J. M.; Cataluña, R.; Conesa, J. C.; Soria, J. Influence of Mutual Platinum-Dispersed Ceria Interactions on the Promoting Effect of Ceria for the CO Oxidation Reaction in a Pt/CeO_2/Al_2O_3 Catalyst. *J. Phys. Chem. B* **1998**, *102*, 4357.

(3) Skarmoutsos, D.; Tietz, F.; Nikolopoulos, P. Structure - property relationships of Ni/YSZ and Ni/(YSZ+TIO_2) cermet. *Fuel Cells* **2001**, *1*, 243.

(4) Takeguchi, T.; Furukawa, S. N.; Inoue, M. Hydrogen spillover from NiO to the large surface area CeO_2-ZrO_2 solid solutions and activity of the NiO/CeO_2-ZrO_2 catalysts for partial oxidation of methane. *J. Catal.* **2001**, *202*, 14.

(5) Sfeir, J.; Philippe, P. A.; Moseki, P.; Xanthopoulos, N.; Vasquez, R.; Hans, J. M.; Jan, V. H.; Thampi, K. R. Lanthanum chromite based catalysts for oxidation of methane directly on SOFC anodes. *J. Catal.* **2001**, *202*, 229.

(6) Mamak, M.; Coombs, N.; Ozin, G. Mesoporous Yttria-Zirconia and Metal-Yttria-Zirconia Solid Solutions for Fuel Cells. *Adv. Mater.* **2000**, *12*, 198.

(7) Mamak, M.; Coombs, N.; Ozin, G. Self-assembling solid oxide fuel cell materials: Mesoporous yttria-zirconia and metal-yttria-zirconia solid solutions. *J. Am. Chem. Soc.* **2000**, *122*, 8932.

(8) Mamak, M.; Coombs, N.; Ozin, G. A. AC Impedance Measurements on Mesoporous Nickel-Yttria-Zirconia Solid Oxide Fuel Cell Materials. *Chem. Mater.* **2001**, *13*, 3564.

(9) Bera, P.; Mitra, S.; Sampath, S.; Hegde, M. S. Promoting Effect of CeO_2 in a Cu/CeO_2 Catalyst: Lowering of Redox Potentials of Cu Species in the CeO_2 Matrix. *Chem. Commun.* **2001**, *10*, 927.

(10) Laosiripojana, N.; Chadwick, D.; Assabumrungrat, S. Effect of high surface area CeO_2 and $Ce\text{-}ZrO_2$ supports over Ni catalyst on CH_4 reforming with H_2O in the presence of O_2, H_2, and CO_2. *Chem. Eng. J.* **2008**, *138*, 264.

(11) Laosiripojana, N.; Assabumrungrat, S. Catalytic dry reforming of methane over high surface area ceria. *Appl. Catal., B* **2005**, *60*, 107.

(12) Rostrup-Nielsen, J. R.; Bak-Hansen, J.-H. CO_2-reforming of Methane over Transition Metals. *J. Catal.* **1993**, *144*, 38.

(13) Laosiripojana, N.; Assabumrungrat, S. Hydrogen Production from Steam and autothermal reforming of LPG over High Surface Area Ceria. *J. Power Sources* **2006**, *158*, 1348.

Received for review February 26, 2010
Revised manuscript received June 11, 2010
Accepted June 14, 2010

IE1004288

Appl Microbiol Biotechnol (2010) 86:1775–1784
DOI 10.1007/s00253-010-2465-y

BIOTECHNOLOGICAL PRODUCTS AND PROCESS ENGINEERING

Recombinant expression of BTA hydrolase in *Streptomyces rimosus* and catalytic analysis on polyesters by surface plasmon resonance

Nitat Sinsereekul · Thidarat Wangkam · Arinthip Thamchaipenet · Toemsak Srikhirin · Lily Eurwilaichitr · Verawat Champreda

Received: 6 November 2009 / Revised: 20 January 2010 / Accepted: 21 January 2010 / Published online: 20 February 2010

Abstract A recombinant polyester-degrading hydrolase from *Thermobifida* sp. BCC23166 targeting on aliphatic-aromatic copolyester (rTfH) was produced in *Streptomyces rimosus* R7. rTfH was expressed by induction with thiostrepton as a C-terminal His_6 fusion from the native gene sequence under the control of *tip*A promoter and purified from the culture supernatant to high homogeneity by a single step affinity purification on Ni-Sepharose matrix. The enzyme worked optimally at 50–55°C and showed esterase activity on C3-C16 *p*-nitrophenyl alkanoates with a specific activity of 76.5 U/mg on *p*-nitrophenyl palmitate. Study of rTfH catalysis on surface degradation of polyester films using surface plasmon resonance analysis revealed that the degradation rates were in the order of poly-ε-caprolactone >Ecoflex®>polyhydroxybutyrate. Efficient hydrolysis of Ecoflex® by rTfH was observed in mild alkaline conditions, with the highest activity at pH 8.0 and ionic strength at 250 mM sodium chloride, with the maximal specific activity of 0.79 $mg^{-1}min^{-1}mg^{-1}$ protein. Under the optimal conditions, rTfH showed a remarkable 110-time higher specific activity on Ecoflex® in comparison to a lipase from *Thermomyces lanuginosus*, while less difference in degradation efficiency of the two enzymes was observed on the aliphatic polyesters, suggesting greater specificities of rTfH to the aliphatic-aromatic copolyester. This study demonstrated the use of streptomycetes as an alternative expression system for production of the multi-polyester-degrading enzyme of actinomycete origin and provided insights on its catalytic properties on surface degradation contributing to further biotechnological application of this enzyme.

Keywords Aliphatic-aromatic copolyester · Ecoflex® · Hydrolase · *Streptomyces rimosus* · Surface plasmon resonance · *Thermobifida* sp.

N. Sinsereekul · A. Thamchaipenet
Department of Genetics, Faculty of Science, Kasetsart University, Chatuchak,
Bangkok 10900, Thailand

T. Wangkam · T. Srikhirin
Department of Physics, Center of Nanoscience and Nanotechnology, Faculty of Sciences, Mahidol University,
Bangkok 10400, Thailand

L. Eurwilaichitr · V. Champreda (✉)
Enzyme Technology Laboratory, Bioresources Technology Unit, National Center for Genetic Engineering and Biotechnology (BIOTEC),
113 Thailand Science Park, Paholyothin Road, Klong Luang, Pathumthani 12120, Thailand
e-mail: verawat@biotec.or.th

Introduction

Biodegradable plastics are promising alternative environmentally friendly materials which play increasing roles in a wide range of conventional and specialized plastic utilization. Continual development in this field has resulted in a diverse range of biodegradable plastics with properties comparable to those from petroleum origins. Polyester is one of the largest groups of biodegradable plastic with diversified physical and chemical properties, which can be either produced from biological or petrochemical origins (Luengo et al. 2003). Aliphatic polyesters, e.g., polyhydroxylakanoates (PHAs), poly-ε-caprolactone (PCL), and polybutylene succinate, are among the most extensively studied commercially promising aliphatic polyesters. These polyesters are completely degradable by microbial processes (Tokiwa and Calabia 2004). However, aliphatic poly-

esters exhibit disadvantages concerning their material properties, e.g., low tensile strength and melting points, which limit their commercial applications. In contrast, aromatic polyesters, e.g., poly(ethylene-terephthalate) (PET) and poly(butylene-terephthalate) have excellent material properties but are not degradable under natural conditions (Müller et al. 2001). Aliphatic-aromatic copolyesters have been developed with the combined biodegradable nature of aliphatic polyesters and practical material properties of the aromatic ones. Copolyesters based on a combination of 1,4-butanediol, terephthalic acid, and adipic acid (BTA) are potential biodegradable plastics based on their desirable material properties (Witt et al. 1997). A number of biodegradable plastics based on the BTA structure are now commercially available, e.g., Ecoflex® (BASF AG, Germany) and Eastar™ (Eastman, US).

Thermophilic actinomycetes are important organisms in the degradation of polyesters under high-temperature composting conditions. Diverse polyester degrading thermophilic actomonycetes have been isolated (Kalabia and Tokiwa 2004; Hoang et al. 2007; Phithakrotchanakoon et al. 2009a). *Thermobifida fusca* was isolated from compost and showed remarkable activities towards degradation of BTA and aliphatic polyesters *e.g.* PHAs (Kleeberg et al. 1998). Extracellular polyester degrading enzymes from this bacterium including BTA hydrolase and PHA depolymerase have been isolated and characterized (Gouda et al. 2002; Phithakrotchanakoon et al. 2009b). The BTA hydrolase (TfH) is a serine hydrolase which is active on degradation of BTA, PCL and even PET (Müller et al. 2005a). The enzyme is classified as a member of the lipase/esterase family with the catalytic behavior between a lipase and esterase, and has been proposed as a cutinase (Müller et al. 2005b). The genes for this enzyme are located on an operon containing two nearly identical genes (*bta*1 and *bta*2) encoding two enzyme homologues with 92% identity. In *T. fusca*, the enzyme is expressed only in the presence of its target polyesters and its level also depends on other phenomena, including enzyme adsorption and inhibition (Gouda et al. 2002). In order to avoid the complicated induction behavior in the wild type, recombinant expression systems have been developed for the production of BTA hydrolase in heterologous hosts, including as an OmpA fusion for secretion in *Escherichia coli* system (Dresler et al. 2006) and in *Bacillus megaterium* using a codon-optimized gene (Yang et al. 2006). These systems allow large-scale production of BTA hydrolase for biochemical characterization and further biotechnological applications, including polyester degradation and textile fiber pretreatment and modifications (Deckwer et al. 2001; Heumann et al. 2006).

Conventional catalysis activity analyses on bioplastic degradation have been based on a variety of mostly insensitive crude methods (reviewed in Jendrossek 2007). Currently, most studies on BTA hydrolase have been based on indirect activity analysis *e.g.* on PCL or synthetic small substrates while the catalytic study on BTA has been based on the assay of released degradation products from BTA nanoparticle and films in solution (Gouda et al. 2002; Kleeberg et al. 2005). Direct mass change determination of BTA hydrolase activity on surface degradation phenomenon of BTA thin films is of interest to provide complementary catalytic and biochemical characteristics of the enzyme. In this study, an alternative recombinant expression system has been developed in an actinomycete to avoid the problems of enzyme secretion and codon usage. This included the expression of the full-length *bta*1 gene with no codon optimization in *Streptomyces rimosus*. The catalytic activity and specificities of the recombinant hydrolase (rTfH) on surface degradation of a commercial BTA films (Ecoflex®) and aliphatic polyesters have been characterized in comparison to the lipase from *Thermomyces lanuginosus*, previously grouped together as "polyesterase" capable on aromatic polyester degradation (Eberl et al. 2008), using the recently introduced technique based on surface plasmon resonance analysis (Phithakrotchanakoon et al. 2009b). The effects of reaction parameters on rTfH catalysis have also been investigated. The study gives insights towards the understanding of the catalytic properties of this potent enzyme and its further biotechnological application.

Materials and methods

Materials

Poly-[*(R)*-3-hydroxybutyrate] (PHB) powder (natural origin; Mw 554,503 Da) and poly(ε-caprolactone) (PCL; Mw 175,693 Da) were purchased from Sigma-Aldrich, Germany. Ecoflex® (Mw 867,885 Da) was from BASF (Ludwidshafen, Germany). Lipase from *T. lanuginosus* was from Sigma-Aldrich. All reagents were analytical or molecular biology grade and purchased from major chemical suppliers.

Strains, plasmids, and culturing conditions

E. coli DH5α was used as a host for plasmid propagation. *E. coli* ET12567 (*dam*⁻, *dcm*⁻) containing pUZ8002 (MacNeil et al. 1992) was used as a donor strain for conjugation. *E. coli* strains were cultured in Luria–Burtani medium (1% tryptone, 0.5% yeast extract, 1% NaCl). *S. rimosus* R7 (ATCC10970; Hranueli et al. 1979) was maintained on mannitol soya agar (MS: 2% mannitol, 2% soya flour, 2% agar; Hobbs et al. 1989) and was

incubated for 3–5 d at 30°C. For submerged culture, *S. rimosus* was grown by inoculating the spore suspension (10^9–10^{10} spores/ml) at 1:100 dilution in tryptone soya broth (TSB; HiMedia Laboratories, Mumbai, India). The culture was incubated at 30°C with rotary shaking at 200 rpm. A thermophilic actinomycete, *Thermobifida* sp. BCC23166 was from the BIOTEC Culture Collection (www.biotec.or.th/bcc). This bacterium was isolated from a landfill site in Suphanburi province, Thailand based on the ability to form a clear zone on PHB suspended agar containing basal medium and identified as previously described (Phithakrotchanakoon et al. 2009b) The isolate was maintained on PHB suspended agar plate (Calabia and Tokiwa 2004). The conjugative vector pIJ8600 (Sun et al. 1999) was used for recombinant expression of the target enzyme in *S. rimosus*.

Construction of expression plasmid

Genomic DNA of *Thermobifida* sp. BCC23166 was extracted from cells grown on MS agar using phenol/chloroform extraction, followed by precipitation with isopropanol (Kieser et al. 2000). The purified DNA was used as a template for polymerase chain reaction for amplification of the complete *bta* gene, including the signal peptide encoding sequence using the primers designed based on the *bta*1 gene from *T. fusca* strain YX (GenBank accession number AJ810119). A His_6 encoding sequence was included in the reverse primer for expression of the enzyme as a C-terminal His_6 fusion protein. The amplification reaction (50 μl) contained 20 ng genomic DNA, 0.2 mM dNTPs, 0.5 μM BTA-F primer (5′-gcgccatatggctgtgatgacccccg-3′) and BTA-R primer (5′-atatggatcctca*gtggtggtggtgg tggtg*tgctgcgaacgggcaggt ggagcgg-3′) (the restriction sites for cloning and the His_6 tag sequence are underlined and shown in italics, respectively), and 0.5 *U* DyNAzyme DNA polymerase (Finnzymes, Espoo, Finland) in ×1 DyNAzyme buffer. The PCR conditions were as follows: pre-denaturation at 94°C, 4 min; 30 cycles of 94°C for 1 min, 55°C for 1 min, 74°C for 2 min; and 74°C for 10 min. Amplicons were gel-purified using a QIAquick Gel Extraction kit (QIAGEN, Hilden, Germany) and cloned into a TA-cloning vector, pTZ57R/T (Fermentas, Vilnius, Lithuania). Recombinant plasmids were DNA sequenced at Macrogen (Seoul, South Korea). The gene was then subcloned by digesting with *Nde*I and *Bam*HI and ligated with pIJ8600 digested with the same restriction enzymes. The ligation mixture was transformed into *E. coli* DH5α and screened for recombinant plasmid on LB agar containing apramycin (50 μg/ml). The resultant plasmid pIJ-BTA contained the *bta*1 gene fused in-frame to the downstream His_6 tag encoding sequence.

Plasmid transfer by intergeneric conjugation

The recombinant plasmid was transferred into *S. rimosus* R7 using intergeneric conjugation. For donor cell preparation, pIJ-BTA was transformed into a donor strain, *E. coli* ET12567 containing pUZ8002 by the conventional heat-shock method (Sambrook and Russell 1989). A single colony of *E. coli* strain containing pIJ-BTA was grown in 5 ml LB containing apramycin (50 μg/ml), chloramphenicol (25 μg/ml), and kanamycin (25 μg/ml) and incubated at 37°C with rotary shaking at 200 rpm overnight. The overnight culture was inoculated at 1:100 dilution into 100 ml of fresh LB medium containing the same antibiotics and incubated at 37°C until the absorbance at 600 nm reached 0.4–0.6; 1.5 ml of the cell culture was then collected and the cells washed twice with 0.5 ml LB before resuspension in 0.5 ml of fresh LB medium. For preparation of recipient cells, a spore suspension of *S. rimosus* R7 (10^9–10^{10} spores/ml) was inoculated at 1:100 dilution in 5 ml TSB and incubated at 28°C with rotary shaking at 200 rpm for 24 h. The culture was then diluted at 10^{-3}–10^{-4} in 0.5 ml of TSB medium. For integeneric conjugation, 0.5 ml of the donor and recipient cells were mixed together and incubated at room temperature for 10 min. The cells were then harvested and resuspended in 0.2 ml TSB before spreading on tryptone soya agar (Oxoid, Hampshire, UK) supplemented with 10 mM $MgCl_2$. The culture was incubated at 30°C for 16–20 h before flooding with 1 ml of solution containing 1 mg/ml thiostrepton and 0.5 mg/ml nalidixic acid in water and further incubated for 7 days under the same conditions. The transconjugant grown on the plate was then subcultivated thrice in MS agar containing antibiotics as described above to obtain the stable recombinant *S. rimosus* strain.

Expression of rTfH

The *S. rimosus* transconjugant containing pIJ-BTA was grown in 50 ml TSB containing 25 μg/ml thiostrepton at 28°C with rotary shaking at 200 rpm. Thiostrepton (5 μl of 50 mg/ml stock solution) was sequentially added everyday during the incubation period for 7 days. The cells were then separated by centrifugation at 10,000×*g* for 10 min, and the supernatant was collected for further analysis of the recombinant protein.

Purification of rTfH

The recombinant enzyme with a C-terminal His_6 tag was purified from the culture supernatant (500 ml total volume) using a Ni-Sepharose Fast Flow column (GE-Healthcare Biosciences, Uppsala, Sweden) according to the manufacturer's protocol. The purified enzyme was desalted and

concentrated by ultrafiltration using an Amicon centrifugal unit, MWCO 10 kDa (Millipore, Billerica, MA) in 50 mM sodium phosphate buffer, pH 7.0. Protein expression and purification profiles were analyzed on SDS-PAGE and stained with Coomassie Brilliant Blue (Sambrook and Russell 1989). Western blot analysis was based on detection of the His_6 tag using an anti-His_6 antibody-linked with alkaline phosphatase (Invitrogen, Carlsbad, CA) as described previously (Phithakrotchanakoon et al. 2009b). Protein concentration was analyzed with Bio-Rad Protein Assay Reagent based on Bradford's method (Bio-Rad, Hercules, CA) using bovine serum albumin as the standard. Identification of the target protein was performed by analyzing the tryptic peptides using LC/MS/MS on a Finnigan LTQ Linear Ion Trap Mass Spectrometer (Thermo Electron, San Jose, CA). MS/MS spectra were searched using Biowork™ 3.3 software (Sequest algorithm) against the NCBI-nr database.

Esterase activity assay

The esterase activity of BTA hydrolase was analyzed from the initial rate of *p*-nitrophenolate formation based on the method modified from Schmidt-Dannert et al. 1994. The standard reaction (1 ml) contained 50 mM sodium phosphate buffer, pH 8.0, 2.5 mM of *p*-nitrophenyl palmitate (*p*NPP; or otherwise indicated) and an appropriate dilution of the purified enzyme. The reaction was incubated at 50°C in a temperature controlled spectrophotometer (Citra 404 equipped with a GBC Thermocell, GBC Scientific Equipment, Dandenong, Australia). The formation of *p*-nitrophenolate was determined by measuring the absorbance at 405 nm over a 5-min time course. Control reactions with no enzyme were included in all experiments to correct for non-enzymatic hydrolysis of substrates. The initial rate was calculated by least square analysis. One unit of the enzyme activity was defined as the amount of enzyme catalyzing the release of 1 μmole *p*-nitrophenolate per min. The reactions were performed in triplicate and the averages of the results were reported (SD<5%).

Surface plasmon resonance analysis

Surface plasmon resonance configuration

A Surface plasmon resonance spectroscope (SPR) was constructed by the Electro-optics laboratory, National Electronics and Computer Technology Center, Thailand. Polymer coated on gold substrate (gold thickness of 50 on 10 nm of chromium) was placed on the prism with index matching fluid. The flow cell contains seven channels; channels 1–6 were used as reaction chambers for enzyme degradation while one channel was used as the control channel. A flow rate of 2.0 μl/min pumped with a syringe pump over the sensor chip surface was used throughout this study.

Sensor chip preparation

Solutions of Ecoflex® and PCL were prepared by dissolving in chloroform. The dissolution of PHB was carried out in boiling chloroform. The polymer solutions were stirred overnight at room temperature. The gold substrates were cleaned with Piranha solution (H_2SO_4: H_2O_2=70:30) for 15 min, sonicated in water and followed by methanol immersion for 15 min, and then dried with nitrogen gas. Ecoflex®, PCL, and PHB were then coated on gold substrates with a spin coater (Model P6700D, Specialty Coating Systems, Indianapolis, IN). The polymer solution was deposited onto the substrate by centrifugation at 1,500 rpm for 60 s.

SPR data analysis

The running buffer (50 mM MOPS or sodium phosphate buffer, pH 8.0, or otherwise indicated) was injected over the multi-channel sensor chip at 2 μl/min in order to establish the baseline. BTA hydrolase at different dilutions, ranging from 4.5–0.0045 μg/ml in the same buffer was injected into the sample channel until the enzyme completely filled the reaction chamber. The flow was then stopped and the enzyme was incubated on the sensor surface for the time indicated. The degradation rate was determined from the sensogram based on the initial slope, assuming from system calibration that an SPR angle shift of 1 millidegree corresponds to a mass change of 1.05 ng/cm^2 (Phithakrotchanakoon et al. 2009b). The specific activity was calculated based on the system configuration of which the mass reduction of 1 ng/cm^2/min is equal to the specific activity of 44.4 $\mu g^{-1} min^{-1} mg^{-1}$ protein (using initial enzyme concentration of 0.45 μg/ml). The reactions with lipase from *T. lanuginosus* were performed using the same method as described above. All of the reactions were carried out at room temperature (25°C). A minimum of two replicates were performed for each experiment, with SD<5%.

Result

Construction of transconjugant *S. rimosus* containing pIJ-BTA

Thermobifida sp. BCC23166, was isolated initially from landfill for its capability on degradation of emulsified PHB

agar. The isolate was found to efficiently degrade Ecoflex® films in liquid basal salt medium within 2 days at 50°C under aerobic conditions, suggesting the presence of BTA hydrolase homologous to the previously reported TfH (Gouda et al. 2002). Amplification of the *bta* gene from the isolate using the primers designed based on the homologous *bta* gene from *T. fusca* strain YX resulted in amplification of a 1.0 kb DNA fragment. Sequencing of the amplicon showed 100% homology to the *bta*1 gene of the reference strain, covering the full-length gene including the native signal peptide. The gene was then ligated to pIJ8600 (Sun et al. 1999), which is an *E. coli–Streptomyces* shuttle vector, at the *Nde*I and *Bam*HI sites. The resultant plasmid, pIJ-BTA was transferred into the expression host *S. rimosus* using intergeneric conjugation. Ten transconjugants were selected after subcultivation of the transconjugants to eliminate non-transconjugant and *E. coli* background. As pIJ8600 is a non-replicative plasmid, incorporation of the recombinant gene is based on site-specific recombination between *att*P on the vector and *att*B sites on the bacterial chromosome (Sun et al. 1999). The presence of *bta* gene in all transconjugants was confirmed using PCR amplication of the target *bta* gene (1.0 kb) and the vector-encoded *tsr* gene (0.8 kb; data not shown).

Recombinant expression of rTfH

In this study, expression of the *bta* gene in the *S. rimosus* transconjugants was regulated under the control of *tip*A promoter, derived from a thiostrepton resistant gene. Heterologous expression of the target enzyme was studied after induction by thiostrepton for 7 days. The secretion of BTA hydrolase in the culture supernatant was analyzed by SDS-PAGE and western blot analysis using an antiHis$_6$ antibody, revealing an induction of the target enzyme with the corresponding size (29.38 kDa, without the signal peptide) in comparison to the non-induced transconjugant and the wild-type (non-conjugated) *S. rimosus* (Fig. 1a, b). The peptide was recognized by an antibody against His$_6$, indicating that it was in a C-terminally intact form. The bands of low molecular weight peptides with increased intensity in the induced transconjugants observed on the SDS-PAGE were not reacted with the antibody, suggesting that they were not the C-terminally truncated forms of the target enzyme; however, the identities of these peptides were not further investigated. The target enzyme was then purified to high homogeneity (>95% purity as determined from Coomassie Brilliant Blue staining) with a single step Ni-Sepharose affinity chromatography from the starting culture volume of 500 ml with the purification yield of 82.5%. Its identity was confirmed using LC/MS/MS analysis in which the peptide sequence showed 100% match to a triacyl glycerol lipase (BTA hydrolase) from *T. fusca* YX (P-value=7.54E-12; GenBank accession YP_288944.1). The purified recombinant BTA hydrolase rTfH was then used for subsequent study.

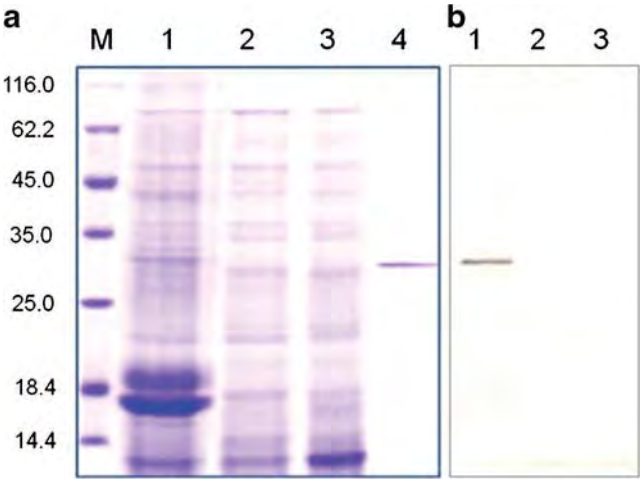

Fig. 1 Expression and purification of rTfH in *S. rimosus* transconjugant containing pIJ-BTA. **a** Protein profiles on SDS-PAGE. *Lane M*, protein molecular weight marker; *lane 1*, culture supernatant of *S. rimosus* transconjugant induced with thiostrepton; *lane 2*, non-induced *S. rimosus* transconjugant; *lane 3*, wild-type (non-conjugated) *S. rimosus*; *lane 4*, purified rTfH. **b** Western blot analysis using antiHis6 antibody. The lane labels are corresponded to A

Biochemical characterization of rTfH

The purified exhibited an optimal temperature range of 50–55°C and optimal pH in the mild basidic range based on the assay on *p*NPP (Fig. 2a, b). Substrate specificity of the enzyme was assayed on *p*-nitrophenyl alkanoates with different alkyl chain length (C4–C16). The enzyme showed esterase activity with preference towards short side chain *p*-nitrophenyl alkanoates with the highest activity on *p*-nitrophenyl butyrate (5.5-fold of that for *p*NPP), while significant activity on long chain alkanoates (myristate and palmitate) was also observed. The rTfH specific activity on *p*NPP was 76.5 U/mg under the assay conditions.

Surface plasmon resonance analysis

Degradation kinetics on different polyesters

To demonstrate the measurement of rTfH activity on different polyesters, different concentrations of rTfH were incubated over the sensor surface containing Ecoflex®, PCL, and PHB and the change in the reflectivity was measured at different angles. The angle shift corresponds to the reduction of the adsorbed polyester mass on the chip surface upon enzymatic degradation, which results in the alteration of the refractive index. The kinetics of polyester degradation by rTfH was monitored by recording the

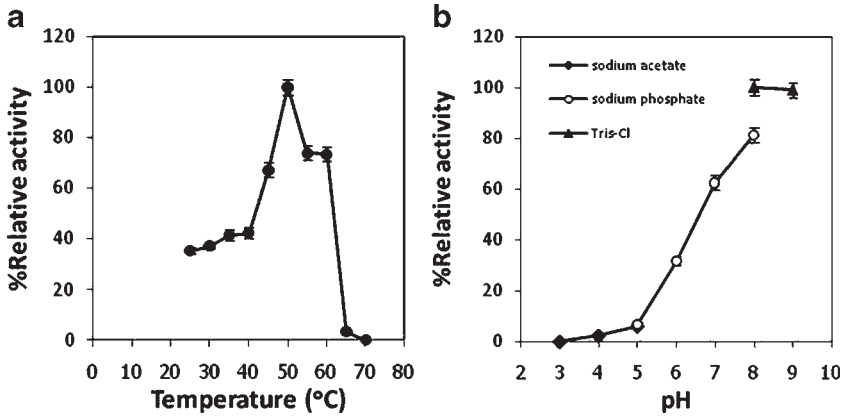

Fig. 2 Optimal working conditions of rTfH. The reaction contained an appropriate dilution of rTfH with 2.5 mM *p*-nitrophenyl palmitate. **a** Temperature dependence in 50 mM sodium phosphate buffer, pH 8.0; **b** pH dependence at 50 °C. The activity at 50 °C and pH 8 (76.5 U/mg) represents 100% relative activity

change in the reflectivity at the linear range of the SPR curve as a function of time. Different concentrations of rTfH ranging from 4.5 to 0.0045 μg/ml were used under the initial conditions in 50 mM MOPS buffer, pH 8.0 based on Phithakrotchanakoon et al. (2009b) in order to determine the comparative catalytic activity and the limit of sensitivity on different polyesters (Fig. 3). After injection, the enzyme was incubated on the sensor surface for up to 120 min while the change of the SPR angle was recorded as a function of time. The rate of change of SPR angle was proportional to rTfH concentration, and no change was seen in the control indicating that autohydrolysis of the polyester films was negligible under the experimental conditions tested.

At the lowest enzyme concentration (0.0045 μg/ml), the SPR sensogram was poorly defined, whereas exponential decay was observed at higher concentrations (≥0.045 μg/ml). The degradation of polyesters can be quantified from the SPR sensograms. The degradation of polyesters was linear in the early phase (0–10 min) and the degradation rates were estimated at 2.0, 15.7, 1.8 $ng^{-1}cm^{-2}min^{-1}$ equivalent to 88.3, 698, and 80 $\mu g^{-1}min^{-1}$mg protein for Ecoflex®, PCL, and PHB, respectively, using rTfH at 0.45 μg/ml. The degradation rates declined thereafter for all polyesters. At the maximal enzyme concentration, continual PCL and PHB degradation was seen over the 120 min incubation period although the rate tended to decrease along the incubation. In contrast, degradation of Ecoflex® almost ceased after 60 min of incubation under identical conditions (data not shown). The differences in degradation rate and kinetics would reflect the differences in the relative crystalline/amorphous phases of different polyesters and the enzyme adsorption kinetics and catalysis on the polyester surface.

Effects of reaction parameters on Ecoflex® degradation

Further investigation was focused on the study of reaction conditions on degradation of Ecoflex®. The effect of pH on rTfH catalysis was studied in the pH range from 5–8 in sodium phosphate buffer while fixing the enzyme concentration at 0.45 μg/ml. Degradation kinetics were pH dependent and the enzyme worked optimally in the mild basidic pH range with the highest degradation rate at pH 8.0, equivalent to 2.49 $ng^{-1}cm^{-2}min^{-1}$, which was higher than the degradation rate in MOPS, pH 8.0 (Fig. 4). At pH 8.0, the catalytic activity was strongly affected by the buffer component, in which the highest activity was observed in sodium phosphate, which was 1.25 and 1.44 times higher than that in MOPS and Tris-HCl buffer, respectively. This suggested the effect of buffer components on rTfH catalysis or enzyme interaction with the polyester surface.

The effects of ionic strength on rTfH catalysis were also studied in different NaCl concentrations ranging from 0–1 M in 50 mM sodium phosphate buffer, pH 8.0. The degradation rate increased at low ionic strength with the optimal NaCl concentration at 250 mM and then decreased at higher NaCl concentration (Fig. 5). The highest degradation rate at the optimal conditions (pH 8.0 and 250 mM NaCl) was estimated at 17.9 $ng^{-1}cm^{-2}min^{-1}$, equivalent to the specific activity of 0.79 $mg^{-1}min^{-1}mg^{-1}$ protein.

Comparison of polyester degradation by rTfH and lipase from *T. lanuginosus*

The comparison of rTfH and the lipase from *T. lanuginosus* (Lipase LT) activities on degradation of different aliphatic

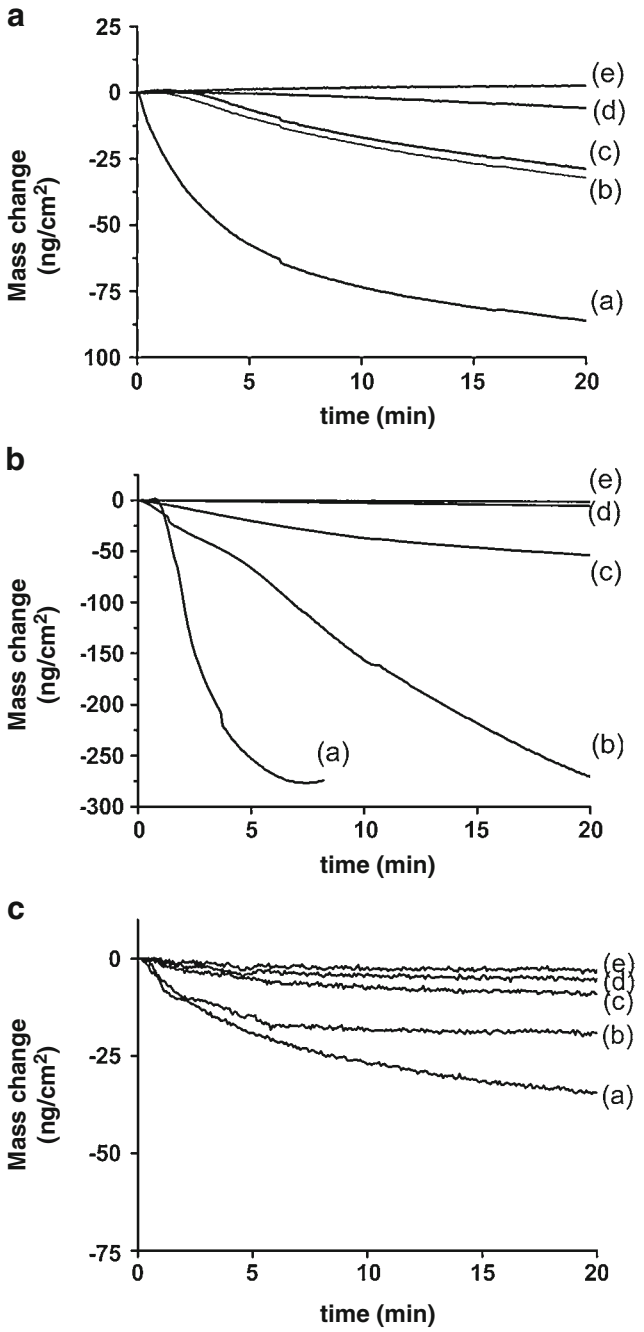

Fig. 3 SPR sensograms on degradation of polyesters at different rTfH concentration. The polymer thin films were incubated with different concentrations of rTfH in 50 mM MOPS buffer, pH 8.0. **a** Ecoflex®; **b** PCL; **c** PHB. rTfH concentration: *a* 4.5 μg/ml; *b* 0.45 μg/ml; *c* 0.22 μg/ml; *d* 0.045 μg/ml; *e* 0.0045 μg/ml

and aliphatic-aromatic polyesters is shown in Fig. 6. Lipase LT was relatively active on degradation of aliphatic polyesters with the specific activities of 0.80 and 0.21 $mg^{-1}min^{-1}mg^{-1}$ protein for PHB and PCL, respectively. However, the enzyme showed rather low specific activity on degradation of Ecoflex® (7.1 $\mu g^{-1}min^{-1}mg^{-1}$

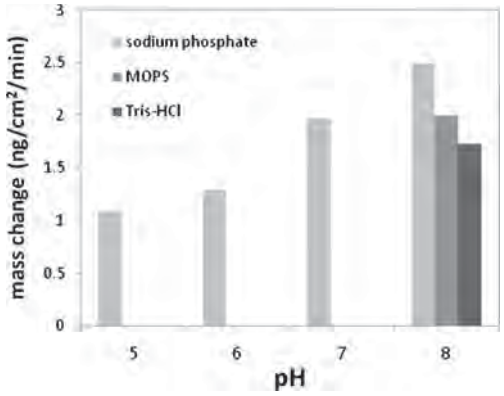

Fig. 4 Effects of pH on degradation of Ecoflex®. The polymer film was incubated with 0.45 μg/ml rTfH in 50 mM sodium phosphate (pH 5.0–8.0); MOPS (pH 8.0); and Tris-HCl (pH 8.0) for 10 min

protein). Obviously, a remarkable higher specific activity was shown for rTfH on Ecoflex® (0.79 $mg^{-1}min^{-1}mg^{-1}$ protein), which corresponded to 110 times higher degradation activity in comparison to that of Lipase LT while comparable activities was observed on PHB and only 17 times higher activity was observed on PCL. It can be clearly seen that rTfH displayed a marked higher catalytic and reaction specificities towards the aliphatic-aromatic copolyester Ecoflex® when compared to the lipase counterpart. The result thus implied significant differences on substrate specificities between these two enzymes.

Discussion

Study on microbial and enzymatic degradation of promising biodegradable polyesters is a key issue for their commercial application as well as their recycling. The *Thermobifida* BTA hydrolase has been reported as the first

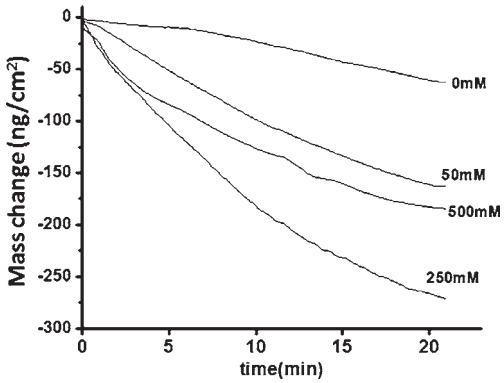

Fig. 5 Effects of ionic strength on degradation of Ecoflex®. The polymer film was incubated with 0.45 μg/ml rTfH in 50 mM sodium phosphate buffer, pH 8.0 containing 0–1 M sodium chloride for 10 min

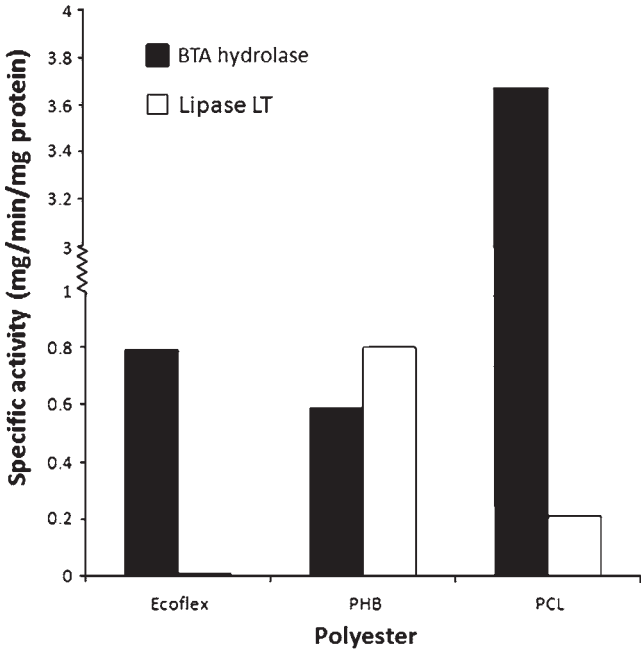

Fig. 6 Specific activity of rTfH and lipase from *T. lanuginosus* (Lipase LT) on different polyesters. The polymer thin films were incubated with 0.45 μg/ml enzyme in 50 mM sodium phosphate buffer, pH 8.0 and 250 mM NaCl for 10 min

enzyme efficiently attacking the commercial aliphatic-aromatic copolyester. The enzyme has been considered very potent for application on degradation of BTA and related polyesters, together with an interest on investigation on its biochemical mechanism and molecular characteristics for further engineering of the enzyme. Our initial trial on recombinant expression of BTA hydrolase as an intracellular mature form in *E. coli* and as a secreted form in *Pichia pastoris* resulted in no significant expression of the target enzyme (data not shown). In order to develop a system for production of BTA hydrolase for further study, development of a heterologous expression system in a phylogenetically related streptomycete was considered an attractive approach owing to compatible codon usage in actinomycetes and the nature of the strain on high level protein secretion (Vrancken and Anné 2009).

Streptomyces species are potential hosts for heterologous protein production (Beki et al. 2003; Díaz et al. 2008). This genus has been described for general usefulness and versatility as a host for the expression of bioactive proteins (Brawner et al. 1991; Gilbert et al. 1995). The application of streptomycetes system for heterologous expression has been increasingly reported with the development on more efficient gene transfer systems via intergeneric conjugation (Mazodier et al. 1989; Flett et al. 1997). Among streptomycetes expression systems, *S. rimosus* R7 was previously reported for expression of green fluorescent protein and was described as a reliable host for expression under the *tip*A promoter from plasmid pIJ8600 (Phornphisutthimas et al, unpublished data). In this work, we used *S. rimosus* R7 as an expression host for the target enzyme in order to take the advantage of its highly protein secretion nature and the similarity in codon usage, with C or G preferentially. Our results showed that the expression of the *bta*1 gene with a codon usage similar to *Streptomyces* clearly improved the probability of success. Compared to previous studies, our system allows production of rTFH from the full-length unmodified gene with no prior codon optimization (as for *B. megaterium* system; Yang et al. 2006) or gene modification by fusion to surface protein (as for *E. coli* system; Dresler et al. 2006). However, at this stage the initial yield of expression was rather low (0.058 mg/L) in comparison to those from the *E. coli* or *B. megaterium* systems. There have been several reports on yield improvement such as using alternative strong promoter (Díaz et al. 2008) for expression or morphological engineering to reduce viscosity and pellet formation, resulting in enhanced growth rates in batch fermentations (van Wezel et al. 2006). To our knowledge, this is the first report on heterologous expression of a bacterial bioplastic degrading enzyme in a streptomycete system and provides a promising alternative system for expression of heterologous bio-plastic degrading enzymes originated from actinomycetes, which might be difficult for expression in commonly used recombinant systems.

Specific activity of rTfH in this study was in the same range as those from previous reports based on the activity analysis on *p*-nitrophenyl alkanoate substrates (Dresler et al. 2006; Yang et al. 2006). However, the optimal working temperature of rTfH (50–55°C) differs significantly from that previously reported (65–70°C) (Gouda et al. 2002; Kleeberg et al. 2005), which may be due to the use of different substrates and assay techniques. The higher optimal temperatures were observed for the enzymes assayed with polymers in comparison to short chain *p*-nitrophenyl substrates. The apparent lower optimal temperature observed in this study would be due to the influence of temperature on the mobility of macromolecular polymer substrate, which resulted in increased temperature maximum (Marten et al. 2003). In addition, it would also be of interest to further explore the effect of polymer substrate on stabilization of the enzyme at high temperature, analogous to the protection effect of carbohydrate polymers on hydrolytic enzymes (Champreda et al. 2007). The pH dependence of rTfH based on SPR analysis agreed well with the optimal pH from spectroscopic assay using the *p*-nitrophenyl substrate. The pH optimum of rTfH in this study was similar to that previously reported by Gouda et al. 2002 in which a pH-stat titration technique on analysis of BTA nanoparticle degradation was used but slightly differed to the optimal pH reported for the purified enzyme

based on UV test (pH 6–7) (Kleeberg et al. 2005). This would be due to the effect of buffer concentration, reaction components, and ionic strength on the optimal enzyme working conditions as previously reported (Gouda et al. 2002; Kleeberg et al. 2005).

Application of the surface plasmon resonance technique to study hydrolysis of biodegradable plastic has been recently introduced for catalytic activity characterization of the PHB depolymerase from this *Thermobifida* strain based on direct substrate mass determination via optical property analysis (Phithakrotchanakoon et al. 2009b). In this work, using the SPR-based analytical technique, we demonstrated the substrate preference of rTfH on different aliphatic and aliphatic-aromatic polyesters in the order of PCL>Ecoflex®>PHB. This would be due to (1) the specificities inherent in the enzyme structure which results in variation in binding (enzyme adsorption) kinetics and catalytic specificity on different polyesters; and (2) differences in the physicochemical property of substrates e.g. relative crystalline/amorphous content. The specific activity on degradation of Ecoflex® with rTfH obtained in our study under the initial conditions (88.3 μg/min/mg) was comparable to that of the purified wild-type BTA hydrolase on polybutyleneadipate SP4/6 nanoparticle determined by titration method (Eberl et al. 2008). Optimization of the reaction conditions led to a marked increase (9 times) on the enzyme's catalysis on Ecoflex®, resulting in the specific activity of 0.79 mg/min/mg protein under the optimal conditions. The reactivity of rTfH on PHB was different to that previously reported for the purified BTA hydrolase which was inactive on PHB degradation (Kleeberg et al. 2005). This could be due to differences on substrate film preparation methods and assay techniques. The catalytic activities of rTfH on polyesters tested in this study were higher compared to the previously reported activity of the recombinant PHB depolymerase from the *Thermobifida* strain on polyhydroxyalkanoates, which was in the range of 1.02 μg/min/mg protein at its optimal condition for polyhydroxybutyrate-co-valerate (Phithakrotchanakoon et al. 2009b).

Lipases are generally active on degradation of aliphatic polyester substrates and the polymer-related factors controlling its catalysis have been systematically investigated (Marten et al. 2003). BTA hydrolase has been shown to possess a unique catalysis behavior between a lipase and esterase based on its substrate specificities and activation mechanism, and previously proposed as a cutinase. However, this classification has been still questionable as mentioned by Kleeberg et al. (2005). Recent study has suggested that the BTA hydrolase and the lipase from *T. lanuginosus* together with few other serine hydrolases capable of aromatic polymer degradation constitute a so-called "polyesterases" group and cannot be classified into any distinct EC class of enzymes (Eberl et al. 2008). In comparison to the lipase from *T. lanuginosus*, rTfH showed efficient degradation efficiency on various polyester substrates with different structures and physicochemical properties and displayed remarkably higher reaction specificities towards degradation of the aliphatic-aromatic copolyester. The higher reaction specificities of rTfH on Ecoflex® was corresponded to the previous work showing higher efficiency of this enzyme on degradation of a linear aromatic polyester poly(trimethylene terephthalate) (PTT) in comparison to the lipase from *T. lanuginosus* (Eberl et al. 2008). Our recent analysis using sequence homology search revealed that BTA hydrolase showed high similarity (62% identities and 76% similarity) to a predicted lipase with putative diene lactone hydrolase function from *S. albus* J1074 (ZP_04702335), in addition to several lipases of acinomycete origins. Together with its specificities towards degradation of aromatic containing polyester substrates, this would suggest classification of the enzyme into a new subgroup in lipase/esterase family. However, further systematic analysis is needed.

In conclusion, an alternative recombinant expression system for the multi-polyester-degrading hydrolase from *Thermobifida* sp. has been reported in this study, which would be applicable on heterologous expression of bioplastic degrading enzymes of actinomycete origins. The catalytic activity, reaction kinetics, and substrate specificities of rTfH have been characterized using the sensitive SPR analytical technique focusing on the surface degradation phenomenon on polyester films providing complementary information on catalytic characteristics of this biotechnologically potent enzyme. Further application of the SPR technique on the study of rTfH catalysis and kinetics is of interest for elucidation of the enzyme's catalytic and mechanistic properties.

Acknowledgements This project was supported by the Thailand Research Fund (TRF). The authors would like to thank Dr. Phillip James Shaw for manuscript proofreading. N.S. was granted YSTP senior project studentship from NSTDA. T.W. was granted the Development and Promotion of Science and Technology Talents Project (DPST) Fund.

References

Beki E, Nagy I, Vanderleyden J, Jager S, Kiss L, Fulop L, Hornok L, Kukolya J (2003) Cloning and heterologous expression of a beta-D-mannosidase (EC 3.2.1.25)-encoding gene from *Thermobifida fusca* TM51. Appl Environ Microbiol 69:1944–1952

Brawner M, Poste G, Rosenberg M, Westpheling J (1991) *Streptomyces*: a host for heterologous gene expression. Curr Opin Biotechnol 2:674–681

Calabia BP, Tokiwa Y (2004) Microbial degradation of poly(D-3-hydroxybutyrate) by a new thermophilic streptomyces isolate. Biotechnol Lett 26:15–19

Champreda V, Kanokratana P, Sriprang R, Tanapongpipat S, Eurwilaichitr L (2007) Purification, biochemical characterization, and gene cloning of a new extracellular thermotolerant and glucose tolerant maltooligosaccharide forming α-amylase from an endophytic ascomycete *Fusicoccum* sp. BCC4124. Biosci Biotechnol Biochem 71:2010–2020

Deckwer W-D, Müller RJ, Van den Heuvel J, Kleeberg I (2001) Enzyme which cleaves ester groups and which is derived from *Thermomonospora fusca*. GBF patent W001123581A1

Díaz M, Ferreras E, Moreno R, Yepes A, Berenguer J, Santamaría R (2008) High-level overproduction of *Thermus* enzymes in *Streptomyces lividans*. Appl Microbiol Biotechnol 79:1001–1008

Dresler K, van den Heuvel J, Müller R-J, Deckwer W-D (2006) Production of a recombinant polyester-cleaving hydrolase from *Thermobifida fusca* in *Escherchia coli*. Bioprocess Biosys Eng 29:169–183

Eberl A, Heumann S, Kotek R, Kaufmann F, Mitsche S, Cavaco-Paulo A, Gübitz GM (2008) Enzymatic hydrolysis of polymers and oligomers. J Biotechnol 135:45–51

Flett F, Mersinias V, Smith CP (1997) High efficiency intergeneric conjugal transfer of plasmid DNA from *Escherichia coli* to methyl DNA-restricting streptomycetes. FEMS Microbiol Lett 135:223–229

Gilbert M, Morosoli R, Shareck F, Kluepfel D (1995) Production and secretion of proteins by streptomycetes. Crit Rev Biotechnol 15:13–39

Gouda MK, Kleeberg I, van den Heuvel J, Müller R-J, Deckwer W-D (2002) Production of a polyester degrading extracellular hydrolase from *Thermomonospora fusca*. Biotechnol Prog 18:927–934

Heumann S, Eberl A, Pobeheim H, Liebminger S, Fischer-Colbrie G, Almansa E, Cavaco-Paulo A, Gübitz GM (2006) New model substrates for enzyme hydrolyzing polyethyleneterepthalate and polyamide fibers. J Biochem Biophys Methods 69:89–99

Hoang K-C, Tseng M, Shu W-J (2007) Degradation of polyethylene succinate (PES) by a new thermophilic Microbispora strain. Biodegradation 18:333–342

Hobbs G, Frazer CM, Gardner DCJ, Cullum JA, Oliver SG (1989) Dispersed growth of *Streptomyces* in liquid culture. Appl Microbiol Biotechnol 31:272–277

Hranueli D, Pigac J, Vesligaj M (1979) Characterization and persistence if actinophage RP2 isolated from *Streptomyces rimosus* ATCC10970. J Gen Microbiol 114:295–303

Jendrossek D (2007) Peculiarities of PHA granules preparation and PHA depolymerase activity determination. Appl Microbiol Biotechnol 74:1186–1196

Kalabia BP, Tokiwa Y (2004) Microbial degradation of poly(D-3-hydroxybutyrate) by a new thermophilic *Streptomyces* isolate. Biotechnol Lett 26:15–19

Kieser T, Bibb MJ, Buttner MJ, Chater KF, Hopwood DA (2000) Practical *Streptomyces* Genetics. Society for General Microbiology, Reading UK

Kleeberg I, Hetz C, Kroppenstedt RM, Müller R-J, Deckwer W-D (1998) Biodegradation of aliphatic-aromatic copolyesters by *Thermomonospora fusca* and other thermophilic compost isolates. Appl Environ Microbiol 64:1731–1735

Kleeberg I, Welzel K, VandenHeuvel J, Müller R-J, Deckwer W-D (2005) Characterization of a new extracellular hydrolase from *Thermobifida fusca* degrading aliphatic-aromatic copolyesters. Biomacromolecules 6:262–270

Luengo JM, Garsia B, Sandoval A, Naharro G, Olivera ER (2003) Bioplastics from microorganisms. Curr Opin Microbiol 6:251–260

MacNeil DJ, Gewain KM, Ruby CL, Dezeny G, Gibbons PH, MacNeil T (1992) Analysis of *Streptomyces avermitilis* genes required for avermectin biosynthesis utilizing a novel integration vector. Gene 111:61–68

Marten E, Müller R-J, Deckwer W-D (2003) Studies on the enzymatic hydrolysis of polyesters I. Low molecular mass model esters and aliphatic polyesters. Polym Degrad Stab 80:485–501

Mazodier P, Petter R, Thompson C (1989) Intergeneric conjugation between *Escherichia coli* and *Streptomyces* species. J Bacteriol 171:3583–3585

Müller RJ, Kleeberg I, Deckwer W-D (2001) Biodegradation of polyesters containing aromatic constituents. J Biotechnol 86:87–95

Müller RJ, Schrader H, Profe J, Dresler K, Deckwer W-D (2005a) Enzymatic degradation of poly(ethylene terephthalate): rapid hydrolyse using a hydrolase from *T. fusca*. Macromol Rapid Commun 26:1400–1405

Müller I, Welzel K, VandenHeuvel J, Müller R-J, Deckwer WD (2005b) Characterization of a new extracellular hydrolase from *Thermobifida fusca* degrading aliphatic-aromatic copolyesters. Biomacromolecules 6:262–270

Phithakrotchanakoon C, Rudeekit Y, Tanapongpipat S, Leejakpai T, Aiba S, Noda I, Champreda V (2009a) Microbial degradation and physico-chemical alteration of polyhydroxyalkanoates by a thermophilic *Streptomyces* sp. Biologia 64:246–251

Phithakrotchanakoon C, Daduang R, Thamchaipenet A, Wangkam T, Srikhirin T, Eurwilaichitr L, Champreda V (2009b) Heterologous expression of polyhydroxyalkanoate depolymerase from *Thermobifida* sp. in *Pichia pastoris* and catalytic analysis by surface plasmon resonance. Appl Microbiol Biotechnol 82:131–140

Sambrook J, Russell DW (1989) Molecular cloning: a laboratory manual, 3rd edn. Cold Spring Harbor Laboratory, New York

Schmidt-Dannert C, Sztajer H, Stocklein W, Menge U, Schmid RD (1994) Screening, purification and properties of a thermophilic lipase from *Bacillus thermocatenulatus*. Biochim Biophys Acta 1214:43–53

Sun J, Kelemen GH, Fernandez-Abalos JM, Bibb MJ (1999) Green fluorescent protein as a receptor for spatial and temporal gene expression in Streptomyces coelicolor A3(2). Microbiology 145:2221–2227

Tokiwa Y, Calabia BP (2004) Degradation of microbial polyesters. Biotechnol Lett 26:1181–1189

van Wezel GP, Krabben P, Traag BA, Keijser BJF, Kerste R, Vijgenboom E, Heijnen JJ, Kraal B (2006) Unlocking *Streptomyces* spp. for use as sustainable industrial production platforms by morphological engineering. Appl Environ Microbiol 72:5283–5288

Vrancken K, Anné J (2009) Secretory production of recombinant proteins by *Streptomyces*. Future Microbiol 4:181–188

Witt U, Müller RJ, Deckwer WD (1997) Biodegradation behavior and material properties of aliphatic-aromatic polyesters of commercial importance. J Environ Polym Degrad 5:81–89

Yang Y, Malten M, Grote A, Jahn D, Deckwer W-D (2006) Codon optimized *Thermobifida fusca* hydrolase secreted by *Bacillus megaterium*. Biotechnol Bioeng 96:780–794

Catalysis Communications 12 (2010) 25–29

Contents lists available at ScienceDirect

Catalysis Communications

journal homepage: www.elsevier.com/locate/catcom

Catalytic activity of ultrafine $Ce_xGd_ySm_zO_2$ synthesized by metal organic complex method toward steam reforming of methane

A. Laobuthee [a,*], C. Veranitisagul [b], N. Koonsaeng [c], V. Bhavakul [d], N. Laosiripojana [e,*]

[a] Department of Materials Engineering, Faculty of Engineering, Kasetsart University, Thailand
[b] Department of Materials and Metallurgical Engineering, Faculty of Engineering, Rajamangala University of Technology Thanyaburi, Thailand
[c] Department of Chemistry, Faculty of Science, Kasetsart University, Thailand
[d] Department of Chemistry, Faculty of Science, King Mongkut's University of Technology Thonburi, Thailand
[e] The Joint Graduate School of Energy and Environment, CHE Center for Energy Technology and Environment, King Mongkut's University of Technology Thonburi, Thailand

ARTICLE INFO

Article history:
Received 6 May 2010
Received in revised form 4 August 2010
Accepted 5 August 2010
Available online 13 August 2010

Keywords:
CeO_2
Gd
Sm
Steam reforming
SOFC

ABSTRACT

$Ce_xGd_ySm_zO_2$ synthesized by metal organic complex method has useful methane steam reforming activity under moderate temperatures. This preparation technique offers materials with fluorite structure and ultrafine particle (having particle sizes less than 106.54 nm after calcined at 900 °C). Among the materials with various Ce/Gd/Sm ratios, $Ce_{0.8}Gd_{0.05}Sm_{0.15}O_2$ showed the highest reforming rate (102.9 $mol_{CH4}\ kg^{-1}\ h^{-1}$) compared to 23.1 $mol_{CH4}\ kg^{-1}\ h^{-1}$ observed over undoped-CeO_2. This good performance was proven to relate with the improvements of oxygen storage capacity (OSC) and lattice oxygen mobility by Sm- and Gd-doping, according to the temperature programmed reduction/temperature programmed oxidation (TPR/TPO) and $^{18}O/^{16}O$ isotope exchange studies.

1. Introduction

Cerium oxide (CeO_2) based material contains a high concentration of mobile oxygen vacancies, which act as local sources or sinks for oxygen involved in reactions taking place on its surface. These properties render CeO_2 very interesting for a wide range of catalytic applications [1–8]. Currently, one potential application of CeO_2-based material is in solid oxide fuel cell (SOFC) as an electrolyte material and an in-stack reforming catalyst (IIR-SOFC) [9,10]. In addition, successful development of a direct internal reforming (DIR-SOFC), in which the hydrocarbons are reformed internally at the CeO_2-based anode of SOFC, has also been proposed [11–16].

It has been well established that the reaction between lattice oxygen (O_O^x) on CeO_2 surface and CH_4 produces synthesis gas with H_2/CO ratio of two, according to the following reaction [17]:

$$CH_4 + O_O^x = 2H_2 + CO + V_{O}^{\bullet\bullet} + 2e' \quad (1)$$

$V_O^{\bullet\bullet}$ denotes as an oxygen vacancy with an effective charge 2^+. It was also demonstrated that the reactions of the reduced CeO_2 with CO_2 and/or H_2O produce CO and H_2 along with regenerate O_O^x (Eqs. 2–3) [18,19]:

$$V_{O}^{\bullet\bullet} + 2e' + CO_2 = O_O^x + CO \quad (2)$$

$$V_{O}^{\bullet\bullet} + 2e' + H_2O = O_O^x + H_2 \quad (3)$$

The great benefit of CeO_2-based catalysts for the reforming reactions is their high resistance toward carbon deposition compared to the conventional metal catalysts i.e. Ni [10]; however, the main weaknesses are its high deactivation due to the thermal sintering when operated at high temperature (e.g. above 900 °C) [20]. The doping of Gd and Sm to CeO_2, as Gd-CeO_2 (or CGO) and Sm-CeO_2, have been reported to improve the properties of CeO_2 and are now interested as materials for SOFC applications i.e. as oxygen-ion conducting electrolyte. Eguchi et al. [9] reported that the oxide-ion conductivity of Sm- and/or Gd-doped CeO_2 show the highest conductivity among several rare-earth-doped CeO_2. Furthermore, CGO has also been reported to improve the resistance toward thermal sintering [10]. In the present work, the co-doping of Gd and Sm over CeO_2 (as $Ce_xGd_ySm_zO_2$) was synthesized and tested toward the methane steam reforming reaction with an aim to later apply as the in-stack reforming catalyst in IIR-SOFC operation. The materials were prepared by a simple metal organic complex method, which offers

* Corresponding authors. Tel.: +66 2 872 9014; fax: +66 2 872 6736.
E-mail address: navadol_l@jgsee.kmutt.ac.th (N. Laosiripojana).

1566-7367/$ – see front matter © 2010 Elsevier B.V. All rights reserved.
doi:10.1016/j.catcom.2010.08.006

non-complicated and low operating temperature route to provide the high purity and homogeneity products. In detail, the rate of methane steam reforming reaction over these materials at various Sm/Gd/Ce ratios were studied; in addition, their resistance toward carbon formation, the degrees of oxygen storage capacity (OSC), and the lattice oxygen mobility were determined. Based on these results, the relation between the doping elements, the redox properties, and the reforming performance were identified.

2. Experimental

2.1. Catalyst preparations and characterizations

Cerium (III) nitrate hexahydrate [$Ce(NO_3)_3 \cdot 6H_2O$] and gadolinium (III) nitrate pentahydrate [$Gd(NO_3)_3 \cdot 5H_2O$] were purchased from Acros Organics. Samarium (III) nitrate hexahydrate [$Sm(NO_3)_3 \cdot 6H_2O$] was purchased from Sigma-Aldrich, Inc. Triethanolamine [TEA, $N(CH_2CH_2OH)_3$,] and propan-1-ol [$CH_3CH_2CH_2OH$] were obtained from Carlo Erba. The complexes were prepared by mixing these precursors with Ce/Gd/Sm molar ratios of 1.0:0:0, 0.8:0.1:0.1, 0.8:0.15:0.05, 0.8:0.05:0.15, 0.85:0.075:0.075, 0.85:0.1:0.05, 0.85:0.05:0.1, 0.85:0.15:0 and 0.85:0:0.15 with 80 ml of propan-1-ol (denoted as CeO_2, $Ce_{0.8}Gd_{0.1}Sm_{0.1}O_2$, $Ce_{0.8}Gd_{0.15}Sm_{0.05}O_2$, $Ce_{0.8}Gd_{0.05}Sm_{0.15}O_2$, $Ce_{0.85}Gd_{0.075}Sm_{0.075}O_2$, $Ce_{0.85}Gd_{0.1}Sm_{0.05}O_2$, $Ce_{0.85}Gd_{0.05}Sm_{0.1}O_2$, $Ce_{0.85}Gd_{0.15}O_2$ and $Ce_{0.85}Sm_{0.15}O_2$, respectively). TEA was added in the 1:1 molar ratio of metal ions to TEA. After mixing, the as-prepared transparent solution was distilled for 3 h to obtain the precipitates. The complexes were separated by evaporating propan-1-ol solvent under vacuum. The thermal decomposition of the obtained complexes was studied by simultaneous thermogravimetric/differential thermal analysis (Model TGA/SDTA 851e, Mettler Toledo).

Phase identification of the obtained powders was determined via X-ray diffraction analysis (XRD; Philips X-Pert-MPD X-ray diffractometer) operating at 40 kV/30 mA, using monochromated CuKα radiation, while the powder morphology was observed using a scanning electron microscope (SEM, XL30 series, Phillips). The specific surface areas (S_{BET}) of the powders were calculated by the Brunauer–Emmett–Teller (BET) equation on the basis of the nitrogen adsorption isotherms, obtained using a Micromeritics ASAP 2020 surface analyzer. It is noted that the samples were degassed at 350 °C under high vacuum for 20 h before measurements. The degrees of OSC and lattice oxygen mobility of these materials were determined by the temperature programmed reduction/temperature programmed oxidation (TRP/TPO) and $^{18}O/^{16}O$ isotope exchange methods. Details of these testing are given in Section 3.2.

2.2. Methane steam reforming testing

To study the steam reforming reaction, the components of interest (CH_4 and H_2O in helium) were fed to a quartz reactor filled with catalyst and mounted vertically inside a tubular furnace. The weight of catalyst loading was 50 mg, while a typical range of total gas flow was 20–200 $cm^3\ min^{-1}$ depending on the desired space velocity. A Type-K thermocouple was inserted in the middle of the quartz tube in order to measure the reaction temperature. After reaction, the gas mixture was transferred via trace-heated lines to a gas chromatograph (GC) with Porapak Q column and a mass spectrometer (MS). The post-reaction temperature programmed oxidation (TPO) was applied for studying the resistance toward carbon formation (performed by introducing 10% O_2 in helium into the system and increased the temperature to 900 °C). In addition, the amount of carbon deposition was also confirmed by the carbon balance calculating, which theoretically equals to the difference between the inlet carbon containing components (CH_4) and the outlet carbon containing components (CO, CH_4, and CO_2).

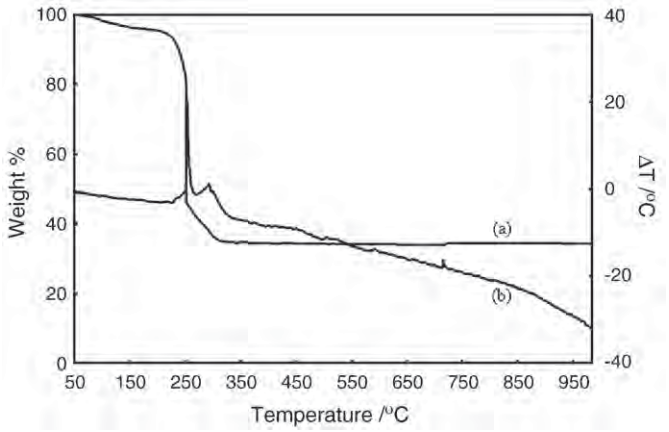

Fig. 1. Thermogram of $Ce_{0.8}Gd_{0.05}Sm_{0.15}O_2$: (a) TGA curve and (b) DTA curve.

3. Results and discussion

3.1. Catalyst characterizations

According to the thermal decomposition behavior studies, all obtained complexes exhibit the same pattern of TG/DTA thermograms. Fig. 1 shows the example of $Ce_{0.8}Gd_{0.05}Sm_{0.15}O_2$; the broad endothermic peak at low range of temperature on the DTA curve was mainly caused by the loss of physisorbed moisture and propan-1-ol, while the sharp exothermic peak with its maximum at 250 °C, accompanied by an abrupt weight loss in the TGA curve, was caused

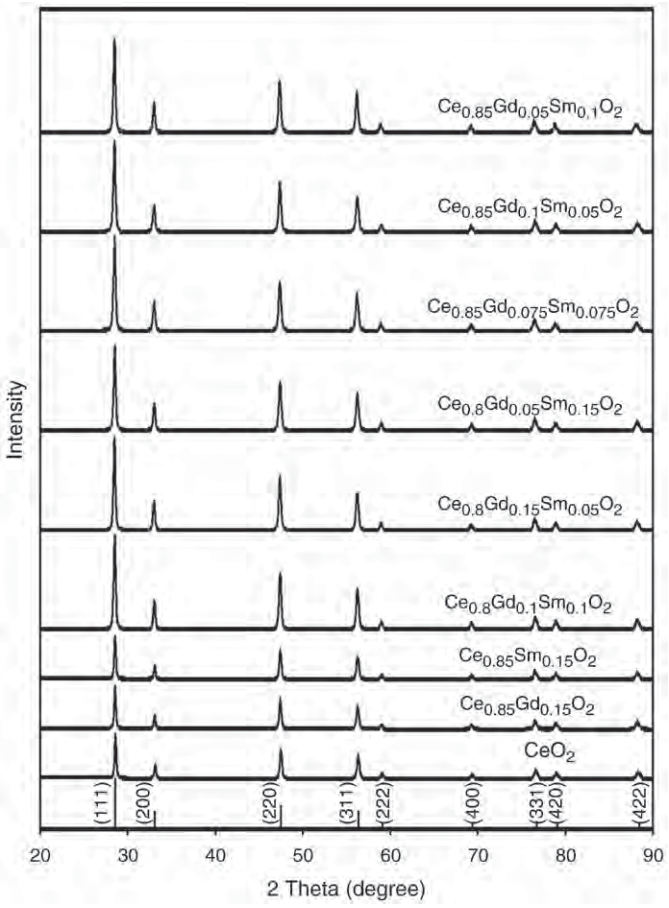

Fig. 2. XRD patterns of CeO_2 based materials calcined at 900 °C for 2 h.

Table 1
Specific surface areas of CeO_2 based materials after calcination at 900 °C for 2 h.

Sample	Specific surface area (m^2/g)
$Ce_{0.8}Gd_{0.1}Sm_{0.1}O_2$	9.5
$Ce_{0.8}Gd_{0.15}Sm_{0.05}O_2$	11.6
$Ce_{0.8}Gd_{0.05}Sm_{0.15}O_2$	10.3
$Ce_{0.85}Gd_{0.075}Sm_{0.075}O_2$	8.9
$Ce_{0.85}Gd_{0.1}Sm_{0.05}O_2$	9.7
$Ce_{0.85}Gd_{0.05}Sm_{0.1}O_2$	7.8
$Ce_{0.85}Gd_{0.15}O_2$	7.9
$Ce_{0.85}Sm_{0.15}O_2$	10.1
CeO_2	3.8

by the decomposition of the organic ligand and generated char as a by-product. A weight loss together with broad exothermic effects at 300–600 °C was ascribed to the burning of the residual organic components. Above 600 °C, no weight loss was observed, indicating that the appropriate calcination temperature is above 600 °C. Based on these TGA/SDTA results, all complexes were calcined at 900 °C prior the reaction testing. It is noted that the ceramic yields of all complexes were 30–35%.

Fig. 2 shows the XRD patterns for all $Ce_xGd_ySm_zO_2$ samples after calcined at 900 °C. Clearly, all compositions show the same pattern corresponding to the cubic fluorite structure of CeO_2 (JCPDS Powder Diffraction File No. 34-0394); furthermore, no crystalline phases corresponding to Gd_2O_3 and Sm_2O_3 were found. According to the BET measurements and the SEM micrographs of all samples (as presented in Table 1 and Fig. 3), the particle agglomeration occurs after calcination due to the thermal sintering. It was found that the specific surface area of $Ce_xGd_ySm_zO_2$ decreased from 95–107 $m^2 g^{-11}$ to 7.8–11.6 $m^2 g^{-1}$ after calcined at 900 °C, whereas that of commercial CeO_2 (from Aldrich) decreased from 55 $m^2 g^{-1}$ to 3.8 $m^2 g^{-1}$.

3.2. Measurements of oxygen storage capacity and lattice oxygen mobility

As described earlier, the OSC values of the synthesized materials was investigated by the TPR study, which was performed by heating the catalysts up to 900 °C with the heating rate of 10 °C min^{-1} in 5%H_2 (in helium) under the total flow rate of 100 cm^3 min^{-1}. The amount of hydrogen uptake is correlated to the amount of oxygen stored in the catalysts. As presented in Table 2, among all $Ce_xGd_ySm_zO_2$ samples, the amount of hydrogen uptake from $Ce_{0.8}Gd_{0.05}Sm_{0.15}O_2$ is the highest, suggesting its greatest OSC value. Furthermore, compared to the single Sm- and Gd-doping samples (i.e., $Ce_{0.85}Gd_{0.15}O_2$ and $Ce_{0.85}Sm_{0.15}O_2$), the amount of hydrogen uptake from $Ce_{0.8}Gd_{0.05}Sm_{0.15}O_2$ is significantly higher than $Ce_{0.85}Gd_{0.15}O_2$ and closed to that of $Ce_{0.85}Sm_{0.15}O_2$. After being purged the system with helium, the reversibility of OSC was determined by applying TPO following with the second time TPR

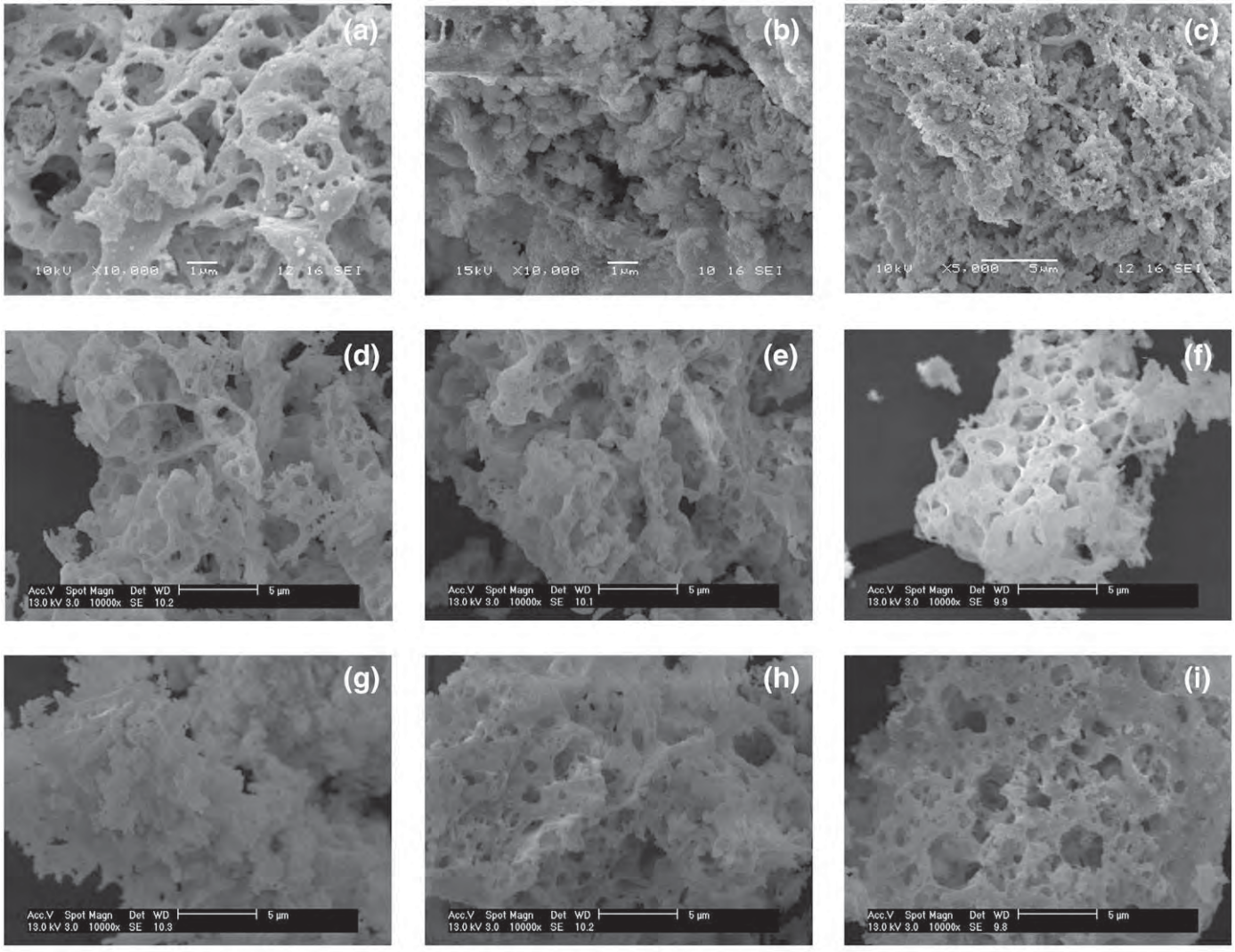

Fig. 3. SEM micrographs of (a) CeO_2, (b) $Ce_{0.85}Gd_{0.15}O_2$, (c) $Ce_{0.85}Sm_{0.15}O_2$, (d) $Ce_{0.8}Gd_{0.1}Sm_{0.1}O_2$, (e) $Ce_{0.8}Gd_{0.15}Sm_{0.05}O_2$, (f) $Ce_{0.8}Gd_{0.05}Sm_{0.15}O_2$, (g) $Ce_{0.85}Gd_{0.075}Sm_{0.075}O_2$, (h) $Ce_{0.85}Gd_{0.1}Sm_{0.05}O_2$, (i) $Ce_{0.85}Gd_{0.05}Sm_{0.1}O_2$ powders calcined at 900 °C for 2 h.

Table 2
Results of TPR-1, TPO, TPR-2 analyses of CeO_2-based materials after calcination.

Catalyst	Total H_2 uptake from TPR-1 ($\mu mol/g_{cat}$)	Total O_2 uptake from TPO ($\mu mol/g_{cat}$)	Total H_2 uptake from TPR-2 ($\mu mol/g_{cat}$)
$Ce_{0.8}Gd_{0.1}Sm_{0.1}O_2$	5203 (±14)[a]	2600 (±11)	5209 (±8)
$Ce_{0.8}Gd_{0.15}Sm_{0.05}O_2$	3176 (±19)	1532 (±17)	3170 (±9)
$Ce_{0.8}Gd_{0.05}Sm_{0.15}O_2$	5718 (±6)	2842 (±15)	5790 (±12)
$Ce_{0.85}Gd_{0.075}Sm_{0.075}O_2$	4227 (±22)	2109 (±8)	4210 (±15)
$Ce_{0.85}Gd_{0.1}Sm_{0.05}O_2$	2493 (±11)	1218 (±19)	2484 (±7)
$Ce_{0.85}Gd_{0.05}Sm_{0.1}O_2$	4679 (±19)	2311 (±25)	4680 (±13)
$Ce_{0.85}Gd_{0.15}O_2$	2107 (±7)	1059 (±16)	2092 (±10)
$Ce_{0.85}Sm_{0.15}O_2$	5769 (±15)	2881 (±3)	5714 (±9)
CeO_2	1709 (±12)	853 (±11)	1698 (±9)

[a] Deviation from the experiments.

(TPR-2). The TPO was carried out by heating the catalysts up to 900 °C with the heating rate of 10 °C min^{-1} in 10%O_2 (in helium) under the total flow rate of 100 cm^3 min^{-1}. As also reported in Table 2, the amounts of hydrogen uptake from TPR-2 were approximately identical to those of TPR-1, indicating the OSC reversibility of these materials.

The lattice oxygen mobility of these materials was then investigated by $^{18}O/^{16}O$ isotope exchange method. The sample (200 mg) was placed in the quartz reactor and thermally treated under high-purity helium (99.995%) flow (100 cm^3 min^{-1}) at the desired temperatures (300–600 °C) for 1 h. Then, $^{18}O_2$ (in helium as carrier gas) was multiply pulsed to the system and the outlet gases (i.e. $^{18}O_2$, $^{16}O_2$ and $^{18}O^{16}O$) were monitored by the MS. It can be seen from Table 3 that $Ce_{0.8}Gd_{0.05}Sm_{0.15}O_2$ shows the highest lattice oxygen mobility among all $Ce_xGd_ySm_zO_2$ samples. Furthermore, the results in this table also indicate that the homoexchange in gas phase is negligible due to the strong difference in $^{18}O^{16}O$ concentration over different samples ($^{18}O^{16}O$ concentration should be rather similarly if the exchange in gas phase is dominant the overall reaction [21]). It is noted that Fig. 4 shows the effect of temperature on $^{18}O_2$, $^{16}O_2$ and $^{18}O^{16}O$ concentrations over $Ce_{0.8}Gd_{0.05}Sm_{0.15}O_2$ compared to $Ce_{0.85}Gd_{0.15}O_2$ and CeO_2. Clearly, the conversion of $^{18}O_2$ increases with increasing temperature to form $^{16}O_2$ and $^{18}O^{16}O$ for all materials.

3.3. Activity toward methane steam reforming

Prior the catalyst testing, preliminary experiments to find the range of suitable operating conditions where the mass transfer effect is not predominant were carried out by varying the total gas flow rate between 10 and 200 cm^3 min^{-1} under a constant residence time of 5×10^{-4} g min cm^{-3}. It was found that the reforming rates were independent of the gas velocity when the gas flow rate was higher than 60 cm^3 min^{-1}, indicating the absence of external mass transfer effects at this high velocity. Therefore, the total flow rate was kept constant at 100 cm^3 min^{-1} in all studies.

Table 3
Results of $^{18}O/^{16}O$ isotope exchange for all CeO_2-based materials at 600 °C.

Catalyst	Outlet $^{18}O_2$ concentration (%)	Outlet $^{16}O_2$ concentration (%)	Outlet $^{18}O^{16}O$ concentration (%)
$Ce_{0.8}Gd_{0.1}Sm_{0.1}O_2$	63.4 (±1.3)[a]	21.3 (±1.0)	15.8 (±0.7)
$Ce_{0.8}Gd_{0.15}Sm_{0.05}O_2$	74.1 (±0.9)	16.2 (±0.7)	10.2 (±0.9)
$Ce_{0.8}Gd_{0.05}Sm_{0.15}O_2$	59.3 (±1.1)	22.8 (±0.5)	18.4 (±1.2)
$Ce_{0.85}Gd_{0.075}Sm_{0.075}O_2$	68.0 (±0.7)	17.9 (±0.9)	14.1 (±1.3)
$Ce_{0.85}Gd_{0.1}Sm_{0.05}O_2$	75.2 (±1.5)	15.1 (±0.2)	10.2 (±0.4)
$Ce_{0.85}Gd_{0.05}Sm_{0.1}O_2$	65.1 (±1.1)	20.3 (±1.4)	15.0 (±0.9)
$Ce_{0.85}Gd_{0.15}O_2$	81.5 (±1.7)	13.8 (±0.9)	6.9 (±0.2)
$Ce_{0.85}Sm_{0.15}O_2$	57.3 (±1.2)	24.8 (±0.6)	19.3 (±1.0)
CeO_2	86.4 (±1.8)	11.9 (±1.1)	2.1 (±0.8)

[a] Deviation from the experiments.

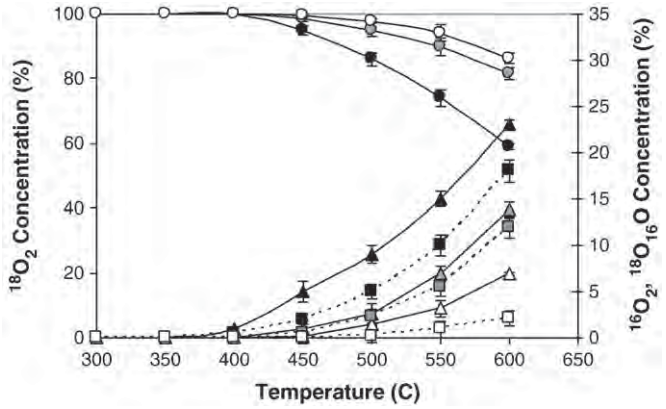

Fig. 4. $^{18}O/^{16}O$ isotope exchange over (i) $Ce_{0.8}Gd_{0.05}Sm_{0.15}O_2$ (●: $^{18}O_2$, ▲ : $^{16}O_2$ and ■: $^{18}O^{16}O$), (ii) $Ce_{0.85}Gd_{0.15}O_2$ (●: $^{18}O_2$, ▲: $^{16}O_2$ and ■: $^{18}O^{16}O$), and (iii) CeO_2 (○: $^{18}O_2$, △: $^{16}O_2$ and □: $^{18}O^{16}O$).

The methane steam reforming was then studied at 900 °C by feeding CH_4/H_2O in helium with the inlet CH_4/H_2O molar ratio of 1.0/1.0 to the catalytic system. It was found that the main products from the reaction over these CeO_2-based materials were H_2 and CO with some CO_2. The observed H_2/CO production ratios were higher than 3.0 in all conditions (Table 4) indicating a contribution from the water–gas shift reaction at this operating temperature. Fig. 5 shows the rate of methane steam reforming measured as a function of time. After 10 h of operation, $Ce_{0.8}Gd_{0.05}Sm_{0.15}O_2$ showed the highest reaction rate among all $Ce_xGd_ySm_zO_2$ samples (102.9 mol_{CH4} $kg^{-1}h^{-1}$). Compared to CeO_2, $Ce_{0.85}Gd_{0.15}O_2$ and $Ce_{0.85}Sm_{0.15}O_2$, the reaction rate of $Ce_{0.8}Gd_{0.05}Sm_{0.15}O_2$ is considerably higher than CeO_2 and $Ce_{0.85}Gd_{0.15}O_2$ but slightly lower than that of $Ce_{0.85}Sm_{0.15}O_2$. It was also found that the H_2/CO production ratios observed over $Ce_xGd_ySm_zO_2$, $Ce_{0.85}Gd_{0.15}O_2$ and $Ce_{0.85}Sm_{0.15}O_2$ are in the range of 4.4–4.9, whereas that observed over CeO_2 is 3.8; this indicates the higher contribution of the water–gas shift reaction by doping of Gd and Sm. After reaction, the post-reaction TPO was continuously carried out to determine the degree of carbon formation. The TPO detected small amount of carbon (between 0.03 and 0.18 mmol g_{cat}^{-1} for $Ce_{0.8}Gd_{0.1}Sm_{0.1}O_2$, $Ce_{0.8}Gd_{0.05}Sm_{0.15}O_2$, $Ce_{0.85}Gd_{0.075}Sm_{0.075}O_2$, $Ce_{0.85}Gd_{0.05}Sm_{0.1}O_2$, and $Ce_{0.85}Sm_{0.15}O_2$; and between 0.36 and 0.42 mmol g_{cat}^{-1} for $Ce_{0.8}Gd_{0.15}Sm_{0.05}O_2$, $Ce_{0.85}Gd_{0.1}Sm_{0.05}O_2$, $Ce_{0.85}Gd_{0.15}O_2$, and CeO_2), as presented in Table 4. It is noted that these values are relatively in good agreement with the values observed from the carbon balance calculation. It can be revealed from these TPO studies that the amount of carbon formation decreased as the Sm-doping content increased.

Table 4
Amount of carbon deposition, the changing in specific surface areas of CeO_2 based materials and H_2/CO production ratio after exposure in methane steam reforming at 900 °C for 16 h.

Catalyst	Amount of carbon ($mmol/g_{cat}$)	Specific surface area after reaction (m^2/g)	% Reduction of surface area	H_2/CO production ratio
$Ce_{0.8}Gd_{0.1}Sm_{0.1}O_2$	0.09[a] (0.08)[b]	8.9	5.8	4.7
$Ce_{0.8}Gd_{0.15}Sm_{0.05}O_2$	0.42 (0.43)	10.7	7.4	4.5
$Ce_{0.8}Gd_{0.05}Sm_{0.15}O_2$	0.03 (0.05)	9.8	5.4	4.9
$Ce_{0.85}Gd_{0.075}Sm_{0.075}O_2$	0.18 (0.17)	8.2	8.2	4.5
$Ce_{0.85}Gd_{0.1}Sm_{0.05}O_2$	0.36 (0.35)	9.0	7.5	4.4
$Ce_{0.85}Gd_{0.05}Sm_{0.1}O_2$	0.14 (0.15)	7.3	6.3	4.6
$Ce_{0.85}Gd_{0.15}O_2$	0.37 (0.41)	6.6	16.4	4.1
$Ce_{0.85}Sm_{0.15}O_2$	0.05 (0.05)	9.0	10.9	4.9
CeO_2	0.41 (0.39)	2.0	47.7	3.8

[a] Observed from TPO.
[b] Calculated from carbon balance.

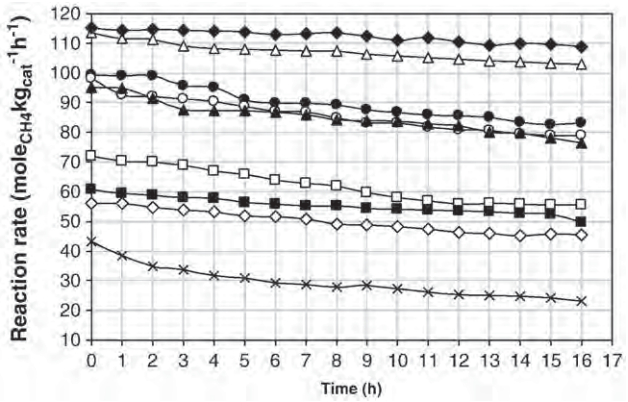

Fig. 5. The variation of reaction rate at 900 °C with CH_4/H_2O molar ratio of 1.0/1.0 over $Ce_{0.85}Sm_{0.15}O_2$ (♦), $Ce_{0.8}Gd_{0.05}Sm_{0.15}O_2$ (△), $Ce_{0.8}Gd_{0.1}Sm_{0.1}O_2$ (●), $Ce_{0.85}Gd_{0.05}Sm_{0.1}O_2$ (○), $Ce_{0.85}Gd_{0.075}Sm_{0.075}O_2$ (▲), $Ce_{0.8}Gd_{0.15}Sm_{0.05}O_2$ (□), $Ce_{0.85}Gd_{0.1}Sm_{0.05}O_2$ (■), $Ce_{0.85}Gd_{0.15}O_2$ (◊) and CeO_2 (×).

Previously, the redox mechanism was reported to explain the reforming behavior of CeO_2-based catalysts, from which the CH_4 reaction pathway for CeO_2-based materials involves the reaction between absorbed CH_4 (formed intermediate surface hydrocarbon species) with O_O^x at CeO_2 surface; and the steady state reforming rate is due to the continuous supply of the oxygen source by H_2O that reacted with the catalyst reduced state to recover O_O^x [22]. It can be seen from the results in Sections 3.2 and 3.3 that the improvements in steam reforming activity and resistance toward carbon deposition are closely related to the increasing in the degrees of OSC and lattice oxygen mobility by doping with Sm (and Gd). We suggested here that the great reforming activity for $Ce_{0.8}Gd_{0.05}Sm_{0.15}O_2$ could be due to the sufficient amount and high mobility of O_O^x on its surface, which promotes the reaction between O_O^x and CH_4 (Reaction (1)) since we have previously reported the strong dependence between the OSC and the steam and dry reforming activity of CeO_2-based catalysts [22]. Furthermore, He et al. [21] also suggested the strong relation between the oxygen mobility of CeO_2-based materials and their catalytic reactivity toward the conversion of automotive exhaust. Regarding the good resistance toward carbon deposition of $Ce_{0.8}Gd_{0.05}Sm_{0.15}O_2$, theoretically, the carbon formation during the reforming reaction occurs mainly from the Boudouard reaction ($2CO \Leftrightarrow CO_2 + C$) and the decomposition of CH_4 ($CH_4 \Leftrightarrow 2H_2 + C$) [23,24]. By applying CeO_2-based catalysts, both reactions could be inhibited by the redox reaction between the surface carbon (C) with O_O^x at CeO_2 surface ($C + O_O^x \rightarrow CO + V_O{}^{\bullet\bullet} + 2\ e'$). From the TPR/TPO and $^{18}O/^{16}O$ isotope exchange results, the greater amount of OSC with high mobility of $Ce_{0.8}Gd_{0.05}Sm_{0.15}O_2$ could lead to its high resistance toward carbon deposition due to the sufficient amount of high mobility O_O^x to react with deposited carbon. It was also found from the post-reaction BET measurements (Table 4) that the surface area reduction percentage of $Ce_{0.8}Gd_{0.05}Sm_{0.15}O_2$ is lower than other catalysts, which indicates the better stability toward the thermal sintering of this material.

4. Conclusions

$Ce_xGd_ySm_zO_2$ solid solutions with fluorite structure and ultrafine particle can be achieved from the metal organic complex method. Among $Ce_xGd_ySm_zO_2$ with various Ce/Gd/Sm molar ratio, $Ce_{0.8}Gd_{0.05}Sm_{0.15}O_2$ exhibited the highest methane steam reforming rate with considerably low carbon deposition. It was revealed from the TRP/TPO and $^{18}O/^{16}O$ isotope exchange methods that the doping of Sm and Gd enhances the high and reversible OSC with good lattice oxygen mobility compared to undoped-CeO_2 and strongly leads to the good methane steam reforming performance.

Acknowledgement

The financial support from the Thailand Research Fund (TRF) throughout this project is gratefully acknowledged.

References

[1] A. Trovarelli, Catal. Rev. Sci. Eng. 38 (1996) 439.
[2] P. Fornasiero, G. Balducci, R.D. Monte, J. Kaspar, V. Sergo, G. Gubitosa, A. Ferrero, M. Graziani, J. Catal. 164 (1996) 173.
[3] T. Miki, T. Ogawa, M. Haneda, N. Kakuta, A. Ueno, S. Tateishi, S. Matsuura, M. Sato, J. Phys. Chem. 94 (1990) 339.
[4] C. Padeste, N.W. Cant, D.L. Trimm, Catal. Lett. 18 (1993) 305.
[5] S. Kacimi, J. Barbier Jr., R. Taha, D. Duperz, Catal. Lett. 22 (1993) 343.
[6] G.S. Zafiris, R.J. Gorte, J. Catal. 143 (1993) 86.
[7] G.S. Zafiris, R.J. Gorte, J. Catal. 139 (1993) 561.
[8] S. Imamura, M. Shono, N. Okamoto, R. Hamada, S. Ishida, Appl. Catal. A 142 (1996) 279.
[9] K. Eguchi, T. Kunisaki, H. Arai, J. Am. Ceram. Soc. 69 (1986) C282.
[10] E. Ramírez-Cabrera, A. Atkinson, D. Chadwick, Appl. Catal. B 47 (2004) 127.
[11] R.J. Gorte, J.M. Vohs, S. McIntosh, Solid State Ionics 175 (1–4) (2004) 1.
[12] S. Jung, C. Lu, H. He, K. Ahn, R.J. Gorte, J.M. Vohs, J. Power Sources 154 (2006) 42.
[13] T. Kim, G. Liu, M. Boaro, S.-I. Lee, J.M. Vohs, R.J. Gorte, O.H. Al-Madhi, B.O. Dabbousi, J. Power Sources 155 (2006) 231.
[14] O. Costa-Nunes, R.J. Gorte, J.M. Vohs, J. Power Sources 141 (2) (2005) 241.
[15] S. An, C. Lu, W.L. Worrell, R.J. Gorte, J.M. Vohs, Solid State Ionics 175 (1-4) (2004) 135.
[16] D.J.L. Brett, A. Atkinson, D. Cumming, E. Ramírez-Cabrera, R. Rudkin, N.P. Brandon, Chem. Eng. Sci. 60 (21) (2005) 5649.
[17] K. Otsuka, M. Hatano, A. Morikawa, J. Catal. 79 (1983) 493.
[18] K. Otsuka, M. Hatano, A. Morikawa, Inorg. Chim. Acta 109 (1985) 193.
[19] P.J. Gellings, H.J.M. Bouwmeester, Catal. Today 58 (2000) 1.
[20] D. Terribile, A. Trovarelli, J. Llorca, C. Leitenburg, G. Dolcetti, J. Catal. 178 (1998) 299.
[21] H. He, H.X. Dai, L.H. Ng, K.W. Wong, C.T. Au, J. Catal. 206 (2002) 1.
[22] N. Laosiripojana, S. Assabumrungrat, Appl. Catal. B 82 (2008) 103.
[23] Y. Lwin, W.R.W. Daud, A.B. Mohamad, Z. Yaakob, Int. J. Hydrogen Energy 25 (1) (2000) 47.
[24] J.N. Amor, Appl. Catal. A 176 (1999) 159.

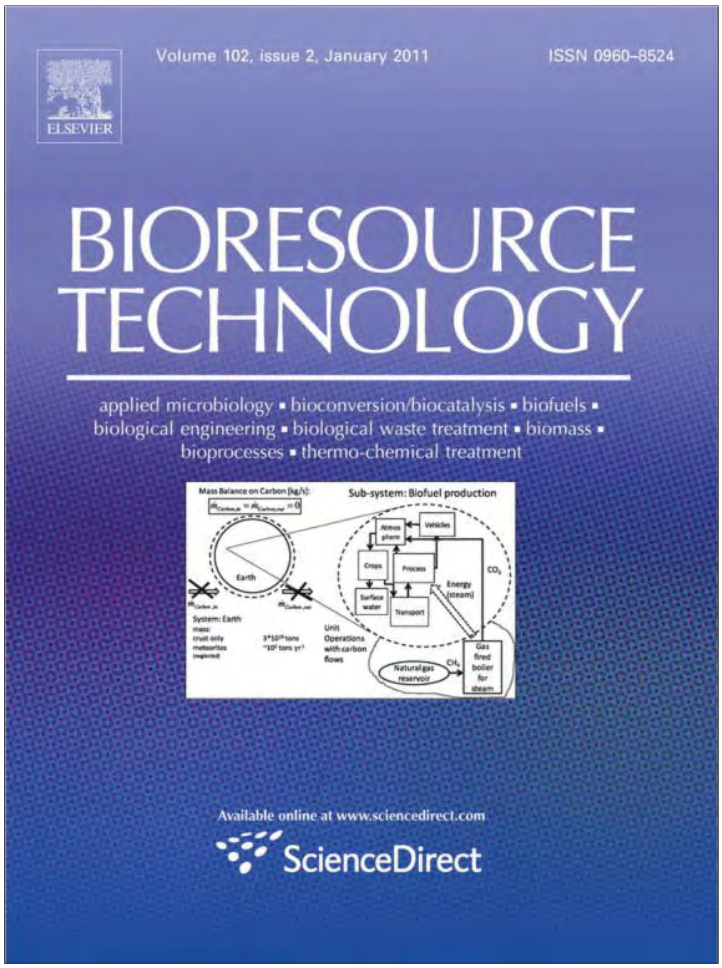

Bioresource Technology 102 (2011) 2040–2046

Contents lists available at ScienceDirect

Bioresource Technology

journal homepage: www.elsevier.com/locate/biortech

Hydrolysis/dehydration/aldol-condensation/hydrogenation of lignocellulosic biomass and biomass-derived carbohydrates in the presence of $Pd/WO_3–ZrO_2$ in a single reactor

W. Dedsuksophon [a], K. Faungnawakij [b], V. Champreda [c], N. Laosiripojana [a,*]

[a] The Joint Graduate School of Energy and Environment, CHE Center for Energy Technology and Environment, King Mongkut's University of Technology Thonburi, Thailand
[b] National Nanotechnology Center (NANOTEC), Pathumthani, Thailand
[c] National Center for Genetic Engineering and Biotechnology (BIOTEC), Pathumthani, Thailand

ARTICLE INFO

Article history:
Received 31 May 2010
Received in revised form 7 September 2010
Accepted 16 September 2010
Available online 22 September 2010

Keywords:
Lignocellulosic biomass
Biomass-derived carbohydrate
$Pd/WO_3–ZrO_2$
Furan
Alkane

ABSTRACT

Hydrolysis/dehydration/aldol-condensation/hydrogenation of lignocellulosic-biomass (corncobs) and biomass-derived carbohydrates (tapioca flour) to produce water-soluble $C_5–C_{15}$ compounds was developed in a single reactor system. $WO_3–ZrO_2$ efficiently catalyzed the hydrolysis/dehydration of these feedstocks to 5-hydroxymethylfurfural and furfural, while the impregnation of $WO_3–ZrO_2$ with Pd allowed sequential aldolcondensation/hydrogenation of these furans to $C_5–C_{15}$ compounds. The highest $C_5–C_{15}$ yields of 14.8–20.3% were observed at a hydrolysis/dehydration temperature of 573 K for 5 min, an aldol-condensation temperature of 353 K for 30 h, and a hydrogenation temperature of 393 K for 6 h. The $C_5–C_{15}$ yield from tapioca flour was higher than that from corncobs (20.3% compared to 14.8%). Tapioca flour produced more $C_6/C_9/C_{15}$, whereas corncobs generated more $C_5/C_8/C_{13}$ compounds due to the presence of hemicellulose in the corncobs. These water-soluble organic compounds can be further converted to liquid alkanes with high cetane numbers for replacing diesel fuel in transportation applications.

1. Introduction

The efficient conversion of currently underutilized biomass (e.g. bagasse, rice husk, rice straw, corncob, coconut, and palm) into gasoline and/or diesel fuel replacements could contribute to a more sustainable and environmentally benign energy sector. Several thermo-chemical and biological processes for biomass conversion have already been implemented (McKendry, 2002; Gnansounou and Dauriat, 2010) and additional processes are being investigated. Huber et al. (2005) described a process for the conversion of carbohydrates into $C_7–C_{15}$ alkanes via a series of reaction steps starting with acid-catalyzed dehydration of carbohydrates to carbonyl-containing furan compounds (i.e. 5-hydroxymethylfurfural (HMF) and furfural). Subsequently, these compounds are condensed via an aldol reaction to produce larger organic molecules ($>C_6$) in the presence of base catalysts to form a C–C bond between two carbonyl-containing compounds. HMF and furfural cannot undergo self-condensation reactions since these compounds do not contain a-H atom; nevertheless, both HMF and furfural have aldehyde groups, which can efficiently condense with acetone to form carbanion species in the presence of magnesia–zirconia (MgO–ZrO_2) and magnesia–titania (MgO–TiO_2) (Aramendía et al., 2004) or NaOH (Gutsche et al., 1967; Shigemasa et al., 1994). After the aldol-condensation step, the aldol-products are further hydrogenated to form large water-soluble organic compounds in the presence of Pd. The selective hydrogenation of the furan ring in HMF and furfural can lead to additional carbonyl-containing compounds that can undergo aldol self-condensation to form heavier alkanes. Lastly, these hydrogenated molecules are converted to liquid alkanes (ranging from $C_7–C_{15}$) by an aqueous-phase dehydration/hydrogenation (APD/H) process.

In order to convert lignocellulosic biomass to alkane-based fuel, the feedstock must be hydrolyzed to sugar compounds via an acid-catalyzed reaction, hot compressed water (HCW), subcritical water and supercritical water technologies (Laopaiboon et al., 2010; Yat et al., 2008; Karimi et al., 2006; Bower et al., 2008; Watanabe et al., 2005a,b; Asghari and Yoshida, 2006; Bicker et al., 2003; Aida et al., 2007; Yang and Montgomery, 1996; Kabyemela et al., 1999; Moreau et al., 2000; Sasaki et al., 2002). Recently, simultaneous hydrolysis/dehydration of three lignocellulosic biomasses (i.e. sugarcane bagasse, rice husk and corncob) to HMF and furfural under hot compressed water conditions in the presence of ZrO_2-based catalysts (i.e. ZrO_2, $TiO_2–ZrO_2$, and $SO_4–ZrO_2$) was described (Chareonlimkun et al., 2010a,b). The reaction was dependent on the acidity–basicity of the catalyst, and $TiO_2–ZrO_2$ produced the highest HMF and furfural yields with the fewest byproducts (i.e. glucose, fructose, xylose,

* Corresponding author. Tel.: +66 662 872 9014; fax: +66 662 872 6736.
E-mail address: navadol_l@jgsee.kmutt.ac.th (N. Laosiripojana).

0960-8524/$ - see front matter © 2010 Elsevier Ltd. All rights reserved.
doi:10.1016/j.biortech.2010.09.073

and 1,6-anhydroglucose). In the present study, we aimed to combine the hydrolysis/dehydration and aldol-condensation/hydrogenation reactions in a single reactor in order to convert corncobs and tapioca flour into water-soluble C_5–C_{15} compounds. TiO_2–ZrO_2 (Chareonlimkun et al., 2010a), WO_3–ZrO_2 (Furuta et al., 2004; Lopez et al., 2005; Rao et al., 2006) and H_3PO_4 (Asghari and Yoshida, 2006; Gámez et al., 2006) were compared as hydrolysis/dehydration catalysts, and Pd/TiO_2–ZrO_2, Pd/WO_3–ZrO_2 and Pd/MgO–ZrO_2 as catalysts for the aldol-condensation/hydrogenation of HMF and furfural. Optimal reaction conditions were determined.

2. Methods

2.1. Materials and chemicals

Corncobs and tapioca flour were obtained from National Center for Genetic Engineering and Biotechnology (Thailand). The corncobs were ground with a ball-milling into particles with an average diameter of 75 μm, according to the measurement by the particle size analyzer. Cellulose, xylan, HMF, acetone and dimethyl sulfoxide (DMSO) were supplied by Aldrich, while all chemicals for catalyst preparation (i.e. $ZrO(NO_3)_2$, $Mg(NO_3)_2$, $Ti(NO_3)_4$ and $Pd(NO_3)_2$) were also obtained from Aldrich.

2.2. Catalyst preparation and characterization

TiO_2–ZrO_2 and MgO–ZrO_2 (with Ti/Zr and Mg/Zr molar ratios of 1/1) were prepared by co-precipitation of $ZrO(NO_3)_2$ with $Mg(NO_3)_2$ and/or $Ti(NO_3)_4$. A solution of these salts was slowly dropped into a well-stirred reactor (stirring speed, 100 rpm) precipitating solution of ammonium hydroxide (NH_4OH) (2.5 wt.%) at room temperature. The solution was controlled at pH of 11 using the pH meter. The precipitate was washed with deionized water until Cl^- was no longer detectable with a silver nitrate ($AgNO_3$) solution. The solid sample was dried overnight at 383 K and calcined at 873 K under continuous air flow for 6 h with a temperature ramping rate of 10 K min^{-1}. WO_3–ZrO_2 was prepared by incipient wetness impregnation of ammonium metatungstate over ZrO_2 (prepared from the co-precipitation of $ZrO(NO_3)_2$ precursor) providing tungsten weight contents of 20 wt.% at 343 K for 30 min, then dried overnight at 383 K and calcined at 1073 K for 3 h.

The Brunauer–Emmett–Teller (BET) surface area, cumulative pore volume and average pore measurements of the catalysts were carried out by the N_2 physisorption technique using a surface area and porosity analyzer (Micromeritics ASAP 2020). Temperature programmed desorption (TPD) experiments were carried out using a flow apparatus; the catalyst sample (0.1 g) was treated at 773 K in helium for 1 h and then saturated with 15% NH_3/He mixture or pure CO_2 flow after cooling to 373 K. After purging with helium, the sample was heated to 923 K under helium and the amount of acid–base sites on the catalyst surface was calculated from the desorption amount of NH_3 and CO_2, which was determined by measuring the areas of the desorption profiles obtained from the chemisorption system analyzer (Micromeritics ChemiSorb 2750).

Pd/MgO–ZrO_2, Pd/TiO_2–ZrO_2 and Pd/WO_3–ZrO_2 (5 wt.% Pd) were prepared by impregnating MgO–ZrO_2, TiO_2–ZrO_2 and WO_3–ZrO_2 with $Pd(NO_3)_2$ solution. The catalysts were further calcined and reduced with 10% H_2/He at 773 K for 6 h before use. The weight contents of Pd in Pd/MgO–ZrO_2, Pd/TiO_2–ZrO_2 and Pd/WO_3–ZrO_2 were determined by X-ray fluorescence (XRF) elemental analyzer. The reducibility percentage of Pd was measured and calculated from the degree of H_2 uptake from the temperature-programmed reduction (TPR) test (Laosiripojana et al., 2008) using 5% H_2 with the total flow rate of 100 cm^3 min^{-1} and temperature from room temperature to 773 K, while the dispersion percentage of Pd was identified from the volumetric H_2 chemisorption measurement using a chemisorption analyzer (Micromeritics ChemiSorb 2750). The specific surface areas of the catalysts were obtained with BET measurements.

2.3. Reaction system and testing

The three main reactions (i.e. simultaneous hydrolysis/dehydration, aldol-condensation, and hydrogenation) were first tested separately. All reactions were carried out in a 0.5 in. diameter stainless steel reactor placed vertically inside a tubular furnace. For hydrolysis/dehydration, 0.1 g of sample (i.e. corncob and tapioca flour) and catalyst (i.e. TiO_2–ZrO_2, WO_3–ZrO_2 and H_3PO_4) were mixed with 1 cm^3 of aqueous solution (acetone with and without DMSO as co-solvent in water). It is noted that acetone solution was applied as aqueous-phase since we principally aims at the integration of hydrolysis/dehydration reactions with aldol-condensation reaction, from which theoretically requires acetone as the reactant. Therefore, the simultaneous use of acetone as both solvent for hydrolysis/dehydration reactions and reactant for aldol-condensation reaction would be a good approach for this integrating system. Furthermore, since it was previously reported that the acetone–DMSO mixture was an effective solvent for the dehydration of fructose to HMF (Qi et al., 2008); hence, the effect of DMSO adding as co-solvent along with the reactant mixture was also studied in this work by mixing DMSO in acetone with acetone:DMSO of 70:30 (Qi et al., 2009) prior the reaction.

N_2 was loaded to raise the reactor pressure to 3.5 MPa, measured by a pressure transducer (Kyowa, PGM-500 KD), before placing the reactor in the furnace. A Type-K thermocouple (Protronics) was placed into the annular space between the reactor and furnace with close contact to the catalyst bed. The reaction was carried out at several isothermal temperatures (473, 523, 573, 623, and 673 K); then it was stopped by quenching of the reactor in a water bath. For aldol-condensation/hydrogenation, the reactor was loaded with the reactant mixture (0.1 g of HMF, furfural and acetone) and catalysts (0.1 g), and helium was added up to 1 MPa to start the aldol-condensation reaction at 326 K for the reaction of HMF with acetone and 353 K for the reaction of furfural with acetone (Barrett et al., 2006) for 30 h. After stopping the aldol-condensation reaction by removal of the reactor from the furnace, the hydrogenation reaction was continued by pressurizing pure H_2 into the reactor and the reactor was heated and held at 393 K, 5 MPa for 6 h (Barrett et al., 2006). The reaction was stopped by quenching of the reactor in a water bath.

For combined hydrolysis/dehydration/aldol-condensation/hydrogenation, 0.1 g of the reactant mixture (i.e. corncob and tapioca flour) and 0.1 g of selected catalyst (i.e. Pd/TiO_2–ZrO_2, Pd/WO_3–ZrO_2 and Pd/MgOZrO_2) were mixed with 1 cm^3 of acetone/DMSO in water and loaded in the reactor and hydrolysis/dehydration followed by aldol-condensation and hydrogenation were carried out at the selected operating conditions based on the above studies (hydrolysis/dehydration at 523 K for 5 min, following with aldol-condensation at 353 K for 30 h and hydrogenation at 393 K for 6 h). Lastly, the effects of feedstock/solvent molar ratio, hydrogenation temperature and hydrogenation time on the product yield and selectivity were also determined.

2.4. Product analysis

The quantification and identification of gaseous products were conducted by gas chromatography (Shimadzu GC-14B with Porapak Q and capillary DB-5 columns) connected with a thermal conductivity detector (TCD) and a flame ionization detector (FID). In order to satisfactorily separate all compounds, the following temperature profile was used. In the first 3 min, the column

temperature was constant at 333 K, then increased at a rate of 15 K min^{-1} until 393 K and decreased to 333 K at a rate of 10 K min^{-1}. The amounts of HMF and furfural were analyzed by High Performance Liquid Chromatography (Summit, Dionex Co., Germany), which consisted of a Dionex PDA-100 photodiode array detector, a Dionex P680 pump system, a Dionex STH585 column oven and a Dionex ASI-100 automated sample injector equipped with a Shodex RSpak KC-811 (8.0 mmID * 300 mm) column. Compounds were detected by their absorbance at 280 nm and comparison of their peak areas with the corresponding areas of standard compounds. H_3PO_4 was used as the eluent, the injection volume was 20 μl, and the flow rate was 0.4 cm^3 min^{-1}. The retention time for HMF and furfural was 49.5 and 80.5 min, respectively. The selectivity and yield of water-soluble organic compounds (C_5–C_{15}) production were analyzed with a GC-FID instrument (Shimadzu 2010 model) with a capillary column (50 m × 0.2 mm and 0.5 μm) at injector, detector and column temperatures of 493, 553, and 473 K, respectively. From the reaction, the amounts of glucose, fructose, xylose, furfural, HMF and 1,6-anhydroglucose (AHG) were quantified by the HPLC and the conversion of sugars into furans and the conversion of furans into water-soluble organic compounds were calculated by measuring the disappearance of each reactant and dividing with the amount of each inlet feed. The yield of each product was calculated by the carbon balance defined as the ratio of the specified product to the loaded feedstock, while the selectivity of water-soluble organic compounds (C_5–C_{15}) was reported as the ratio of specified water-soluble organic compound species to the total water-soluble organic compounds in final liquid product. Eqs. (1) and (2) present the calculations of water-soluble organic compound yields from the reactions of furfural and HMF, respectively.

$$\text{Yield of water-soluble organic compounds(\%)from the reaction of furfural} = \frac{5xmolesC_5 + 8xmolesC_8 + 13xmolesC_{13}}{5xmoles_{furfural(in)} + 3xmoles_{acetone(in)}} \quad (1)$$

$$\text{Yield of water-soluble organic compounds(\%)from the reaction of HMF} = \frac{6xmolesC_6 + 9xmolesC_9 + 15xmolesC_{15}}{6xmoles_{HMF(in)} + 3xmoles_{acetone(in)}} \quad (2)$$

3. Results and discussion

3.1. Hydrolysis/dehydration of cellulose, helicellulose, lignocellulose and biomass-derived carbohydrate

Fig. 1 shows the conversion and liquid product yield from the hydrolysis/dehydration reactions of cellulose and xylan (in acetone solution; with cellulose/acetone and xylan/acetone molar ratios of 1/1) at 523 K with and without the presence of catalysts. It is noted according to the measurement of total carbon amount in the aqueous solution after reaction that the TOC (total organic carbon) values for all experiments were always higher than 86% indicated that the quantity of gaseous products from the reactions were considerably less than that of liquid products. Hence, we here reported the results and discussion only for the liquid products from the reactions. It can be seen that the presence of DMSO positively affected the catalyst activity as was also observed by Qi et al. (2008, 2009). At steady state (with a reaction time of 5 min), the main product from the conversion of cellulose was HMF, and only small amounts of glucose, fructose, furfural and AHG were also observed in the liquid product. Xylan was converted to furfural with small amounts of xylose detectable in the product. The most active catalysts for the reactions of cellulose and xylan were WO_3–ZrO_2 and H_3PO_4 possibly because of the interference of the acetone–DMSO mixture and/or the requirement of pressurized water for the reaction over TiO_2–ZrO_2. The good performance of WO_3–ZrO_2 is related to good hydrolysis along with strong isomerization activities for converting feedstocks to fructose which can be dehydrated to HMF and furfural with a higher rate than glucose (Watanabe et al., 2005a,b). The reactions of corncob and tapioca flour were also studied at various temperatures in the presence of WO_3–ZrO_2. As shown in Fig. 2, the yield of HMF from tapioca flour is higher than that from corncob at a slightly lower temperature of 20 K presumably due to more rapid hydrolysis of the carbohydrates.

3.2. Sequential aldol-condensation/hydrogenation of HMF and furfural

The aldol-condensation and hydrogenation reactions over HMF and furfural compounds were studied. Firstly, the single aldol-condensation reaction was carried out in the presence of WO_3–ZrO_2,

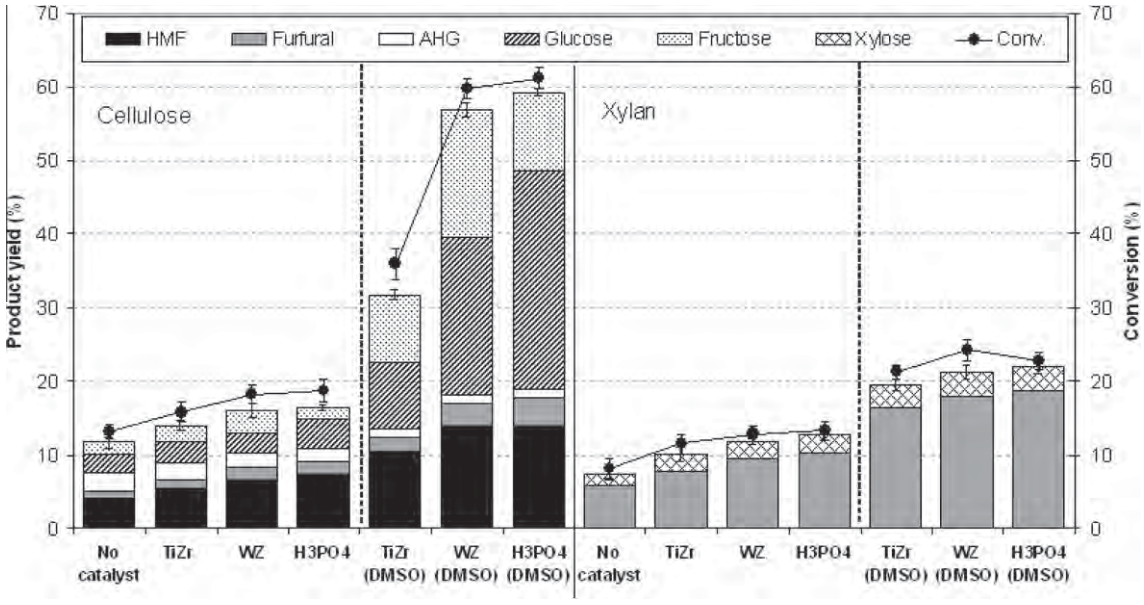

Fig. 1. Conversions and average product yields from the hydrolysis/dehydration of cellulose and xylan with and without the presence of various catalysts (feedstock/acetone molar ratio of 1/1 at 523 K).

TiO_2–ZrO_2, and MgO–ZrO_2 at 353 K with inlet HMF/acetone and furfural/acetone molar ratios of 1/1. Fig. 3 shows that the conversion of HMF and furfural increased with increasing reaction time and reached a steady state after 27–30 h. WO_3–ZrO_2 and MgO–ZrO_2 showed considerably greater activity than TiO_2–ZrO_2 (86–90% HMF and furfural conversions compared to 68–71% HMF and furfural conversions). This result suggests that TiO_2–ZrO_2 is unsuitable for the reaction in the presence of acetone, while the comparable

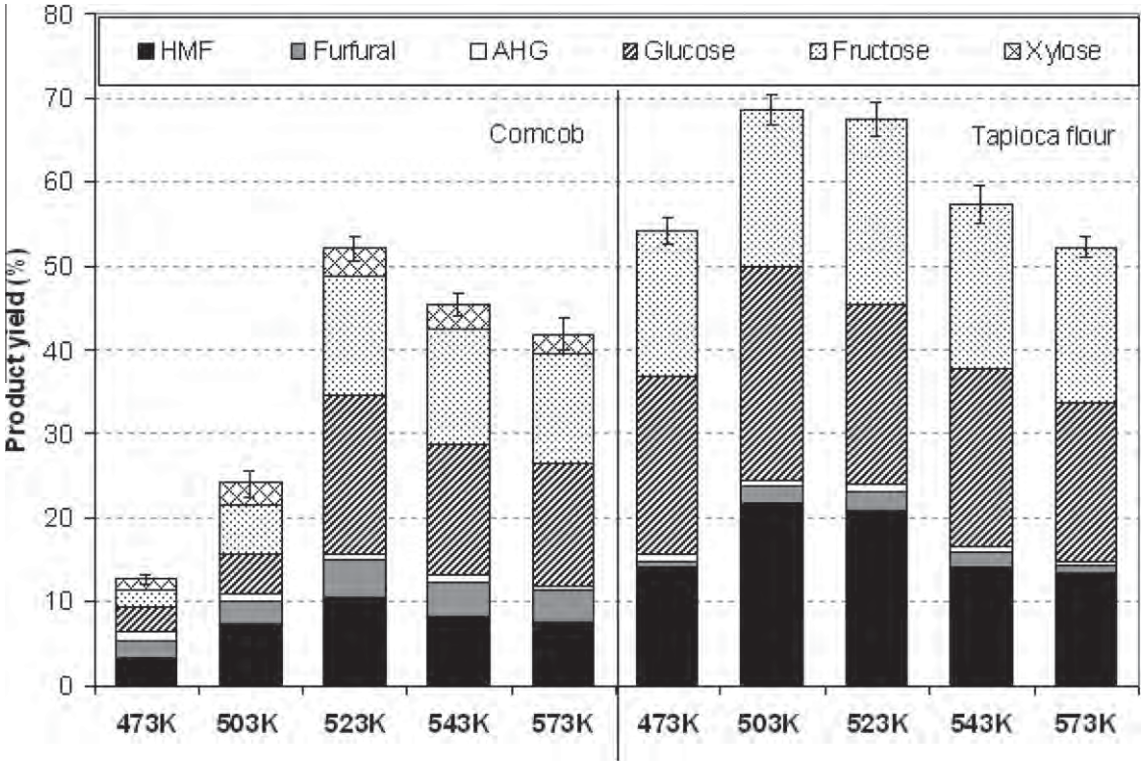

Fig. 2. Effect of reaction temperature on the product yields from the hydrolysis/dehydration of corncob and tapioca flour in the presence of WO_3–ZrO_2.

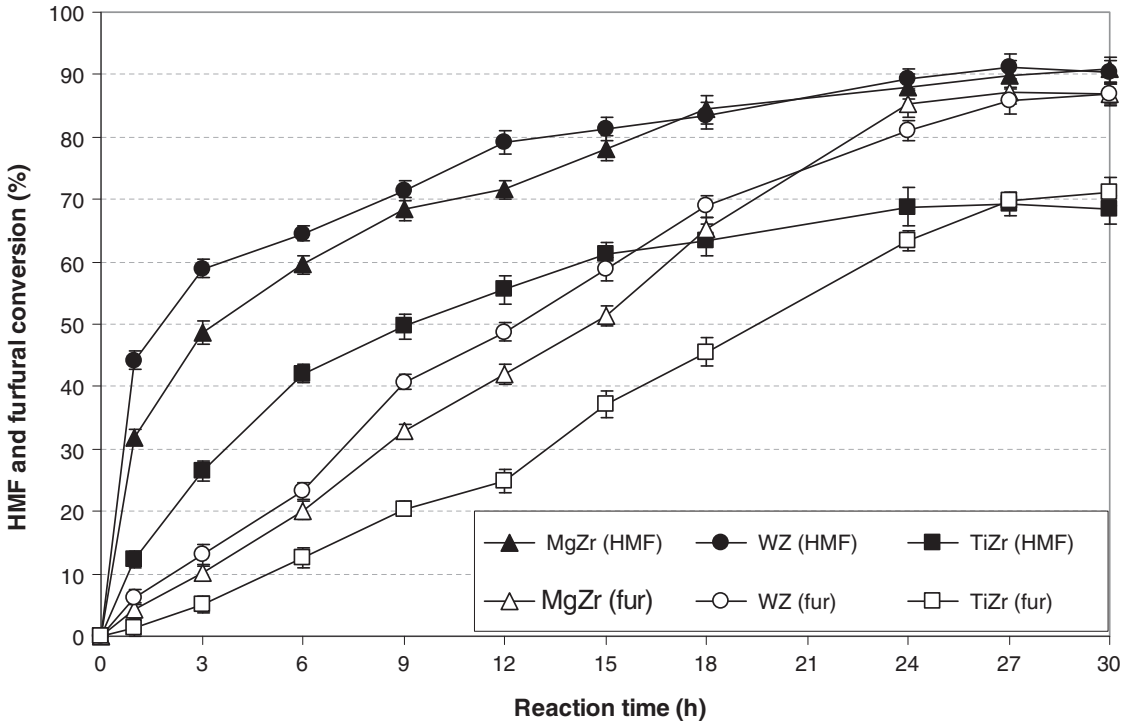

Fig. 3. Variations of HMF and furfural conversions with time from the aldol-condensation reaction in the presence of WO_3–ZrO_2, TiO_2–ZrO_2, and MgO–ZrO_2 (at 353 K with inlet reactant/acetone molar ratio of 1/1).

activities of WO_3–ZrO_2 and MgO–ZrO_2 could be due to their almost identical amount of base and acid sites (according to the TRD studies, the amounts of acid sites for WO_3–ZrO_2 and MgO–ZrO_2 are 281.5 and 82.4 μmol g^{-1}, while the amounts of base sites for these catalysts are 42.1 and 44.9 μmol g^{-1}).

As the next step, the sequential aldol-condensation/hydrogenation of HMF and furfural were carried out. Instead of WO_3–ZrO_2, TiO_2–ZrO_2, and MgO–ZrO_2, Pd/WO_3–ZrO_2, Pd/TiO_2–ZrO_2, and Pd/MgO–ZrO_2 were applied as catalysts. The aldol-condensation was catalyzed almost identically by Pd/WO_3–ZrO_2, Pd/TiO_2–ZrO_2, and Pd/MgO–ZrO_2 as the corresponding Pd-free catalysts (the conversions of HMF and furfural slightly decreased within the range of 2.1–8.3%). This outcome was likely due to the fact that only slight changes in the specific surface areas, cumulative pore volumes, and average pore diameters of the catalysts were observed after Pd loading (as presented in Table 1). The yields of water-soluble organic compounds from the sequential aldol-condensation/hydrogenation were higher for the Pd/WO_3–ZrO_2- and Pd/MgO–ZrO_2-catalyzed than the Pd/TiO_2–ZrO_2-catalyzed reactions (Fig. 4); as a consequence of the high activities of WO_3–ZrO_2 and MgO–ZrO_2 toward the aldol-condensation reaction. Similar physicochemical properties of all Pd-loaded catalysts, i.e. Pd loading, reducibility, and dispersion (as presented in Table 1) also encourage the claim that the catalyst activity toward the sequential aldol-condensation/hydrogenation is mainly related to the activity of support toward the aldol-condensation reaction since the activities of these catalysts toward the hydrogenation reaction, which occurs at Pd surface, should be identical.

3.3. Hydrolysis/dehydration/aldol-condensation/hydrogenation of biomass (lignocellulose) and biomass-derived carbohydrates in a single reactor

The hydrolysis/dehydration/aldol-condensation/hydrogenation of corncob and tapioca flour in the single reactor was carried out. Four catalyst systems including (i) single Pd/WO_3–ZrO_2; (ii) single Pd/MgO–ZrO_2; (iii) combination of WO_3–ZrO_2 with Pd/MgO–ZrO_2; and (iv) combination of H_3PO_4 with Pd/MgO–ZrO_2 were investigated (with the same total catalyst weight). Fig. 5 presents the yield of water-soluble organic compounds from the reactions of corncob and tapioca flour. Differences in the C_5, C_6, C_8, C_9, C_{13} and C_{15} fractions were observed depending on the feedstock. The

Table 1
Physicochemical properties of synthesized catalysts.

Catalysts	BET surface Area[a] (m^2 g^{-1})	Cumulative pore volume[b] (cm^3 g^{-1})	Average pore diameter[c] (nm)	Metal loading[d] (wt.%)	Metal reducibility[e] (Pd%)	Metal dispersion[f] (Pd%)
WO_3–ZrO_2	92	0.189	3.4	–	–	–
TiO_2–ZrO_2	173	0.335	3.1	–	–	–
MgO–ZrO_2	112	0.245	3.0	–	–	–
Pd/WO_3–ZrO_2	88	0.172	3.6	4.9	94.9	4.83
Pd/TiO_2–ZrO_2	164	0.289	3.3	5.0	94.1	4.96
Pd/MgO–ZrO_2	103	0.216	3.1	4.9	95.2	4.92

[a] Error of measurement = ± 5%.
[b] BJH desorption cumulative volume of pores between 1.7 and 300 nm diameter.
[c] BJH desorption average pore diameter.
[d] Measured from X-ray fluorescence analysis.
[e] Pd reducibility (from temperature-programmed reduction with 5% hydrogen).
[f] Pd dispersion (from the volumetric H_2 chemisorption measurement using chemisorption analyzer).

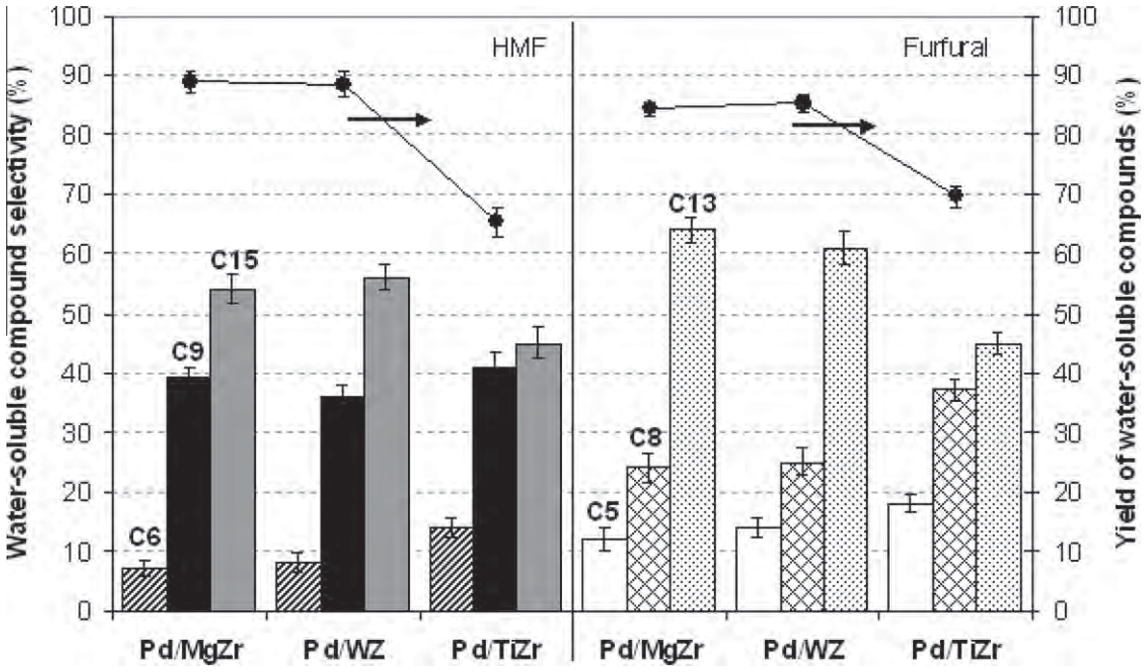

Fig. 4. Yields and selectivity of water-soluble C_5–C_{15} organic compounds from the sequential aldol-condensation/hydrogenation of furfural and HMF (aldol-condensation temperature of 353 K for 30 h and hydrogenation temperature of 393 K for 6 h).

reaction of tapioca flour relatively produced higher C_6, C_9, and C_{15}, whereas the reaction of corncob generated more C_5, C_8, and C_{13} compounds. This difference is mainly due to the hemicellulose in corncob, which is converted mainly into xylose and furfural. In contrast, the hydrolysis of tapioca flour produced mostly glucose and fructose, which are converted to HMF. The yield of water-soluble organic compounds from the reaction of tapioca flour is higher than that from the reaction of corncob likely due to the lignin

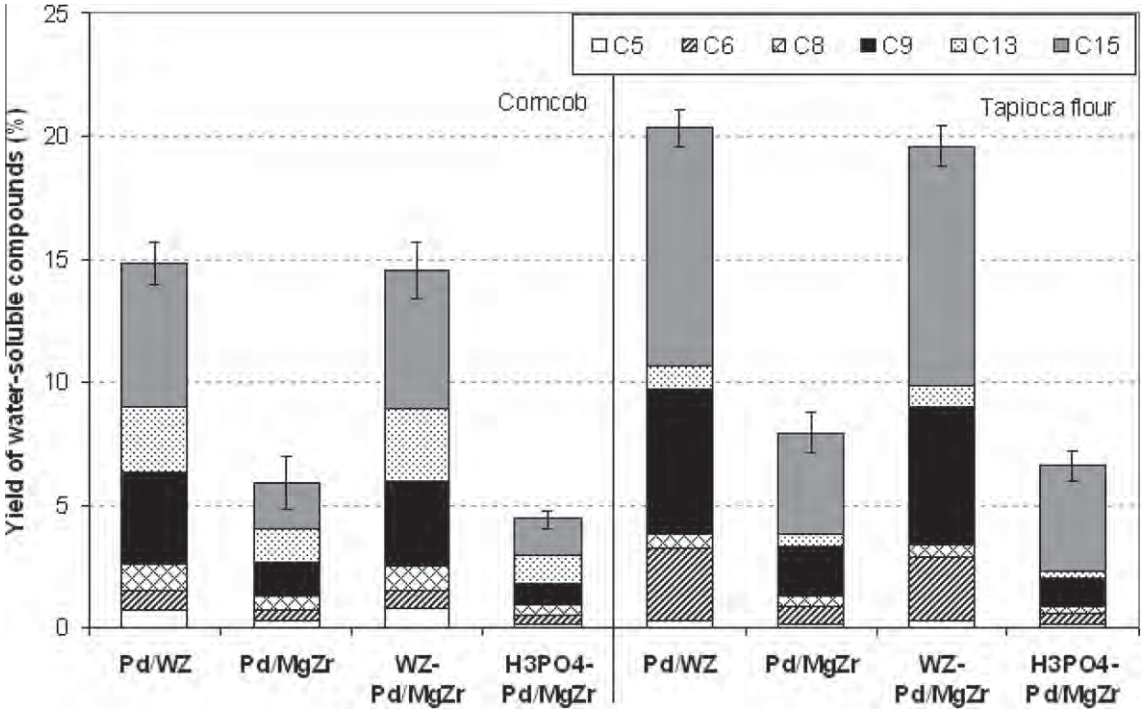

Fig. 5. Yield of water-soluble C_5–C_{15} organic compounds from the integrative hydrolysis/dehydration/aldol-condensation/hydrogenation of corncob and tapioca flour in the presence of various catalyst systems. (These integrative reactions sequentially occur following the steps as (i) hydrolysis/dehydration at 523 K for 5 min; (ii) aldol-condensation at 353 K for 30 h and (iii) hydrogenation at 393 K for 6 h).

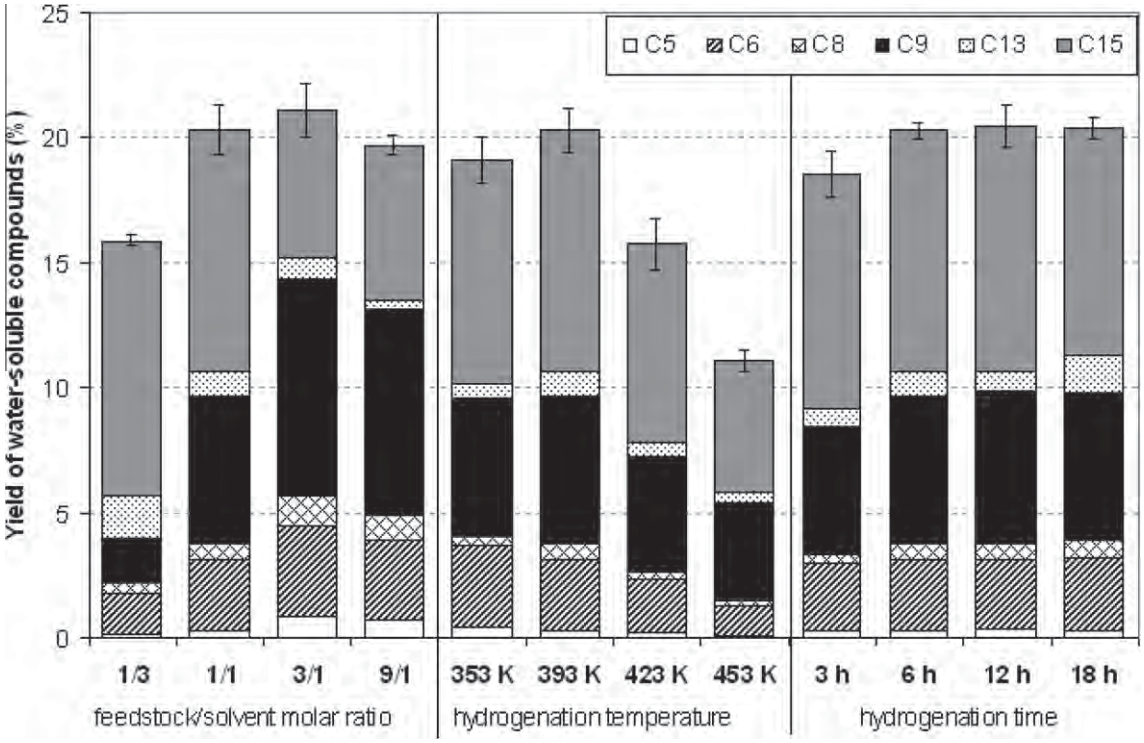

Fig. 6. Effects of feedstock/solvent molar ratio, hydrogenation temperature and hydrogenation time on the yield of water-soluble C_5–C_{15} organic compounds from the integrative hydrolysis/dehydration/aldol-condensation/hydrogenation of tapioca flour in the presence of Pd/WO_3–ZrO_2 (hydrolysis/dehydration temperature of 523 K for 5 min; aldol-condensation temperature of 353 K for 30 h).

present in the corncobs which cannot be converted to water-soluble compounds under the reaction conditions used. To prove this clarification, the reaction of lignin was also studied separately and it was found that no formation of sugar, furan, and water-soluble organic compounds was detected from the reaction. Among these catalyst systems, $Pd/WO_3–ZrO_2$ provided the highest yield of water-soluble organic compounds, comparable to the combination of $WO_3–ZrO_2$ and $Pd/MgO–ZrO_2$ for both reactions. It is likely that $WO_3–ZrO_2$ catalyzed the hydrolysis/dehydration reaction and provided support for Pd, which catalyzed the hydrogenation.

Further investigations regarding the effect of operating conditions on the product yield and selectivity from the reaction of tapioca flour in the presence of $Pd/WO_3–ZrO_2$ were then performed by varying the inlet feedstock/solvent molar ratio (from 1/1 to 1/3, 3/1, and 9/1), the hydrogenation temperature (from 393 K to 353 K, 423 K, and 453 K), and the hydrogenation time (from 6 h to 3 h, 12 h, and 18 h). As shown in Fig. 6, at a low inlet feedstock/solvent molar ratio (i.e. 1/3), a low organic compound yield was achieved due to the dilution of liquid product by excess solvent, whereas at a too high inlet feedstock/solvent molar ratio (i.e. 9/1), a low organic compound yield resulted from the incomplete conversion of HMF and furfural by the aldol-condensation reaction. The yield increased with increasing reaction temperatures from 353 K to 393 K, but decreased at higher reaction temperatures (i.e. 423 K and 453 K), which could be due to the further conversion or cracking of water-soluble organic compounds. The organic compound yield increased with increasing reaction time from 3 h to 6 h and remained constant thereafter. Thus, the optimum conditions for the production of water-soluble organic compounds from corncobs and tapioca flour were a feedstock/solvent molar ratio of 3/1, a hydrolysis/dehydration temperature of 573 K for 5 min, aldol-condensation at 353 K for 30 h and hydrogenation at 393 K for 6 h.

4. Conclusion

$WO_3–ZrO_2$ efficiently catalyzes the hydrolysis/dehydration reaction that converts the carbohydrates in corncobs and tapioca flour into HMF and furfural, while the impregnation of this compound with Pd efficiently catalyzes the aldol-condensation/hydrogenation of the furans into $C_5–C_{15}$ organic compounds. $Pd/WO_3–ZrO_2$ thus allows for hydrolysis/dehydration/aldol-condensation/hydrolysis/dehydration to be carried out in a single reactor. These water-soluble organic compounds could be further converted to liquid alkanes via the APD/H process, according to the report by Huber et al. (2005). The great beneficial of this aqueous phase conversion of lignocellulosic biomass and biomass-derived carbohydrates is its low energy requirement and its capability to produce high cetane number alkane-based fuel for replacing diesel fuel in transportation applications.

Acknowledgement

The financial support from The Thailand Research Fund (TRF) throughout this project is gratefully acknowledged.

References

Aida, T.M., Watanabe, M., Aizawa, Y., Iida, T., Levy, C., Sue, K., Inomata, H., 2007. Dehydration of D-glucose in high temperature water at pressures up to 80 MPa. J. Supercritical Fluids 40, 381–388.

Aramendía, M.A., Borau, V., Jiménez, C., Marinas, A., Marinas, J.M., Ruiz, J.R., Urbano, F.J., 2004. Magnesium-containing mixed oxides as basic catalysts: base characterization by carbon dioxide TPD-MS and test reactions. J. Mol. Catal. A: Chem. 218, 81–90.

Asghari, F.S., Yoshida, H., 2006. Dehydration of fructose to 5-hydroxymethylfurfural in sub-critical water over heterogeneous zirconium phosphate catalysts. Carbohydr. Res. 341, 2379–2387.

Barrett, C.J., Chheda, J.N., Huber, G.W., Dumesic, J.A., 2006. Single-reactor process for sequential aldol-condensation and hydrogenation of biomass-derived compounds in water. Appl. Catal. B 66, 111–118.

Bicker, M., Hirth, J., Vogel, H., 2003. Dehydration of fructose to 5-hydroxymethylfurfural in sub- and supercritical acetone. Green Chem. 5, 280–284.

Bower, S., Wickramasinghe, R., Nagle, N.J., Schell, D.J., 2008. Modeling sucrose hydrolysis in dilute sulfuric acid solutions at pretreatment conditions for lignocellulosic biomass. Bioresour. Technol. 99, 7354–7362.

Chareonlimkun, A., Champreda, V., Shotipruk, A., Laosiripojana, N., 2010a. Catalytic conversion of sugarcane bagasse, rice husk and corncob in the presence of TiO_2, ZrO_2 and mixed-oxide $TiO_2–ZrO_2$ under hot compressed water (HCW) condition. Bioresour. Technol. 101, 4179–4186.

Chareonlimkun, A., Champreda, V., Shotipruk, A., Laosiripojana, N., 2010b. Reactions of C_5 and C_6-sugars, cellulose, and lignocellulose under hot compressed water (HCW) in the presence of heterogeneous acid catalysts. Fuel 89, 2873–2880.

Furuta, S., Matsuhashi, H., Arata, K., 2004. Biodiesel fuel production with solid super acid catalyst in fixed bad reactor under atmospheric pressure. Catal. Commun. 5, 721–723.

Gámez, S., González-Cabriales, J.J., Ramírez, J.A., Garrote, G., Vázquez, M., 2006. Study of the hydrolysis of sugar cane bagasse using phosphoric acid. J. Food Eng. 74, 78–88.

Gnansounou, E., Dauriat, A., 2010. Techno-economic analysis of lignocellulosic ethanol: a review. Bioresour. Technol. 101, 4980–4991.

Gutsche, C.D., Redmore, D., Buriks, R.S., Nowotny, K., Grassner, H., Armbruster, C.W., 1967. Base-catalyzed triose condensations. J. Am. Chem. Soc. 89, 1235–1245.

Huber, G.W., Chheda, J.N., Barrett, C.J., Dumesic, J.A., 2005. Production of liquid alkanes by aqueous-phase processing of biomass-derived carbohydrates. Science 308, 1446–1450.

Kabyemela, B.M., Adschiri, T., Malaluan, R.M., Arai, K., 1999. Glucose and fructose decomposition in subcritical and supercritical water: detailed reaction pathway, mechanisms, and kinetics. Ind. Eng. Chem. Res. 38, 2888–2895.

Karimi, K., Kheradmandinia, S., Taherzadeh, M.J., 2006. Conversion of rice straw to sugars by dilute-acid hydrolysis. Biomass Bioenergy 30, 247–253.

Laopaiboon, P., Thani, A., Leelavatcharamas, V., Laopaiboon, L., 2010. Acid hydrolysis of sugarcane bagasse for lactic acid production. Bioresour. Technol. 101, 1036–1043.

Lopez, D.E., Goodwin Jr., J.G., Bruce, D.A., Lotero, E., 2005. Transesterification of triacetin with methanol on solid acid and base catalysts. Appl. Catal. A 295, 97–105.

Laosiripojana, N., Chadwick, D., Assabumrungrat, S., 2008. Effect of high surface area CeO_2 and $Ce–ZrO_2$ supports over Ni catalyst on CH_4 reforming with H_2O in the presence of O_2, H_2, and CO_2. Chem. Eng. J. 138, 264–273.

McKendry, P., 2002. Energy production from biomass (part 2): conversion technologies. Bioresour. Technol. 83, 47–54.

Moreau, C., Durand, R., Roux, A., Tichit, D., 2000. Isomerization of glucose into fructose in the presence of cation-exchanged zeolites and hydrotalcites. Appl. Catal. A 193, 257–264.

Qi, X., Watanabe, M., Aida, T.M., Richard, L., Smith Jr., 2008. Selective conversion of D-fructose to 5-hydroxymethylfurfural by ion-exchange resin in acetone/dimethyl sulfoxide solvent mixtures. Ind. Eng. Chem. Res. 47, 9234–9239.

Qi, X., Watanabe, M., Aida, T.M., Richard, L., Smith Jr., 2009. Sulfated zirconia as a solid acid catalyst for the dehydration of fructose to 5-hydroxymethylfurfural. Catal. Commun. 10, 1771–1775.

Rao, K.N., Sridhar, A., Lee, A.F., Tavener, S.J., Young, N.A., Wilson, K., 2006. Zirconium phosphate supported tungsten oxide solid acid catalysts for the esterification of palmitic acid. Green Chem. 8, 790–797.

Sasaki, M., Goto, K., Tajima, K., Adschiri, T., Arai, K., 2002. Rapid and selective retro-aldol condensation of glucose to glycolaldehyde in supercritical water. Green Chem. 4, 285–287.

Shigemasa, Y., Yokoyama, K., Sashiwa, H., Saimoto, H., 1994. Synthesis of threo- and erythro-3-pentulose by aldol type reaction in water. Tetrahedron Lett. 35, 1263–1266.

Watanabe, M., Aizawa, Y., Iida, T., Aida, T.M., Levy, C., Sue, K., Inomata, H., 2005a. Glucose reactions with acid and base catalysts in hot compressed water at 473 K. Carbohydr. Res. 340, 1925–1930.

Watanabe, M., Aizawa, Y., Iida, T., Nishimura, R., Inomata, H., 2005b. Catalytic glucose and fructose conversions with TiO_2 and ZrO_2 in water at 473 K: relationship between reactivity and acid–base property determined by TPD measurement. Appl. Catal. A 295, 150–156.

Yang, B.Y., Montgomery, R., 1996. Alkaline degradation of glucose: effect of initial concentration of reactants. Carbohydr. Res. 280, 27–45.

Yat, S.C., Berger, A., Shonnard, D.R., 2008. Kinetic characterization for dilute sulfuric acid hydrolysis of timber varieties and switchgrass. Bioresour. Technol. 99, 3855–3863.

Fuel 90 (2011) 136–141

Contents lists available at ScienceDirect

Fuel

journal homepage: www.elsevier.com/locate/fuel

Steam reforming of LPG over Ni and Rh supported on Gd-CeO_2 and Al_2O_3: Effect of support and feed composition

N. Laosiripojana [a,*], W. Sutthisripok [b], S. Charojrochkul [c], S. Assabumrungrat [d]

[a] The Joint Graduate School of Energy and Environment, CHE Center for Energy Technology and Environment, King Mongkut's University of Technology Thonburi, Thailand
[b] Department of Mining and Materials Engineering, Faculty of Engineering, Prince of Songkla University, Songkhla, Thailand
[c] National Metal and Materials Technology Center (MTEC), Pathumthani, Thailand
[d] Center of Excellence in Catalysis and Catalytic Reaction Engineering, Department of Chemical Engineering, Faculty of Engineering, Chulalongkorn University, Bangkok 10330, Thailand

ARTICLE INFO

Article history:
Received 4 March 2010
Received in revised form 16 July 2010
Accepted 29 July 2010
Available online 20 August 2010

Keywords:
LPG
Steam reforming
Hydrogen
Gd-CeO_2
Nickel

ABSTRACT

The steam reforming of liquefied petroleum gas (LPG) over Ni- and Rh-based catalysts supported on Gd-CeO_2 (CGO) and Al_2O_3 was studied at 750–900 °C. The order of activity was found to be Rh/CGO > Ni/CGO ~ Rh/Al_2O_3 > Ni/Al_2O_3; we indicated that the comparable activity of Ni/CGO to precious metal Rh/Al_2O_3 is due to the occurring of gas–solid reactions between hydrocarbons and lattice oxygen (O_0^x) on CGO surface along with the reaction taking place on the active site of Ni, which helps preventing the carbon deposition and promoting the steam reforming of LPG.

The effects of O_2 (as oxidative steam reforming) and H_2 adding were further studied over Ni/CGO and Ni/Al_2O_3. It was found that the additional of these compounds significantly reduced the amount of carbon deposition and promoted the conversion of hydrocarbons (i.e., LPG as well as CH_4, C_2H_4 and C_2H_6 occurred from the thermal decomposition of LPG) to CO and H_2. Nevertheless, the addition of too high O_2 oppositely decreased H_2 yield due to the oxidizing of Ni particle and the possible combusting of H_2 generated from the reaction, while the addition of too high H_2 also negatively affect the catalyst activity due to the occurring of catalyst active site competition and the inhibition of gas–solid reactions between the gaseous hydrocarbon compounds and O_0^x on the surface of CGO (for the case of Ni/CGO).

1. Introduction

Hydrogen can be efficiently produced from the reforming of several hydrocarbon compounds e.g., methane, methanol, ethanol, liquefied petroleum gas (LPG), and other oil derivatives. Among these feedstocks, LPG is a good candidate for hydrogen production in remote areas where natural gas pipeline is not available [1]. LPG typically consists of C_3H_8 and C_4H_{10} (with various ratios depending on its source) that exist as liquid under modest pressure at ambient temperature [2]. Currently, steam reforming process catalyzed by precious metal catalysts (e.g., Rh, Ru, and Pt) has generally been applied to convert LPG to hydrogen [3–10]. The main products from this reaction are H_2, CO, and CO_2; nevertheless, the formations of C_2H_6, C_2H_4, and CH_4 are also observed in the product gas due to the decomposition of LPG and methanation reaction. By-products formation and/or decomposition to carbon can contribute to decline in the catalytic activity. The O_2 addition to LPG and H_2O during oxidative steam reforming has been reported to improve the catalyst stability and reduce the carbon formation [5,6]. Another attractive benefit of the oxidative steam reforming is that the exothermic heat from the partial oxidation can directly supply the energy required for the endothermic steam reforming reaction, thus it can be considered as thermal self-sustaining process. In the process, the O_2 amount must be properly controlled because an excess could reduce the yield of H_2 due to the oxidation of H_2 generated from the reaction.

In this study, we aimed at the development of Ni-based catalyst that enables to reform LPG with high stability and activity. Although the precious metals have been generally reported to be active for this reaction with higher resistance toward carbon formation than Ni-based catalyst, the current prices of these metals are very high for commercial uses [11–13]. Selection of a support material is another important issue since there was evidence that metal catalysts are not very active for the steam reforming when supported on inert oxides [14]. Previously, various catalyst supports have been investigated i.e., α-Al_2O_3 [15], γ-Al_2O_3 and γ-Al_2O_3 with alkali metal oxide and rare earth metal oxide [16], $CaAl_2O_4$ [17] and ceria-based supports [18]. A promising catalytic system for the reforming reactions appeared to be a metal on ceria-based supports [19–27]. Ceria-based materials are extensively used as a catalyst and support for a variety of reactions involving

* Corresponding author. Tel.: +66 2 872 9014; fax: +66 2 872 6736.
E-mail address: navadol_l@jgsee.kmutt.ac.th (N. Laosiripojana).

0016-2361/$ - see front matter © 2010 Elsevier Ltd. All rights reserved.
doi:10.1016/j.fuel.2010.07.053

oxidation of hydrocarbons; the high oxygen mobility [28], high oxygen storage capacity (OSC) [29], strong interaction with the supported metal (strong metal–support interaction) [30] and the redox properties [31] render ceria-based materials very interesting for catalysis. It is noted that the doping ceria with some rare earth elements e.g., Gd (as Gd-CeO_2 or as called CGO) has been reported to improve the redox properties of ceria. Recently, CGO has been applied in a wide variety of reactions involving oxidation or partial oxidation of hydrocarbons (e.g., automotive catalyst) and as material component for SOFC. Besides, CGO showed activity for the decomposition of CH_4 at such a high temperature (800–1000 °C) with great resistance toward carbon deposition [32]. Thus, CGO was chosen as catalyst support in this work.

In detail, the stability and activity towards the steam reforming of LPG over Ni supported on CGO was studied and compared to Ni supported on conventional Al_2O_3. It is noted that the reaction over Rh-based catalysts was also studied for comparison since Rh is known as one of the most active metals for reforming and relevant reactions. In addition, the effect of oxygen-containing feed and hydrogen-containing feed on the reaction activity was also investigated. All experiments were carried out in the temperature range of 750–900 °C with a simulated LPG composition (60%C_3H_8 and 40%C_4H_{10}) based on the compositions of LPG in Thailand.

2. Experimental

2.1. Catalyst preparation and characterization

CGO was prepared by co-precipitation of $Ce(NO_3)_3$ with $Gd(NO_3)_3$ in the presence of 0.1 M cetyltrimethylammonium bromide solution (from Aldrich) as a cationic surfactant. The ratio between $Ce(NO_3)_3$ and $Gd(NO_3)_3$ was calibrated to achieve Ce/Gd molar ratios of 0.9/0.1, while the molar ratio of (([Ce]+[Gd])/[cetyltrimethylammonium bromide] was kept constant at 0.8. The solid solution was formed by slow mixing of this metal salt solution with 0.4 M of urea. After preparation, the precipitate was filtered and washed with deionised water and ethanol to prevent the agglomeration of the particles. It was dried overnight in an oven at 110 °C, and then calcined in air at 900 °C for 6 h.

Ni/CGO, Ni/Al_2O_3, Rh/Al_2O_3 and Rh/CGO (5 wt.% Ni and Rh) were prepared by impregnating either synthesized CGO or α-Al_2O_3 with $Ni(NO_3)_2$ and $Rh(NO_3)_2$ solutions (from Aldrich). The catalysts were further calcined and reduced with 10%H_2/He at 500 °C for 6 h before use. After reduction, the catalysts were characterized by several physicochemical methods. The Ni or Rh loads in Ni/CGO, Ni/Al_2O_3, Rh/Al_2O_3 and Rh/CGO were determined by X-ray fluorescence (XRF) analysis. The reducibility and dispersion percentages of Ni and Rh were measured from temperature-programmed reduction (TPR) with 10%H_2/He and temperature-programmed desorption (TPD), while the catalyst specific surface areas were obtained from BET measurements. All physicochemical properties of the synthesized catalysts are presented in Table 1. Apart from these characterizations, the catalyst phase formation was confirmed by the X-ray diffraction analysis (XRD; Philips X-Pert-MPD X-ray diffractometer) operating at 40 kV/30 mA, using monochromated CuKα radiation. It was found that, for the case of Ni/Al_2O_3, the formation of $NiAl_2O_4$ phase was also detected. It should be noted that the degree of OSC over these synthesized materials were also analyzed by the isothermal reduction measurement. Detail of this experiment is presented in Section 3.1.

Table 1
Physicochemical properties of the catalysts after reduction.

Catalyst	Metal-load (wt.%)	BET surface area ($m^2\ g^{-1}$)	Metal-dispersion (%)	Metal-reducibility (%)
Rh/CGO	4.9	33.7	93.6	4.12
Rh/Al_2O_3	5.0	38.5	94.9	4.74
Ni/CGO	4.8	34.2	94.1	4.36
Ni/Al_2O_3	5.0	40.0	94.5	4.85

2.2. Apparatus and procedures

An experimental system was constructed as shown elsewhere [33,34]. The feed gases including LPG, O_2, H_2 and helium were mixed with steam (generated from the evaporator) and introduced to a 10-mm diameter quartz reactor, which was mounted vertically inside a tubular furnace. The inlet LPG concentration was kept constant at 5 kPa (C_3H_8/C_4H_{10} ratio of 0.6/0.4), while the inlet H_2O concentration was varied depending on the inlet LPG/H_2O molar ratio requirement for each experiment. The temperature of the reactor was measured by Type-K thermocouples, which were placed into the annular space between the reactor and the furnace and also inserted in the middle of the quartz tube in order to re-check the possible temperature gradient. Catalysts with the weight of 100 mg were loaded in this quartz reactor. Based on the results from our previous publications [33,34], in order to avoid any limitations by intraparticle diffusion, the total gas flow rate was kept constant at 100 $cm^3\ min^{-1}$ under a constant residence time of 10^{-3} g min cm^{-3} in all experiments.

After the reactions, the exit gas mixture was transferred via trace-heated lines to gas chromatograph (GC, Shimadzu 14B equipped with a Porapak Q column) and mass spectrometer (MS). The GC was applied in order to investigate the steady state condition experiments, whereas the MS was used for the transient carbon formation experiment. In the present work, the isothermal oxidation measurement at 900 °C was applied to determine the amount of carbon formation by introducing 10% O_2 in helium (with the flow rate of 100 $cm^3\ min^{-1}$) into the system, after being purged with helium. The amount of carbon formation was determined by measuring CO and CO_2 yields from the oxidation results. Furthermore, the amount of carbon deposition was confirmed by the carbon balance calculation, from which the value equals to the difference between the inlet carbon containing components (LPG) and the outlet carbon containing components (CO, CO_2, CH_4, C_2H_6, and C_2H_4).

In order to study the steam reforming activity, the rate of steam reforming was defined in terms of LPG conversion, H_2 yield, and other by-product selectivities. H_2 yield (Y_{H_2}) was calculated by the hydrogen balance, defined as the molar fraction of H_2 produced to the consumed moles of hydrogen in the reactants. Other by-product selectivities (i.e., S_{CO}, S_{CO_2}, S_{CH_4}, $S_{C_2H_6}$, and $S_{C_2H_4}$) were calculated by the carbon balance, defined as the ratios of the product moles to the consumed moles of hydrocarbon, accounting for stoichiometry.

3. Results and discussion

3.1. Measurement of OSC

The degree of OSC for all synthesized catalysts after reduction (as well as fresh CGO after calcination) was investigated using the isothermal reduction measurement, which was performed by purging the catalysts at 900 °C in 5%H_2 in helium. The amount of H_2 uptake is correlated to the amount of O_2 stored in the catalysts. As presented in Fig. 1, the amount of H_2 uptakes over Ni/CGO and Rh/CeGO are in the same range (4645–4652 μmol g_{cat}^{-1}) and slightly lower than that over CGO (4913 μmol g_{cat}^{-1}), suggesting that the OSC results unaffected by Ni and Rh impregnation. As expected, no H_2 uptake occurred from the TPR over Ni/Al_2O_3. The

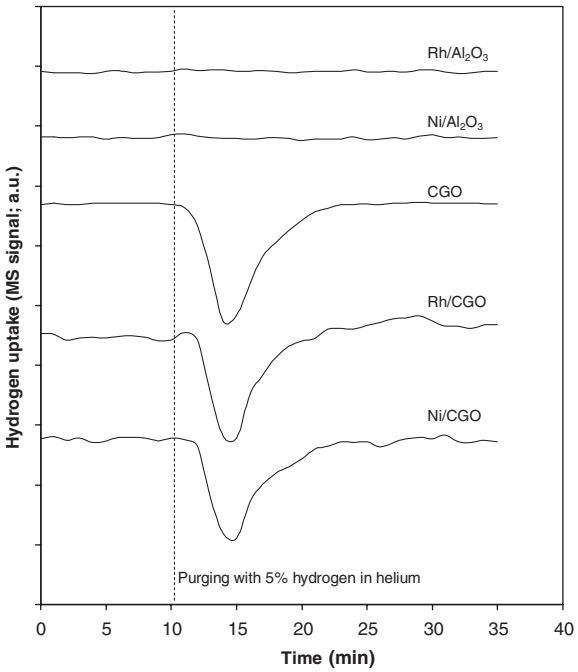

Fig. 1. Reduction measurement (at 900 °C) of fresh catalysts after treatments.

benefit of OSC on the reforming reaction is later presented in Section 3.3.

3.2. Homogenous (non catalytic) LPG steam reforming

Before undergo the catalyst activity testing, the homogeneous steam reforming of LPG was firstly investigated by feeding LPG and steam (with LPG/H_2O molar ratio of 1.0/4.0) to the system without catalyst while the temperature increased from ambient to 900 °C. As presented in Fig. 2, C_3H_8 and C_4H_{10} were cracked to CH_4, C_2H_6, C_2H_4, and H_2 at the temperature above 700 °C (Eqs. (1)–(3)). It should be noted that, in all range of temperature studied, the inlet H_2O was not consumed and neither CO nor CO_2 was detected, suggesting that no homogenous reforming reaction between steam and LPG occurred in this range of temperature.

$$C_3H_8 \rightarrow C_2H_4 + CH_4 \quad (1)$$

$$C_4H_{10} \rightarrow C_2H_6 + C_2H_4 \quad (2)$$

$$C_2H_6 \rightarrow C_2H_4 + H_2 \quad (3)$$

It is noted that, after exposure for 6 h, significant amount of carbon was detected in the blank reactor. At such a high temperature in the present work, C_{2+} hydrocarbons (C_3H_8 and C_4H_{10} as well as the formations of C_2H_6 and C_2H_4) are the major course of carbon deposition since these components act as strong promoters for carbon formation. Theoretically, under this operating condition, the decomposition of these hydrocarbons on the catalyst active site (∗) (Eq. (4)) is the major pathways for carbon formation as they show the largest change in Gibbs energy [26].

$$C_nH_m + * \rightarrow nC\text{-}* + 0.5mH_2 \quad (4)$$

3.3. Activity toward LPG steam reforming

The steam reforming of LPG over Ni/CGO, Ni/Al_2O_3, Rh/Al_2O_3 and Rh/CGO were then studied at the temperature range of 750–900 °C. After treatments, the catalysts were heated up under helium flow to these setting temperatures; and at the isothermal conditions, LPG and H_2O (with LPG/H_2O molar ratio of 1.0/4.0) were introduced. In all range of temperature studied, the conversions of C_3H_8 and C_4H_{10} were closed to 100%, while the conversions of H_2O (not showed) were in the range of 70–85%. Furthermore, it was found that the trends of H_2 and CO produced increased with increasing temperature, whereas the distributions of CO_2, C_2H_4 and C_2H_6 in the product decreased. The dependence of CH_4 on the operating temperature was non-monotonic, the maximum production of CH_4 occurred at approximately 800–850 °C. Among these catalysts, Rh/CGO enhanced the highest H_2 yield (88.5% at 900 °C) and the main products from the LPG steam reforming at 900 °C over this catalyst were only H_2 CO, and CO_2 with very small amount of CH_4 detected (Fig. 3(a)). As for Rh/Al_2O_3 and Ni/CGO, the yields of H_2 for both catalysts were in the same range (78.8–79.1% at 900 °C), which are relatively less than Rh/CGO. Furthermore, significant amount of CH_4 and C_2H_4 were observed particularly at low temperature (20–22% CH_4 and 8–9% C_2H_4 selectivities at 750 °C); these formations significantly decreased at higher temperature and at 900 °C only small amount of CH_4 (9–11% CH_4 selectivity) was observed. In contrast for Ni/Al_2O_3, significantly lower H_2 yield was produced (31.9% at 900 °C); furthermore, high contents of CH_4 and C_2H_4 remains observed even at temperature as high as 900 °C (Fig. 3(b)).

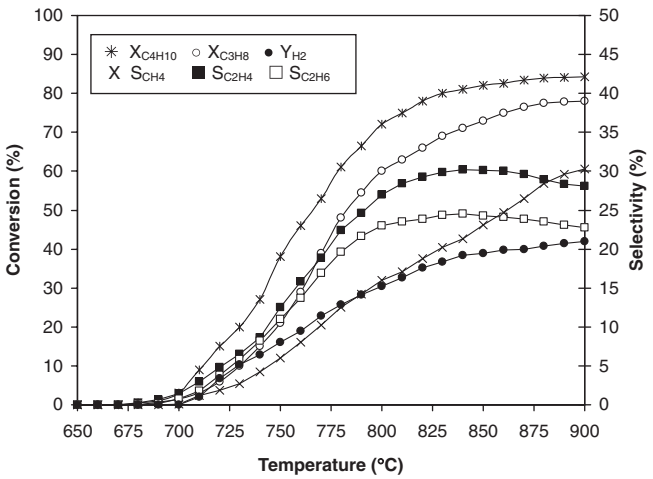

Fig. 2. Homogeneous (in the absence of catalyst) steam reforming of LPG (with LPG/H_2O molar ratio of 1.0/4.0).

After exposure for 10 h, the post-reaction oxidation experiments were carried out by introducing of 10% O_2 in helium (after a helium purge) in order to determine the degree of carbon formation. Fig. 4 shows the oxidation results over these catalysts after exposure in LPG steam reforming at 900 °C; huge peak of CO_2 were observed for Ni/Al_2O_3, while smaller peaks were detected for Rh/Al_2O_3, Ni/CGO, and particularly Rh/CGO indicating their greater resistance toward carbon deposition. Based on CO_2 yield calculation, the quantities of carbon deposited over Rh/CGO, Rh/Al_2O_3, Ni/CGO and Ni/Al_2O_3 were 2.04, 2.87, 2.89 and 4.64 mmol g_{cat}^{-1}). These values were ensured by the calculation of carbon balance in the system. Regarding the calculation, the moles of carbon deposited per gram of Rh/CGO, Rh/Al_2O_3, Ni/CGO and Ni/Al_2O_3 were 2.01, 2.90, 2.91 and 4.58 mmol g^{-1}, which are in good agreement with the values observed from the oxidation experiments.

It is clear from the above experiments that Rh catalyst presents greater reforming activity with better resistance toward carbon deposition than Ni catalysts; in addition, CGO support plays important role to improve the reforming performance. We indicate that the benefit from the use of CGO support is related to its OSC. For the cases of Ni/CGO and Rh/CGO, in addition to the reaction on Ni- or Rh-surface, the gas–solid reactions between hydrocarbons and the lattice oxygen (O_O^x) also takes place on CGO surface; and

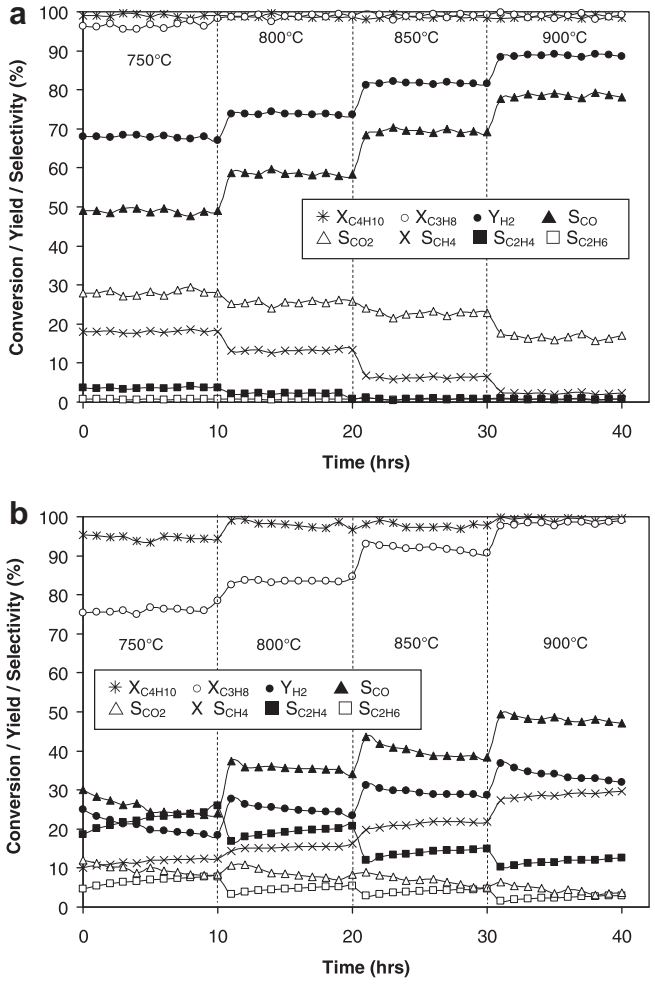

Fig. 3. Conversions and product distributions from steam reforming of LPG over (a) Rh/CGO and (b) Ni/Al_2O_3 (with LPG/H_2O ratio of 1.0/4.0) at several temperatures.

simultaneously O_O^x is regenerated by reaction with oxygen containing compound (i.e., steam) in the system (Eqs. (5)–(8)).

$$C_nH_m + (n+m)S \rightarrow n(C\text{-}S) + m(H\text{-}S) \quad (5)$$

$$C\text{-}S + O_O^x \rightarrow CO + V_O^{\cdot\cdot} + 2e' + S \quad (6)$$

$$H\text{-}S \rightarrow 0.5H_2 + S \quad (7)$$

$$H_2O + V_O^{\cdot\cdot} + 2e' \rightarrow O_O^x + H_2 \quad (8)$$

S is the CGO surface site, while C-S and H-S are the absorbed surface carbon and hydrogen species. Using the Kroger–Vink notation, $V_O^{\cdot\cdot}$ denotes as an oxygen vacancy with an effective charge 2^+, and e' is an electron which can either be more or less localized on a cerium ion or delocalized in a conduction band. These reactions inhibit the occurrences of intermediate hydrocarbons (i.e., C_2H_4 and C_2H_6) and consequently minimize the degree of carbon deposition since these hydrocarbons are efficiently converted to H_2 and CO_2, which are thermodynamically unflavored to form carbon species. It is noted that CO_2 can also be generated along with CO and H_2 due to the occurring of water gas shift reaction ($CO + H_2O \rightarrow CO_2 + H_2$) and the gas–solid reaction between CO and O_O^x ($CO + O_O^x \rightarrow CO_2 + V_O^{\cdot\cdot} + 2e'$). In order to prove the above redox mechanism (Eqs. (5)–(8)), the reactivities of CGO toward the steam reforming of LPG was also carried out. Fig. 5 shows the conversion and product distributions at various temperatures. Clearly, LPG was efficiently converted mainly to H_2, CO, CO_2 and CH_4 and the conversions of C_3H_8 and C_4H_{10} were almost 100% when the temperature reached 800 °C.

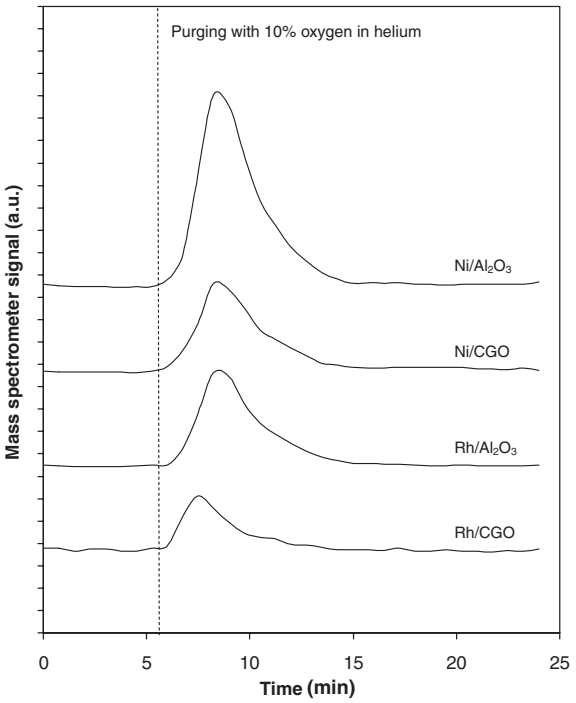

Fig. 4. CO_2 peak from the isothermal oxidation measurement of spent catalysts after exposure in steam reforming of LPG at 900 °C for 10 h.

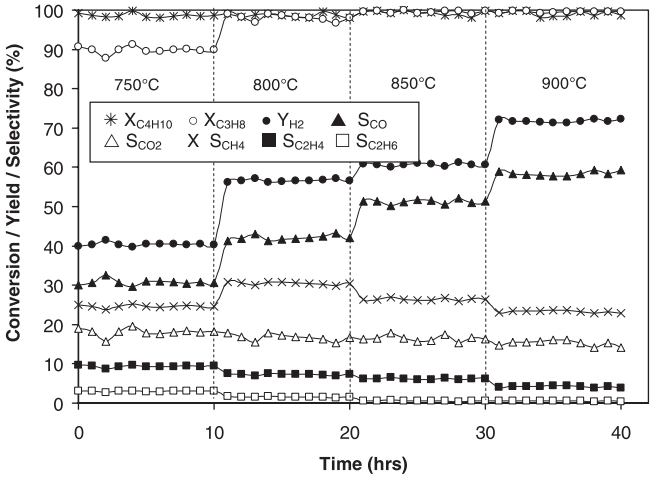

Fig. 5. Conversions and product distributions from steam reforming of LPG over CGO (with LPG/H_2O molar ratio of 1.0/4.0) at several temperatures.

The effect of inlet steam content on the reforming activity was also studied over Ni/CGO by varying the inlet LPG/H_2O molar ratio from 1.0/1.0 to, 1.0/2.0, 1.0/4.0, 1.0/6.0 and 1.0/10.0. As shown in Fig. 6, it was found that H_2 and CO_2 increased with increasing inlet H_2O concentration, whereas CO, CH_4, C_2H_4 and C_2H_6 decreased. The changing of H_2, CO_2, and CO are due to the influence of water–gas shift reaction, whereas the decreasing in CH_4, C_2H_4 and C_2H_6 could be due to the further reforming with excess steam to generate more CO and H_2.

3.4. Activity toward LPG steam reforming with oxygen-containing feed

Ni/CGO and Ni/Al_2O_3 were selected for further studies by adding O_2 together with LPG and H_2O as oxidative steam reforming

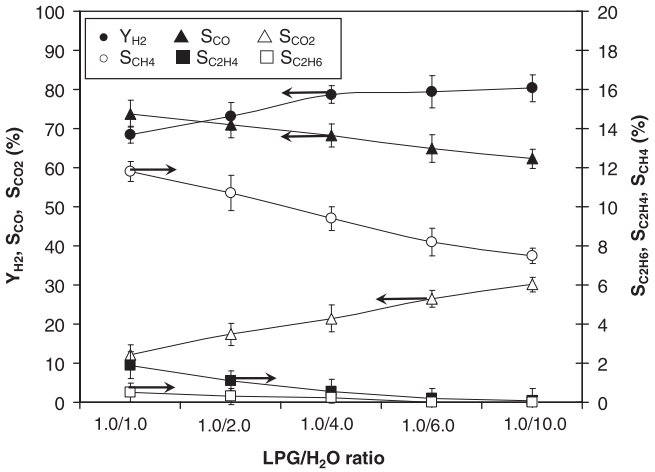

Fig. 6. Effect of inlet H_2O/LPG ratio on the product distributions from steam reforming of LPG over Ni/CGO at 900 °C.

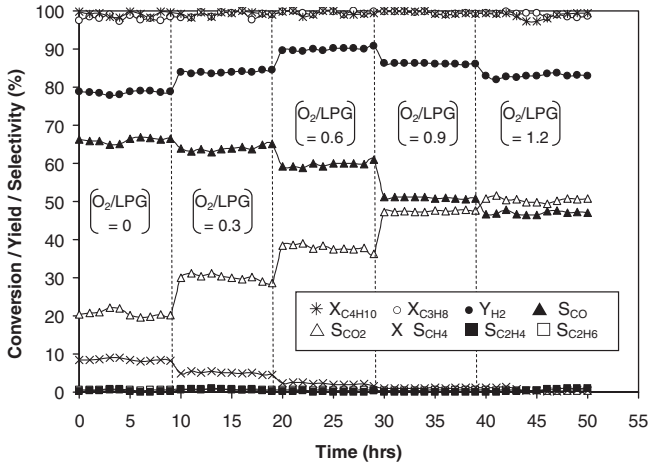

Fig. 7. Effect of O_2 adding on the conversions and product distributions from steam reforming of LPG over Ni/CGO at 900 °C.

operation. The inlet LPG/H_2O molar ratio was kept constant at 1.0/4.0, while the inlet O_2/LPG molar ratios were varied from 0 to 0.3, 0.6, 0.9 and 1.2. Fig. 7 shows the effect of O_2 on the H_2 yield and other by-product selectivities at 900 °C for Ni/CGO. It was found that the dependences of O_2 on H_2 yield are non-monotonic; the yield increased with increasing O_2/LPG molar ratio until the ratio reached 0.6 and oppositely decreased at higher O_2/LPG ratios. At the O_2/LPG ratio of 0.6, relatively higher H_2 yield (90.1%) with less CH_4, C_2H_4 and C_2H_6 selectivities were observed compared to the steam reforming operation. It is noted that similar trend was observed over Ni/Al_2O_3 but the optimum O_2/LPG ratio for this catalyst was 0.9, which enhances the highest H_2 yield of 50.9%. The post-reaction oxidation was then carried out to determine the degree of carbon formation on catalyst surface under this operation. As shown in Table 2, the quantities of carbon deposited significantly reduced with increasing O_2 content for both catalysts. Nevertheless, regarding the TPR experiments over the spent catalysts after exposure in the oxidative steam reforming condition, the addition of too high O_2 content could lead to the oxidation of Ni to NiO (Table 2).

Theoretically, the oxidation of O_2 with LPG can prevent the formation of C_2H_4 and C_2H_6 from the cracking of C_3H_8 and C_4H_{10}. In addition, O_2 can also prevent the formation of carbon species on

Table 2
Effect of O_2 adding on the amount of carbon formation and degree of catalyst reducibility after exposure at 900 °C for 10 h at each condition.

Catalyst	Inlet O2/LPG molar ratio	Carbon formation (mmol g_{cat}^{-1})	Metal-reducibility (%)
Ni/CGO	0.0	2.89 (2.91)*	94.1
	0.3	2.42 (2.40)	93.7
	0.6	1.73 (1.68)	93.0
	0.9	1.55 (1.52)	91.6
	1.2	1.24 (1.27)	89.5
Ni/Al_2O_3	0.0	4.64 (4.58)	94.5
	0.3	4.39 (4.32)	94.2
	0.6	4.05 (4.00)	93.6
	0.9	3.74 (3.71)	93.2
	1.2	3.52 (3.47)	91.4

* By carbon balance calculation.

the surface of catalyst by oxidizing these hydrocarbons. In the case of Ni/CGO, the presence of O_2 also helps steam to regenerate O_O^x on CGO surface ($0.5O_2 + V_{O..} + 2e' \rightarrow O_O^x$). Nevertheless, it was revealed that the amount of O_2 adding must be properly controlled since the addition of too high O_2 could oppositely decrease H_2 yield due to the oxidizing of Ni particle and the possible combusting of H_2 generated from the reaction.

3.5. Activity toward LPG steam reforming with hydrogen-containing feed

Instead of O_2, H_2 was added along with LPG and H_2O to the catalytic system. The inlet LPG/H_2O molar ratio was kept constant at 1.0/4.0, while the inlet H_2/LPG molar ratios were varied from 0.0 to 5.0. Since H_2 was fed at the inlet feed, the effect of this component adding on Ni/CGO and Ni/Al_2O_3 performances was investigated in term of other product selectivities (i.e., CO, CO_2, CH_4, C_2H_4, and C_2H_6). As shown in Fig. 8, for the case of Ni/CGO, the presence of CH_4 in the product gas decreases with increasing H_2 content, whereas CO production considerably increased. The increase of CO is due to the increasing of reverse water–gas shift reaction by adding H_2 to the system, whereas the decreases of CH_4 indicate the higher conversions of these components. Nevertheless, when H_2/LPG molar ratio reached 3.0 (5.0 for Ni/Al_2O_3), the effect of H_2 becomes less pronounce and then CH_4 slightly grow up. According to the post-reaction oxidation testing, the additional of H_2 reduces the amount of carbon deposited (as presented in Table 3), which could be due to the hydrogenation of carbon deposited on the catalyst surface by H_2 ($C\text{-}* + 2H_2 \rightarrow CH_4 + *$). By

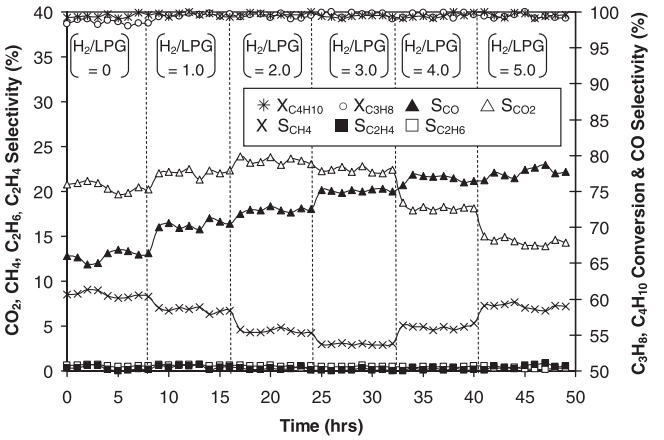

Fig. 8. Effect of H_2 adding on the conversions and product distributions from steam reforming of LPG over Ni/CGO at 900 °C.

Table 3
Effect of H_2 adding on the amount of carbon formation after exposure at 900 °C for 8 h at each condition.

Catalyst	Inlet H2/LPG molar ratio	Carbon formation s(mmol g_{cat}^{-1})
Ni/CGO	0.0	2.89 (2.91)*
	1.0	2.73 (2.71)
	2.0	2.54 (2.55)
	3.0	2.21 (2.17)
	4.0	2.10 (2.04)
	5.0	1.97 (1.91)
Ni/Al_2O_2	0.0	4.64 (4.58)
	1.0	4.55 (4.50)
	2.0	4.38 (4.39)
	3.0	4.12 (4.11)
	4.0	4.09 (4.07)
	5.0	3.74 (3.81)

* By carbon balance calculation.

adding higher H_2 content, the increase in CH_4 could be due to the influences of methanation and reverse methane steam reforming [35,36]. In addition, the occupying of H_2 atom on some active sites of Ni particle ($H_2 + 2* \leftrightarrow 2H\text{-}*$) could also lead to the decrease in CH_4 conversion due to the catalyst active site competition, as explained by Xu and Froment [35,36]. Furthermore, for the case of Ni/CGO, the additional of H_2 could inhibit the reaction of O_O^x with the absorbed surface carbon (Eq. (6)) and consequently lower the LPG reforming rate, as suggested in our previous reports [33,37].

4. Conclusions

Rh/CGO provided excellent activity toward the steam reforming of LPG in terms of high H_2 yield achievement and good resistance toward carbon deposition. Ni/CGO showed comparable reforming activity to Rh/Al_2O_3 but lower than Rh/CGO. We indicated that CGO support plays important role to improve the catalyst reforming activity and the resistance toward carbon deposition due to the occurring of gas–solid reactions between hydrocarbons and O_O^x on CGO surface along with the reaction taking place on the active site of metal catalyst (i.e., Ni and Rh). The additions of O_2 and H_2 along with LPG and H_2O can reduce the degree of carbon deposition and promote the conversion of hydrocarbons to CO and H_2. Nevertheless, the amount of these adding compounds must be properly controlled since the presence of too high O_2 could reduce H_2 yield from the reaction, while too high H_2 adding also decrease the catalyst activity.

Acknowledgement

The financial support from The Thailand Research Fund (TRF) throughout this project is gratefully acknowledged.

References

[1] Ahmed K, Gamman J, Föger K. Demonstration of LPG-fueled solid oxide fuel cell systems. Solid State Ionics 2002;152–153:485–92.
[2] Falkiner RJ. Liquefied petroleum gas. Glen Burnie, MD: ASTM International; 2003.
[3] Gökaliler F, Çağlayan BS, Önsan ZI, Aksoylu AE. Production by autothermal reforming of LPG for PEM fuel cell applications. Int J Hydrogen Energy 2008;33:1383–91.
[4] Suzuki T, Iwanami H, Iwamoto O, Kitahara T. Pre-reforming of liquefied petroleum gas on supported ruthenium catalyst. Int J Hydrogen Energy 2001;26:935–40.
[5] Avci AK, Trimm DL, Aksoylu AE, Önsan ZI. Ignition characteristics of Pt, Ni and Pt–Ni catalysts used for autothermal fuel processing. Catal Lett 2003;88:17–22.
[6] Ghenciu AF. Review of fuel processing catalysts for hydrogen production in PEM fuel cell systems. Curr Opinion Solid State Mater Sci 2002;6:389–99.
[7] Rampe T, Heinzel A, Vogel B. Hydrogen generation from biogenic and fossil fuels by autothermal reforming. J Power Sources 2000;86:536–41.
[8] Joensen F, Rostrup-Nielsen JR. Conversion of hydrocarbons and alcohols for fuel cells. J Power Sources 2002;105:195–201.
[9] Recupero V, Pino L, Vita A, Cipitı F, Cordaro M, Laganà M. Development of a LPG fuel processor for PEFC systems: laboratory scale evaluation of autothermal reforming and preferential oxidation subunits. Int J Hydrogen Energy 2005;30:963–71.
[10] Pino L, Vita A, Cipitì F, Laganà M, Recupero V. Performance of Pt/CeO_2 catalyst for propane oxidative steam reforming. Appl Catal A 2006;306:68–77.
[11] Mattos LV, Rodino E, Resasco DE, Possos FB, Noronha FB. Partial oxidation and CO_2 reforming of methane on Pt/Al_2O_3, Pt/ZrO_2, and Pt/Ce–ZrO_2 catalysts. Fuel Process Technol 2003;83:147–61.
[12] Roh HS, Jun KW, Park SE. Methane-reforming reactions over Ni/Ce-ZrO_2/θ-Al_2O_3 catalysts. Appl Catal A 2003;251:275–83.
[13] Rostrup-Nielsen JR, Bak-Hansen JH. CO_2-reforming of methane over transition metals. J Catal 1993;144:38–49.
[14] Wang X, Gorte RJ. A study of steam reforming of hydrocarbon fuels on Pd/ceria. Appl Catal A 2002;224:209–18.
[15] Roh HS, Jun KW, Dong WS, Chang JS, Park SE, Joe YI. Highly active and stable Ni/Ce–ZrO_2 catalyst for H_2 production from methane. J Mol Catal A 2002;181:137–42.
[16] Miao Q, Xiong G, Sheng S, Cui W, Xu L, Guo X. Partial oxidation of methane to syngas over nickel-based catalysts modified by alkali metal oxide and rare earth metal oxide. Appl Catal A 1997;154:17–27.
[17] Lemonidou AA, Goula MA, Vasalos IA. Carbon dioxide reforming of methane over 5 wt.% nickel calcium aluminate catalysts–effect of preparation method. Catal Today 1998;46:175–83.
[18] Dong WS, Roh HS, Jun KW, Park SE, Oh YS. Methane reforming over Ni/Ce-ZrO2 catalysts: effect of nickel content. Appl Catal A 2002;226:63–72.
[19] Mamak M, Coombs N, Ozin G. Mesoporous Yttria-Zirconia and metal-Yttria-Zirconia solid solutions for fuel cells. Adv Mater 2000;12:198–202.
[20] Mamak M, Coombs N, Ozin G. Self-assembling solid oxide fuel cell materials: mesoporous Yttria-Zirconia and metal-Yttria-Zirconia solid solutions. J Am Chem Soc 2000;122:8932–9.
[21] Mamak M, Coombs N, Ozin GA. AC impedance measurements on mesoporous nickel-Yttria-Zirconia solid oxide fuel cell materials. Chem Mater 2001;13:3564–70.
[22] Bera P, Mitra S, Sampath S, Hegde MS. Promoting effect of CeO_2 in a Cu/CeO_2 catalyst: lowering of redox potentials of Cu species in the CeO_2 matrix. Chem Commun 2001;10:927–8.
[23] Martinez-Arias A, Coronado JM, Cataluna R, Conesa JC, Soria JC. Influence of mutual platinum-dispersed ceria interactions on the promoting effect of ceria for the CO oxidation reaction in a Pt/CeO_2/Al_2O_3 catalyst. J Phys Chem B 1998;102:4357–65.
[24] Skarmoutsos D, Tietz F, Nikolopoulos P. Fuel cells: from fundamentals to systems. Fuel Cells 2001;1:243–8.
[25] Takeguchi T, Furukawa SN, Inoue M. Hydrogen spillover from NiO to the large surface area CeO_2–ZrO_2 solid solutions and activity of the NiO/CeO_2–ZrO_2 catalysts for partial oxidation of methane. J Catal 2001;202:14–24.
[26] Sfeir J, Philippe PA, Moseki P, Xanthopoulos N, Vasquez R, Hans JM, et al. Lanthanum chromite based catalysts for oxidation of methane directly on SOFC anodes. J Catal 2001;202:229–44.
[27] Kiratzis N, Holtappels P, Hatchwell CE, Mogensen M, Irvine JTS. Preparation and characterization of Copper/Yttria Titania Zirconia cermets for use as possible solid oxide fuel cell anodes. Fuel Cells 2001;1:211–8.
[28] Fornasiero P, Balducci G, Monte RD, Kaspar J, Sergo V, Gubitosa G, et al. Modification of the redox behaviour of CeO_2 induced by structural doping with ZrO_2. J Catal 1996;164:173–83.
[29] Imamura S, Shono M, Okamoto N, Hamada R, Ishida S. Effect of cerium on the mobility of oxygen on manganese oxides. Appl Catal A 1996;142:279–88.
[30] Fan L, Fujimoto K. Reaction mechanism of methanol synthesis from carbon dioxide and hydrogen on ceria-supported palladium catalysts with SMSI effect. J Catal 1997;172:238–42.
[31] Pijolat M, Prin M, Soustelle M, Touret O, Nortier P. Thermal stability of doped ceria-experimental and modeling. J Chem Soc Faraday Trans 1995;91:3941–8.
[32] Ramirez E, Atkinson A, Chadwick D. Reactivity of ceria, Gd- and Nb-doped ceria to methane. Appl Catal B 2002;36:193–206.
[33] Laosiripojana N, Assabumrungrat S. Catalytic dry reforming of methane over high surface area ceria. Appl Catal B 2005;60:107–16.
[34] Laosiripojana N, Assabumrungrat S. Hydrogen production from steam and autothermal reforming of LPG over high surface area ceria. J Power Sources 2006;158:1348–57.
[35] Xu J, Froment GF. Methane steam reforming, methanation and water–gas shift. 1. intrinsic kinetics. AIChE 1989;35:88–96.
[36] Xu J, Froment GF. Methane steam reforming. 2. diffusional limitations and reactor simulation. AIChE 1989;35:97–103.
[37] Laosiripojana N, Assabumrungrat S. Kinetic dependencies and reaction pathways in hydrocarbon and oxyhydrocarbon conversions catalyzed by ceria-based materials. Appl Catal B 2008;82:103–13.

Journal of Molecular Catalysis B: Enzymatic 73 (2011) 74–79

Contents lists available at ScienceDirect

Journal of Molecular Catalysis B: Enzymatic

journal homepage: www.elsevier.com/locate/molcatb

Biocatalytic esterification of palm oil fatty acids for biodiesel production using glycine-based cross-linked protein coated microcrystalline lipase

Marisa Raita [a], Thanaporn Laothanachareon [b], Verawat Champreda [b,*], Navadol Laosiripojana [a]

[a] Joint Graduate School for Energy and Environment (JGSEE), King Mongkut's University of Technology Thonburi, Bangmod, Bangkok 10140, Thailand
[b] Enzyme Technology Laboratory, National Center for Genetic Engineering and Biotechnology, 113 Thailand Science Park, Paholyothin Road, Klong Luang, Pathumthani 12120, Thailand

ARTICLE INFO

Article history:
Received 20 January 2011
Received in revised form 29 July 2011
Accepted 30 July 2011
Available online 17 August 2011

Keywords:
Biodiesel
Crosslinked protein coated microcrystals
Esterification
Lipase
Palm fatty acid distillate

ABSTRACT

Conversion of feedstocks containing high free fatty acid contents to alkyl esters is limited by the currently used alkali-catalyzed biodiesel synthesis process. In this study, esterification of palm fatty acids to ethyl esters was studied using heterogeneous cross-linked protein coated microcrystalline (CL-PCMC) lipase. Optimization of biocatalyst synthesis by variation of matrix components and organic solvents showed that highly active CL-PCMCs could be prepared from *Thermomyces lanuginosus* lipase with glycine as the core matrix in acetone. The optimized reaction contained 20% (w/w) glycine-based CL-PCMC-lipase, a 1:4 fatty acid molar equivalence to ethanol in the presence of an equimolar amount of *tert*-butanol which led to production of 87.2% and 81.4% (mol/mol) of ethyl ester from palmitic acid and industrial palm fatty acid distillate (PFAD), respectively after incubation at 50 °C for 6 h. CL-PCMC-lipase is more catalytically efficient than protein coated microcrystalline (PCMC) lipase, Novozyme®435 and Lipolase 100T for both free fatty acids and palm fatty acid distillate. The CL-PCMC-lipase showed high operational stability with no significant loss in product yield after 8 consecutive batch cycles. The glycine-based microcrystalline lipase is thus a promising alternative economical biocatalyst for biodiesel production from inexpensive feedstocks with high free fatty acid contents.

1. Introduction

Biodiesel is an alternative fuel for diesel engines produced mainly by transesterification of vegetable oils or animal fats with short chain alcohols. In Thailand and Southeast Asian countries, the main local feedstock for biodiesel production is purified palm oil (PPO), which is derived from refinery crude palm oil (CPO), a product of the palm oil processing industry. Typically, an alkali-catalyzed transesterification reaction is used for conversion of triacylglycerol in the feedstock to fatty acid alkyl esters. However, this process is sensitive to free fatty acids (FFAs), which cause undesirable saponification, leading to low product yields and complication in the subsequent separation steps [1]. Due to increasing demand of palm oil for biodiesel and food industry, the price of crude palm oil has been increasing in the past few years (1100 US$/ton in 2011). Conversion of cheaper alternative feedstocks to biodiesel is thus of interest in order to economically compete with petroleum-based fuel. Palm fatty acid distillate (PFAD) is a by-product from the refinement of CPO to PPO which has a high free fatty acid content. Typically, 3–10% of PFAD is obtained from crude palm oil, which is produced at 800,000 tons/year in Thailand, making it an economically promising feedstock for biodiesel production. The development of an efficient process to convert PFAD and feedstocks containing high FFAs to biodiesel is thus needed for improving the economics of the biodiesel industry.

Typically, conversion of FFAs to biodiesel can be carried out by acid-catalyzed esterification processes using strong acids, mostly H_2SO_4. However, a major limitation of the homogeneous acid catalyzed process is the difficulty in catalyst recovery and waste treatment, as well as corrosion of the equipment, which thus increase the overall cost of the process. Several alternative approaches for biodiesel production from feedstocks containing high FFA content have been reported, including heterogeneous acid catalyzed processes [2] and the non-catalytic or catalytic near- and super-critical methanol processes [3,4]. However, these approaches still have drawbacks due to high cost of the heterogeneous catalysts and the high energy consumption of the thermal processes. Research on a less energy-intensive and environmentally-friendly alternative process for biodiesel synthesis from PFAD or other feedstocks containing high FFA contents is thus of great interest.

Biocatalytic processes employing lipase biocatalysts have gained increasing interest for industrial biodiesel production [5]

Abbreviations: CL-PCMCs, crosslinked protein coated microcrystals; EtOH, ethanol; FFA, fatty acid; FAEE, fatty acid ethyl ester; PFAD, palm fatty acid distillate; *t*-BuOH, *tert*-butanol.

* Corresponding author. Tel.: +66 2564 6700x3473; fax: +66 2564 6707.
E-mail address: verawat@biotec.or.th (V. Champreda).

1381-1177/$ – see front matter © 2011 Elsevier B.V. All rights reserved.
doi:10.1016/j.molcatb.2011.07.020

which allows high conversion efficiency of feedstocks containing glycerides with high FFA contents under mild operational conditions with no requirement for subsequent wastewater treatment [6]. Development on enzymatic processes for biodiesel production has been focused on the cost reduction for lipases and improvement of the enzyme's operational time and reusability, which would benefit the commercialization of the biocatalytic process. Immobilization is a potential approach for optimizing the operational performance of enzymes and cost of biocatalysts in industrial processes, especially for non-aqueous systems. Enzyme immobilization by precipitation is a cost efficient approach for biocatalyst preparation for use in organic media. This alternative immobilization method involves several forms of biocatalysts including cross-linked enzyme aggregates (CLEAs) [7], cross-linked enzyme crystals (CLECs) [8], and protein-coated microcrystals (PCMCs) [9–12]. Recently, cross-linked PCMCs (CL-PCMCs) have been reported as an improved biocatalyst design based on conventional PCMCs [13]. CL-PCMCs are characterized as a cross-linked enzyme layer on the surface of micron-sized inner core matrix, which can be prepared by rapid dehydration and co-precipitation of enzyme and the matrix component in an organic solvent, the same as for conventional PCMC preparation, with an extra step on enzyme covalent crosslinking. CL-PCMCs possess several advantages over existing carrier-based or carrier-free immobilization methods, including a low mass-transfer limitation and high catalytic performance, with improved stability and reusability. In this study, the synthesis of CL-PCMC lipase biocatalysts has been optimized using various core matrices and precipitating organic solvents for efficient esterification of FFAs, used as model reactants and PFAD from palm oil industry. The effects of reaction parameters have been investigated based on the biocatalyst's reactivity on ethyl ester synthesis. The results of this study could be applied for synthesis of biodiesel from feedstocks with high fatty acid content, thus providing an economically and environmentally attractive approach for biodiesel production.

2. Materials and methods

2.1. Materials

Palm fatty acid distillate (PFAD) was obtained from the Pathum Vegetable Oil, Co. Ltd. (Pathumthani, Thailand). The PFAD sample contained 93% (w/w) free fatty acid (45.6% palmitic, 33.3% oleic, 7.7% linoleic as the major FFA) and the rest comprising triglycerides, diglycerides, monoglycerides and trace impurities. Free fatty acids (palmitic, oleic and linoleic acids) and fatty acid ester standards were obtained from Sigma–Aldrich. Liquid *Thermomyces lanuginosus* lipases, from genetically modified *Aspergillus* sp., DELIP 50L (50 KLU/g) was supplied by Flexo Research, Pathumthani, Thailand (1 KLU is defined as the amount of enzyme liberating 1 mmol of titratable butyric acid from tributyrin in 1 min). Lipase activity on *p*-nitrophenyl palmitate was assayed according to Raita et al. [12]. Novozymes® 435 (immobilized *Candida antarctica* lipase B) and Lipolase 100 T (granulated silica immobilized *T. lanuginosus* lipase) were from Novozymes (Bagsvaerd, Denmark). Chemicals and reagents were analytical grade and obtained from major companies. All reagents were dehydrated with 3 Å molecular sieves (Fluka, Buchs, Switzerland) before use.

2.2. Optimization of CL-PCMC-lipase preparation

CL-PCMC-lipase was prepared based on the method modified from Shah et al. [13] with modification on synthesis conditions and variation in core matrices and solvents. Commercial lipase preparation DELIP 50L (192 ml) was clarified by centrifugation (12,000 × *g*, 10 min) and pre-concentrated (3×, to 64 ml) using ultrafiltration on a Minimate tangential flow filtration system using a Minimate TFF capsule with 10 kDa MWCO membrane (Pall, Easthills, NY, USA). For optimization of CL-PCMC-lipase synthesis, 1.5 volume (96 ml) of a saturated solution of the matrix component (potassium sulphate, glucose, MOPS (3-morpholinepropanesulfonic acid), or glycine) was added to 1 volume of the concentrated lipase solution. This combined mixture was then added drop-wise to a stirring vial (150 rpm) containing 7.5 volume of organic solvent (acetone, ethanol, or *tert*-butanol). The precipitate was obtained by centrifugation at 2200 × *g* for 5 min and then washed thrice with 0.5 volume of the corresponding solvent. The enzyme precipitate (*i.e.* PCMCs) was resuspended in 160 ml of the solvent, followed by addition of 3.2 ml of glutaraldehyde (25% v/v in water). The mixture was incubated at 4 °C with stirring at 300 rpm for 1 h and then washed with the corresponding solvent. The air dried precipitate (265 mg from initial lipase solution of 1 ml) was used as the biocatalyst in this study. The protocol for preparation of the optimal glycine-based CL-PCMC-lipase is shown in Fig. 1. Protein content was determined at the PCMC stage with Bio-Rad protein assay reagent based on Bradford's method using bovine serum albumin as the standard.

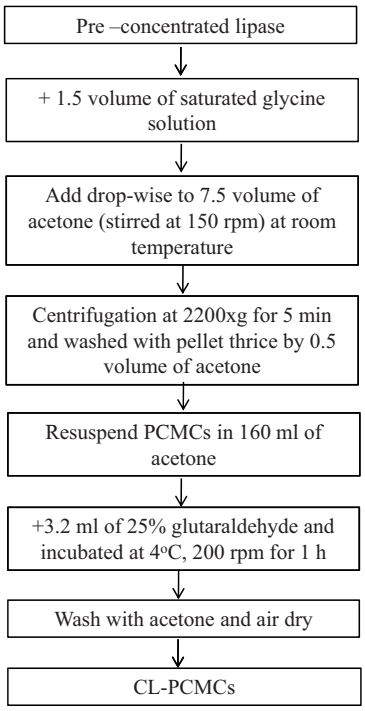

Fig. 1. Preparation of glycine-based CL-PCMC-lipase.

2.3. Lipase catalyzed esterification

For the optimized reaction, 250 mg of FFA or PFAD and ethanol was reacted in a molar ratio of 4:1 ([EtOH]/[FFA]) in the presence of *tert*-butanol at a 1:1 molar ratio ([*t*-BuOH]/[FFA]). The optimal CL-PCMC-lipase prepared with glycine and acetone was added at 20% (w/w based on FFA or PFAD) in the reaction and incubated at 50 °C on a vertical rotator. Samples were withdrawn at time intervals. The samples (2 μl) were diluted with hexane (10 μl) and mixed with lauric acid methyl ester (5 μl) as an internal standard. The amount of esters formed was then determined by gas chromatography according to Raita et al. [12]. The FAEE production yield (%) is the amount of fatty acid ethyl esters converted from available fatty acid equivalence (as FFAs and glycerides) on a molar basis. For reusability study, the biocatalyst was recovered by centrifugation,

washed with 1 ml of the organic solvent twice (if indicated), and air-dried before use in the next batch. The reactions were done in triplicate and standard deviations were reported for all experimental results.

2.4. Gas chromatography analysis of alkyl esters

The alkyl esters were analyzed by gas chromatography on a Shimadzu 2010, equipped with a flame ionization detector (Shimadzu, Kyoto, Japan) and a polyethylene glycol capillary column (Carbowax 20 M, 30 m × 0.32 mm, Agilent Technologies, Santa Clara, CA). The column oven temperature was at 200 °C, with injector and detector temperatures at 250 and 260 °C, respectively. Helium was used as the carrier gas at a constant pressure of 64.1 kPa with linear velocity at 25 cm/s. The amount of FAEE was determined based on the standard curves using the corresponding esters.

2.5. Physical analysis techniques

The structure and morphology of the CL-PCMC-lipase was analyzed by scanning electron microscope (SEM) using a JSM-6301F Scanning Electron Microscope (JEOL, Tokyo, Japan). The samples were dried and coated with gold for analysis. An electron beam energy of 5 kV was used for analysis. X-ray diffraction (XRD) data were collected at room temperature on a Rigaku TTRAX III X-ray diffractometer using Cu Kα radiation (λ = 1.5418 Å). The sample was scanned in the 2θ value of 10–45° at a rate of 2°/min.

3. Results and discussion

3.1. Optimization of CL-PCMC synthesis

In the first stage, the synthesis conditions for CL-PCMC-lipase biocatalyst were optimized based on their reactivity towards production of ethyl palmitate from palmitic acid used as a model reactant. *Thermomyces* (*Humilcola*) *lanuginosus* lipase was used for its high reactivity on biodiesel production from palm oil feedstock [12]. The 3× pre-concentrated enzyme in solution showed high hydrolysis activity towards *p*-nitrophenyl palmitate with the specific activity of 6.93×10^{-3} IU/mg equivalent to the volumetric activity of 0.27 IU/ml, and was used for preparation of CL-PCMC conjugate. Two key factors for CL-PCMC synthesis were investigated, namely (i) the matrix components, which were selected to represent inorganic and organic matrices (K_2SO_4, glucose, MOPS, and glycine) and (ii) the precipitating organic solvents (ethanol, *tert*-butanol, and acetone). The reactions were optimized based on ethanolysis due to the *T. lanuginosus* lipase's higher stability in ethanol in comparison to methanol, which showed inactivation effect to the lipase from *T. lanuginosus* [12]. The use of ethanol as nucleophile is also advantageous for the development of green biodiesel, where all the reactants are from recyclable biological sources.

The highest reactivity of lipase biocatalyst was obtained using glycine as the matrix component with acetone as the precipitating organic solvent (Table 1). The glycine-based CL-PCMCs formed fine crystalline particles and had the protein content of 155 μg/mg of CL-PCMCs. This optimized combination led to FAEE synthesis at 85.0% yield after 6 h in the presence of *tert*-butanol under the optimal synthesis conditions while the control reaction with no biocatalyst led to no detectable products under the same conditions. Lower FAEE yields were obtained with glycine-based CL-PCMCs using ethanol and *tert*-butanol as the precipitating solvents or CL-PCMCs prepared using other matrix components. K_2SO_4 is the most commonly used matrix for synthesis of several forms of biocatalyst *e.g.* PCMCs and CL-PCMCs of various enzymes [10,12,13]. However, lower FAEE yields were obtained

Table 1
Optimization of CL-PCMC synthesis. CL-PCMC-lipases were prepared with different matrix component in different organic solvents.

Matrix component	FAEE yield (%)		
	Acetone	Ethanol	*tert*-Butanol
K_2SO_4	69.9 ± 3.3	74.7 ± 3.3	73.6 ± 2.2
Glucose	67.2 ± 2.5	49.8 ± 1.2	NA
MOPS	45.9 ± 1.5	NA	NA
Glycine	85.0 ± 2.3	17.5 ± 0.2	27.0 ± 0.7

The reactions contained 250 mg of palmitic acid, 4:1 [EtOH]/[FFA] molar ratio, in the presence of 1:1 [*t*-BuOH]/[FFA] molar ratio with 20% (w/w) CL-PCMC-lipase. The reactions were incubated at 50 °C for 6 h.
NA: not analyzed due to no or low amount of CL-PCMCs obtained.

for the K_2SO_4-based CL-PCMC-lipase prepared using different solvents (range: 69.9–74.7%). Glucose and MOPS were found to be unsuitable matrix for CL-PCMC-lipase preparation due to their lower catalytic efficiency per weight basis and the low amount of biocatalysts obtained after precipitation. Different core matrices including salts, sugars, amino acids, and inorganic/organic buffer substances with protic or aprotic solvents were previously used for optimization of PCMC synthesis from various enzymes [14,15]. Amino acids, including L-glutamine and DL-valine were previously used for preparation of PCMCs for biocatalysts and for vaccine formulation [9,16,17]. The effects of core matrix components in microcrystalline biocatalyst preparation are generally dependent on manipulation of the micro-environment of the enzyme and the physical properties and morphology of the carrier, which are the result of the intrinsic properties of the carrier, coupled with the choice of precipitating solvent [14]. Matrix components prepared from solid-state buffer substances as the core matrix have been reported to give biocatalysts with improved reactivity and stability as demonstrated for PCMCs of subtilisin prepared with organic or inorganic buffer carriers (either as a mixture of the Na^+ salt and the zwitterionic form or as a one-component solid state buffer *e.g.* Na-AMPSO, $NaCO_3$, and $NaHCO_3$) in comparison to that prepared using the non-buffered inert K_2SO_4 [14]. In PCMCs, the intimate association of the enzyme and solid-state buffer compound would allow efficient equilibration of the ionization state of the biocatalyst. To our knowledge, our study is the first report on the use of zwitterionic glycine as the core matrix for biocatalyst synthesis for application in water immiscible organic solvent systems. Addition of external glycine/Na^+ salt was previously used for ionization state control for biocatalysis in organic media [18]. However, due to the use of only the zwitterioinic form of glycine and its pK_a in aqueous system, the mechanism of improved catalytic performance of the optimized glycine-based CL-PCMC lipase may not be clearly understood based on the hypothesis on ionization state control of the enzyme by solid-state buffer. The finding thus suggested further detailed study on the roles of core matrix component and its interaction with the enzyme in CL-PCMC preparation. Acetone was used as the precipitating solvent for preparation of various forms of lipase biocatalyst *e.g.* PCMCs [10,12], CL-PCMCs [13], and acetone rinsed enzyme preparation (AREP) [19]. The preference of acetone as the precipitating solvent to a series of alcohols with different polarities was different to that reported for preparation of different biocatalyst designs *e.g. n*-propanol for PCMCs of subtilisin [9,14] and 1,2-dimethoxyethane for enzymes prepared and rinsed with organic solvent (EPROS) of lipases [20]. The result thus suggests the prerequisite to screen the best combination of the core matrix and precipitating solvent for obtaining a high performance biocatalyst for a specific process in organic media.

The physical characteristics of CL-PCMC-lipase were examined using SEM (Fig. 2). The biocatalysts had a variable size distribution in the micron size range of 10–20 μm. The overall surface of CL-PCMC-lipase was different to the glycine salt control, which showed

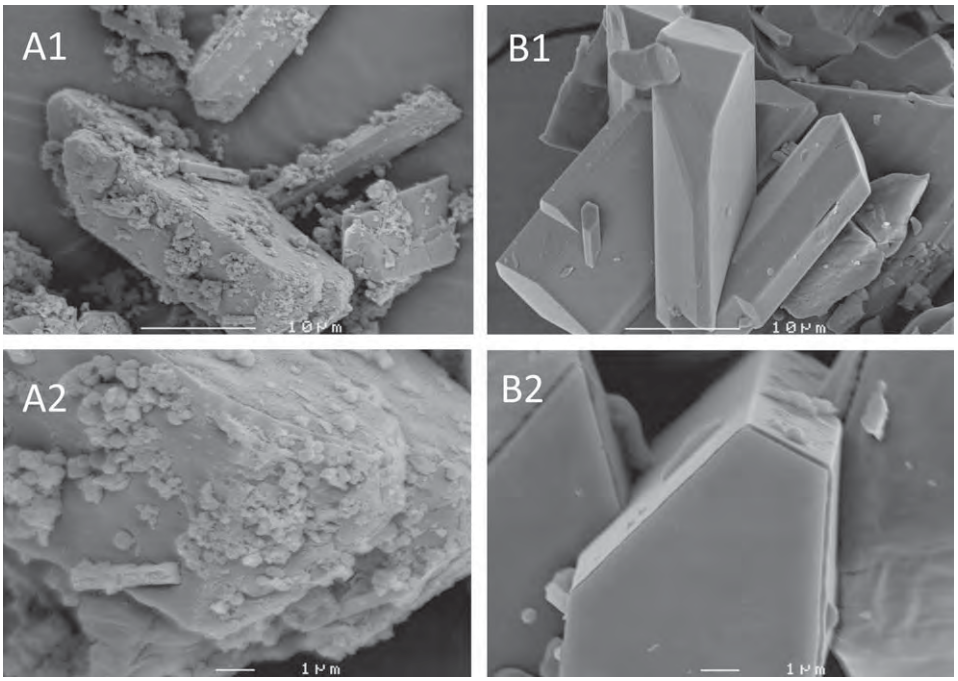

Fig. 2. SEM analysis of CL-PCMC-lipase. (A) CL-PCMC-lipase prepared from glycine in acetone; (B) glycine crystals control, no lipase added.

a homogeneous monoclinic crystal structure. The biocatalysts were formed as protein aggregates on the glycine crystal surface, suggestive of enzyme molecule aggregation on the amino acid crystals. XRD analysis showed that the glycine-based CL-PCMCs were highly crystalline (Fig. 3). Signature peaks of α-glycine were identified (JCPDS number 32-1702), reflecting crystal structure of the core matrix. The formation of enzyme layer on the salt crystals in CL-PCMCs results in higher exposed reactive surface area of the biocatalyst (based on the same enzyme content on weight basis) and lower mass transfer limitation to the lipase active site in comparison to CLEAs or CLECs [7,8]. However, characterization of the biocatalyst surface area using BET surface area analysis was limited by the low melting temperature of glycine.

3.2. Effects of reaction parameters on esterification

Initial trials on optimization of the operational conditions for biodiesel synthesis were focused on the effects of nucleophile and co-solvent ratios to free fatty acids based on esterification of palmitic acid (Fig. 4). Systematic optimization of ethanol and *tert*-butanol contents was investigated for all combinations. The reaction temperature in this study was set at 50 °C to allow complete solubilization of FFAs. In most cases, increasing the ethanol:FFAs ratio led to increased FAEE yields at all *tert*-butanol ratios. The optimal [EtOH]/[FFA] ratio of 4:1 is comparable to previous reports on biocatalytic transesterification of different vegetable oils [11,12]. The presence of *tert*-butanol at a 1:1 molar ratio ([*t*-BuOH]/[FFA]) in the reaction led to an increase in FAEE yield from 78.1% in the solvent-free system to 84.4% at the optimal [EtOH]/[FFA] ratio. However, further increase of *tert*-butanol led to lower FAEE yields when compared at the same ethanol content. A sharp increase in FAEE yield was observed during the early phase of incubation, leading to >95% of the maximized conversion yields after 6 h incubation at 50 °C (Fig. 5). CL-PCMC-lipase loading at 20% (w/w) based on FFA was found to be optimal (data not shown). The biocatalyst loading in this study was in the same range (4–50%)

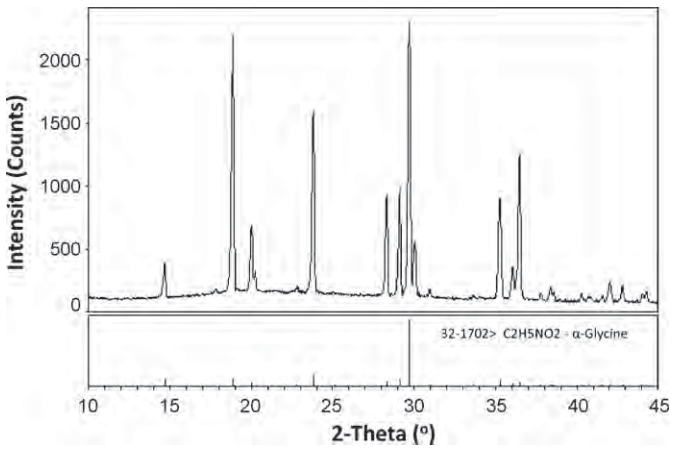

Fig. 3. X-ray diffraction analysis of glycine-based CL-PCMC-lipase. Reference XRD pattern of α-glycine (JCPDS number 32-1702) is shown in the lower panel.

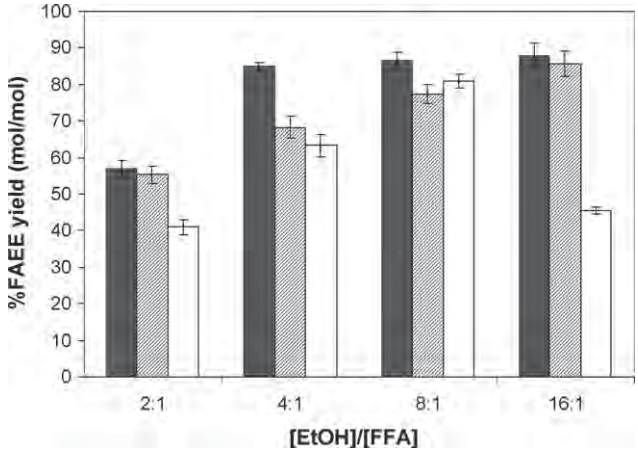

Fig. 4. Effects of nucleophile and co-solvent concentrations on FAEE synthesis. The reactions contained 250 mg of palmitic acid as the substrate with 20% (w/w) CL-PCMC-lipase with varying ethanol and *tert*-butanol ratios to FFA. The reactions were incubated at 50 °C for 6 h. [*t*-BuOH]/[FFA] = 1:1 (black); 2:1 (shaded); and 4:1 (white).

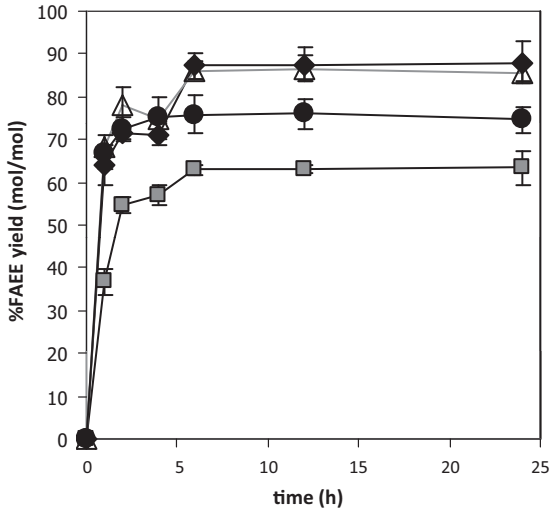

Fig. 5. Reactivity of CL-PCMC-lipase on biodiesel synthesis from FFAs and PFAD. The reactions contained 250 mg of FFAs or PFAD, 4:1 [EtOH]/[FFA] molar ratio, in the presence of 1:1 [*t*-BuOH]/[FFA] molar ratio with 20% (w/w) CL-PCMC-lipase. The reactions were incubated at 50 °C. Substrate: Palmitic acid (diamond); Oleic acid (square); Linoleic (triangle); and PFAD (circle).

as those previously reported using different forms of immobilized lipase on transesterification [10,12,21,22]. The optimal reaction conditions for CL-PCMC-lipase catalyzed reactions were thus at 4:1 [EtOH]/[FFA] in the presence of 1:1 [*t*-BuOH]/[FFA] as the co-solvent with CL-PCMC-lipase loading at 20% (w/w) and incubation at 50 °C for 6 h. The optimal conditions were used for subsequent experiments in this study.

The trend observed of increasing FAEE yield with increasing nucleophile concentration is the opposite to that previously reported for transesterification of refined palm olein using PCMC-lipase [12]. This can be explained by different sensitivity of the biocatalysts to the nucleophile (ethanol) in the reaction, involving deactivation effect on the biocatalyst contact of the lipases with the immiscible polar organic phase [21]. Although a decrease in FAEE yield might be observed at a very high nucleophile and co-solvent ratio, the results shown here suggest an improved ethanol tolerance of CL-PCMC for esterification reactions compared to the conventional PCMCs.

The enhancing effect of *tert*-butanol in the reaction medium has been reported for different forms of immobilized lipases *e.g.* PCMCs and whole-cell biocatalysts for transesterification of triacylglyceride based feedstocks [23–25]. The optimal equimolar ratio of *tert*-butanol and FFA is similar to the previous studies using PCMC-lipase [12] and lower than that for the commercial immobilized lipases and whole-cell biocatalysts in which 1–1.5:1 volume ratio of the co-solvent to oil feedstock was used [23,24]. Addition of *tert*-butanol to the reaction mixture was shown to increase catalytic activity and operational stability of lipases, resulting in increasing conversion yields [23,26]. The activation and stabilization of lipases in esterification could be due to the effects of *tert*-butanol on lipase stabilization from the nucleophile inactivation by linear low molecular weight alcohols [25]. To our knowledge, although the catalysis and stability enhancing effects of *tert*-butanol have been shown for lipase-catalyzed transesterification and whole-cell catalyzed esterification of FFAs [23,27], this study is the first to demonstrate these effects on precipitation-based immobilized lipases in esterification of FFAs on the biodiesel synthesis reaction.

The potential of CL-PCMC-lipase on esterification of FFAs and PFAD was compared with other types of immobilized lipases under the same enzyme loading (20%) and reaction conditions (Fig. 6). CL-PCMC-lipase led to high FAEE yields from palimitic acid (87.1%) and PFAD (81.4%). Ethyl palmitate shared the highest fraction in the esterification product from PFAD in comparison with ethyl oleate and ethyl linoleate, reflecting the FFA composition in PFAD and the biocatalyst reactivity towards different FFAs. The FAEE yields from CL-PCMC-lipase were higher than those using PCMC-lipase prepared on glycine in acetone (75.7% and 67.5% for palmitic and PFAD, respectively), suggesting the additional effects of crosslinking in higher performance of CL-PCMCs and also the widely used immobilized *Candida antarctica* lipase (Novozyme®435) (79.5% and 63.3% for palmitic acid and PFAD, respectively). In contrast, Lipolase 100T led to low FAEE yields from both substrates. PCMC-lipase prepared on K_2SO_4 showed the optimal operational temperature at 45 °C [12] suggesting partial inactivation of PCMC-lipase at 50 °C. The higher product yields from CL-PCMCs could thus be partially due to the improved thermostability of the biocatalyst in comparison with PCMCs by the effect of enzyme molecule crosslinking [13]. Addition of molecular sieve for continuous removal of water from the reaction led to no significant increase in FAEE yields from FFAs and PFAD, which was in contrast to some previous reports in which simultaneous dehydration resulted in significant improved product yields [27,28]. This would suggest the less sensitivity of CL-PCMC-lipase on water activity in esterification of FFAs. In overall, the reactivity of the glycine-based CL-PCMC-lipase in this study was comparable to that of various forms of immobilized lipases for esterification of feedstock

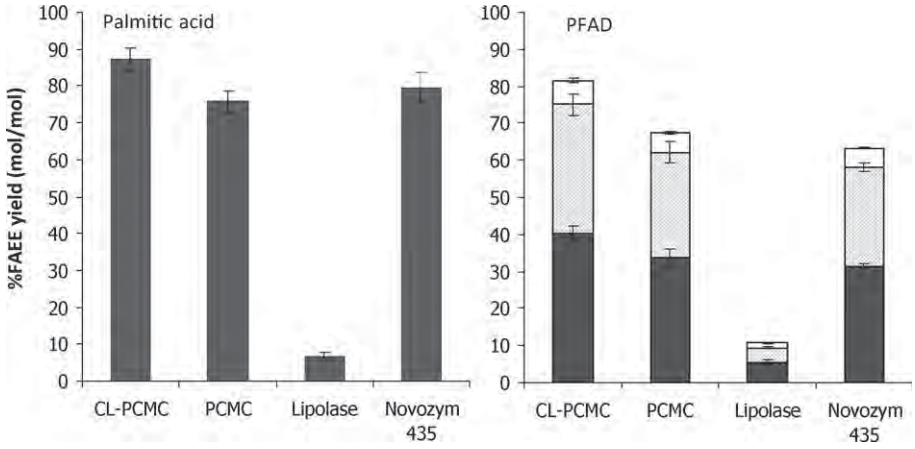

Fig. 6. Comparison of FAEE synthesis using different immobilized lipases. The reactions contained 250 mg of palmitic acid or PFAD, 4:1 [EtOH]/[FFA] molar ratio, in the presence of 1:1 [*t*-BuOH]/[FFA] molar ratio with 20% (w/w) CL-PCMC-lipase. The reactions were incubated at 50 °C for 6 h. CL-PCMC: CL-PCMC-lipase prepared from glycine in acetone; PCMC: PCMC-lipase prepared from glycine in acetone. FAEE products: ethyl palmitate (black); ethyl oleate (shaded); and ethyl linoleate (white).

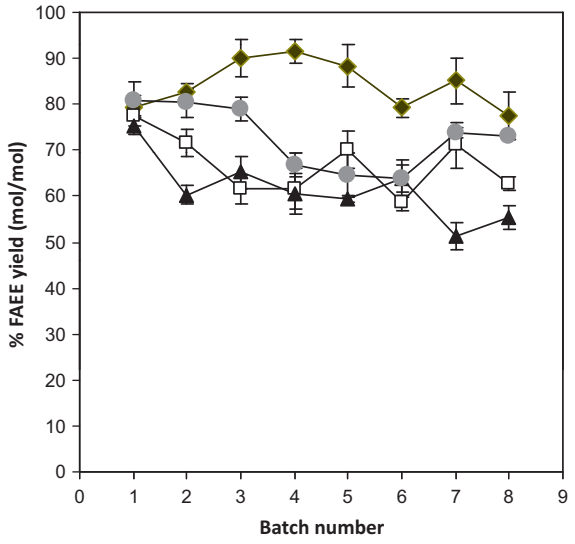

Fig. 7. Stability of CL-PCMC-lipase in consecutive batch reactions. CL-PCMC-lipase was reused in consecutive batch reactions with or without organic solvent treatment. The reactions contained 250 mg of palmitic acid, 4:1 [EtOH]/[FFA] molar ratio, in the presence of 1:1 [*t*-BuOH]/[FFA] molar ratio with 20% (w/w) CL-PCMC-lipase. The reactions were incubated at 50 °C for 6 h. CL-PCMC-lipase was treated by washing with 1 ml of the solvent twice before using in the consecutive batch. No solvent wash treatment (diamond); ethanol (square); *n*-propanol (triangle), and *tert*-butanol (circle).

containing high FFA content *e.g.* soybean oil deodorizer distillate [29] and used palm oil [30], although this cannot be directly compared due to the sensitivity of biocatalysts to the feedstock (*i.e.* type of substrates and contaminants) and reaction conditions. The high conversion yields thus demonstrated the potential of the glycine-based CL-PCMC-lipase as an economical heterogeneous biocatalyst for biodiesel production by esterification of FFAs in feedstocks.

3.3. Reusability of CL-PCMC-lipase

The reusability of CL-PCMC-lipase was studied by analyzing the conversion efficiency after consecutive batch cycles under the optimal reaction conditions (Fig. 7). CL-PCMC-lipase showed high stability in esterification of palmitic acid with no significant alteration in FAEE yield for at least 8 consecutive batch processes with the average product yields of 84.8% ± 5.0%. Treatment by organic solvents with different polarities (ethanol, *n*-propanol and *tert*-butanol) led to no improvement on FAEE yields, leading to 62.7, 55.3, and 73.0% FAEE yield in batch 8. The effect of *tert*-butanol on the biocatalyst stability was different to the K_2SO_4-based PCMC-lipase, in which *tert*-butanol treatment led to improved stability of the biocatalyst in consecutive batches of palm olein transesterification [12]. This could be due to the nucleophilic deactivation effect of short chain alcohols, particularly ethanol and propanol on the biocatalyst stability. The result thus suggested the potential of recycling CL-PCMC-lipase in further consecutive batch process development with no additional organic solvent treatment.

4. Conclusion

Biocatalytic synthesis by CL-PCMC-lipase is considered a promising approach for biodiesel production from feedstocks containing high FFA contents. The optimized process led to high product yields comparable to those previously reported for acid-catalyzed [31], thermocatalytic [4] and whole-cell biocatalytic methods [25]; however, with its key advantages over the existing methods, including mild operating conditions and low catalyst preparation cost. The use of glycine as the core matrix for precipitation-based immobilized enzyme was reported, suggesting the potential on using glycine as the core matrix component for preparation of high performance CL-PCMCs for catalysis in non-aqueous systems. The biocatalytic process developed in this study thus provides a promising approach for production of biodiesel from inexpensive feedstocks with high FFA contents. Further development of the CL-PCMC-lipase based processes would lead to an improvement on the process economics of biodiesel industry.

Acknowledgements

This project was supported by the Discovery Based Development Grant from the National Science and Technology Development Agency and Thailand Research Fund. Raita M. was supported by the Royal Golden Jubilee Scholarship. Manuscript proofreading by Dr. Philip James Shaw is appreciated. The authors also would like to thank Ms. Suphakan Kijamnajsuk, National Center for Metal and Material Technology for XRD analysis.

References

[1] J. Van Gerpen, Fuel Proc. Technol. 86 (2005) 1097–1107.
[2] P. Mongkolbovornkij, V. Champreda, W. Sutthisripok, N. Laosiripojana, Fuel Proc. Technol. 91 (2010) 1510–1516.
[3] D. Yujaroen, M. Goto, M. Sasaki, A. Shotipruk, Fuel 88 (2009) 2011–2016.
[4] A. Petchmala, N. Laosiripojana, B. Jongsomjit, M. Goto, J. Panpranot, O. Mekasuwandumrong, A. Shotipruk, Fuel 89 (2010) 2387–2392.
[5] A. Robles-Medina, P.A. González-Morino, L. Esteban-Cerdán, E. Molina-Grima, Biotechnol. Adv. 27 (2009) 398–408.
[6] Y. Shimada, Y. Watanabe, A. Sugihara, Y. Tominaga, J. Mol. Catal. B: Enzym. 17 (2002) 133–142.
[7] S. Shah, A. Sharma, M.N. Gupta, Anal. Biochem. 351 (2006) 207–213.
[8] T.S. Lee, J.D. Vaghjiani, G.J. Lye, M.K. Turner, Enzym. Microb. Technol. 26 (2000) 582–592.
[9] M. Kreiner, B.D. Moore, M.C. Parker, Chem. Commun. (2001) 1096–1097.
[10] S. Shah, A. Sharma, D. Varandani, B. Mehta, M.N. Gupta, J. Nanosci. Nanotechnol. 7 (2007) 2157–2160.
[11] V. Kumari, S. Shah, M.N. Gupta, Energy Fuels 21 (2007) 368–372.
[12] M. Raita, V. Champreda, N. Laosiripojana, Proc. Biochem. 45 (2010) 829–834.
[13] S. Shah, A. Sharma, M.N. Gupta, Biocatal. Biotrans. 26 (2008) 266–271.
[14] M. Kreiner, M.C. Parker, Biotechnol. Bioeng. 87 (2004) 24–33.
[15] J.C. Wu, J.X. Yang, S.H. Zhang, Y. Chow, M.M.R. Talukder, W.J. Choi, Biocatal. Biotrans. 27 (2009) 283–289.
[16] S. Murdan, S. Somavarapu, A.C. Ross, H.O. Alpar, M.V. Parker, Int. J. Pharm. 296 (2005) 117–121.
[17] A. Khosravani, M.-C. Parker, R. Parton R., J. Coote, Vaccine 25 (2007) 4361–4367.
[18] N. Harper, M. Dolman, B.D. Moore, P.J. Halling, Chem. Eur. J. 6 (2000) 1923–1929.
[19] S. Shah, M.N. Gupta, Bioinorg. Med. Chem. Lett. 17 (2007) 921–924.
[20] K. Solkanki, M.N. Gupta, Bioinorg. Med. Chem. Lett. 21 (2011) 2934–2936.
[21] E. Hernández-Mártin, C. Otero, Bioresour. Technol. 99 (2008) 277–286.
[22] A. Salis, M. Pinna, M. Monduzzi, V. Solinaz, J. Mol. Catal. B: Enzym. 54 (2008) 19–26.
[23] L.L. Li, W. Du, D.H. Liu, J. Mol. Catal. B: Enzym. 43 (2006) 58–62.
[24] L. Li, W. Du, D. Liu, Proc. Biochem. 43 (2007) 1481–1485.
[25] W. Du, D. Liu, L. Li, D. Dai, Biotechnol. Prog. 23 (2007) 1087–1090.
[26] D. Royon, M. Daz, G. Ellenrieder, S. Locatelli, Bioresour. Technol. 98 (2007) 648–653.
[27] W. Li, W. Du, D. Liu, Energy Fuels 22 (2008) 155–158.
[28] L. Wang, W. Liu, D. Liu, L. Li, N. Dai, J. Mol. Catal. B: Enzym. 43 (2006) 29–32.
[29] M.S. Souza, E.C.G. Aguieiras, M.A.P. Da Silva, M.A.P. Langone, Appl. Biochem. Biotechnol. 154 (2009) 253–267.
[30] K. Tongboriboon, B. Cheirsilp, A. H-Kittikun, J. Mol. Catal. B: Enzym. 67 (2010) 52–59.
[31] S. Chongkhong, C. Tongurai, P. Chetpattananondh, C. Bunyakan, Biomass. Bioener. 31 (2007) 563–568.

Partial Oxidation of Palm Fatty Acids Over Ce-ZrO_2: Roles of Catalyst Surface Area, Lattice Oxygen Capacity and Mobility

Navadol Laosiripojana
The Joint Graduate School of Energy and Environment, CHE Center for Energy Technology and Environment, King Mongkut's University of Technology Thonburi, Bangkok 10140, Thailand

Worapon Kiatkittipong
Dept. of Chemical Engineering, Faculty of Engineering and Industrial Technology, Silpakorn University, Nakhon Pathom 73000, Thailand

Suttichai Assabumrungrat
Dept. of Chemical Engineering, Faculty of Engineering, Chulalongkorn University, Bangkok 10330, Thailand

DOI 10.1002/aic.12491
Published online in Wiley Online Library (wileyonlinelibrary.com).

Nanoscale Ce-ZrO_2, synthesized by cationic surfactant-assisted method, has useful partial oxidation activity to convert palm fatty acid distillate (PFAD; containing C_{16}–C_{18} compounds) to hydrogen-rich gas with low carbon formation problem under moderate temperatures. At 1123 K with the inlet O/C ratio of 1.0, the main products from the reaction are H_2, CO, CO_2, and CH_4 with slight formations of gaseous high hydrocarbons (i.e., C_2H_4, C_2H_6, and C_3H_6), which could all be eliminated by applying higher O/C ratio (above 1.25) or higher temperature (1173 K). Compared with the microscale Ce-ZrO_2 synthesized by conventional coprecipitation method, less H_2 production with relatively higher C_2H_4, C_2H_6, and C_3H_6 formations are generated from the reaction over microscale Ce-ZrO_2. The better reaction performances of nanoscale Ce-ZrO_2 are linearly correlated with its higher specific surface area as well as higher oxygen storage capacity and lattice oxygen mobility, according to the reduction/oxidation measurement and $^{18}O/^{16}O$ isotope exchange study. © 2010 American Institute of Chemical Engineers *AIChE J*, 00: 000–000, 2010

Keywords: palm fatty acid distillate, hydrogen, partial oxidation, reforming, Ce-ZrO_2

Introduction

Hydrogen-rich gas is the major fuel for solid oxide fuel cell, which can be readily produced from the reactions of several hydrocarbons, i.e., methane, methanol, ethanol, liquefied petroleum gas, gasoline, and other oil derivatives with oxygen-containing coreactants, i.e., O_2, H_2O, and CO_2. Partial oxidation, steam reforming, and the combination of both reactions (as called autothermal reforming) have been known as feasible processes to produce hydrogen-rich fuel from several hydrocarbons.[1,2] Steam reforming is currently the most common process for producing hydrogen[1]; however, it has a disadvantage of slow startup, which makes it more suitable for a stationary system rather than for a mobile system.[2] Recently, catalytic partial oxidation[3–6] and autothermal reforming[7,8] appear to have attracted much interest. The partial oxidation consists of substoichiometric oxidation of hydrocarbons, whereas the autothermal reforming integrates

Correspondence concerning this article should be addressed to N. Laosiripojana at navadol_l@jgsee.kmutt.ac.th.

partial oxidation with steam reforming. Theoretically, both partial oxidation and autothermal reforming offer significant lower energy requirement and higher gas-space velocity than steam reforming reaction.[9]

Focusing on fuel selection, because of the current oil crisis and shortage of fossil fuels, the development of H_2 production process from biomass-based feedstock attracts much attention. Among them, palm oil is one of the current attractive feedstocks that has widely been converted to transportation fuel (e.g., biodiesel via transesterification process). Generally, crude palm oil (CPO) always contains high amount of free fatty acid (FFA), and the presence of too high FFA could easily result in high amounts of soap produced during the transesterification reaction. To avoid this reaction, FFA must be initially removed from CPO (as called palm fatty acid distillate or PFAD). The conversion of this PFAD to valuable products, e.g., hydrogen-rich gas would provide the great benefit in terms of energy and environmental aspects as well as reducing the cost of biodiesel production, enabling biodiesel to compete economically with conventional petroleum diesel fuels. Practically, PFAD consists mainly of palmitic acid ($C_{16}H_{32}O_2$: $CH_3(CH_2)_{14}COOH$), oleic acid ($C_{18}H_{34}O_2$: $CH_3(CH_2)_7CH{=}CH(CH_2)_7COOH$), and linoleic acid ($C_{18}H_{32}O_2$: $CH_3(CH_2)_4CH{=}CHCH_2CH{=}CH(CH_2)_7CO_2H$) with various ratios depending on the source of oils. These high hydrocarbon compounds should be efficiently used as the feedstock for H_2 production. Nevertheless, until now, only a few works have presented the catalytic reforming or cracking of acetic acid and/or heavy hydrocarbons to H_2.[10-12] Theoretically, the major difficulty to reform the heavy hydrocarbon compounds like PFAD is the possible degradation of catalyst due to the carbon deposition as PFAD can homogenously decompose to several gaseous hydrocarbon elements, which could further decompose to carbon species and deposit on the surface of catalyst.

In this work, Ce-ZrO_2 was applied as oxidative catalyst because ceria-based materials were known as an alternative reforming catalyst, which can reform hydrocarbons and oxyhydrocarbons efficiently with high resistance toward carbon formation because of their high oxygen storage capacity (OSC) and redox property.[13–19] The addition of zirconium oxide (ZrO_2) to ceria has also been known to improve the specific surface area, the OSC, the redox property, the thermal stability and the catalytic activity of ceria.[20–26] In this study, Ce-ZrO_2 was mainly prepared by cationic surfactant-assisted method because we previously reported the achievement of nanoscale material with high surface area and good stability from this preparation technique, which is mainly due to the interaction of hydrous oxide with cationic surfactants under basic condition.[27,28] It is noted that the performances of Ce-ZrO_2 prepared by this method in terms of partial oxidation activity, resistance toward carbon formation, and the redox properties (i.e., OSC and lattice oxygen mobility) were also compared with those of Ce-ZrO_2 synthesized by the typical coprecipitation method.

Experimental

Raw material

PFAD was obtained from Chumporn Palm Oil Industry Public Company, Thailand. It consists of 93 wt % FFA (mainly contains 46% palmitic acid, 34% oleic acid, and 8% linoleic acid with small amount of other fatty acids, i.e., stearic, myristic, tetracosenoic, linolenic, ecosanoic, ecosenoic, and palmitoleic acid). The rest of the elements are triglycerides, diglycerides, monoglycerides, and traces of impurities.

Catalyst preparation and characterization

Ce-ZrO_2 was chosen as an oxidative catalyst in this work. The materials with different Ce/Zr molar ratios were prepared by coprecipitation of cerium nitrate ($Ce(NO_3)_3{\cdot}H_2O$) and zirconium oxychloride ($ZrOCl_2{\cdot}H_2O$) (from Aldrich) in the presence of 0.1 M cetyltrimethylammonium bromide solution (from Aldrich) as a cationic surfactant. The ratio between both solutions was altered to achieve Ce/Zr molar ratios of 1/3, 1/1, and 3/1, whereas the molar ratio of (([Ce]+[Zr])/[cetyltrimethylammonium bromide] was kept constant at 0.8. The solid solution was formed by the slow mixing of this metal salt solution with 0.4 M urea. After preparation, the precipitate was filtered and washed with deionized water and ethanol to prevent an agglomeration of the particles. It was dried overnight in an oven at 383 K and then calcined in air at 1173 K for 6 h. According to the preparation of Ce-ZrO_2 by coprecipitation method, similar procedure as described above without adding of cetyltrimethylammonium bromide solution was applied. From the preparations, high specific surface area Ce-ZrO_2 (with the specific surface area of 46.5, 47, and 49 $m^2\ g^{-1}$ for the catalysts with Ce/Zr of 3/1, 1/1, and 1/3, respectively) and average particle size of 50–80 nm (less than 100 nm; so-called nanoscale Ce-ZrO_2) can be achieved from the surfactant-assisted method, whereas relatively lower specific surface area (20, 20.5, and 22 $m^2\ g^{-1}$ for the catalysts with Ce/Zr of 3/1, 1/1, and 1/3, respectively) with average particle size of 100–150 μm was obtained from the coprecipitation method. It is noted that the average catalyst particle sizes were estimated by the nanosizer and the particle size analyzer. To investigate the OSC and lattice oxygen mobility of synthesized catalysts, the reduction/oxidation measurement and $^{18}O/^{16}O$ isotope exchange study were applied; details of these studies are described in Section "reactivity of Ce-ZrO_2 toward partial oxidation of PFAD."

It is noted that, for comparison, Ni/Ce-ZrO_2 (with 5 wt % Ni) was also tested for steam reforming reaction in this work. They were prepared by impregnating Ce-ZrO_2 with $Ni(NO_3)_2$ solution (from Aldrich). The catalysts were calcined at 1173 K and reduced under H_2 flow at 573 K for 6 h before use. After treatment, the catalysts were characterized by several physicochemical methods, i.e., the weight contents of Ni were determined by X-ray fluorescence analysis; the reducibility of catalyst was calculated from the degree of H_2 uptakes from the temperature-programed reduction testing; the dispersion percentage was identified from the volumetric H_2 chemisorption measurement using chemisorption analyzer; and the catalyst specific surface area was obtained from BET measurement. According to these characterizations, the catalyst consists of 5.01% Ni loading content with the reducibility and Ni dispersion of 92.6 and 8.95%, respectively. Furthermore, the specific surface area was observed to be 41.5 $m^2\ g^{-1}$.

Apparatus and procedures

An experimental system was designed and constructed as shown elsewhere.[27] The feed gases, i.e., He (as carrier gas), O_2 and H_2 (used to reduce Ni/Ce-ZrO_2) were controlled by three mass flow controllers, whereas PFAD and water were introduced by the heated syringe pump (with the reactant feed flow rate of 2.54 $cm^3\ h^{-1}$) and vaporized by our designed quartz vaporizer-mixer system. These gaseous feed was introduced to the 10-mm-diameter quartz reactor, which was mounted vertically inside a tubular furnace. A Type-K thermocouple was placed into the annular space between the reactor and furnace. This thermocouple was mounted on the tubular reactor in close contact with the catalyst bed to minimize the temperature difference between the catalyst bed and thermocouple. Another Type-K thermocouple was inserted in the middle of quartz tube to recheck possible temperature gradient; this inner-system thermocouple is covered with small closed-end quartz rod to prevent the catalytic reactivity of thermocouple during reaction. The recorded values showed that maximum temperature fluctuation during the reaction was always $\pm 1.0°C$ or less from the temperature specified for the reaction. It is noted that all experiments were carried out at isothermal condition after the system temperature was raised up to its setting temperature and waited until reaching steady state.

Catalysts (50 mg) were diluted with SiC (to obtain the total weight of 500 mg) to avoid temperature gradients and loaded in the quartz reactor. Preliminary experiments were carried out to find suitable conditions in which internal and external mass transfer effects are not predominant. Considering the effect of external mass transfer, based on the results from our previous publications,[27,28] the total flow rate was kept constant at 100 $cm^3\ min^{-1}$ under a constant residence time in all testing. The suitable average sizes of catalysts were also verified to confirm that the experiments were carried out without the effect of internal mass transfer limitation. After the reactions, the exit gas mixture was transferred via trace-heated lines to Porapak Q column Shimadzu 14B gas chromatograph (GC) and mass spectrometer (MS). The MS in which the sampling of exit gas was done by a quartz capillary and differential pumping was used for transient and carbon formation experiments, whereas the GC was applied to investigate steady-state condition experiments and to recheck the results from MS. It should be noted that, in this work, the reactivity was defined in terms of PFAD conversion and product distribution. PFAD conversion can be calculated based on the percent difference between PFAD in the feed and in the final product. Regarding the product distribution, the gaseous products from the reaction include H_2, CO, CO_2, CH_4, C_2H_6, C_2H_4, and C_3H_6; the yield of H_2 production (Y_{H_2}) was calculated by hydrogen balance defined as molar fraction of H_2 produced to total H_2 in the products. Other byproduct selectivities (i.e., S_{CO}, S_{CO_2}, S_{CH_4}, $S_{C_2H_6}$, $S_{C_2H_4}$, and $S_{C_3H_6}$) were calculated by carbon balance, defined as ratios of each product mole to the consumed moles of hydrocarbon, accounting for stoichiometry; this information was presented in terms of (relative) fraction of these byproduct components, which are summed to 100%.

Measurement of carbon formation

To investigate the amount of carbon formed on catalyst surface, the oxidation reaction was carried out by introducing 10% O_2 in He (with the flow rate of 100 $cm^3\ min^{-1}$) into the system at isothermal condition (1173 K), after being purged with He; the amount of carbon formation was determined by measuring the CO and CO_2 yields. The calibrations of CO and CO_2 productions were performed by injecting a known amount of these calibration gases from a loop in an injection valve in the bypass line. It is noted that the spent sample was further tested with TGA-MS (PerkinElmer, USA) at the maximum temperature of 1273 K to ensure that no carbon formation remains on the surface of catalyst, and no weight loss or CO/CO_2 productions were detected from all catalysts after oxidation reaction.

Results and Discussion

Reactivity of Ce-ZrO_2 toward partial oxidation of PFAD

The partial oxidation of PFAD over nanoscale Ce-ZrO_2 prepared by surfactant-assisted method (with Ce/Zr ratios of 1/3, 1/1, and 3/1) was first studied at 1123 K by feeding PFAD and O_2 with O/C molar ratio of 1.0. It can be seen in Figures 1a–c that, at this condition, H_2, CO, CH_4, and CO_2 are the main products with small amount of C_2H_4, C_2H_6, and C_3H_6 generated from the reaction. Furthermore, the conversions of PFAD and O_2 are always close to 100%, and small amount of water formation (<1%) is observed. For comparison, the homogeneous (noncatalytic) partial oxidation of PFAD was also investigated by feeding PFAD and O_2 with O/C molar ratio of 1.0 to the quartz tube filled with 500 mg of SiC at 1123 K. It was found that more than 90% of PFAD are converted; nevertheless, the main gaseous products formed are hydrocarbon compounds (i.e., CH_4, C_2H_4, C_2H_6, and C_3H_6 with the selectivities of 27.7, 23.3, 22.7, and 10.5%, respectively) with slight formations of CO and CO_2 (12.8% S_{CO} and 3.0% S_{CO_2}). Furthermore, significant amount of carbon was also detected in the blank reactor after exposure for 6 h.

The results from Figures 1a–c reveal that Ce-ZrO_2 with Ce/Zr ratio of 3/1 shows the best performance in terms of its high H_2 production with lowest C_2H_4, C_2H_6, and C_3H_6 formations. Furthermore, according to the postreaction oxidation experiment, the amount of carbon formation on the surface of Ce-ZrO_2 with Ce/Zr ratio of 3/1 after reaction (48 h) was relatively lower than other two ratios (3.4 mmol g_{cat}^{-1} compared with 4.3 and 4.7 mmol g_{cat}^{-1} observed over Ce-ZrO_2 with Ce/Zr ratios of 1/1 and 1/3, respectively). For comparison, the partial oxidation of PFAD over microscale Ce-ZrO_2 prepared by coprecipitation method (with Ce/Zr ratios of 1/3, 1/1, and 3/1) was also carried out at the same operating conditions (1123 K with O/C molar ratio of 1.0). As shown in Figure 2, less H_2 production with relatively higher C_2H_4, C_2H_6, and C_3H_6 formations was observed over this microscale Ce-ZrO_2. In addition, the postreaction oxidation also detected significantly higher amount of carbon formation over this catalyst (4.2, 4.9, and 5.6 mmol g_{cat}^{-1} over Ce-ZrO_2 with Ce/Zr ratios of 3/1, 1/1, and 1/3, respectively). These results strongly indicate the better reaction performance for nanoscale Ce-ZrO_2 (with Ce/Zr molar ratio of 3/1); hence, this catalyst was chosen for further studies and analyses.

The effect of inlet O_2 content on the catalytic reactivity was then studied by introducing PFAD and O_2 with O/C molar ratios of 0.5, 0.75, 1.0, 1.25, and 1.5 to the catalytic

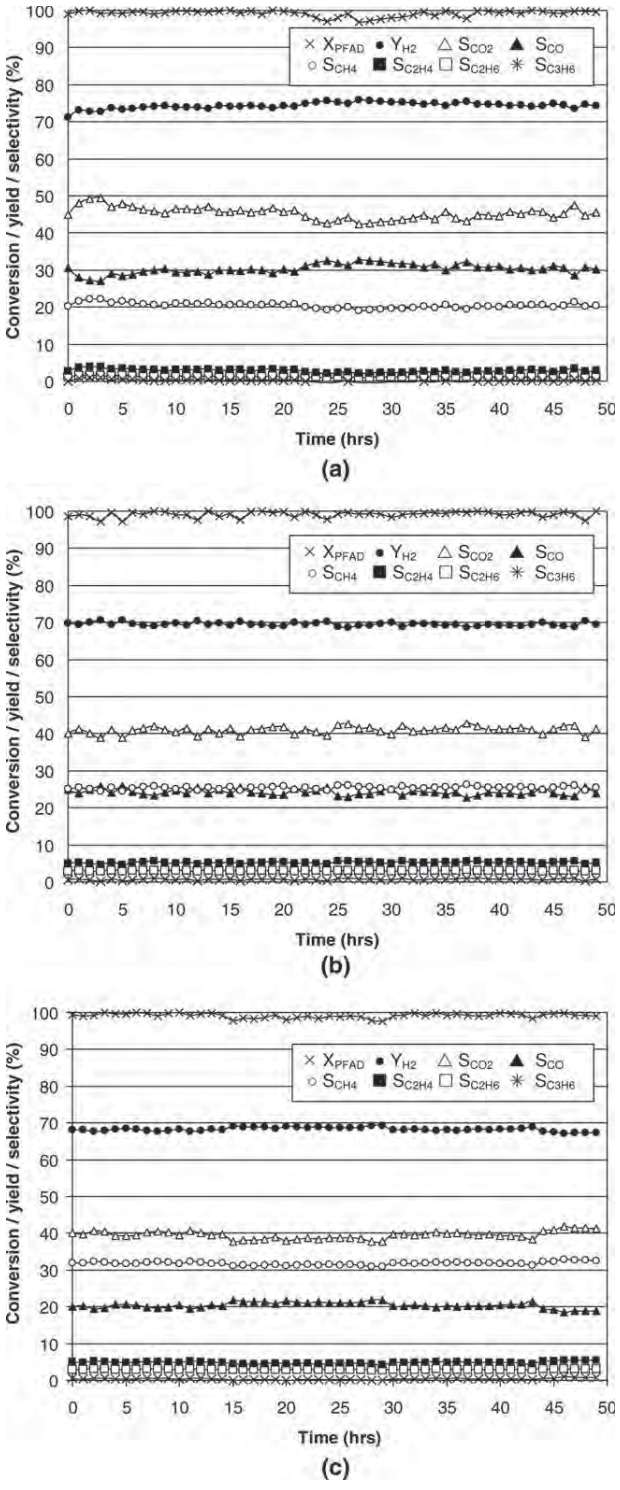

Figure 1. Reactivities of nanoscale Ce-ZrO_2 with various Ce/Zr molar ratios toward the partial oxidation of PFAD (at 1123 K with O/C molar ratio of 1.0).

The variations in conversion and product distributions with time from partial oxidation of PFAD over (a) Ce-ZrO_2 (Ce/Zr molar ratio of 3/1), (b) Ce-ZrO_2 (Ce/Zr molar ratio of 1/1), and (c) Ce-ZrO_2 (Ce/Zr molar ratio of 1/3).

reactor. At steady-state condition, H_2 production and the distribution of all gaseous byproducts (i.e., hydrocarbons, CO, and CO_2) were measured as shown in Figure 3. It can be seen that H_2 and CO increased with increasing O_2 content until inlet O/C ratio reached 1.25. On the contrary, these products decreased when the ratio was higher, whereas the distribution of CO_2 grew up. This is mainly due to the combustion of H_2 and CO by O_2 in the feed. With increasing O_2 content, the conversions of C_2H_4, C_2H_6, and C_3H_6 increased and reached 100% at O/C molar ratio of 1.25. For CH_4 formation, it increased when inlet O/C molar ratio changed from 0.5 to 1.25 but slightly decreased at higher O_2 content. These behaviors are related to the decompositions of C_2H_4, C_2H_6, and C_3H_6 to CH_4 at low inlet O_2 concentration and the further conversion of CH_4 to CO, CO_2, and H_2 at higher O_2 content. We previously reported the efficient decomposition of C_2H_6 and C_2H_4 to CH_4 in this range of temperature studied.[28]

It is noted that the effect of temperature on the conversion and product distribution was also carried out by varying the operating temperatures from 973 to 1173 K while keeping O/C molar ratio constant at 1.0. It was observed that H_2, CO, and CH_4 increased with increasing temperature, whereas CO_2, C_2H_6, and C_2H_4 considerably decreased, as shown in Figure 4. The decrease of CO_2 is due to the influence of reverse water–gas shift reaction ($CO_2 + H_2 \rightarrow CO + H_2O$), whereas the increases of CH_4, CO, and H_2 come from the decomposition and (partial) oxidation of C_2H_6 and C_2H_4 at higher temperature. Theoretically, the formations of gaseous hydrocarbon (i.e., CH_4, C_2H_4, C_2H_6, and C_3H_6) occur from the decomposition of PFAD (Eq. 1), whereas H_2, CO, and CO_2 are generated from both thermal decomposition and partial oxidation reactions (Eqs. 2–4). It should also be noted that, apart from thermal decomposition of PFAD, CH_4 can also be generated from methanation reactions (Eqs. 5 and 6).

Thermal decomposition of fatty acids

$$C_xH_yCOOH \rightarrow C_nH_mO_k + \text{coke} + \text{gases}(H_2, CO, CO_2, C_nH_m) \quad (1)$$

Partial oxidation of gaseous hydrocarbons and possible side reactions

$$2C_nH_m + nO_2 \rightarrow n2CO + 2mH_2 \quad (2)$$

$$2CO + O_2 \rightarrow 2CO_2 \quad (3)$$

$$2H_2 + O2 \rightarrow 2H_2O \quad (4)$$

$$n\text{CO} + 3n\text{H2} \rightarrow n\text{CH4} + n\text{H}_2\text{O} \quad (5)$$

$$n\text{CO}_2 + 4n\text{H}_2 \rightarrow n\text{CH}_4 + 2n\text{H}_2\text{O} \quad (6)$$

We suggested that the good partial oxidation reactivity of Ce-ZrO_2 is related to the OSC of this material because we previously reported that at moderate temperature, lattice oxygen (O_O^x) at ceria surface can oxidize gaseous hydrocarbons (e.g., CH_4).[27,28] In addition, the doping of CeO_2 with Zr has been observed to improve OSC as well as thermal stability of the material.[29–32] These benefits were associated with enhanced reducibility of cerium (IV) in Ce-ZrO_2 because of

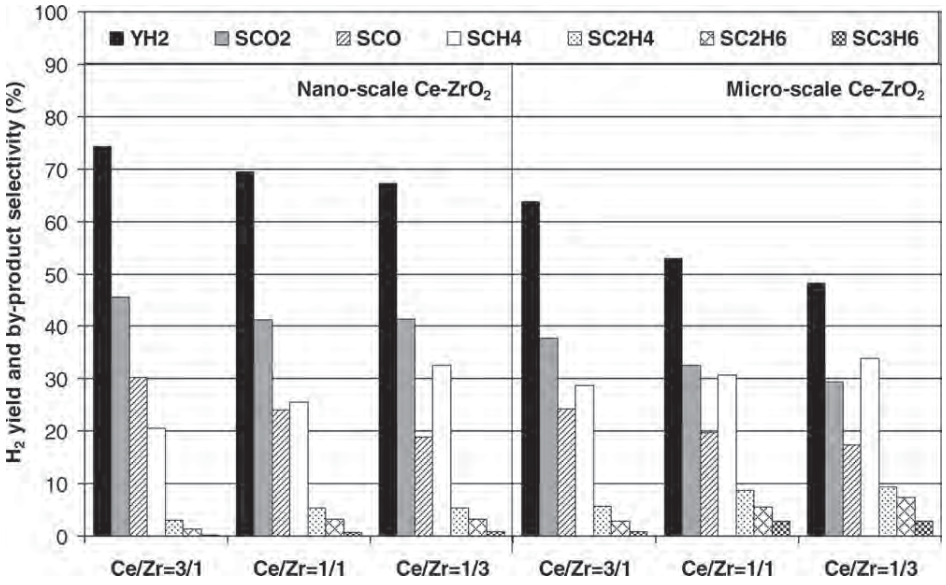

Figure 2. Reactivities of nanoscale and microscale Ce-ZrO_2 with various Ce/Zr molar ratios toward the partial oxidation of PFAD (at 1123 K with O/C molar ratio of 1.0).

The variations in product distributions from partial oxidation of PFAD at steady state (after 24 h) over nanoscale and microscale Ce-ZrO_2 with Ce/Zr molar ratios of 3/1, 1/1, and 1/3.

the high O^{2-} mobility inside the fluorite lattice.[26] During partial oxidation reaction, the gas–solid reactions between hydrocarbons present in the system (i.e., CH_4, C_2H_4, C_2H_6, and C_3H_6) and $O_O{}^x$ take place forming CO and H_2 from which the formation of carbon is thermodynamically unfavorable. The possible reaction pathway for partial oxidation of PFAD over Ce-ZrO_2 is illustrated below:

C_nH_m adsorption

$$CnHm + (n+m)^* \rightarrow (CH_x^*) + (H^*) \rightarrow n(C^*) + m(H^*) \quad (7)$$

Coreactant (O_2) adsorption

$$O_2 + 2^* \Leftrightarrow 2O^* \quad (8)$$

Redox reactions of lattice oxygen ($O_O{}^x$) with C* and O*

$$C^* + O_O^x \rightarrow CO^* + V_o^{\bullet\bullet} + 2e' \quad (9)$$

$$V_o^{\bullet\bullet} + 2e' + O^* \Leftrightarrow O_O{}^x + * \quad (10)$$

Desorption of products (CO and H_2)

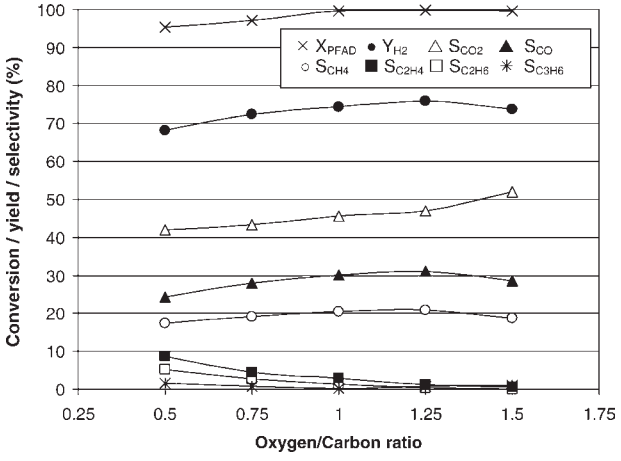

Figure 3. Partial oxidation of PFAD over nanoscale Ce-ZrO_2 (Ce/Zr molar ratio of 3/1) at various inlet O/C molar ratios.

Effect of inlet O/C molar ratio on the product compositions from the partial oxidation of PFAD over nanoscale Ce-ZrO_2 (Ce/Zr molar ratio of 3/1).

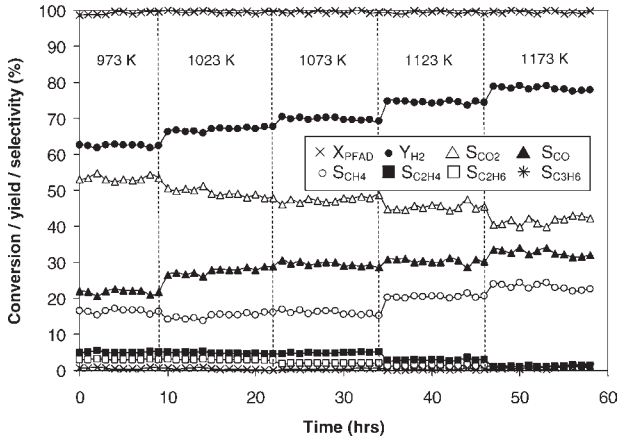

Figure 4. Product compositions from the partial oxidation of PFAD over nanoscale Ce-ZrO_2 (Ce/Zr molar ratio of 3/1) at various temperatures.

Effect of temperature on the product compositions from the partial oxidation of PFAD over nanoscale Ce-ZrO_2 (Ce/Zr molar ratio of 3/1).

Table 1. Effects of Temperature and Oxygen/Carbon Molar Ratio on the Degrees of Carbon Formation Over Ce-zrO_2 After Exposure to Partial Oxidation of PFAD

Catalyst	Temperature (K)	Oxygen/Carbon Molar Ratio	Carbon Formation (mmol g_{cal}^{-1})
Ce-ZrO_2 (Ce/Zr = 3/1)	1123	0.5	5.3 ± 0.15
	1123	0.75	4.2 ± 0.09
	1123	1.0	3.4 ± 0.10
	1123	1.25	2.9 ± 0.24
	1123	1.5	2.7 ± 0.17
	973	1.0	4.3 ± 0.11
	1023	1.0	3.9 ± 0.02
	1073	1.0	3.6 ± 0.15
	1173	1.0	3.0 ± 0.19

$$CO^* \Leftrightarrow CO + * \quad (11)$$

$$2(H^*) \Leftrightarrow H_2 + 2^* \quad (12)$$

Based on the Kroger–Vink notation, $V_O^{\bullet\bullet}$ denotes an oxygen vacancy with an effective charge 2^+, and e′ is an electron which can either be more or less localized on a cerium ion or delocalized in a conduction band. * is the surface active site of ceria-based materials. During the reaction, hydrocarbons adsorbed on * forming intermediate surface hydrocarbon species (CH_x* and eventually C* and H*) (Eq. 7). This C* later reacted with lattice oxygen (O_O^x) (Eq. 9). The steady-state rate is due to the continuous supply of oxygen source by inlet O_2 that reacted with the reduced-state catalyst to recover lattice oxygen (O_O^x) (Eqs. 8 and 10). It is noted that, according to our previous studies, * can be considered as unique site or same site as lattice oxygen (O_O^x).[27,28] During the reaction, hydrocarbons adsorbed on either unique site or lattice oxygen (O_O^x), whereas O_2 reacted with the catalyst reduced site to regenerate O_O^x as well as remove the formation of carbon species on the catalyst surface. In this work, the amount of carbon formation (mmol g_{cat}^{-1}) on the surface of Ce-ZrO_2 after exposure to the partial oxidation at several inlet conditions (various O/C molar ratios and operating temperatures) was also determined, as reported in Table 1. Clearly, the carbon formation decreased with increasing temperature and oxygen content. Theoretically, the following reactions are the most probable reactions that could lead to carbon formation during the partial oxidation of PFAD

$$2CO \Leftrightarrow CO_2 + C \quad (13)$$

$$C_nH_m \Leftrightarrow 0.5mH_2 + nC \quad (14)$$

$$CO + H_2 \Leftrightarrow H_2O + C \quad (15)$$

$$CO_2 + 2H_2 \Leftrightarrow 2H_2O + C \quad (16)$$

At low temperature, reactions (15)–(16) are favorable, whereas reactions (13) and (14) are thermodynamically unfavored. The Boudouard reaction (Eq. 13) and the decomposition of hydrocarbons (Eq. 14) are the major pathways for carbon formation at such a high temperature as they show the largest decreased in Gibbs energy.[33,34] Based on the range of temperature in this study, carbon formation would be formed via the decomposition of hydrocarbons and Boudouard reactions especially at low inlet O/C molar ratio. By applying ceria-based catalysts, both reactions could be inhibited by the redox reaction between surface carbon (C) and lattice oxygen (O_O^x) (Eq. 9), whereas the oxygen vacancy is recovered via the reactions with supply of O_2 source (Eqs. 8 and 10).

Oxygen storage capacity and lattice oxygen mobility measurements

The higher reactivity with greater resistance toward carbon deposition for nanoscale Ce-ZrO_2 with Ce/Zr ratio of 3/1 compared with microscale Ce-ZrO_2 and Ce-ZrO_2 with Ce/Zr ratios of 1/1 and 1/3 could be due to the better redox properties (e.g., OSC) of this catalyst. To prove this explanation, the OSC of all Ce-ZrO_2 was determined by the isothermal reduction measurement (R-1), which was performed by purging the catalysts with 5% H_2 in He at 1173 K. The amount of H_2 uptake is correlated to the amount of O_2 stored in the catalysts. As presented in Figure 5 and Table 2, the amount of H_2 uptake over nanoscale Ce-ZrO_2 with Ce/Zr of 3/1 is significantly higher than other Ce-ZrO_2. The redox reversibilities of these catalysts were also determined by applying the oxidation measurement (Ox-1) followed by second-time reduction measurement (R-2) at the same conditions. The amounts of O_2 chemisorbed and H_2 uptakes (from both R-1 and R-2) are presented in Table 2. From these results, the amounts of H_2 uptake from R-2 were approximately identical to those from R-1, indicating the reversibility of OSC for these synthesized Ce-ZrO_2.

In addition to the OSC, the $^{18}O/^{16}O$ isotope exchange experiment was carried out to investigate the lattice oxygen mobility of these Ce-ZrO_2. The sample (200 mg) was placed in the quartz reactor and thermally treated under the flow of high-purity helium (99.995%) at the desired temperatures for 1 h. Then, $^{18}O_2$ (in helium as carrier gas) was multiple times pulsed to the system and the outlet gases were monitored by

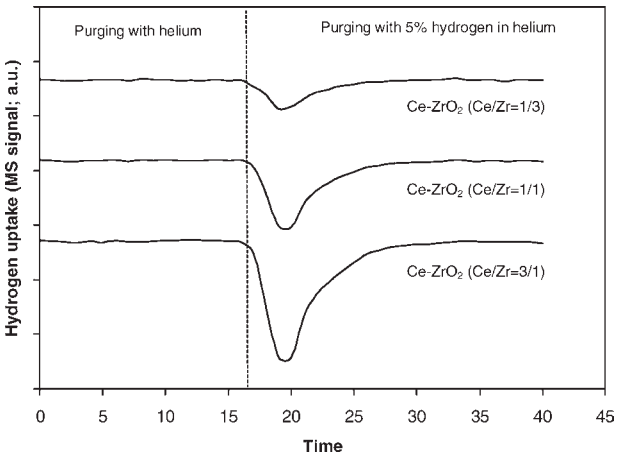

Figure 5. Oxygen storage capacity measurement of nanoscale Ce-ZrO_2 with various Ce/Zr molar ratios.

Isothermal reduction testing (at 1123 K) over nanoscale Ce-ZrO_2 with Ce/Zr molar ratios of 1/3, 1/1, and 3/1.

Table 2. Results of R-1, Ox-1, and R-2 Analyses of Nanoscale and Microscale Ce-ZrO_2 with Different Ce/Zr Ratios

Catalyst	H_2 Uptake from R-1 (μmol g_{cal}^{-1})	O_2 Uptake from Ox-1 (μmol g_{cal}^{-1})	H_2 Uptake from R-2 (μmol g_{cal}^{-1})
Nanoscale Ce-ZrO_2 (Ce/Zr = 1/3)	2883	1423	2879
Nanoscale Ce-ZrO_2 (Ce/Zr = 1/1)	3692	1848	3687
Nanoscale Ce-ZrO_2 (Ce/Zr = 3/1)	5221	2620	5213
Microscale Ce-ZrO_2 (Ce/Zr = 1/3)	1087	551	1075
Microscale Ce-ZrO_2 (Ce/Zr = 1/1)	1701	709	1694
Microscale Ce-ZrO_2 (Ce/Zr = 3/1)	2625	1305	2621

the MS. According to our results, the productions of $^{16}O_2$ and $^{18}O^{16}O$ for nanoscale Ce-ZrO_2 with Ce/Zr of 3/1 were 18 and 14% at 600°C, whereas those for nanoscale Ce-ZrO_2 with Ce/Zr of 1/1 and Ce-ZrO_2 with Ce/Zr of 1/3 were 13 and 6% (Ce/Zr of 1/1) and 9 and 2% (Ce/Zr of 1/3) at the same temperature. Thus, the higher oxygen mobility of Ce-ZrO_2 with Ce/Zr of 3/1 can be confirmed. As for the testing over microscale Ce-ZrO_2, the productions of $^{16}O_2$ and $^{18}O^{16}O$ at 600°C for this Ce-ZrO_2 with Ce/Zr of 3/1, 1/1, and 1/3 were 11 and 7%, 9 and 5%, and 6 and 2%, respectively.

It can be seen that the partial oxidation reactivity, the OSC, and the lattice oxygen mobility of Ce-ZrO_2 are in the same trend (nanoscale Ce-ZrO_2 < microscale Ce-ZrO_2; Ce-ZrO_2 with Ce/Zr of 3/1 > Ce-ZrO_2 with Ce/Zr of 1/1 > Ce-ZrO_2 with Ce/Zr of 1/3), indicating the strong impact of the catalyst specific surface area, the OSC, and the lattice oxygen mobility on the catalyst reactivity.

The application of Ce-ZrO_2 as preoxidative catalyst

From Section "reactivity of Ce-ZrO_2 toward partial oxidation of PFAD," the great benefit of partial oxidation over nanoscale Ce-ZrO_2 is its high resistance toward carbon deposition; nevertheless, the remaining detectable of hydrocarbons (i.e., CH_4, C_2H_4, C_2H_6, and C_3H_6) in the product indicates the incomplete conversion of PFAD by this catalyst. Therefore, we further studied the potential for applying Ce-ZrO_2 as preoxidative catalyst to initially convert PFAD to light products; the product gas from this primary partial oxidation part was then mixed with steam and simultaneously fed to the secondary steam reforming over Ni/Ce-ZrO_2 to complete the hydrocarbon conversion and maximize H_2 yield. In this experiment, the initial feed was PFAD and O_2 with O/C molar ratio of 1.25. At the exit of the partial oxidation reaction, the steam was then added with H_2O/C molar ratio of 3.0. It is noted that the carbon considered for this H_2O/C ratio is based on the amount of unconverted carbon compounds (i.e., CH_4, C_2H_4, C_2H_6, and C_3H_6) from the partial oxidation part. Figure 6 presents the H_2 yield and other gaseous products from this coupling system at various temperatures; it can be seen that H_2 production is significantly high, and the formations of hydrocarbons, i.e., CH_4, C_2H_4,

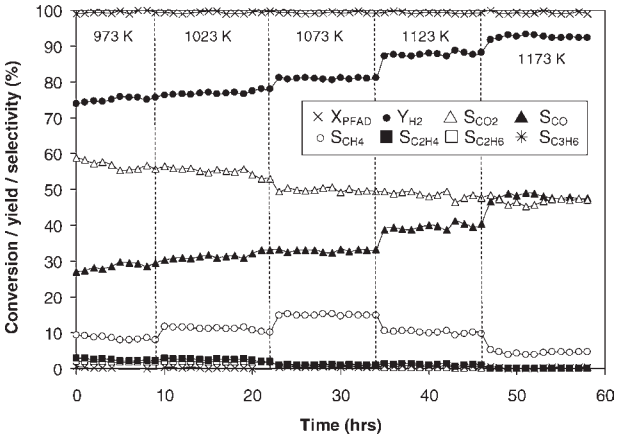

Figure 6. Preoxidation of PFAD with nanoscale Ce-ZrO_2 followed by the steam reforming over Ni/Ce-ZrO_2 at various temperatures.

Effect of temperature on the product compositions from the preoxidation of PFAD with nanoscale Ce-ZrO_2 followed by the steam reforming over Ni/Ce-ZrO_2.

and C_2H_6, are closed to 0 particularly at high operating temperature. It was also revealed that CO and H_2 increase with increasing temperature, whereas CO_2, C_2H_4, and C_2H_6 decrease. The dependence of CH_4 on the operating temperature was nonmonotonic, and the maximum production of CH_4 occurred at ~1073 K. The increase of CH_4 at low temperature comes from the decomposition of all hydrocarbons (PFAD, C_2H_4, and C_2H_6), whereas the decrease at higher temperature could be due to the further reforming to CO and H_2; the increase in H_2O conversion (from 41% at 1073 K to 45 and 48% at 1123 and 1173 K) strongly supports this explanation. It is noted according to the postreaction oxidation measurement that low carbon formation (in the range of 3.2–4.7 mmol g_{cat}^{-1}) was observed from the spent catalysts; moreover, the amount of carbon formation (as well as the percentage of CH_4 in the end product) can be further minimized by increasing the inlet steam content, as presented in Table 3 and Figure 7. For comparison, the steam reforming of PFAD over Ni/Ce-ZrO_2 (without preoxidation with Ce-ZrO_2) was also tested. Unstable profiles of H_2 production, which

Table 3. Effects of Temperature and Inlet Steam/Carbon Molar Ratio on the Degrees of Carbon Formation After Exposure to the Preoxidation of PFAD Over Ce-ZrO_2 (with O/C Molar Ratio of 1.25) Followed by the Steam Reforming Over Ni/Ce-ZrO_2

Catalyst	Temperature (K)	Steam/Carbon Molar Ratio	Carbon Formation (mmol g_{cat}^{-1})
Ce-ZrO_2 + Ni/Ce-ZrO_2	973	3.0	4.7 ± 0.29
	1023	3.0	4.4 ± 0.17
	1073	3.0	3.9 ± 0.11
	1123	3.0	3.6 ± 0.14
	1173	3.0	3.2 ± 0.06
	1173	5.0	3.1 ± 0.18
	1173	7.0	2.9 ± 0.10
	1173	9.0	2.7 ± 0.13
	1173	11.0	2.7 ± 0.07
	1173	13.0	2.6 ± 0.09

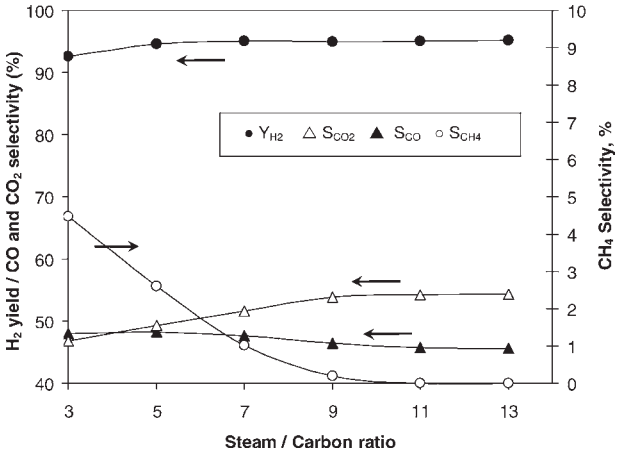

Figure 7. Preoxidation of PFAD with nanoscale Ce-ZrO_2 followed by the steam reforming over Ni/Ce-ZrO_2 at various inlet steam/carbon molar ratios.

Effect of inlet steam/carbon molar ratio on the product compositions from the preoxidation of PFAD with nanoscale Ce-ZrO_2 followed by the steam reforming over Ni/Ce-ZrO_2.

related to the high formation of carbon species on the surface of catalyst, were observed. After purging in He, the postreaction oxidation measurement detected significant amount of carbon over the catalyst (8.4 mmol g_{cat}^{-1}). This result indicates that Ni-based catalyst is inappropriate for the direct reform of PFAD and highlights the great benefit of nanoscale Ce-ZrO_2 as preoxidative catalyst.

Conclusions

Nanoscale Ce-ZrO_2 with Ce/Zr ratio of 3/1 has useful partial oxidation activity for converting PFAD (with almost 100% conversion) to H_2, CH_4, CO, and CO_2 with slight formations of gaseous high hydrocarbon compounds, i.e., C_2H_4, C_2H_6, and C_3H_6 under moderate temperature (1073–1173 K). The good reactivity was found to be closely related with the high OSC and lattice oxygen mobility of this synthesized catalyst, according to the reduction/oxidation measurement and $^{18}O/^{16}O$ isotope exchange study. It was also revealed that this nanoscale Ce-ZrO_2 can be efficiently used as the preoxidative catalyst to initially convert PFAD to light hydrocarbons, from which the latter reforms with steam in the presence of Ni-based catalyst to complete the hydrocarbon conversion and maximize H_2 yield.

Acknowledgment

The financial support from The Thailand Research Fund (TRF) throughout this project is gratefully acknowledged.

Literature Cited

1. Ahmed S, Krumpelt M. Hydrogen from hydrocarbon fuels for fuel cells. *Int J Hydrogen Energy*. 2001;26:291–301.
2. Seo YS, Shirley A, Kolaczkowski ST. Evaluation of thermodynamically favourable operating conditions for production of hydrogen in three different reforming technologies. *J Power Sources*. 2002;108: 213–225.
3. Cheekatamarla PK, Finnerty CM. Synthesis gas production via catalytic partial oxidation reforming of liquid fuels. *Int J Hydrogen Energy*. 2008;33:5012–5019.
4. Wang H, Feldhoff A, Caro J, Schiestel T, Werth S. Oxygen selective ceramic hollow fiber membranes for partial oxidation of methane. *AIChE J*. 2009;55:2657–2664.
5. Tanaka H, Kaino R, Okumura K, Kizuka T, Tomishige K. Catalytic performance and characterization of Rh–CeO_2/MgO catalysts for the catalytic partial oxidation of methane at short contact time. *J Catal*. 2009;268:1–8.
6. Diehl F, Barbier J, Duprez D, Guibard I, Mabilon G. Catalytic oxidation of heavy hydrocarbons over Pt/Al_2O_3. Influence of the structure of the molecule on its reactivity. *Appl Catal B: Environ*. 2010; 95:217–227.
7. Alvarez-Galvan MC, Navarro RM, Rosa F, Briceño Y, Gordillo Alvarez F, Fierro JLG. Performance of La,Ce-modified alumina-supported Pt and Ni catalysts for the oxidative reforming of diesel hydrocarbons. *Int J Hydrogen Energy*. 2008;33:652–663.
8. Shi L, Bayless DJ, Prudich ME. A CFD model of autothermal reforming. *Int J Hydrogen Energy*. 2009;34:7666–7675.
9. Recupero V, Pino L, Leonardo RD, Lagana M, Maggio G. Hydrogen generator, via catalytic partial oxidation of methane for fuel cells. *J Power Sources*. 1998;71:208–214.
10. Basagiannis AC, Verykios XE. Influence of the carrier on steam reforming of acetic acid over Ru-based catalysts. *Appl Catal B: Environ*. 2008;82:77–88.
11. Basagiannis AC, Verykios XE. Catalytic steam reforming of acetic acid for hydrogen production. *Int J Hydrogen Energy*. 2007;32: 3343–3355.
12. Davidian T, Guilhaume N, Daniel C, Mirodatos C. Continuous hydrogen production by sequential catalytic cracking of acetic acid. I. Investigation of reaction conditions and application to two parallel reactors operated cyclically. *Appl Catal A: Gen*. 2008; 335:64–73.
13. Liu N, Yuan Z, Wang C, Wang S, Zhang C, Wang S. The role of CeO_2–ZrO_2 as support in the ZnO–$ZnCr_2O_4$ catalysts for autothermal reforming of methanol. *Fuel Process Technol*. 2008;89:574–581.
14. Damyanova S, Pawelec B, Arishtirova K, Martinez Huerta MV, Fierro JLG. The effect of CeO_2 on the surface and catalytic properties of Pt/CeO_2–ZrO_2 catalysts for methane dry reforming. *Appl Catal B: Environ*. 2009;89:149–159.
15. Vagia EC, Lemonidou AA. Investigations on the properties of ceria–zirconia-supported Ni and Rh catalysts and their performance in acetic acid steam reforming. *J Catal*. 2010;269:388–396.
16. Chen J, Wu Q, Zhang J, Zhang J. Effect of preparation methods on structure and performance of Ni/Ce0.75Zr0.25O_2 catalysts for CH_4–CO_2 reforming. *Fuel*. 2008;87:2901–2907.
17. Cao L, Pan L, Ni C, Yuan Z, Wang S. Autothermal reforming of methane over Rh/Ce0.5Zr0.5O_2 catalyst: effects of the crystal structure of the supports. *Fuel Process Technol*. 2010;91:306–312.
18. Yuan Z, Ni C, Zhang C, Gao D, Wang S, Xie Y, Okada A. Rh/MgO/Ce0.5Zr0.5O_2 supported catalyst for autothermal reforming of methane: the effects of ceria–zirconia doping. *Catal Today*. 2009;146:124–131.
19. Lima SM, Cruz IO, Jacobs G, Davis BH, Mattos LV, Noronha FB. Steam reforming, partial oxidation, and oxidative steam reforming of ethanol over Pt/$CeZrO_2$ catalyst. *J Catal*. 2008;257:356–368.
20. Ozawa M, Kimura M, Isogai A. The application of CeZr oxide solid solution to oxygen storage promoters in automotive catalysts. *J Alloys Compd*. 1993;193:73–75.
21. Balducci G, Kaspar J, Fornasiero P, Graziani M, Islam MS. Surface and reduction energetics of the CeO_2-ZrO_2 catalysts. *J Phys Chem B*. 1998;102:557–561.
22. Vlaic G, Fornasiero P, Geremia S, Kaspar J, Graziani M. Relationship between the zirconia-promoted reduction in the Rh-loaded Ce0.5Zr0.5O_2 mixed oxide and the Zr-O local structure. *J Catal*. 1997;168:386–392.
23. Rao GR, Kaspar J, Meriani S, Dimonte R, Graziani M. NO decomposition over partially reduced metallized CeO_2-ZrO_2 solid solutions. *Catal Lett*. 1994;24:107–112.
24. Fornasiero P, Dimonte R, Rao GR, Kaspar J, Meriani S, Trovarell A, Graziani M. Rh-loaded CeO_2-ZrO_2 solid-solutions as highly efficient oxygen exchangers: dependence of the reduction behavior and

the oxygen storage capacity on the structural-properties. *J Catal*. 1995;151:168–177.
25. Yao MH, Hoost TE, Baird RJ, Kunz FW. An XRD and TEM investigation of the structure of alumina-supported ceria-zirconia. *J Catal*. 1997;166:67–74.
26. Kim D. Lattice parameters, ionic conductivities, and solubility limits in fluorite-structure MO_2 oxide [M = Hf4+, Zr4+, Ce4+, Th4+, U4+] solid solutions. *J Am Ceram Soc*. 1989;72:1415–1421.
27. Laosiripojana N, Assabumrungrat S. Catalytic dry reforming of methane over high surface area ceria. *Appl Catal B: Environ*. 2005; 60:107–116.
28. Laosiripojana N, Assabumrungrat S. Kinetic dependencies and reaction pathways in hydrocarbon and oxyhydrocarbon conversions catalyzed by ceria-based materials. *Appl Catal B: Environ*. 2008; 82: 103–113.
29. Laosiripojana N, Chadwick D, Assabumrungrat S. Effect of high surface area CeO_2 and Ce-ZrO_2 supports over Ni catalyst on CH_4 reforming with H_2O in the presence of O_2, H_2, and CO_2. *Chem Eng J*. 2008;138:264–273.
30. Kruse N, Frennet A, Bastin JM, editors. *Catalysis and Automotive Pollution Control IV*. Amsterdam: Elsevier, 1998.
31. Kaspar J, Fornasiero P, Graziani M. Use of CeO_2-based oxides in the three-way catalysis. *Catal Today*. 1999;50:285–298.
32. Roh HS, Potdar HS, Jun KW. Carbon dioxide reforming of methane over co-precipitated Ni-CeO_2, Ni-ZrO_2 and Ni-Ce-ZrO_2 catalysts. *Catal Today*. 2004;93–95:39–44.
33. Lwin Y, Daud WRW, Mohamad AB, Yaakob Z. Hydrogen production from steam–methanol reforming: thermodynamic analysis. *Int J Hydrogen Energy*. 2000;25:47–53.
34. Amor JN. The multiple roles for catalysis in the production of H_2. *Appl Catal A: Gen*. 1999;176:159–176.

Manuscript received May 12, 2010, revision received Sep. 7, 2010, and final revision received Oct. 29, 2010.

Applied Catalysis B: Environmental xxx (2010) xxx–xxx

Contents lists available at ScienceDirect

Applied Catalysis B: Environmental

journal homepage: www.elsevier.com/locate/apcatb

Conversion of poisonous methanethiol to hydrogen-rich gas by chemisorption/reforming over nano-scale CeO_2: The use of CeO_2 as catalyst coating material

N. Laosiripojana [a,*], S. Assabumrungrat [b]

[a] The Joint Graduate School of Energy and Environment, CHE Center for Energy Technology and Environment, King Mongkut's University of Technology Thonburi, Bangkok, Thailand
[b] Department of Chemical Engineering, Faculty of engineering, Chulalongkorn University, Bangkok, Thailand

ARTICLE INFO

Article history:
Received 20 July 2010
Received in revised form 15 October 2010
Accepted 7 December 2010
Available online xxx

Keywords:
CeO_2
Steam reforming
Methanethiol
Hydrogen

ABSTRACT

Synthesized nano-scale CeO_2 enables to convert poisonous methanethiol (CH_3SH) to hydrogen-rich gas via the solid–gas reaction between CeO_2 and CH_3SH under sufficient condition. In the presence of H_2O, the phase of $Ce(SO_4)_2$ occurs from the reaction and offers high CH_3SH reforming activity. In contrast, without H_2O adding, Ce_2O_2S is formed instead and results in low catalyst activity. Further catalyst improvement was performed by coating this synthesized nano-scale CeO_2 over cylindrical-shape Rh/Al_2O_3 pellet (as called CeO_2-coated Rh/Al_2O_3). This developed catalyst was found to enhance good activity, stability, and reusability (over 5 reaction cycles; 72 h) for converting CH_3SH to hydrogen-rich gas with high hydrogen yield achievement. For more practical application, this catalyst was also tested over olefin offgas containing CH_3SH and ethanethiol (CH_3SCH_3) from an olefin manufacturing; and was found to efficiently convert this offgas to hydrogen-rich gas without sulfur present in the product gas under a proper regeneration time. This result highlights a great benefit of CeO_2-coated Rh/Al_2O_3 for integrating the clean energy generation with toxic-waste treatment, which offers significant energy and environmental benefits.

1. Introduction

Industrial offgas is a gaseous by-product, which usually generated from the petrochemical and olefin manufacturing processes. Sulfur-containing compounds (e.g., hydrogen sulfide, sulfur oxides, thiophenes, mercaptans, and others) are typically present in this vent gas; and are commonly known to cause serious environmental and human health problems when emitted to the atmosphere [1]. Among these emissions, it has been reported that mercaptan compounds (e.g. methanethiol or CH_3SH) exhibit high toxicity to human health by affecting nervous system and causing convulsion and narcosis. It is known that CH_3SH causes paralysis of the respiratory system at high concentrations, while it produces pulmonary edema at lower levels [2]. Apart from the environmental and health problems, CH_3SH is also regularly known as poisonous gas for several catalytic conversion processes, particularly the reaction over metallic-based catalysts. In addition, regarding its high acidity, CH_3SH is corrosive to metals, which is harmful for storage and usage of oil products. Therefore, it is necessary to remove CH_3SH from the feedstock either by extracting or by transforming to innocuous disulfides prior the catalytic conversion processes. Importantly, this separated CH_3SH gas needs to be treated before venting out to the environment; and normally the adsorption and/or combustion processes are applied for this purpose [3–11].

Recently, the regenerative sulfur adsorption capability of cerium oxide (CeO_2) at high temperature was reported [12]. In addition, the capability of this material as catalyst and support in various reactions involving oxidation of hydrocarbons has also been addressed [13–18]. Hence, it is interested to study the behavior of CeO_2 towards the adsorption and conversion of CH_3SH. Theoretically, CeO_2 contains high concentration of highly mobile oxygen vacancies, which act as local sources or sinks for oxygen involved in reactions taking place on its surface; this behavior renders CeO_2-based materials of interest for a wide range of catalytic hydrocarbon conversion applications [19–28]. Previously, we have successfully synthesized nano-scale CeO_2 with high specific surface area and thermal stability by cationic surfactant-assisted method and found that this material efficiently converts several hydrocarbons (i.e. CH_4, C_2H_4, C_2H_6, C_3H_8, C_4H_{10}, CH_3OH and C_2H_5OH) via the steam and dry reforming reactions to hydrogen-rich gas with high resistance toward carbon formation [29,30]. It is known that these reforming reactions occur via the solid–gas reaction between the lattice oxygen (O_O^x) in CeO_2 and hydrocarbon ($C_nH_m + nO_O^x = 0.5mH_2 + nCO + nV_O^{\bullet\bullet} + 2ne'$), from which $V_O^{\bullet\bullet}$

* Corresponding author. Tel.: +66 2 872 9014, fax: +66 2 872 6736.
E-mail address: navadol_l@jgsee.kmutt.ac.th (N. Laosiripojana).

0926-3373/$ – see front matter © 2010 Elsevier B.V. All rights reserved.
doi:10.1016/j.apcatb.2010.12.008

denotes an oxygen vacancy with an effective charge 2^+, e′ is an electron which can either be more or less localized on a cerium ion or delocalized in a conduction band. In addition, the reactions of the reduced CeO_2 with CO_2 and H_2O could produce CO and H_2 along with regenerate O_0^x ($V_O^{\bullet\bullet} + 2e' + CO_2 = O_0^x + CO$; and $V_O^{\bullet\bullet} + 2e' + H_2O = O_0^x + H_2$).

In the present work, the potential use of nano-scale CeO_2 for the reaction (adsorption and conversion) with CH_3SH was studied under several operating conditions (i.e. without inlet steam, with various inlet steam/CH_3SH molar ratios, and under different operating temperatures). Several characterizations including X-ray diffraction (XRD), X-ray photoelectron spectroscopy (XPS), temperature-programmed reduction (TPR), and $^{18}O/^{16}O$ isotope exchange methods were also performed over both fresh and spent catalysts from the reaction under various conditions in order to determine the changing of catalyst phase formation and the redox properties associated with the oxygen storage capacity (OSC) and the mobility of lattice oxygen. Based on the relation between the experimental results and the above characterizations, the mechanistic of CH_3SH reaction over nano-scale CeO_2 was explained. In addition, further catalyst improvement with respect to the study, i.e. by using this ultrafine CeO_2 as catalyst support and as coating material over metallic-based catalyst were investigated with an aim to develop the efficient catalyst for converting CH_3SH and olefin offgas (containing CH_3SH and CH_3SCH_3) to hydrogen-rich gas with high resistance toward sulfur poisoning.

2. Experimental

2.1. Preparation and characterizations of CeO_2

Nano-scale CeO_2 was synthesized by cationic surfactant-assisted method. This preparation technique was reported to offer ultrafine material with high surface area and good thermal stability due to the interaction of hydrous oxide with cationic surfactants under basic condition and the incorporation of surfactants during preparation, which reduces the interfacial energy and eventually decreases the surface tension of water contained in the pores [31]. In preparation, 0.1 M of cerium nitrate ($Ce(NO_3)_3{\cdot}H_2O$ from Aldrich) was mixed with 0.1 M cetyltrimethylammonium bromide by keeping the ([Ce])/[cetyltrimethylammonium bromide] molar ratio constant at 0.8. This solution was continually stirred and added aqueous ammonia until the pH reaches 11.5. It was then sealed and placed in the thermostatic bath before filtering and washing the precipitate with deionized water to remove the free surfactant. The precipitate was dried overnight at 110 °C and calcined at 900 °C for 6 h to prevent the catalyst thermal sintering during the reaction. After calcination, the nano-scale fluorite-structured CeO_2 with good homogeneity was achieved.

The redox properties associated with the OSC and the mobility of lattice oxygen for this synthesized CeO_2 were examined by applying TPR and $^{18}O/^{16}O$ isotope exchange methods. The TPR experiment was carried out in a quartz reactor, which was mounted vertically inside tubular furnace. A Type-K thermocouple was placed into the annular space between the reactor and furnace, while another thermocouple, covering by closed-end quartz tube, was inserted in the middle of the quartz reactor to re-check the possible temperature gradient. The sample (100 mg) was heated from 25 °C to 1000 °C under 5%H_2 in N_2 with the flow rate of 50 $cm^3\ min^{-1}$ and the amount of H_2 consumed during the TPR process at different temperatures was monitored online by the thermal conductivity detector (TCD) and quantified by calibrating the peak areas against the TPR of known amount CuO. The $^{18}O/^{16}O$ isotope exchange experiment was carried out to investigate the lattice oxygen mobility of CeO_2 by placing the sample in the quartz reactor and thermally treated under the flow of high-purity helium (99.995%) at the desired temperatures for 1 h. Then, $^{18}O_2$ (98% purity) were multiply pulsed to the system by six-port valve with sample loop (using helium as carrier gas) the outlet gases were monitored by the mass spectrometer (MS; Omistar GSD 301O3).

2.2. Preparations of Rh/CeO_2 and CeO_2-coated Rh/Al_2O_3

Apart from the synthesis of nano-scale CeO_2, Rh/CeO_2 and CeO_2-coated Rh/Al_2O_3 were also prepared and tested. Rh was selected as metallic material since this precious metal is known as one of the most active catalysts for reforming and relevant reactions. Rh/CeO_2 (5 wt% Rh) was prepared by the wet impregnation of synthesized CeO_2 with an aqueous solution of $Rh(NO_3)_2$ (from Aldrich); furthermore, Rh/Al_2O_3 was also prepared by impregnation of Al_2O_3 with $Rh(NO_3)_2$ for comparison. Prior the reaction testing, these catalysts were calcined in air at 900 °C and reduced with H_2 at 500 °C for 6 h. It is noted that the catalysts (after calcination and reduction) were characterizations by XRF analysis and TPR (with 5% H_2 in helium) to determine the Rh weight contents and reducibility, while the dispersion percentage of Rh was identified from the volumetric H_2 chemisorption measurement using a chemisorption analyzer. From these characterizations, the Rh weight contents for Rh/CeO_2 and Rh/Al_2O_3 were 4.9 and 5.1%; the metal reducibility of Rh/CeO_2 was 91.6%, while that of Rh/Al_2O_3 was 94.8%; and the metal dispersion percentages for Rh/CeO_2 and Rh/Al_2O_3 were 4.78 and 5.04%, respectively.

As another approach, nano-scale CeO_2 was used as a coating barrier over cylindrical-shape Rh/Al_2O_3 pellet. The preparation is divided into 3 main steps: (i) CeO_2 was prepared as a suspension by adding polyvinyl alcohol (PVA; Aldrich) as the suspension solvent to suspend CeO_2 powder into the solution, (ii) Rh/Al_2O_3 pellets were introduced into this suspension solution, and (iii) these pellets were dried and pre-treated. In detail, 10 wt% of CeO_2 powder was suspended into a 0.3 M of PVA solution; this solution was then stirred by magnetic stirring (500 rpm) at room temperature for 1 h. Then, CeO_2 powder was completely suspended in this solution by ultrasonic probe. As the next step, 5 pellets of Rh/Al_2O_3 (~100 mg for each pellet) were dropped into the stirring CeO_2 suspension for 6 h. These pellets were then removed, dried overnight in oven at 110 °C and calcined in air at 900 °C for 6 h before reducing with 10% H_2 for 6 h. It is noted that, after calcination, the catalyst was coated more than 1 time to improve the thickness of coating. After 5 times coating, SEM micrograph confirms a porous and homogeneous structure of coating pellets.

2.3. Reaction testing and analyses

To perform the reaction testing, an experimental reactor system was constructed as presented elsewhere [29]. The feed gases including CH_3SH (20 vol% in helium) and helium were controlled and introduced to the system by the mass flow controllers, while deionized H_2O was fed by a syringe pump passing through an evaporator. For the steam reforming testing, various steam concentrations were added to achieve the steam/CH_3SH ratio between 0.5 and 3.0. The inlet gas mixtures were introduced to the reaction section, in which a quartz reactor was mounted vertically inside tubular furnace. The catalyst (1.0 g) was diluted with SiC in order to avoid temperature gradients and loaded in the quartz reactor, which was packed with quartz wool to prevent the catalyst moving. A Type-K thermocouple was placed into the annular space between the reactor and furnace to measure the reaction temperature; furthermore, another Type-K thermocouple covering by closed-end quartz tube was inserted in the middle of the quartz reactor to re-check the temperature deviation.

Please cite this article in press as: N. Laosiripojana, S. Assabumrungrat, Appl. Catal. B: Environ. (2011), doi:10.1016/j.apcatb.2010.12.008

After the reaction, the exit gas mixture was transferred via trace-heated lines (100 °C) to the analysis section, which consists of a Porapak Q column Shimadzu 14B gas chromatograph (GC) and a quadrupole MS. The GC was applied for the steady state studies, whereas the MS was used for the transient experiments. The outlet of the GC column was directly connected to TCD and frame ionization detector (FID); in addition, the temperature program of GC column was applied in order to satisfactorily separate all compounds. In the present work, the catalyst activity was defined in terms of CH_3SH variation (the changing of CH_3SH with time), H_2 yield (Y_{H_2}) and outlet gaseous by-product selectivity. (Y_{H_2}) was calculated by hydrogen balance, defined as the molar fraction of H_2 produced to the total hydrogen-based compounds generated in the products. Selectivities of other outlet product gases (i.e. S_{CO}, S_{CO_2}, and S_{CH_4}) were calculated by the carbon balance, defined as the mole ratios of the specified component in the outlet gas to the total outlet carbon-based components, accounting for stoichiometry. Eqs. (1)–(4) below present the calculations of Y_{H_2} and all product selectivities.

$$Y_{H_2} = \left(\frac{(X_{H_2,\,out})}{2(X_{CH_4,\,in}) + (X_{H_2S,\,in})} \right) \quad (1)$$

$$S_{CO} = \left(\frac{(X_{CO,\,out})}{(X_{CO,\,out}) + (X_{CO_2,\,out}) + (X_{CH_4,\,out})} \right) \quad (2)$$

$$S_{CO_2} = \left(\frac{(X_{CO_2,\,out})}{(X_{CO,\,out}) + (X_{CO_2,\,out}) + (X_{CH_4,\,out})} \right) \quad (3)$$

$$S_{CH_4} = \left(\frac{(X_{CH_4,\,out})}{(X_{CO,\,out}) + (X_{CO_2,\,out}) + (X_{CH_4,\,out})} \right) \quad (4)$$

3. Results and discussion

3.1. Experiments for determining the suitable operating conditions

Prior to the catalyst testing, experiments to identify the suitable condition, in which internal and external mass transfer effects are not predominant, were carried out. Considering the effect of external mass transfer, the total gas flow rate was varied under a constant modified residence time. It was found that the catalyst activity (in terms of CH_3SH variation, H_2 yield and all by-product selectivities) is independent of the gas velocity when the gas flow rate was higher than 100 $cm^3\,min^{-1}$, indicating the absence of external mass transfer effects at this high velocity. Furthermore, the reaction over catalyst with various average particle sizes (i.e. <50 μm, 50–100 μm, 100–150 μm, 150–200 μm, 200–250 μm, 250–500 μm, and >500 μm) was studied under several isothermal conditions (i.e. 900, 925, 950, 975 and 1000 °C). It was observed that the catalyst activity is unchanged when the catalyst with particle size less than 200 μm is applied, which suggests the absence of intraparticle diffusion limitation under this condition.

3.2. Activity of CeO_2 towards the decomposition and steam reforming of CH_3SH

The decomposition of CH_3SH was firstly tested at 900 °C by introducing CH_3SH without steam to the catalytic system. Fig. 1 shows the variations of CH_3SH, H_2 yield and by-product selectivities with time from the reaction. It can be seen that CH_3SH initially converts and several gaseous products are formed; the main products from the reaction were primarily H_2, CO and CO_2 with slight formations of CH_4 and H_2S. Nevertheless, after 6 min of exposure, the trends of H_2 and CO steadily decreased and reached almost 0% CO production within 30–40 min, whereas the formations of CH_4 and H_2S oppositely increased. The sulfur balance calculation was applied to determine the portion of sulfur present in the gaseous phase and sulfur coverage in the solid phase at various exposure times. It can be revealed from the calculation that, within the first 6 min, most of gaseous sulfur compounds initially adsorbs by CeO_2, nevertheless, the portion of sulfur in gas phase then increases steadily with increasing exposure time (from 9.3% at 6 min to 98.4% at 50 min). After 60 min, nearly 100% of inlet sulfur is present in the outlet gaseous product. This calculation result is in good agreement with the result in Fig. 1, from which the percentages of CH_3SH and H_2S in the outlet increase with increasing exposure time. It is noted according to the homogeneous (non-catalyst) study that CH_3SH could partially decompose to H_2S at 900 °C; furthermore, CH_3SH could also react with H_2 via the hydrodesulfurization to form CH_4 and H_2S ($CH_3SH + H_2 \rightarrow CH_4 + H_2S$). Hence, the trend of H_2 decreases while those of H_2S and CH_4 increases with time for the prolong testing.

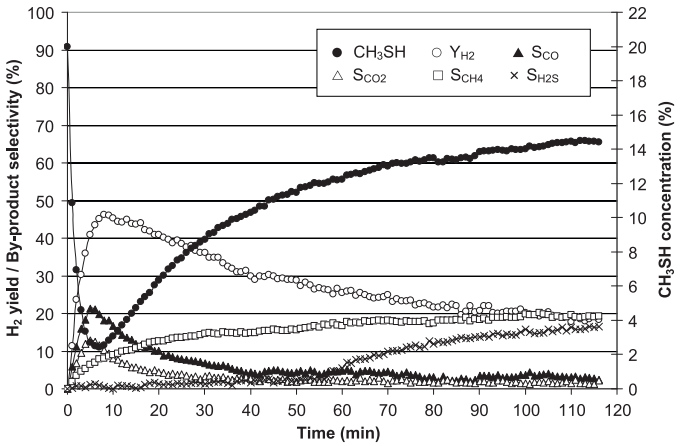

Fig. 1. Variations of CH_3SH, H_2 yield and other by-product selectivities with time from the reaction without steam over CeO_2 at 900 °C.

For comparison, the steam reforming of CH_3SH was then studied at 900 °C by adding steam along with CH_3SH to the catalytic system. It is noted that the inlet steam/CH_3SH ratios were varied from 0.5 to 1.0, 2.0, and 3.0. As seen in Fig. 2, the consumption of CH_3SH increases with increasing the inlet steam/CH_3SH ratio and insignificant deactivation was observed at the inlet steam/CH_3SH ratio of 3.0 (particularly within the first 60 min of exposure). Fig. 3 presents the CH_3SH variation, H_2 yield and by-product selectivities from the steam reforming of CH_3SH (with inlet steam/CH_3SH ratio of 3.0); clearly, the main products are H_2, CO, CO_2 and CH_4. This study

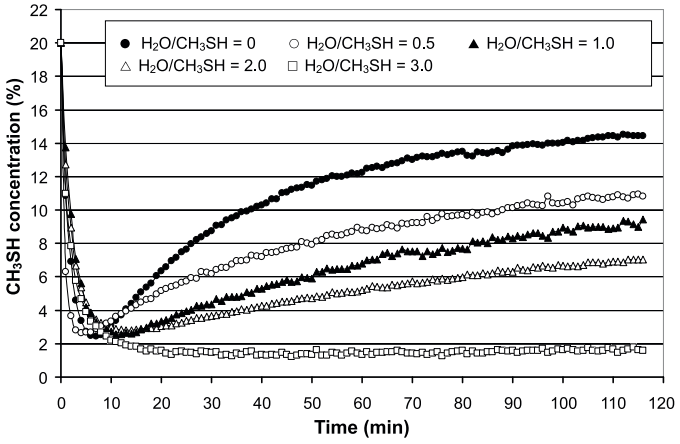

Fig. 2. Effect of steam adding on the consumption of CH_3SH with time from the reaction over CeO_2 at 900 °C.

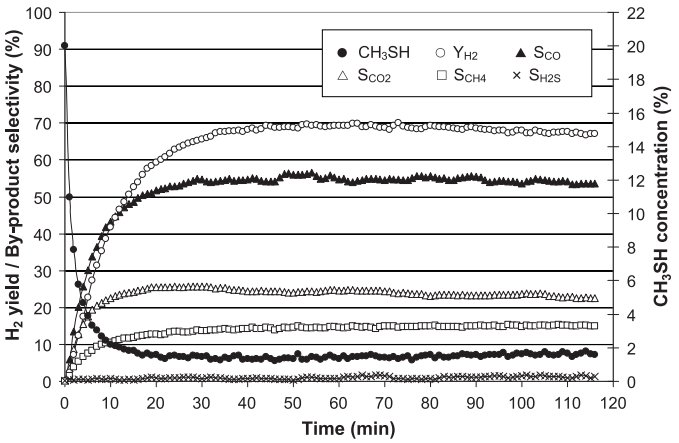

Fig. 3. Variations of CH_3SH, H_2 yield and other by-product selectivities with time from the reaction of CH_3SH in the presence of steam (with inlet H_2O/CH_3SH molar ratio of 3.0) over CeO_2 at 900 °C.

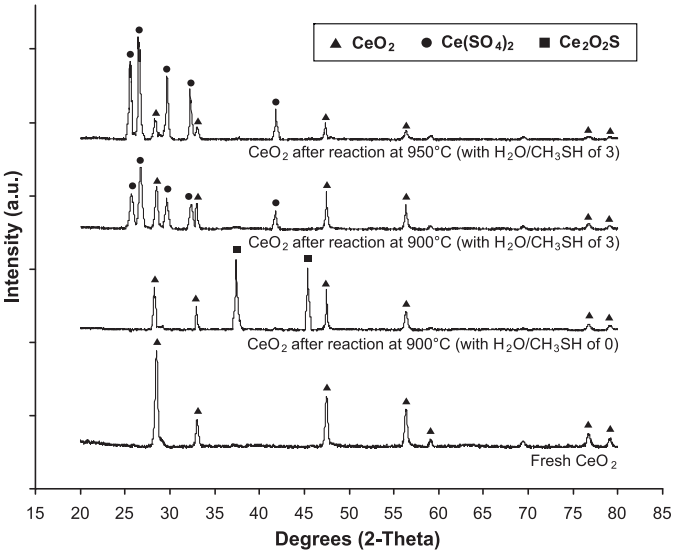

Fig. 4. XRD patterns of CeO_2 at various reaction conditions.

reveals that the capability of nano-scale CeO_2 to reform poisonous CH_3SH and produce hydrogen-rich gas as the clean alternative fuel would offer great benefit in terms of energy and environmental management. Nevertheless, as also seen in Fig. 3, H_2 yield slightly decreases after 80 min of exposure while the trend of CH_3SH oppositely increases. This indicates that the activity of catalyst actually declines though slowly in the latter period of reaction test. The sulfur balance calculation also confirms that the sulfur coverage on CeO_2 continually accumulates with increasing time, therefore it is obvious that the catalyst is subject to deactivation. Therefore, more studies (i.e. the optimization of operating conditions and the regeneration of catalyst) are required.

In order to understand the characteristic of CH_3SH reaction over CeO_2, several characterizations over fresh and spent catalysts from the reaction at various conditions were performed. According to the XRD studies, various Ce–O–S phases, i.e. $Ce(SO_4)_2$, $Ce_2(SO_4)_3$ and Ce_2O_2S are formed over spent catalysts from the reaction with different proportions depending on the operating conditions used (Fig. 4). These XRD results were analyzed and all Ce–O–S phase portions at each condition are summarized in Table 1. It was found that, by introducing CH_3SH and steam (with inlet steam/CH_3SH ratio of 3.0) for 2 h, $Ce(SO_4)_2$ is the main phase formation. In the experiments with inlet steam/CH_3SH ratios of 0.5, 1.0 and 2.0, the phases

Table 1
Percentage of Ce–O–S phase formation after reaction with CH_3SH at various operating conditions for 2 h.

Temperature (°C)	Steam/CH_3SH ratio	Percentage of phase formation (%)			
		CeO_2	$Ce(SO_4)_2$	$Ce_2(SO_4)_3$	Ce_2O_2S
900	0.0	26	0	0	74
900	0.5	4	13	15	68
900	1.0	9	32	14	45
900	2.0	19	57	12	12
900	3.0	22	78	0	0
925	3.0	18	82	0	0
950	3.0	13	87	0	0
975	3.0	9	91	0	0
1000	3.0	6	94	0	0

of $Ce_2(SO_4)_3$ and Ce_2O_2S are also observed along with $Ce(SO_4)_2$. On the other hand, by applying the inlet steam/CH_3SH ratios of 0 and 0.5, Ce_2O_2S become the dominant Ce–O–S phase. The sulfur balance calculation also indicated that the coverage of sulfur on CeO_2 increases with increasing time for all conditions but with different proportion depending on the inlet steam/CH_3SH ratio; the highest sulfur coverage on CeO_2 appears to be for the case with inlet steam/CH_3SH ratio of 3.0. It is suggested from these XRD studies and the sulfur balance calculation that the differences in catalyst activity (in terms of CH_3SH variation, H_2 yield and by-product selectivities) from the reaction of CH_3SH over CeO_2 are mainly related to the amount of sulfur coverage on CeO_2 and the Ce–O–S phase formations at different operating conditions. We proposed that Ce_2O_2S can be formed via the solid–gas reaction of CH_3SH on the surface of CeO_2 (Eqs. (5) and (6)).

$$2CeO_2 + CH_3SH \Leftrightarrow Ce_2O_3 + 2H_2S + CO \quad (5)$$

$$Ce_2O_3 + CH_3SH \Leftrightarrow Ce_2O_2S + 2H_2 + CO \quad (6)$$

By introducing H_2O along with CH_3SH, the phase of $Ce_2(SO_4)_3$ occurs (via Eq. (7)) and turns to $Ce(SO_4)_2$ when higher inlet H_2O content (inlet steam/CH_3SH ratio of 3.0) is applied (via Eq. (8)).

$$2CeO_2 + 11H_2O + 3CH_3SH \Leftrightarrow Ce_2(SO_4)_3 + 15.5H_2 + 3CO \quad (7)$$

$$Ce_2(SO_4)_3 + 5H_2O + CH_3SH \Leftrightarrow 2Ce(SO_4)_2 + 7H_2 + CO \quad (8)$$

It is revealed from Eqs. (7) and (8) that although H_2 generated could play the role of regenerating the sulfur compounds during the reaction, the regeneration rate is slow than the rate of sulfur-compound formation, thereby the activity changes with time. In addition, the steam/CH_3SH ratio can affect H_2 yield production and eventually influences the formation of Ce–O–S phases (i.e. $Ce(SO_4)_2$, $Ce_2(SO_4)_3$ and Ce_2O_2S). We indicated that these $Ce(SO_4)_2$, $Ce_2(SO_4)_3$ and Ce_2O_2S phases provide different CH_3SH reforming activity, from which the formation of $Ce(SO_4)_2$ during the reaction leads to the high reforming activity, whereas the presence of Ce_2O_2S reduces the catalyst activity. To confirm this clarification, the redox properties associated with the OSC and the mobility of lattice oxygen for spent CeO_2 from the reaction with inlet steam/CH_3SH molar ratio of 3.0 (containing 78% $Ce(SO_4)_2$ and 22% CeO_2 phases, according to the XRD study) were examined and compared to fresh CeO_2 by applying TPR and $^{18}O/^{16}O$ isotope exchange methods since it is known that these redox properties are closely related with the catalyst reforming activity. Furthermore, the ratio of Ce^{3+}/Ce^{4+} over sulfate-form samples (i.e. $Ce(SO_4)_2$ and Ce_2O_2S) and CeO_2 was also characterized by XPS (Kratos Amicus); the analyses were carried out with Mg Kα X-ray source under a working pressure of 1×10^{-6} Pa at current of 20 mA and 12 kV, resolution of 0.1 eV/step, and pass energy 7 at 5 eV. The binding energy was calibrated using the C 1s peak at 285.0 eV as reference.

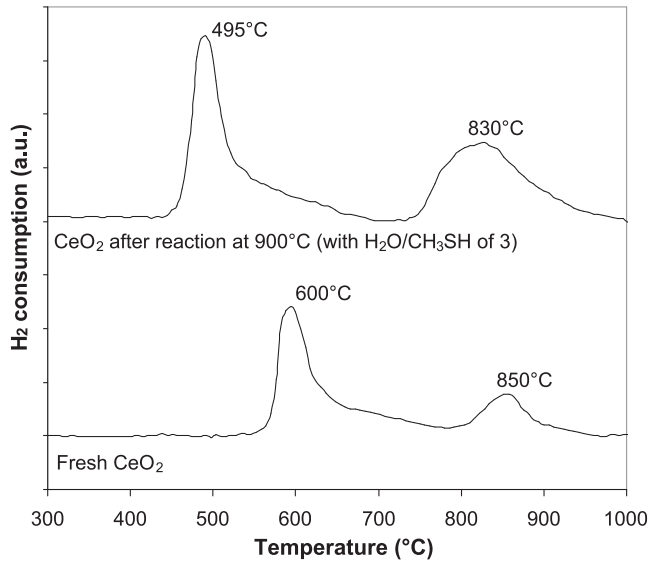

Fig. 5. TPR profiles of fresh CeO_2 and spent CeO_2 from the reaction at 900 °C with H_2O/CH_3SH ratio of 3.0).

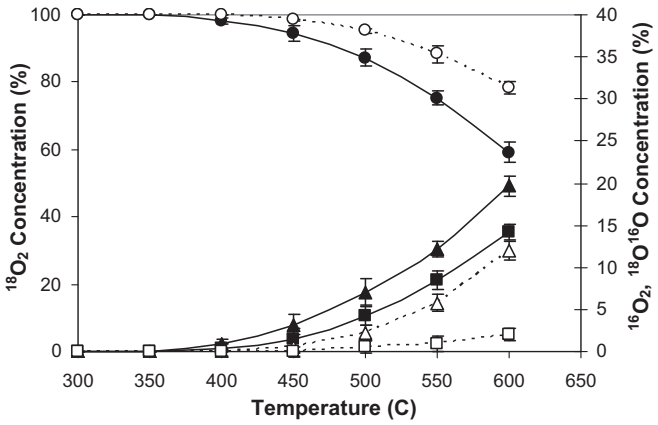

Fig. 6. $^{18}O/^{16}O$ isotope exchange over spent CeO_2 (●: $^{18}O_2$, ▲: $^{16}O_2$ and ■: $^{18}O^{16}O$) and fresh CeO_2 (○: $^{18}O_2$, △: $^{16}O_2$ and □: $^{18}O^{16}O$).

As shown in Fig. 5, the TPR of spent CeO_2 indicated a sharp reduction band at 495 °C and a broader band at 830 °C, whereas smaller peaks were detected at slightly higher temperatures (i.e. 600 °C and 850 °C) for fresh CeO_2. These amounts of H_2 uptake were applied to calculate the amount of reducible oxygen in the catalysts. From the calculation, the amount of reducible oxygen for spent CeO_2 was estimated to be 1.13 mmol g^{-1} compared to 0.71 mmol g^{-1} for fresh CeO_2; this clearly indicates the higher OSC of $Ce(SO_4)_2$. In addition, from the $^{18}O/^{16}O$ isotope exchange study as shown in Fig. 6, the production of $^{16}O_2$ and $^{18}O^{16}O$ from spent CeO_2 is greater than those from CeO_2 at the same operating temperature. For instance, at 600 °C, the productions of $^{16}O_2$ and $^{18}O^{16}O$ for spent CeO_2 are 19.7 and 14.2%, whereas the productions of $^{16}O_2$ and $^{18}O^{16}O$ for fresh CeO_2 are 12 and 2%. This clearly implies the higher oxygen mobility to $Ce(SO_4)_2$ compared to CeO_2. It is noted that the exchanging of $^{18}O/^{16}O$ isotopes over CeO_2 surface could come from: (i) homoexchange in gas phase ($^{18}O_2$ (g) + $^{16}O_2$ (g) → $^{18}O^{16}O$ (g)); and (ii) heteroexchange with the participation of oxygen atom from CeO_2 ($^{18}O_2$ (g) + $^{16}O_2$ (*S*) → $^{18}O^{16}O$ (g) + ^{18}O (*S*) and $^{18}O/^{16}O$ (g) + $^{16}O_2$ (*S*) → $^{16}O_2$ (g) + ^{18}O (*S*)). According to our results, the homoexchange in gas phase is negligible since $^{18}O/^{16}O$ concentration from both materials are different (they should be identical if the exchange in gas phase is dominant the overall reaction [32]). The XPS studies were then performed to quantify Ce^{4+} and Ce^{3+} levels of spent CeO_2 compared to fresh CeO_2 under reducing and oxidizing conditions. It was found that the contents of Ce^{3+} for the spent CeO_2 under reducing and oxidizing conditions are 31.1% and 11.9%, respectively, whereas those for fresh CeO_2 under reducing and oxidizing conditions are 24.9% and 19.8%, respectively. These results suggest that CeO_2 in sulfate form promotes higher reduction/oxidation between Ce^{4+} and Ce^{3+} compared to CeO_2. Based on these results, the higher OSC and lattice oxygen mobility of $Ce(SO_4)_2$ compared to CeO_2, which consequently lead to the higher reforming activity, can be confirmed. It is noted that a few studies in the literature have previously reported the formation of sulfated form CeO_2 during the reaction with SO_2 and also indicated its high oxygen storage capacity [33], which is likely to support the explanation in the present work.

3.3. Practical application (1): the use of CeO_2 as catalyst support

Although it can be summarized from the above section that nano-scale CeO_2 has capability to reform CH_3SH and produce hydrogen-rich gas, this catalyst alone as a reforming catalyst gives relatively low reforming activity and significant amount of unconverted CH_3SH remains present in the gaseous product. Furthermore, some CH_4 also detect in the product due to its incomplete conversion to CO and H_2. Although this problem could be minimized by applying higher reaction temperature as shown in Fig. 7 (from which the CH_3SH and CH_4 contents in the product can be reduced to 0 and 1%, respectively, at 1000 °C), the use of high operating temperature generally requires high energy input to the system and eventually reduce the overall system efficiency. Therefore, we proposed the pairing of CeO_2 with a suitable metallic catalyst to obtain the catalyst with self-desulfurization capability and enhance high reforming activity. For the first approach, CeO_2 was applied as catalyst support and Rh (5 wt% Rh) was impregnated over its surface to form Rh/CeO_2.

As shown in Fig. 8(a), high amounts of H_2 and CO were initially produced from the steam reforming of CH_3SH (with inlet steam/CH_3SH molar ratio of 3.0) over Rh/CeO_2; nevertheless, the rate dramatically dropped in a short period time (20–25 min). For comparison, the reaction over Rh/Al_2O_3 was also tested. After 1 h of operation, H_2S and CH_4 (occurred from the thermal decomposition of CH_3SH) were mainly observed from the reaction over this catalyst, Fig. 8(b). It is noted according to the XRD studies over the spent Rh/CeO_2 and Rh/Al_2O_3 catalysts that the formation of rhodium sulfide was detected for both catalysts and this phase is rarely regenerated. This result indicates that although CeO_2 can efficiently reform CH_3SH to hydrogen-rich gas, the chemisorption of CH_3SH over Rh surface and the coverage of Rh over CeO_2 surface area inhibit the catalyst activity and consequently result in the high deactivation rate. This implies the inappropriate use of CeO_2 as catalyst support for the CH_3SH reaction under the specific conditions in the present work. It should be noted that the use of CeO_2 as catalyst support might still be possible by adjusting the operating conditions, e.g., H_2O/CH_3SH ratio and temperature, which requires more studies on these optimizations.

3.4. Practical application (2): the use of CeO_2 as catalyst coating material

For the second approach, nano-scale CeO_2 was used as a coating barrier over cylindrical-shape Rh/Al_2O_3 pellet with an aim to desulfurize and primary reform CH_3SH at the CeO_2 coating layer prior the secondary reform by Rh catalyst. Fig. 9 shows the variation of CH_3SH with time from the steam reforming of CH_3SH at 900 °C over CeO_2-coated Rh/Al_2O_3 with various coating times (0, 1, 2, 3, 4 and 5

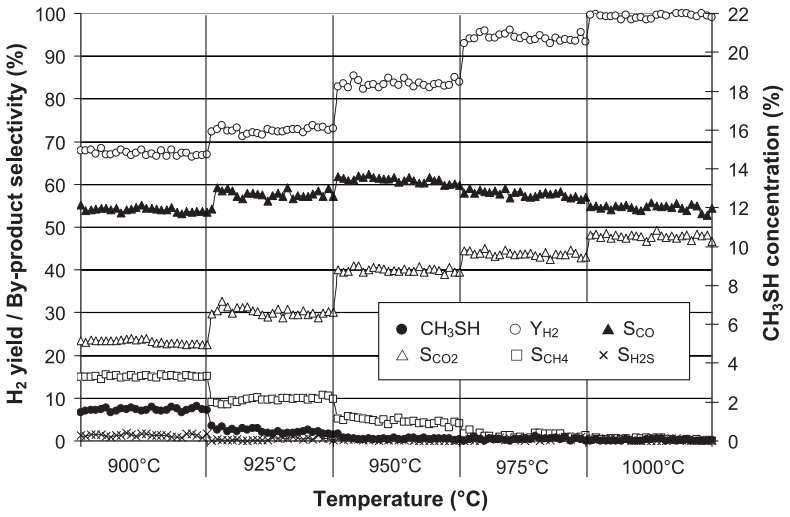

Fig. 7. Effect of temperature on CH_3SH consumption, H_2 yield and other by-product selectivities from the reaction of CH_3SH in the presence of steam (with inlet H_2O/CH_3SH molar ratio of 3.0) over CeO_2.

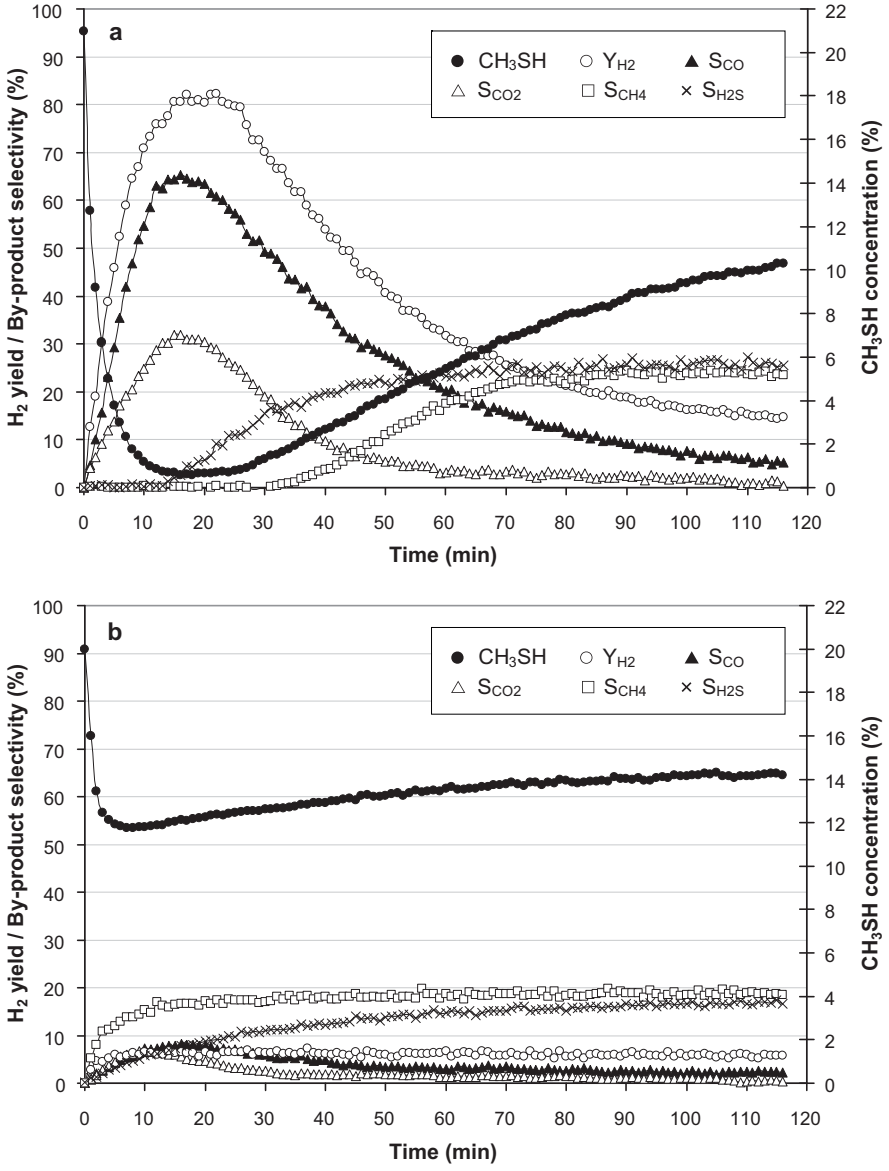

Fig. 8. Variations of CH_3SH, H_2 yield and other by-product selectivities with time from the steam reforming of CH_3SH (with inlet H_2O/CH_3SH molar ratio of 3.0 at 900 °C) over (a) Rh/CeO_2 and (b) Rh/Al_2O_3.

Please cite this article in press as: N. Laosiripojana, S. Assabumrungrat, Appl. Catal. B: Environ. (2011), doi:10.1016/j.apcatb.2010.12.008

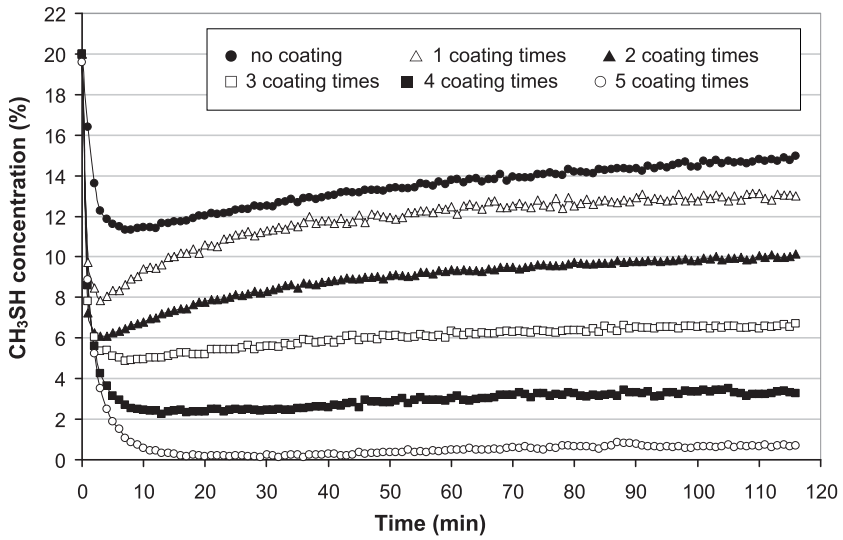

Fig. 9. Effect of CeO_2 coating times over Rh/Al_2O_3 pellet on the CH_3SH consumption from the steam reforming of CH_3SH (with inlet H_2O/CH_3SH molar ratio of 3.0 at 900 °C).

times). It can be seen that the consumption of CH_3SH increases with increasing CeO_2 coating time. After 5 times coating, no deactivation was observed, furthermore, the main products from the reaction were mainly H_2, CO and CO_2 without CH_4 formation (Fig. 10), indicating the complete reforming of CH_3SH. This improvement is due to the proper coating of Rh/Al_2O_3 by CeO_2 and the increase of CeO_2 mass loading over the catalyst. From the weighting of CeO_2-coated Rh/Al_2O_3 with various coating times, the mass loading of CeO_2 over an Rh/Al_2O_3 pellet (with the initial weight of 100 mg) at 1, 2, 3, 4 and 5 coating times are 12, 18, 21, 25 and 30 mg, respectively. These CeO_2 loading values were also confirmed by the TPR/TPO titration experiment, from which the OSC values of CeO_2-coated Rh/Al_2O_3 at various coating times were measured and calibrated with the OSC value of known-amount CeO_2 powder. From this titration experiment, the mass loading of CeO_2 over each pellet of CeO_2-coated Rh/Al_2O_3 with 1, 2, 3, 4 and 5 coating times are estimated to be 10.7, 18.4, 20.2, 24.7 and 29.8 mg, respectively, which is relatively close to those observed by the weighting method.

As the next step, the prolong reaction testing was performed and it was found that the deactivation in H_2 yield start occurs after exposure for 12–15 h (Fig. 11). This deactivation is clearly due to

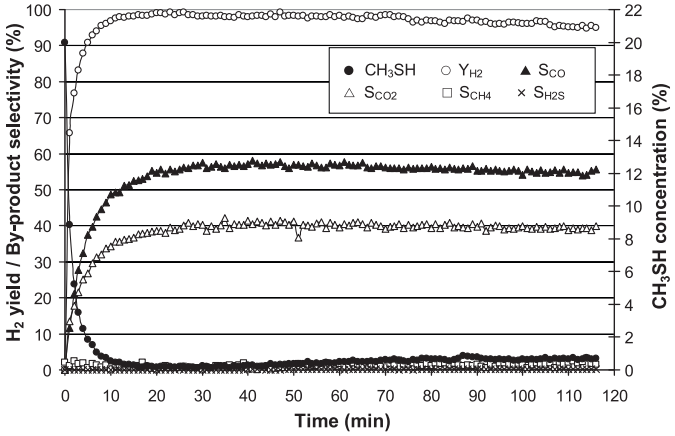

Fig. 10. Variations of CH_3SH, H_2 yield and other by-product selectivities with time from the steam reforming of CH_3SH (with inlet H_2O/CH_3SH molar ratio of 3.0 at 900 °C) over CeO_2-coating Rh/Al_2O_3 (5 times coating).

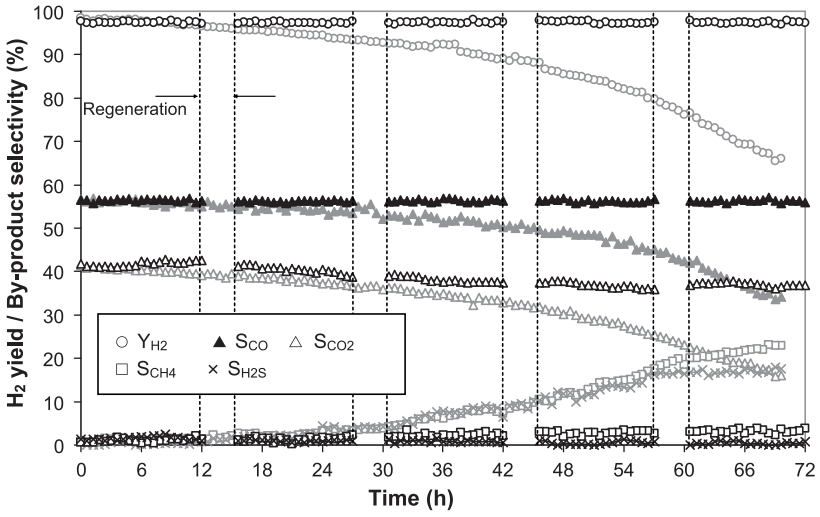

Fig. 11. Variation of H_2 yield and other by-product selectivities with time during pro-long testing from the steam reforming of CH_3SH with inlet H_2O/CH_3SH molar ratio of 3.0 at 900 °C over CeO_2-coating Rh/Al_2O_3 with and without catalyst regeneration (represents as blank and gray symbols, respectively).

Please cite this article in press as: N. Laosiripojana, S. Assabumrungrat, Appl. Catal. B: Environ. (2011), doi:10.1016/j.apcatb.2010.12.008

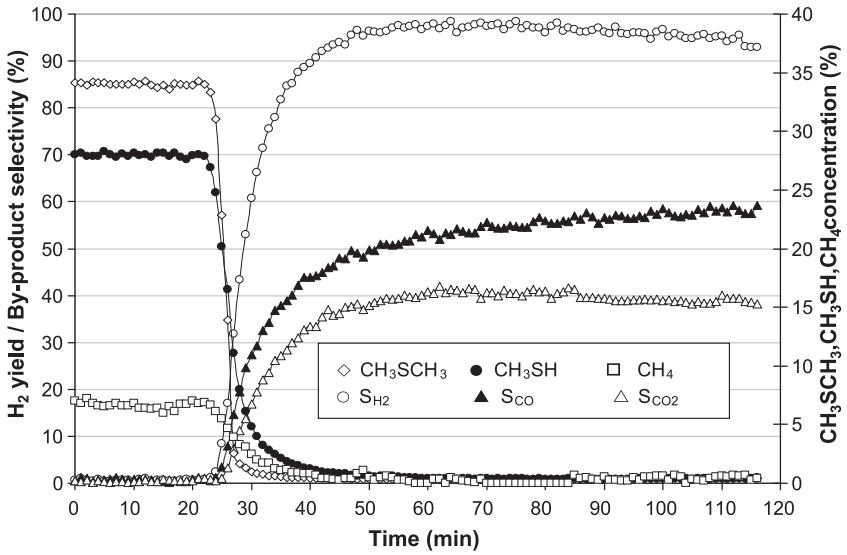

Fig. 12. Conversion of industrial-waste flue gas (containing mercaptan compounds) to hydrogen-rich gas by the steam reforming over CeO_2-coating Rh/Al_2O_3 at 900 °C.

the complete occupied of CeO_2 surface by sulfur compound as confirmed by the sulfur balance calculation (from which the portion of sulfur in the gaseous product is close to 100%) and the XRD analysis of spent catalyst (from which Ce_2O_2S is mainly detected). Hence, the regeneration of CeO_2 is required. In the present work, after operating for 12 h, the catalyst regeneration was performed by purging air at 900 °C for 1 h. The form of gaseous sulfur compound emitted during the catalyst regeneration is mainly SO_2, which occurs from the oxidation of coverage sulfur on CeO_2 with oxygen. Furthermore, by purging Ce_2O_2S with air, the phase of CeO_2 and $Ce(SO_4)_2$ can be regenerated via the gas–solid reaction of $0.2Ce_2O_2S + 0.5O_2 \rightarrow 0.1Ce(SO_4)_2 + 0.3CeO_2$, as suggested by Luo and Gorte [34]. Without the catalyst reactivation required, the same levels of H_2 yield and other by-product selectivities can be achieved after regeneration (Fig. 11), in addition, no significant deactivation is detected after operated for 72 h with 5 reaction cycles. This reveals the successful regeneration of CeO_2 by air and highlights the importance of the regeneration step for prolong reaction run.

Lastly, the potential use of this CeO_2-coated Rh/Al_2O_3 to treat and convert industrial-waste offgas, which contains CH_3SH and CH_3SCH_3, to hydrogen-rich gas was investigated. In this study, the composition of the offgas used (from the olefin manufacturing plant of Siam Cement Group (Thailand)) is 28% CH_3SH, 34% CH_3SCH_3, 7% CH_4 and 18% H_2O balances in nitrogen. It was found that, at 900 °C in the presence of H_2O (with the steam/mercaptans ratio of 3.0), CeO_2-coated Rh/Al_2O_3 efficiently converts this offgas to hydrogen-rich gas (mainly H_2, CO and CO_2) without H_2S present in the outlet gas (Fig. 12). Based on this product composition, it is sufficient to use as the primary fuel for solid oxide fuel cell to general electricity. Therefore, we conclude form the study that this developed catalyst provides great benefit of integrating the clean energy generation with toxic-waste treatment, which offers significant energy and environmental benefits. Nevertheless, before the commercialization, more investigation on the catalyst development, i.e. optimizing the Rh content and/or finding an alternative metal to replace the expensive precious metal Rh-based catalyst should be further studied.

4. Conclusions

Poisonous CH_3SH can be converted to hydrogen-rich gas by the steam reforming over nano-scale CeO_2 under sufficient condition. During the reaction in the presence of H_2O, $Ce(SO_4)_2$ is formed and offers strong hydrocarbon reforming activity. In contrast, without H_2O adding, Ce_2O_2S is formed and lower the catalyst activity. For practical application, CeO_2-coated Rh/Al_2O_3 was developed and tested for the reactions of CH_3SH and industrial-waste offgas containing mercaptan compounds. This catalyst was found to have good activity, stability, and reusability (in 5 reaction cycles for 72 h) for converting these feedstocks to hydrogen-rich gas without sulfur compounds present in the product.

Acknowledgement

The financial support from The Thailand Research Fund (TRF) throughout this project is gratefully acknowledged.

References

[1] L.A. Komarnisky, R.J. Christopherson, T.K. Basu, Nutrition 19 (2003) 54–61.
[2] American Conference of Governmental Industrial Hygienists, Threshold limit values for chemical substances and physical agents in the workroom environment, Cincinnati, OH, 1978.
[3] H. Tamai, H. Nagoya, T. Shiono, J. Colloid Interface Sci. 300 (2006) 814–817.
[4] A. Bagreev, J.A. Menendez, I. Dukhno, Y. Tarasenko, T.J. Bandosz, Carbon 43 (2005) 208–210.
[5] I.A.A.C. Esteves, M.S.S. Lopes, P.M.C. Nunes, J.P.B. Mota, Separ. Purif. Technol. 62 (2008) 281–296.
[6] S. Bashkova, A. Bagreev, T.J. Bandosz, Catal. Today 99 (2005) 323–328.
[7] H.L. Chiang, J.H. Tsai, D.H. Chang, F.T. Jeng, Chemosphere 41 (2000) 1227–1232.
[8] H. Chu, W.T. Lee, K.H. Horng, T.K. Tseng, J. Hazard. Mater. 82 (2001) 43–53.
[9] D. Klvana, J. Delval, J. Kirchnerova, J. Chaouki, Appl. Catal. A 165 (1997) 171–182.
[10] D. Klvana, J. Kirchnerová, J. Chaouki, J. Delval, W. Yaïci, Catal. Today 47 (1999) 115–121.
[11] C.H. Tsai, W.J. Lee, C.Y. Chen, W.T. Liao, Ind. Eng. Chem. Res. 40 (2001) 2384–2395.
[12] M. Flytzani-Stephanopoulos, M. Sakbodin, Z. Wang, Science 312 (2006) 1508–1510.
[13] G.A. Deluga, J.R. Salge, L.D. Schmidt, X.E. Verykios, Science 303 (2004) 993–997.
[14] A. Grirrane, A. Corma, H. García, Science 322 (2008) 1661–1664.
[15] J.A. Rodriguez, S. Ma, P. Liu, J. Hrbek, J. Evans, M. Pérez, Science 318 (2007) 1757–1760.
[16] K. Otsuka, M. Hatano, A. Morikawa, J. Catal. 79 (1983) 493–496.
[17] T. Takeguchi, S.N. Furukawa, M. Inoue, K. Eguchi, Appl. Catal. A 240 (2003) 223–233.
[18] H. Muroyama, S. Hano, T. Matsui, K. Eguchi, Catal. Today 153 (2010) 133–135.
[19] A. Trovarelli, Catal. Rev. Sci. Eng. 38 (1996) 439–520.
[20] P. Fornasiero, G. Balducci, R.D. Monte, J. Kaspar, V. Sergo, G. Gubitosa, A. Ferrero, M. Graziani, J. Catal. 164 (1996) 173–183.
[21] T. Miki, T. Ogawa, M. Haneda, N. Kakuta, A. Ueno, S. Tateishi, S. Matsuura, M. Sato, J. Phys. Chem. 94 (1990) 339–341.
[22] C. Padeste, N.W. Cant, D.L. Trimm, Catal. Lett. 18 (1993) 305–316.
[23] S. Kacimi, J. Barbier Jr., R. Taha, D. Duprez, Catal. Lett. 22 (1993) 343–350.
[24] G.S. Zafiris, R.J. Gorte, J. Catal. 143 (1993) 86–91.

[25] S. Imamura, M. Shono, N. Okamoto, R. Hamada, S. Ishida, Appl. Catal. A 142 (1996) 279–288.
[26] E. Ramírez-Cabrera, A. Atkinson, D. Chadwick, Appl. Catal. B 47 (2004) 127–131.
[27] D.J.L. Brett, A. Atkinson, D. Cumming, E. Ramírez-Cabrera, R. Rudkin, N.P. Brandon, Chem. Eng. Sci. 60 (2005) 5649–5662.
[28] C.T. Campbell, C.H.F. Peden, Science 309 (2005) 713–714.
[29] N. Laosiripojana, S. Assabumrungrat, Appl. Catal. B 60 (2005) 107–116.
[30] N. Laosiripojana, S. Assabumrungrat, Appl. Catal. B 82 (2008) 103–113.
[31] D. Terribile, A. Trovarelli, J. Llorca, C. Leitenburg, G. Dolcetti, J. Catal. 178 (1998) 299–308.
[32] Y. Zeng, S. Kaytakoglu, D.P. Harrison, Chem. Eng. Sci. 55 (2000) 4893–4900.
[33] T. Luo, R.J. Gorte, Appl. Catal. B 53 (2004) 77–85.
[34] T. Luo, R.J. Gorte, Catal. Lett. 85 (2003) 139–146.

Please cite this article in press as: N. Laosiripojana, S. Assabumrungrat, Appl. Catal. B: Environ. (2011), doi:10.1016/j.apcatb.2010.12.008